Department of Imaging and Applied Physics

Wide Bandwidth Focal Plane Array Receiver for Radio Astronomy

Nino Bukilic

This thesis is presented for the Degree of
Doctor of Philosophy
of
Curtin University of Technology

September 2010

Declaration

To the best of my knowledge and belief this thesis contains no material previously published by any other person except where due acknowledgment has been made.

This thesis contains no material which has been accepted for the award of any other degree or diploma in any university.

Signature: …….

Date: ……...

Abstract

Reflective antennas equipped with phase array feeds (PAFs) have been proposed as part of the Square Kilometre Array reference design, since they offer a wide Field of View (FoV) and large collecting area. To achieve a contiguous FoV, and to cancel spill-over radiation, the Focal Plane Array (FPA) must sample the focal field of the reflector at least every half-wavelength at the upper operating frequency. Low-noise operation over a wide bandwidth requires appropriate impedance matching to the low-noise amplifiers, and this is a challenging research problem since the input impedance of the FPA elements can vary strongly with frequency.

Advanced broadband design techniques for antenna arrays have resulted in antenna shapes getting more complex. Modelling of these antennas can only be carried out using numerical computational electromagnetic methods (CEM), and accurate modelling of complex antennas demand the full-wave analysis with fields and currents that vary in three dimensional space. The Frequency Domain Integral Equation model is adopted in this study and used via the Method of Moments (MoM) technique for simulation and modelling of the FPA. The "MoM Antenna Development Toolbox" (MoMADT), 64 bit version of the modelling software, is specifically developed in this study for designing, building and modelling of complex antenna and electromagnetic structures. MoMADT utilizes surface and volume integral equations and provides functions for generating precise meshes and accurate method of moments solutions. MoMADT enables structures to be assembled in an array formation to consist of conductive or dielectric materials, or a combination of both.

Study of the wide bandwidth FPA receiver was achieved through analysis of broadband planar antenna structures. This research investigates a unique design solution for a FPA utilizing the diamond planar strip antenna elements arranged to provide three vectors of polarization (triple-polarized FPA). The most promising FPA identified is the 7×7 Hexagonal Diamond Tripole (HDT) array. This array yields an operating frequency range of 550 to 2100 MHz, providing bandwidth ratio of 3.8:1. It is shown that adequate

impedance match can be achieved across the indicated frequency range with desired directivity and gain. In addition, the 7×7 HDT array offers optimized efficiency and allows the polarization to be distinguished at any angle about the axis normal to the antenna plane to within a theoretical uncertainty of ± 2.2°. This is also true for any function of the FoV allowed by the surface area of the FPA.

Acknowledgements

I would like to take this opportunity to thank my supervisor Professor Mervyn J. Lynch for his help and support during the course of my PhD study, as well as my associate supervisors John Kot and Stuart Hay from CSIRO ICT centre at ATNF for their help and guidance in preparing this project.

I would like to thank my parents and my family, especially my mother who has supported me from the very beginning.

I would also like to extend my thanks to Professor Sergey N. Makarov from Worcester Polytechnic Institute (WPI) Massachusetts, for providing the core volume integral equation codes and consequently the collaborative work we have performed in development of the MoMADT modelling software.

Contents

List of Figures

+Donates additional text

List of Tables

Introduction

Aperture synthesis radio antennas, such as those proposed for the Square Kilometre Array (SKA) radio telescope, generally consist of an array of antennas and receivers (or radio sensors). The received signals or voltages from these sensors are cross-correlated and integrated in a way to reduce noise providing spatial, spectral and temporal sampling of the incoming radiation. The utilization of these new technologies is driven by cost effective solutions. Cost is a major factor forcing the SKA project towards new technologies and architectures. Design solutions being considered for the SKA range in wavelength from 3 m to 3 cm. In order of frequency, the design solutions for the SKA are: Sparse Aperture Arrays (70 to 200 MHz), Dense Aperture Arrays (200 to 500 MHz), parabolic reflectors with Phased Array Feeds (500 to 1100 MHz), and reflectors with Single Pixel Feeds (1100 to 10000 MHz) [1].

Reflector antennas equipped with Phased Array Feeds offer a wide Field of View (FoV) and large collecting area. To achieve a contiguous FoV, and to cancel spill-over radiation, the Focal Plane Array (FPA) must sample the focal field of the reflector at least every half-wavelength at the upper operating frequency. Low-noise operation over a wide bandwidth requires appropriate impedance matching to the low-noise amplifiers, and this is a challenging research problem since the input impedance of the FPA elements can vary strongly with frequency. This is especially the case for wideband arrays, since towards the lower frequency of operation the array spacing can be very small in terms of wavelength, leading to very strong mutual coupling effects between the array elements. For wideband operation, the FPA must yield adequate polarization purity, directivity, gain and efficiency over the required frequency range and these parameters must be reliable as a function of the FoV and/or phase.

This thesis investigates a unique design solution for a wide bandwidth FPA receiver for reflector antennas through the analysis of broadband planar antenna structures. Antenna parameters are studied in relation to structure, shape, element size, element spacing, ground plane distance, array configuration and overall array size. These characteristics are compared against directivity, gain, polarization purity and bandwidth of the antenna. It is found that for wideband operation, some common scaled planar structures such as bowtie, spiral, square, equilateral-triangle antennas requires that the antenna be of appropriate size and length and wide enough for operation at lower frequencies. While these structures may exhibit wideband properties, when used in arrays they generate large element spacing. It is shown that large element spacing deteriorates the gain and directivity of the array at higher frequencies which results in reduced bandwidth. In addition, it is discovered that polarization purity of the array is highly influenced by polarization cross-talk between the oppositely oriented elements. It is concluded that precise dimension, structure and orientation must be considered to insure that low polarisation cross-talk and appropriate element spacing between the oppositely oriented elements of the array is achieved. Finally, this thesis identifies the most promising antenna structure to be used in a FPA for which all of the above parameters are met.

Two unique design solutions, the 5×5 and 7×7 Hexagonal Diamond Tripole (HDT) FPA, are presented in this study utilizing the diamond planar strip antenna elements arranged to provide three vectors of polarization (triple-polarized FPA). The most promising FPA identified is the 7×7 three-axis HDT array. The 7×7 HDT-FPA comprises 37 planar three-axis antenna elements and yields a total of 111 individual receiving ports, providing a bandwidth ratio of 3.8:1 for frequencies 550 to 2100 MHz. Whereas the 5×5 HDT-FPA contains a total of 57 individual receiving ports and offers bandwidth ratio of 3.4:1 for frequencies 500 to 1700 MHz. The array size, total number of elements, as well as the configuration of the antenna shows that the system yields a robust and simple-to-manufacture structure, and offers a relatively cost effective solution.

The FPA presented in this study offers an operating frequency range much larger than originally proposed for the parabolic reflectors with Phased Array Feeds (500 to 1100 MHz). This thesis will show that the 7×7 HDT-FPA yields optimized efficiency over the required bandwidth and allows the polarization to be distinguished at any angle about the axis normal to the antenna plane to within a theoretical uncertainty that varies as a function of frequency by maximum of ± 2.2°. This is also true for any function of the FoV allowed by the surface area of the FPA. It is also shown that adequate impedance match can be achieved across the indicated frequency range with desired directivity and gain.

A large portion of the design work is achieved through modelling carried out using numerical computational electromagnetic methods (CEM). The Frequency Domain Integral Equation model is used via the Method of Moments (MoM) technique for simulating and modelling of the FPA, using both surface and volume integral equations. The "Method of Moments Antenna Development Toolbox" (MoMADT), 64 bit modelling software, is specifically developed in this study for building and modelling of complex antenna structures. Design of the HDT-FPA is derived through modelling utilizing the MoMADT design tool.

After discussing the introduction to antenna theory and arrays, the modelling methods and procedures are introduced in chapter 1. Objectives and contributions of this project are then outlined and described in detail at the end of chapter 1. Antenna design and methodology are presented in chapter 2. Following this, the modelling implementation and solutions of diamond tripole antenna and the HDT-FPA are presented in chapter 3. Various contributions to knowledge are presented throughout chapters 1, 2, 3 and 4. Preliminary behaviour of the 7×7 HDT array and its elements are then demonstrated through application of physical measurements in chapter 4, with the exception to Low Noise Amplifiers. Conclusions and recommendations are presented in chapter 5. Details, including significance and versatility of the MoMADT modelling software are presented in Appendix A.

CHAPTER 1

Chapter 1 - Theory and Objective

Chapter 1 presents an introduction to antenna theory and arrays relating to the SKA and phased array feed technology. Following this, a review of Method of Moments modelling procedure and related computational electromagnetic theory is discussed, as well as the introduction to MoMADT software developed during the course of this study. The objectives and contributions of this dissertation are then outlined and described in detail at the end of this chapter.

1.1 Square Kilometre Array (SKA)

Reflective antennas equipped with phase array feeds (PAFs) have been proposed as part of the Square Kilometre Array (SKA) reference design [1], since they offer a wide Field of View (FoV) and large collecting area. The SKA design requirements are derived from its science goals and constrained by cost and technical performance parameters [2]. Some of these parameters include:

• **Wavelength coverage** – range being from 3 m to 3 cm (see Figure 1.1) [1].
• **Sensitivity** - The sensitivity factor of an antenna is measured with A_{eff}/T_{sys}, where A_{eff} is the effective collecting area of an antenna and T_{sys} is the total system noise [3]. In Phased Array Feeds, T_{sys} is strongly influenced by Low Noise Amplifiers (LNAs).
• **Survey speed** - The rate at which radio sources of a given strength can be detected in a large area of the sky is proportional to $(A_{eff}/T_{sys})^2\Omega$, where Ω is the instantaneous Field of View. This is also termed as the Survey Speed Figure of Merit (SSFoM) [1].
• **Array Configuration** - pattern of antennas on the ground which determine the range of spatial frequencies that the array can sample.

• **Bandwidth** - the instantaneous bandwidth that can be accessed affects the final sensitivity as $B^{1/2}$, where B is the processed bandwidth.

• **Imaging and Spectral Dynamic Range** - Imaging dynamic range is the ratio of the brightest point in an image to the RMS noise level in a region of the image. This also affects the ability to measure polarized component of the received emission, which is important for tracing magnetic fields. Spectral dynamic range is the ability for the instrument to detect the spectral-lines of atoms or molecules, when observed across the field of view. In this case the strong sources in the sidelobes of the antennas can contaminate the image [1].

• **Pulsars -** The SKA science goal also has set a high priority on using radio pulsars to increase understanding of the fundamental physics. These types of observations require the ability to collect data from individual antennas for massive post-processing operations using time-gated averaging and post-processing of array data [1].

• **Time resolution** – impacts the ability to investigate radio transients.

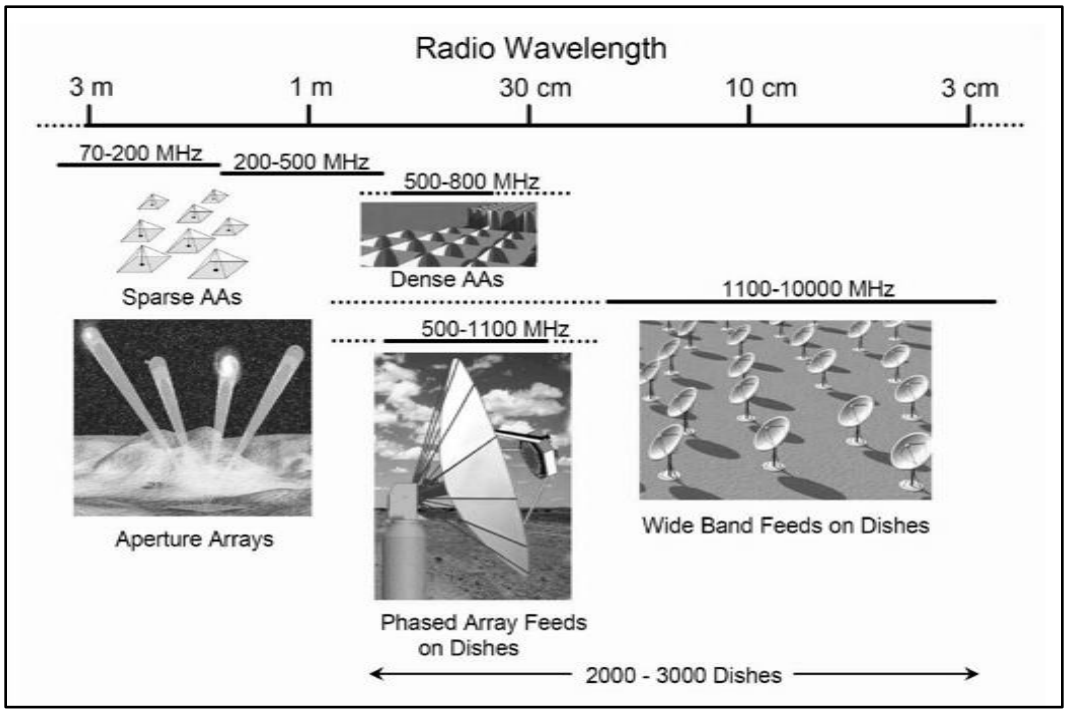

Figure 1-1 Proposed SKA sensor technologies, showing: Sparse Aperture Arrays (70-200 MHz), Dense Aperture Arrays (200-500 MHz), parabolic reflectors with Phased Array Feeds (500-1100 MHz), and reflectors with Single Pixel Feeds (1100-10000 MHz) **[1]**

Parameters explained above, together with the SKA science goals, suggest that such observations may not be achievable using a single technology. As a result, the four indicated SKA sensor technologies in Figure 1.1 are considered for its design.

1.2 Antenna Temperature and System Temperature

A radio telescope antenna (and receiver) may be regarded as a radiometer (or temperature measuring device) for remote sensing the temperature of distant regions coupled to the system through the radiation resistance of the antenna. All objects whose temperatures are not at absolute zero produce radiation which, in principle, may be detected with a radio antenna-receiver. For example, temperature of a distant quasar is said to be over 10^6 K, of Mars 164 K, of a transmitter on the earth 10^6 K, of a man 310 K, of the ground 290 K, while the empty sky at zenith is 3 K [4]. Given that the radiation from these sources is said to be unpolarised [5], [6], any antenna (whether linearly or circularly polarised) receives only half of the available power. Hence, for such sources, the flux density of the source at the antenna is given by the following equation [6], [7]:

$$S = \frac{2k\Delta T_A}{A_e} \quad (W\ m^{-2}Hz^{-1}) \tag{1.1}$$

where,

ΔT_A = is the incremental noise temperature of the antenna

A_e = is the effective aperture of the antenna

K = is the Boltzmann's constant (1.38×10^{-23} J K^{-1}).

The total antenna temperature is then given by [6]:

$$T_A = \frac{1}{\Omega_A}\int_0^{\pi}\int_0^{2\pi} T_s(\theta,\varphi)P_n(\theta,\varphi)d\Omega \qquad (K) \tag{1.2}$$

where,

T_A = total antenna temperature, K

$T_s(\theta,\varphi)$ = brightness temperature of source of sources as function of angle, K

$P_n(\theta,\varphi)$ = normalized antenna power pattern, dimensionless

Ω_A = antenna beam solid angle,

$d\Omega$ = $\sin\theta\, d\theta\, d\varphi$ = infinitesimal element of solid angle.

An antenna system is considered to be a part of a receiving instrument consisting of an antenna, a receiver and a transmission line which connects them. The temperature of a system, or *system temperature*, is a critical factor in determining the sensitivity and signal-to-noise ratio of a receiving system. The system temperature depends on the noise temperature of the sky, the ground, antenna surroundings, antenna pattern, antenna thermal efficiency, receiver noise temperature, and efficiency of the transmission line between the antenna and receiver. The system temperature of the antenna terminals can be approximated using the following equation [6]:

$$T_{sys} = T_A + T_{AP}\left(\frac{1}{\epsilon_1} - 1\right) + T_{LP}\left(\frac{1}{\epsilon_2} - 1\right) + \frac{1}{\epsilon_2}T_R \tag{1.3}$$

where,

T_A = total antenna temperature, K

T_{AP} = antenna physical temperature, K

ε_1 = antenna (thermal) efficiency ($0 \leq \varepsilon_1 \leq 1$), dimensionless

T_{LP} = line physical temperature, K

ε_2 = line efficiency ($0 \leq \varepsilon_1 \leq 1$), dimensionless

T_R = receiver noise temperature (see below), K

The receiver noise temperature (T_R) is then given by:

$$T_R = T_1 + \frac{T_2}{G_1} + \frac{T_3}{G_1 G_2} + \cdots \tag{1.4}$$

where,

T_1 = noise temperature of first stage of receiver, K

T_2 = noise temperature of second stage, K

T_3 = noise temperature of third stage, K

G_1 = power gain [5] of first stage

G_2 = power gain [5] of second stage.

Thus, sensitivity and signal-to-noise ratio of a receiving system can be determined using above methods, however additional stages in equation 1.4 may be required if the temperatures are sufficiently high and the gains sufficiently low [6].

1.3 Phased Array Feed Technology

Antennas exhibit a specific radiation pattern which changes when several antenna elements are combined in an array. This is due to the so called array factor [5]. The array factor quantifies the effect of combining radiating elements in an array without the element specific radiation pattern taken into account. The array factor is evidently influenced by the number of elements, element spacing, amplitude, frequency and phase of the applied signal to each element.

Antenna arrays were first proposed in 1899, and implemented in 1906 [8]. The sole purpose of arrays was to shape or increase the directivity of a radiating system. Whereas the sole purpose of phased arrays was to increase the radar scanning speed [9]. The term *phased array* has come to mean an array of many elements with the phase of each element being a variable, providing control of the beam direction and pattern shape including side-lobes [5], [9]. Another objective of a phased array is to provide beam control at a fixed frequency or at any number of frequencies within a certain bandwidth in a frequency-independent manner. In principle, the beam steering of a phased array can be instantaneous and, with suitable networks, all beams can be formed simultaneously, although the scan angle or field of view of a planar phased array may be restricted [10].

In recent decades, antenna arrays were realised to provide increased FoV and survey speed for radioastronomical observations [11]. In a parabolic reflector antenna, these instruments are referred to as Focal Plane Arrays (FPAs) or Phased Array Feeds (PAFs) [12]. Dense FPA feeds comprise many small elements that are conjugate-matched (combined as a complex weighted sum) to the focal plane field. This enables the instrument to fully sample a region of sky providing contiguous coverage [13].

In order to achieve a contiguous coverage, low-noise operation over a wide bandwidth requires appropriate impedance matching to the low-noise amplifiers (LNAs) [14]. LNAs are devices that are generally designed for standardised input impedances by people with different skills to those who design antennas. When signals from the FPA are electrically balanced, the efficiency depends critically upon the differential mode and common mode load impedances presented by the LNAs. The performance of LNAs is strongly influenced by the driving impedance presented by the PAF [15]. Thus, successful measurement of low noise and wide bandwidth FPA must incorporate testing of the antenna array and the LNAs as an optimized integrated unit [16]. Recent advances in analogue electronics allow the use of uncooled LNAs [17], however the limiting factor of present best LNAs is their wavelength coverage. The best low-noise amplifiers to date generally cover a bandwidth ratio of 2:1 [1]. Instruments that behave outside of this range may require multiple LNAs per feed combination. However, a new generation of wideband LNA feeds are being developed, some of which cover a bandwidth ratio of 15:1 [18].

Over the past two decades, several research organisations have been working intensively on designing and implementing PAF technology for radio astronomy. ASTRON group from Netherlands have performed major work on Vivaldi focal plane arrays [19], [20], [21], and have made advances in areas of beamforming [11]. At present, ASTRON maintain an active program with the FPA development on one of the Westerbork radiotelescope dishes [22], [23]. DRAO/NRC group from Canada have also performed work in development of Vivaldi FPAs [24], with recently released results on the 180 element prototype [25]. BYU/NRAO group from the U.S. have performed work on the

L-Band 19-element phased array feed [26], and the CSIRO group from Australia have invested in the study and design of the chequer board array [12], [14], [15], [27]. CSIRO is currently building the Australian SKA Pathfinder (ASKAP), a radiotelescope with 36 12 m radio dishes fitted with FPAs [28]. The CSIRO and ASTRON PAFs are designed for wideband operation of approximately 2:1 and 3:1 ratios of upper and lower frequency limits [14], [19]. While the L-Band 19-element BYU/NRAO array offers 1.3:1 ratio [26].

Designing FPAs requires a full understanding of the system, including a detailed model of the electromagnetics of the FPA and its relationship to the reflector and the receiving electronics [14], [29], [30]. During development of an array, it is common to measure the scattering matrix and radiation patterns of the array separately from the receiver electronics [12]; once accomplished, knowledge of the characteristics of electronics can be used and overall performance of the array can be predicted. However, when the system is assembled, an approach referred to as black-box [12] can be used for measurements. In this approach, the measured data from beamformed outputs and correlated inputs against each element are used to determine the weights and see how they relate to the common figure of merit [5], [12]. The CSIRO group responsible for the development of the ASKAP and the chequer-board FPA, explain that the maximum figure of merit [5] can be determined using a simpler weighing method which involves normalizing the conjugate match signal with the noise from each element [12].

1.4 Antenna Structures and Frequency Selective Surfaces

In wideband FPAs, the input impedance of the FPA elements can vary strongly with frequency. This is especially the case towards the lower frequency of operation since the array spacing can be very small in terms of wavelength, leading to very strong mutual coupling effects between the array elements. There are two design approaches widely considered to this problem: 1) broadband arrays above ground plane, and 2) broadband travelling wave structures.

Travelling wave antennas (eg. Vivaldi antenna) rely on electrical length to produce unidirectional radiation. Unless such structures are well-matched, the length of the structure causes sharp resonances, leading to large variations in the input impedance. Whereas the broadband arrays over a ground plane create reflections and coupling effects from the ground, thereby placing basic limits on operating frequency.

Broadband arrays above a ground can be designed with elements that consist of wide bandwidth characteristics. It is said that the surface of these elements is frequency selective for a wider band of frequencies [31]. A frequency selective surface is a surface which exhibits different reflection and/or transmission properties as a function of frequency. For example, an array of resonant dipoles as shown in Figure 1.2a, acts as a band-stop filter, passing waves above and below the dipole resonant frequency but not at the resonant frequency. The complementary array of slots (Figure 1.2b) acts as a band-pass filter, passing waves at the resonant frequency of the slots but rejecting them at higher and lower frequencies [32].

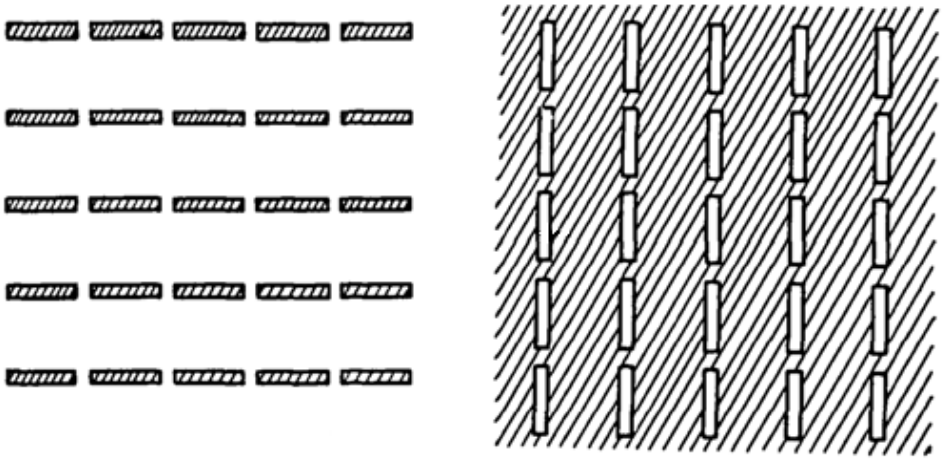

a) Band-stop b) Band-pass

Figure 1-2 Basic frequency selective surface, showing: (a) array of dipoles that acts as a band-stop filter, and (b) array of complementary slots in a perfectly conducting sheet acts as a band-pass filter **[32]**.

If the dipole array in Figure 1.2a is aligned and placed on top of the slot array in Figure 1.2b, this would yield a complete perfectly conducting surface. It is said that the two surfaces are therefore complementary to each other [32]. This means that the reflection and transmission coefficients for one surface will equal the transmission and reflection coefficients of the other, respectively, assuming that the angle of incidence of the electro-magnetic (EM) wave is constant. The above statement illustrates a simple example of Babinet's principle [32].

Antenna structures should always be carefully examined for variations with the angle of incidence as well as polarisation, because the change of angle of incidence can alter the resonant frequency and the bandwidth [33], [34], [35]. One example of this is to examine the dipole antenna shown in Figure 1.3a. It is said that when the dipole antenna is of length λ/2 (half-wavelength), it will resonate and scatter effectively. However, this resonance may change considerably with angle of incidence because the inter-element spacing needed becomes larger than λ/2. One correction to this problem is to shorten the elements and tune them back to resonance by "loading" them with a small inductance (see Figure 1.3b). Alternatively, this inductance can be replaced by a two-wire transmission line (Figure 1.3c). In addition, this can also be converted into a bipolarised version called "four-legged loaded element" (Figure 1.3d), and the "three-legged loaded element" (Figure 1.3e) [31].

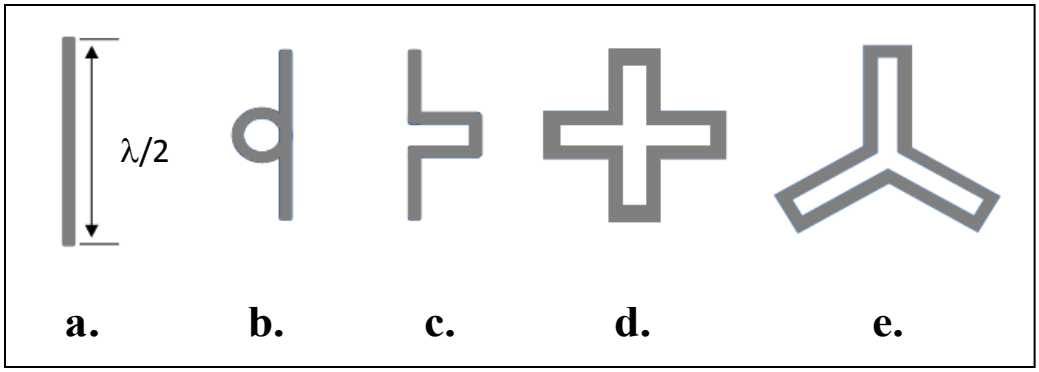

Figure 1-3 Development of loop elements showing: a) simple λ/2 dipole, b) shortened and inductively loaded dipole, c) shortened dipole with inductively loaded two-wire transmission line, d) four-legged loaded element and e) three-legged loaded element **[33]**

Structures in Figure 1.3 show that a simple development of a straight dipole can lead to elements that can be considered a loop. These loop elements (Figure 1.3d-e) resonate when circumference is equal to λ [31]. Other element types are also possible from these variations by "shooting" elements out from the centre [33].

The λ/2 dipole (Figure 1.3a), is not considered to be a particularly good element by itself [31]. However, when two dipoles are crossed, the resulting "cross-dipole" element (Figure 1.4a) can lead to presence of deep nulls in middle of resonance band for oblique angles of incidence and parallel polarization [36]. It is shown by Pelton and Munk [36] that reflection coefficient versus frequency of symmetrical crossed-dipole arrays (Figure 1.4b) exhibits two distinct resonances with null between them. This occurs when the dipole elements are on the order of a λ/2. It is also demonstrated by [36] that the null phenomenon occurring from the cross-dipole array is caused by the presence of two distinct current components on the elements, each having different resonant frequencies. Munk [31] points out that the problem with double resonance can be avoided if an "unloaded tripole" element is used instead (see Figure 1.4c). In case of the unloaded tripole, the two resonances degenerate into one [31]. Another possibility is to add end capacitances to obtain the anchor tripole element shown in Figure 1.4d [33].

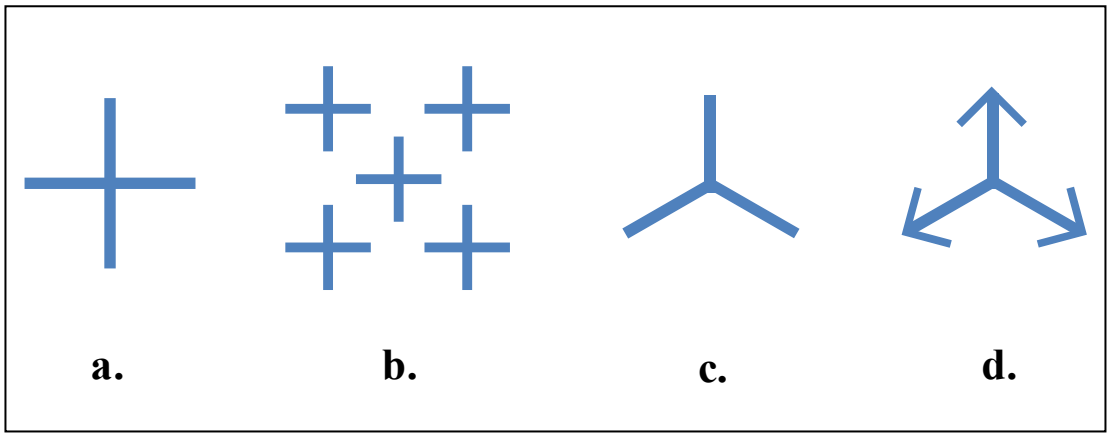

Figure 1-4 Center Connected or N-pole elements, showing: a) Cross-dipole antenna, b) Cross-dipole array, c) Unloaded tripole element, and d) Anchor tripole element **[33]**.

All elements described in Figure 1.4 are called "centre connected" or "N-poles" because they are characterized by having all of their element arms connected at the centre [31]. This means that not only can an even mode exist on these elements, but also an odd mode for oblique incidence [33]. Further discussion on the unloaded tripole antenna and its significance to the work is presented in Chapter 2.

1.5 Embedded Antennas and Ground Planes

In idealized situations, the fields of most antennas are affected by the presence of the ground. The change in the pattern and impedance relations may differ from those when the antenna or the array is in free space. This is especially the case if the antenna or antenna array is very close to the ground.

If we consider the λ/2 dipole above a perfectly conducting surface (see Figure 1.5), the field at some point P can be determined using the *method of images* approach [37]. In this method, the ground is replaced by an image of the antenna situated at some distance *h* below the ground plane (see Figure 1.5).

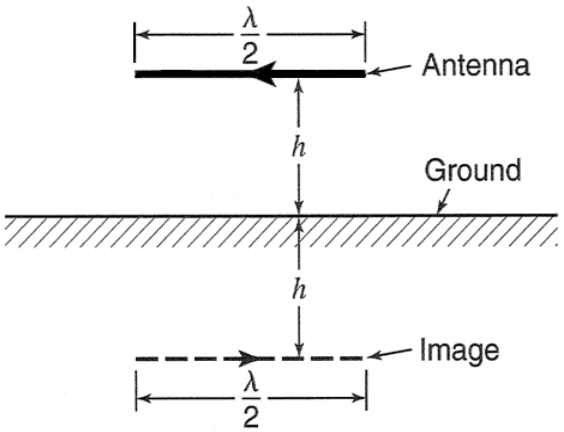

Figure 1-5 Horizontal λ/2 antenna at height *h* above ground with image of equal distance below ground **[37]**

If the ground in Figure 1.5 is considered to be perfectly conducting, the tangential component of the electric field must vanish at the surface. This means that the current in the "image" must be equal in magnitude but reversed in phase by 180°. Thus, using this method, the horizontal antenna above ground can be treated as an end-fire array whose pattern and impedance can be determined as described by Kraus [37], [38]. The "method of images" can also be used for horizontally or vertically stacked elements or arrays, as well as for ground planes of infinite but finite conductivity of dielectric constant (ε), by properly adjusting the relative magnitude and phase of the image current with respect to the antenna current [37], [39]. However, if the antenna is in contact or embedded in a dielectric medium, this method no longer applies. For embedded antennas, the pattern and impedance must be determined using alternative means.

If a λ/2 dipole is embedded in a dielectric medium, it will resonate when its physical length is equal to $0.5\lambda/\sqrt{\varepsilon_r}$, where ε_r is the relative permittivity of the dielectric [40]. This enables the antenna size to be reduced with increasing relative permittivity. For example, Kraus [40] describes that in Bluetooth technology [41], antennas operate at frequency of approximately 2.6 GHz. At this frequency, a λ/2 dipole of size 5.8 cm is normally used, however, due to space restrictions in Bluetooth technology this dipole is embedded in dielectric medium of relative permittivity $\varepsilon_r = 3.0$. Which enables the antenna size to be reduced from 5.8 cm to 3.5 cm (see Figure 1.6) [40].

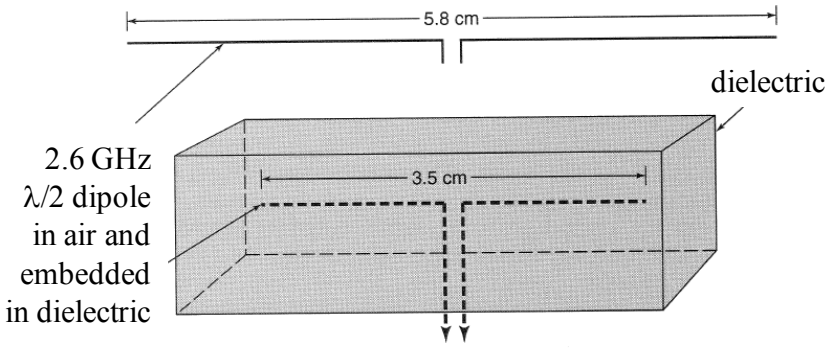

Figure 1-6 Half-wavelength dipole embedded in a dielectric medium for Bluetooth applications **[40]**

1.6 Baluns

The term *balun* is an abbreviation of the word *bal*ance and *un*balance [42]. It is a device that is used to connect a balanced two-conductor line to an unbalanced coaxial line. Thus, in measuring the impedance or radiation pattern of a balanced antenna using a coaxial cable, it is important to place a balun between the cable and the antenna feed. Unbalanced currents that may otherwise flow on the cable will make the measured antenna impedance sensitive to the configuration of the feed cable; in turn, the radiation pattern of the antenna may be distorted by radiation from the cable.

Figure 1.7a shows that when a horizontal dipole is fed directly from a coaxial line, the inner conductor feeds one half (in this case, the left half) of the dipole, generating current I_1, while the outer conductor feeds the right half generating current I_2. However, current I_3 will also flow down the outside of the outer conductor making it a part of the radiating system. The resulting pattern yields a mixture of horizontal polarization from the dipole itself (Figure 1.7b) and vertical-plus-horizontal polarization resulting from current I_3 (see Figure 1.7c). Thus, the overall pattern is not that of a horizontal dipole [42]. Under this circumstance a balun is essential.

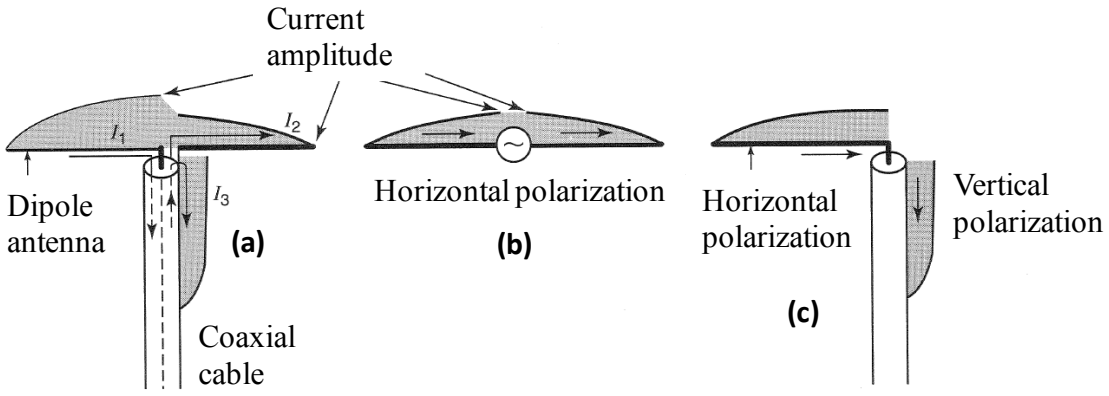

Figure 1-7 A horizontal dipole fed directly from a coaxial line produces: a) a mixture of balanced horizontal polarization and, b) a vertical-plus-horizontal polarization. Image obtained from **[42]**

In addition to providing transition from balanced to unbalanced terminals, baluns can also provide impedance transformation in situations where the impedance between the line and the antenna needs to be matched. However, besides the added complexity and expense to the system, baluns must also be customized for particular needs depending on the bandwidth [42]. Munk [42] describes a range of baluns that can be used for wide-bandwidth applications as well as baluns with built in transformers (Figure 1.8). It is said that some Type III baluns [42] (Figure 1.8a), have a very desirable feature since they can provide a perfect balance and a wide bandwidth. In addition, this type of balun can be modified to provide transitions to other types of baluns. Choke baluns such as the ferrite beads (Figure 1.8d) can also be used in some wide bandwidth applications [42].

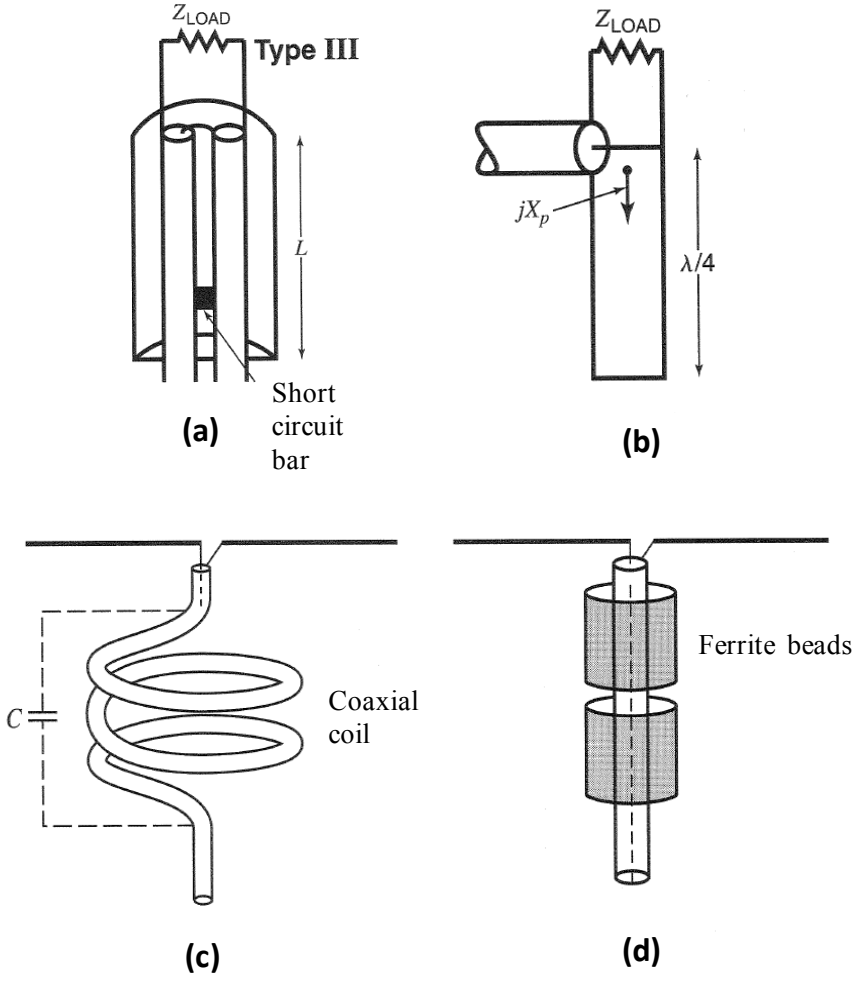

Figure 1-8 Balun types: a) Type III balun, b) Type III balun equivalent circuit, c) Choke balun with coaxial cable wound into coil, d) Choke balun cylindrical ferrite bead placed on the outside of the coaxial cable **[42]**

1.7 Parabolic Reflectors and Focal Field

When a parabolic reflector [5] is irradiated by an incident plane wave, the reflected or scattered field generates a focal field illumination pattern shown in Figure 1.9a. Figure 1.9a shows the focal plane illumination pattern generated from an on-axis focal field. Dotted line in Figure 1.9a represents the surface edge of the FPA. The total number of focal rings as well as the total power flux density incident on the focal plane, depend on the ratio between the diameter of the dish and the focal plane distance, termed as the F/D ratio [27] (see Figure 1.10). Furthermore, the size of the rings and the relative size of the central power flux density depend on the operating frequency and the overall FPA size (see Figure 1.9 and 1.10).

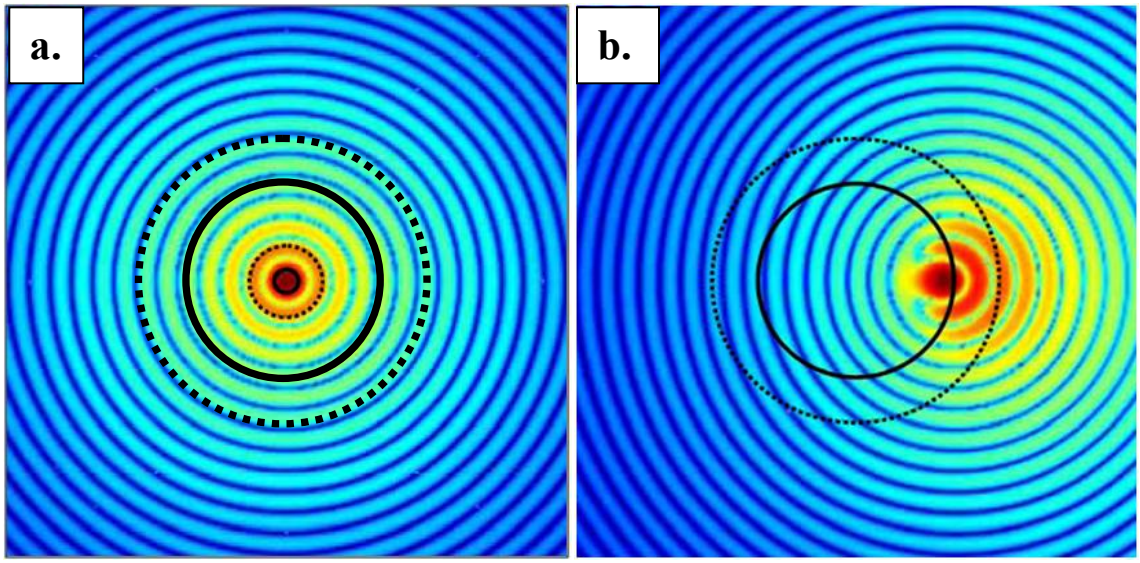

Figure 1-9 Focal plane illumination pattern showing, a) On-axis focal field and, b) Off-axis focal field **[27]**. The dotted line represents the edge of the FPA.

If the incident plane wave is displaced off-axis, which generally occurs as function of the field of view (FoV), then the scattered field or the central power of the focal field is also displaced off-axis, as illustrated in Figure 1.9b. This displacement of the focal field occurs in such a way that a large portion of the central power flux density is transferred on the forward rings with respect to the direction of the displaced field, see Figure 1.11.

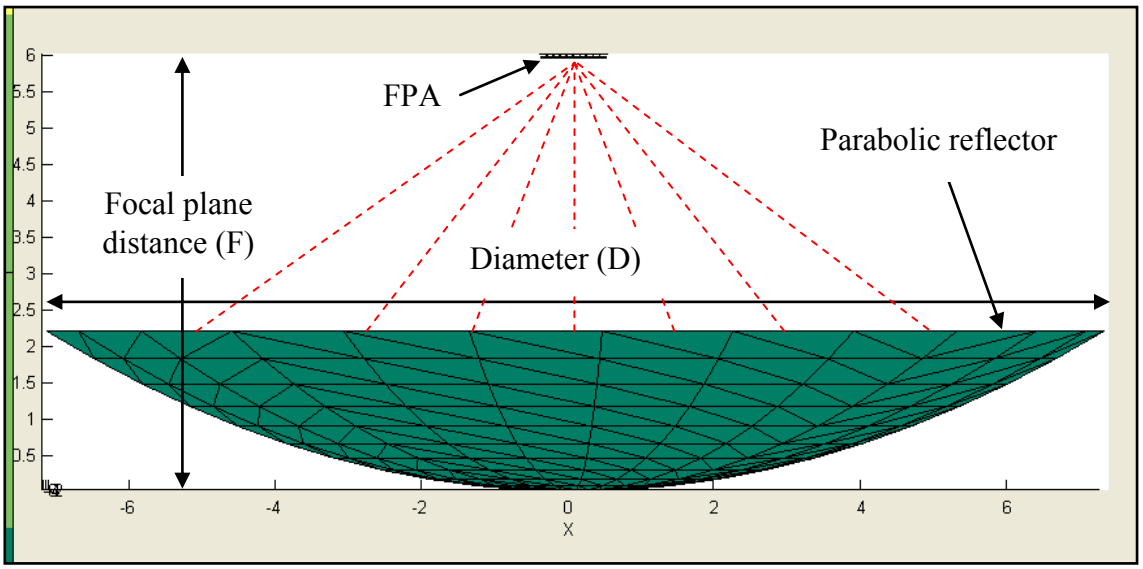

Figure 1-10 Parabolic reflector with the FPA located at the focal plane (F/D = 0.4)

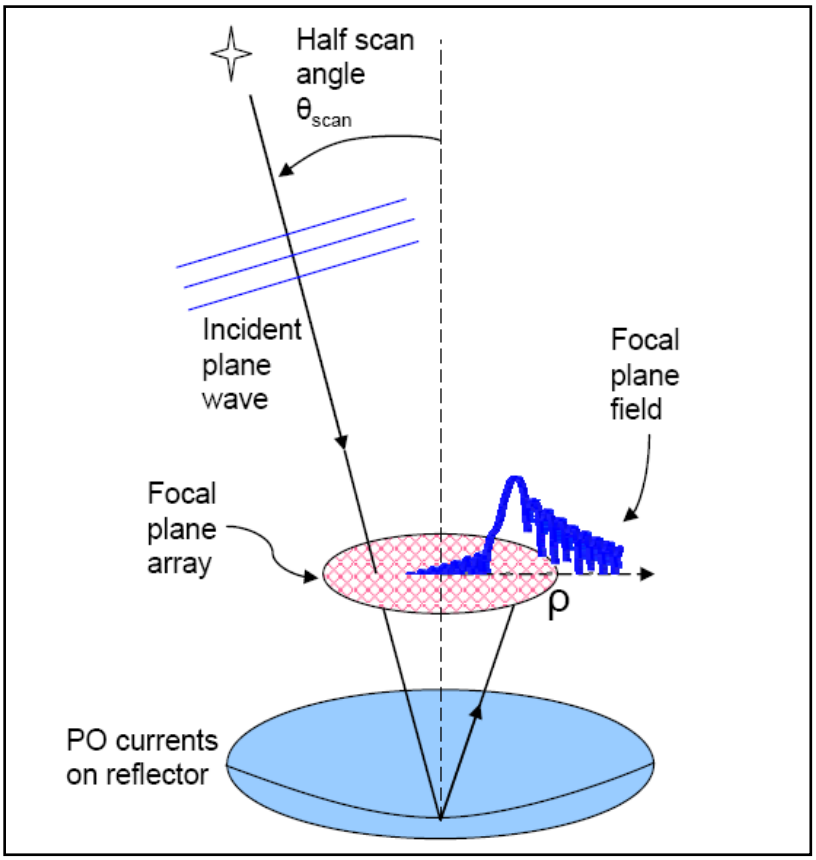

Figure 1-11 Parabolic reflector antenna showing the focal plane field at a specific off-axis value of θ (image obtained from [27])

Depending on the scan angle, the portion of the power transferred on the forward rings can be spilled outside the surface area of the FPA, see Figure 1.11. Practical solutions to reduction of spill-over noise can be obtained by introduction of an edge taper within the dish aperture. It has been shown that the tapered dish aperture scatters less power outside of the central spot of the focal field [27]. Understanding these factors is important for successful design of FPAs since the mutual coupling and polarization purity of the FPA is largely influenced by the displacement and distribution of the focal field. Additionally, the overall size, design and production cost of the FPA are critical to the selection of F/D ratios. An F/D ratio of 0.4 - 0.6 seem to be a reasonable choice [27].

1.8 Characteristic Modes

As briefly discussed in section 1.7, when the frequency of the incident electromagnetic field changes, or is increased, the shape of the focal field scattered from the parabolic reflector is altered. The relationship is such that at higher frequencies the central power flux density (poynting vector normal to the focal plane) will become narrower, as illustrated in Figure 1.12. When this occurs, the reception behaviour of the array situated at the focal plane can change significantly.

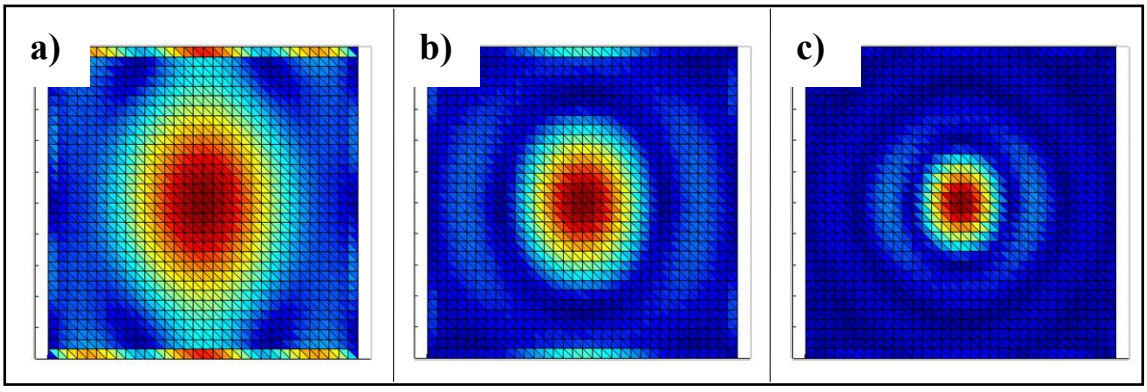

Figure 1-12 Effective change the focal field endures as function of frequency when a 1 m² conductive plate is irradiated by an incident focal beam at, a) 200 MHz, b) 300 MHz, and c) 500 MHz, reflected from a 15 m parabolic reflector of F/D ratio 0.4

Figure 1.12 shows the effective change the focal field endures as function of frequency when a 1 m² conductive plate is irradiated by an incident focal beam from a 15 m parabolic reflector, with an F/D ratio of 0.4. Result is modelled using method of moments. If the plate, in Figure 1.12, is treated as an array, the physical size and/or surface area would enable the antenna to capture fields that are viewed outside of the directional centre of the radio dish, thus allowing larger fields of view (FoV). Under this circumstance, the focal field is displaced off-axis with respect to the centre of the focal plane, see Figure 1.13. Thus, during reception, not only does the focal field change in size as a function of frequency, as illustrated in Figure 1.12, but it is also displaced off centre as function of the FoV as shown in Figure 1.13.

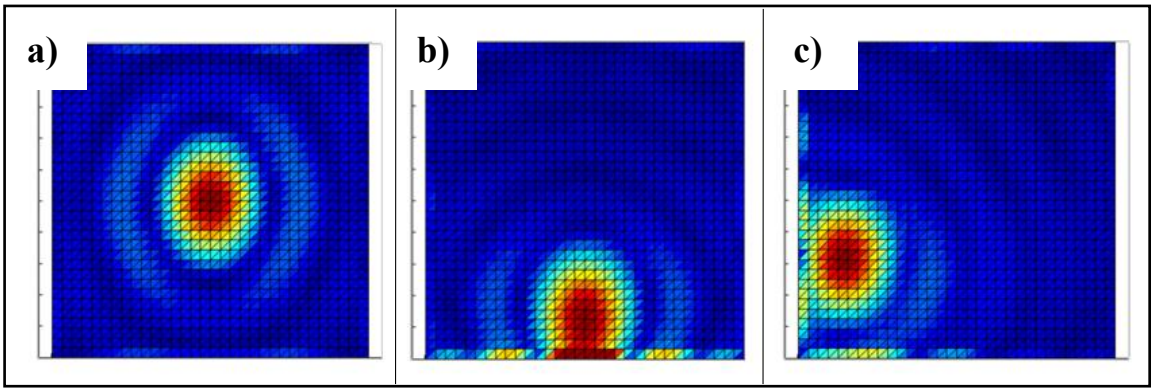

Figure 1-13 Figure illustrates the focal field displacement as function of the FoV, with characteristic modes generated at the edge of the 1 m² conducting plate at 500 MHz.

It is interesting to note from Figure 1.12 and Figure 1.13, that when the field is altered or displaced towards the edge of the conducting surface, strong currents are generated on the edges of the conducting plate. These surface currents are called characteristic modes. Characteristic modes are surface currents that are induced on surfaces of conducting bodies from an incident electromagnetic field or an applied electromotive force. These currents depend on the shape and size of the conducting body and are independent of any specific source or excitation [43], apart from the directional vector or polarization. Some examples of characteristic modes of arbitrary shaped planar structures are shown in Figure 1.14 and Figure 1.15.

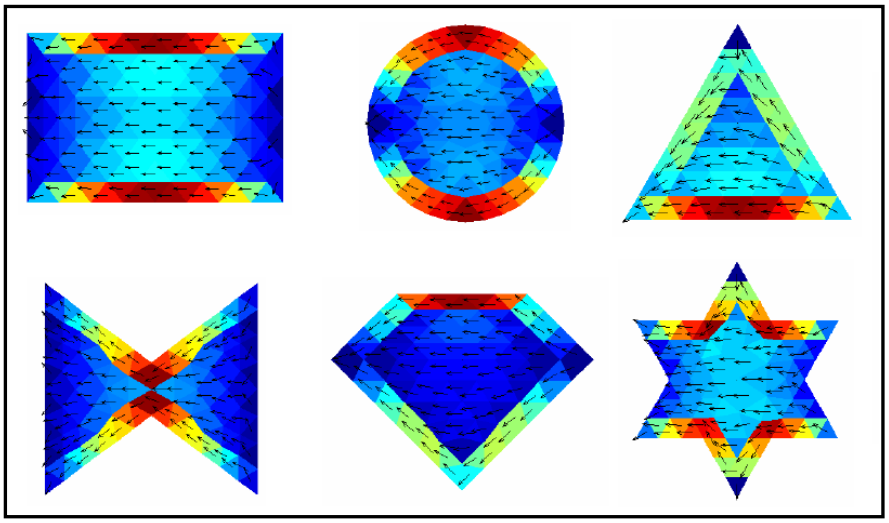

Figure 1-14 Horizontal characteristic modes on arbitrary shaped planar structures **[43]**

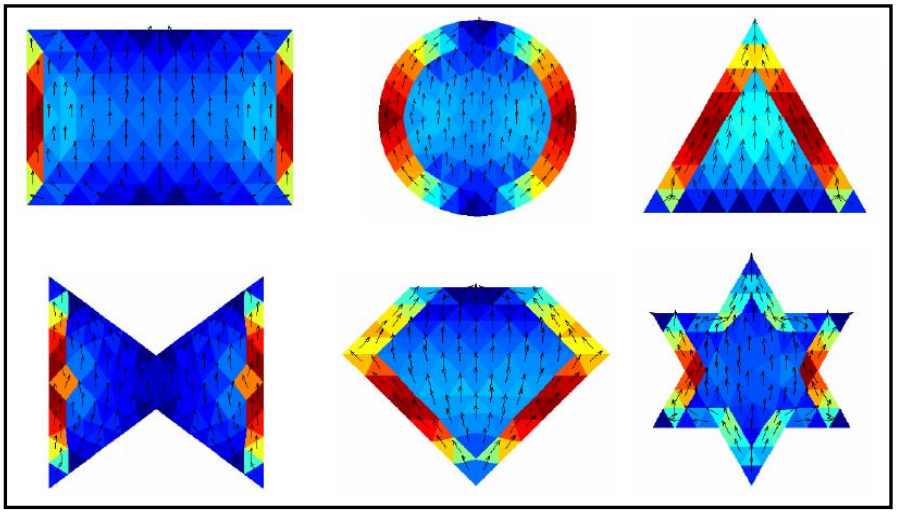

Figure 1-15 Vertical characteristic modes on arbitrary shaped planar structures **[43]**

Figures 1.14 and 1.15 show the horizontal and vertical characteristic modes induced on surfaces of arbitrary shaped planar structures. The maximum surface current density tends to occur at the very edge of objects. These currents radiate strong scattering fields

which, in turn, couple with neighbouring conductive bodies, such as a radiating element, ground plane, reflector, scatterer or a feed line. As a result, the reception behaviour of the array can be greatly altered both from reflections as well as the induced currents that result from the characteristic modes formed on the ground plane itself. Such systems should be designed so that characteristic modes are constructive to the reception of signals, and minimized or eliminated in situations where the interferences could be destructive.

Therefore, it is important to understand the basic behaviour of characteristic modes since the theory gives clear insight into the resonances occurring within the conducting body and helps in antenna design [44].

1.9 Computational Electromagnetic Design Tools

Advanced broadband design techniques for antenna arrays have resulted in antenna shapes getting more complex. Modelling of these antennas can only be carried out using numerical computational electromagnetic methods (CEM), and accurate modelling of complex antennas demand the full-wave analysis with fields and currents that vary in three dimensional space. In these methods, Maxwell's equations are transformed into matrix or chain equations and solved iteratively or by matrix inversion.

Computational electromagnetic methods have evolved rapidly during the past two decades to a point where very accurate predictions can be made for scattering on range of antenna structures. There are four major, first-principles, models in CEM [45]:

1) Time Domain Differential Equation (TDDE) models,
2) Time Domain Integral Equation (TDIE) models,
3) Frequency Domain Integral Equation (FDIE) models, and
4) Frequency Domain Differential Equation (FDDE) models.

The use of TDDE models has increased considerably over the past several years as a result of much larger and faster computers [45]. The Finite Difference Time Domain (FDTD) method uses the TDDE model. One of the widely used commercially available FDTD simulators is the Microwave Studio (http://www.cst.com/). TDIE models, on the other hand, have gained increased attention over the past decade. However, their use was not originally high because they tended to be unstable and computationally expensive. FDIE models remain to be the most widely studied and used models, as they were the first to receive detailed development [45]. Method of Moments (MoM) technique uses the FDIE model and the two commercially available MoM solvers are the Agilent Momentum (http://eesof.tm.agilent.com/products/momentum_main.html) and FEKO (http://www.feko.info/). Use of FDDE models have also increased over the years. The Finite Element Method (FEM) solver uses the FDDE model, and Ansoft HFSS (http://www.ansoft.com /products/hf /hfss/) is a commercially available FEM simulator.

The above four choices of CEM models (TDDE, TDIE, FDIE and FDDE) can in fact be narrowed down to two: a) Integral Equation (IE) models, and b) Differential Equation (DE) models, depending on their mathematical formulation.

The differential equation methods generate a sparse matrix, while the integral equation methods generate full matrices. Homogeneous/inhomogeneous/anisotropic materials can be handled in a relatively simple manner using the DE method, while the level of complexity for the IE methods varies enormously for each of these cases [46]. Rao et. al [45], [46] explain that the code implementation is generally straightforward for DE methods, while this is usually not the case for integral equation methods. In addition, for DE methods, the solution space includes the object's surroundings and the radiation condition is not enforced in an exact sense, thus leading to certain error in the solution, while the IE space solution is confined to the object and the radiation condition is automatically enforced using the corresponding Green's function [47]. Moreover, spurious solutions (numerical instability) exist in DE methods whereas such solutions are absent in IE methods. As a result, the IE solutions are generally more accurate and efficient [45].

1.10 Method of Moments

Combined conductor-dielectric radiators, such as planar microstrip and stripline antennas, have received the most attention in modelling technique development [48], [49], [50], [51]. Modelling of the combined conductor-dielectric objects are typically performed using the finite element method (FEM), the finite-difference time-domain method (FDTD), and the method of moments (MoM). Of the three methods, the MoM is the only one free of the requirement that the modelling environment be closed, either naturally or artificially [52].

Due to complexity in designing and modelling of antenna arrays, conditions such as structure size, shape, solution mode (transmit or receive mode), introduction of phase, noise, and modelling of both metallic and dielectric materials, means that a specific type of solver and modification flexibility of this solver is required. The FDIE model was adopted in this study and used via the MoM technique for simulation and modelling of the FPA. The "Method of Moments Antenna Development Toolbox" (MoMADT), 64 bit version of the modelling software, was developed for designing, building and modelling of complex antenna and electromagnetic structures (see Appendix A for more detail). MoMADT was developed under Matlab and C++ as part of this dissertation work by the author and collaboration with the antenna research group from Worcester Polytechnic Institute (WPI), Massachusetts. Details, including proof of concept of this modelling tool, are presented in Appendix A. Theoretical derivations of the MoMADT are outlined in section 1.10.1 - 1.10.3 of this dissertation. The MoMADT software provides the ability to model antenna or electromagnetic structures via Method of Moments utilizing both metallic and dielectric materials, while calculations are performed using a 64 bit processing architecture. This computational advantage enables full system memory (8 GB or more) to be utilized during modelling procedures, providing solutions on structures that consist of larger metallic and dielectric basis functions [53]. The importance and versatility of the MoMADT modelling software is discussed in Appendix A. The subsequent section provides an introduction to theory and mathematical formulations used within the MoMADT modelling software.

1.10.1 Implementation of Method of Moments to Metal Structures

Method of Moments for a pure metal structure is derived utilizing the Rao-Wilton-Glisson (RWG) basis functions [54]. In this technique, the surface of a conducting body is divided into a small triangular mesh. Each pair of triangles, having a common edge, constitutes the corresponding RWG edge element, see Figure 1.16. One of the triangles is assigned a positive charge and the other a negative charge.

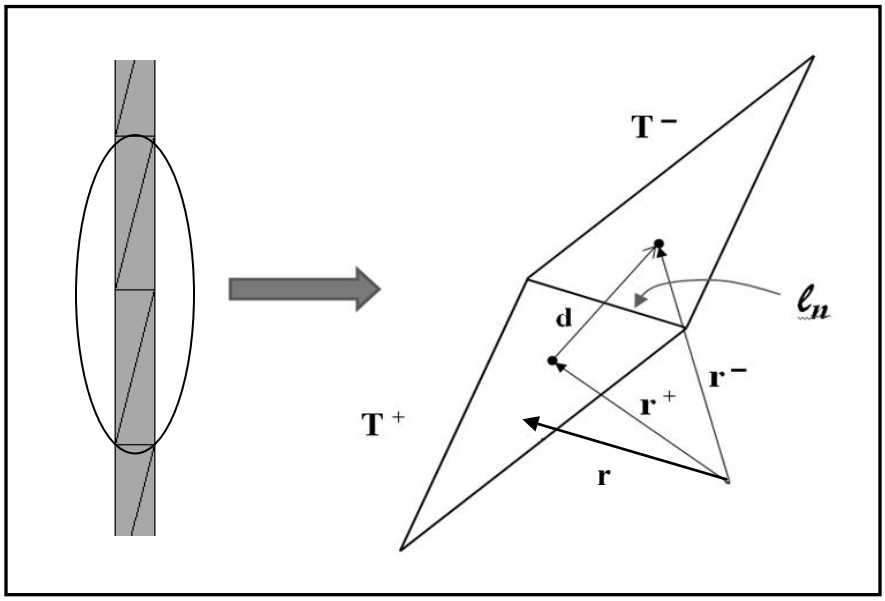

Figure 1-16 RWG basis with two adjacent triangles, showing a surface of a conducting body divided into a triangular mesh **[54]**

The RWG basis function f(r) for a specific edge is, in fact, a vector function that is then assigned to the edge element and given by equation 1.5 [54]:

$$\mathbf{f}(\mathbf{r}) = \begin{cases} \frac{l_n}{2A^+}(\rho^+), & r \ in \ T^+ \\ \frac{l_n}{2A^-}(\rho^-), & r \ in \ T^- \\ 0 \quad , & otherwise, \end{cases} \tag{1.5}$$

where, $\boldsymbol{l_n}$ = the common edge length

A = the area of each triangle

$\boldsymbol{\rho^-}$ and $\boldsymbol{\rho^+}$ = vectors that connect the free vertex of each triangle to an arbitrary observation point.

The above basis function corresponds to small but finite electric dipole of length $d = |r^- - r^+|$. Thus, the division of the antenna structure into multiple RWG elements approximately corresponds to division of the antenna current (I) into small elementary electric dipoles [55].

If two distinct edge elements *m* and *n*, of a triangularly discretized perfectly conducting body (eg. antenna surface), are treated as small distinct electric dipoles, then impedance matrix Z_{mn} would describe the contribution of dipole *n* (through the radiated field) to the electric current of dipole *m*, and vice versa. This contribution, is the actual impedance matrix Z_{mn}, and is generally calculated by employing the electric field integral equation (EFIE) [56].

The impedance matrix of the electric field integral equation is then given by equation 1.6 [57]

$$Z_{mn} = l_m \left[\left(A_{mn}^{+} \cdot \frac{\rho_{mn}^{c+}}{2} + A_{mn}^{-} \cdot \frac{\rho_{mn}^{c-}}{2} \right) + \Phi_{mn}^{-} - \Phi_{mn}^{+} \right] \tag{1.6}$$

where *m* and *n* correspond to two edge elements. $\boldsymbol{l_m}$ is the edge length of element *m*, $\boldsymbol{\rho_m^{c\pm}}$ are vectors between the free vertex points. ρ_m^{c+} is directed away from the vertex of triangle T_m^+ , where as ρ_m^{c-} is directed towards the vertex of triangle T_m^+.

The expressions for the magnetic vector potential **A**, and the scalar potential **Φ**, are then derived and given by equations 1.7 and 1.8 [54]:

$$\mathbf{A}_{mn}^{\pm} = \frac{\mu}{4\pi}\left[\frac{l_n}{2A_n^+}\int_{T_n^+}\rho_n^+(r')g_m^{\pm}(r')dS' + \frac{l_n}{2A_n^-}\int_{T_n^-}\rho_n^-(r')g_m^{\pm}(r')dS'\right] \tag{1.7}$$

$$\mathbf{\Phi}_{mn}^{\pm} = -\frac{1}{4\pi j\omega\varepsilon}\left[\frac{l_n}{A_n^+}\int_{T_n^+}g_m^{\pm}(r')dS' - \frac{l_n}{A_n^-}\int_{T_n^-}g_m^{\pm}(r')dS'\right] \tag{1.8}$$

where

$$\boldsymbol{g_m^{\pm}}(r') = \frac{e^{-jk\left|r_m^{\pm}-r'\right|}}{\left|r_m^{\pm}-r'\right|} \quad . \tag{1.9}$$

Since the division of the antenna structure into RWG elements approximately corresponds to division of the antenna current into small elementary electric dipoles, the surface current **J** (A/m) of the antenna structure can then be calculated by expanding the RWG basis functions over M edge elements using equation 1.10 [57]:

$$\mathbf{J} = \sum_{\mathbf{m=1}}^{\mathbf{M}} \mathbf{I_m f_m} \quad (\mathrm{A/m}), \tag{1.10}$$

where $\mathbf{f_m}$ is the given RWG basis function. The surface current **J** can then be determined by substituting

$$Z \cdot \mathbf{I} = \mathbf{V}. \tag{1.11}$$

Depending on the choice of source or excitation, for the transmitting case, the variable V is generally set explicitly, eg. V=1 volt for the feeding edge. In the receiving case, the voltage for each edge elements is calculated based on the conditions of the incident electromagnetic field.

Once the surface currents are known on the antenna surface, a radiated electromagnetic signal in free space is generally found using the so called dipole model approach [58], where the surface current contribution for each RWG edge element is replaced by an

infinitesimal dipole. The total radiated field is then obtained as a sum of all these contributions of infinitesimal dipoles [58]:

$$dipole\ moment\ (\boldsymbol{dm}) = \int_{T_m^+ + T_m^-} \mathrm{f_m(r)dS} = l_m \mathrm{I_m}(\mathrm{r_m^- - r_m^+})$$

(1.12)

where $\mathbf{f_m(r)}$ is the RWG basis function corresponding to edge element *m*. The radiated magnetic and electric near fields of an infinitesimal dipole, at a point **r**, are then expressed in terms of vector notation using equations 1.13 and 1.14 [59]:

$$\boldsymbol{H}(\boldsymbol{r}) = \frac{jk}{4\pi}(\boldsymbol{dm} \times \boldsymbol{r})Ce^{-jkr}, \quad \text{where } C = \frac{1}{r^2}\left[1 + \frac{1}{jkr}\right]$$

(1.13)

$$\boldsymbol{E}(\boldsymbol{r}) = \frac{\eta}{4\pi}\left((\boldsymbol{M} - \boldsymbol{dm})\left[\frac{jk}{r} + C\right] + 2\boldsymbol{M}C\right)e^{-jkr}, \quad \text{where } \boldsymbol{M} = \frac{(\boldsymbol{r}\cdot\boldsymbol{dm})\boldsymbol{r}}{r^2}$$

(1.14)

where, $r = |\mathbf{r}|$, and $\eta = \sqrt{\mu/\varepsilon} = 377\ \Omega$ is the impedance of free space. The total electric and magnetic fields at a point **r**, are then obtained as a sum over all edge elements [57], using

$$\mathbf{E}(\mathbf{r}) = \sum_{m=1}^{M} \mathbf{E}_m\left(\mathbf{r} - \frac{1}{2}(r_m^+ + r_m^-)\right), \qquad \mathbf{H}(\mathbf{r}) = \sum_{m=1}^{M} \mathbf{H}_m\left(\mathbf{r} - \frac{1}{2}(r_m^+ + r_m^-)\right).$$

(1.15)

From these variables, all required radiating parameters, relating to both the near and far fields of the radiating structure, can be calculated. For instance, the Poynting vector at a point **r** gives us the average power of the radiated field per unit area by substituting equation 1.15 into 1.16 [59]:

$$\mathbf{W}(\mathbf{r}) = \frac{1}{2}\mathrm{Re}[\mathbf{E}(\mathbf{r}) \times \mathbf{H}^*(\mathbf{r})], \quad (\mathrm{W/m^2})$$

(1.16)

where $\mathbf{H}^{*}\mathbf{(r)}$ is the complex conjugate of **H(r)**. This result also yields the *radiation density* of the radiated signal. Furthermore, *radiation intensity, U,* can also be determined [59], using

$$U = r^2\mathbf{W}, \qquad \text{(W)}. \tag{1.17}$$

Consequently, these solutions also yield the *antenna directivity* (D) and *antenna gain* (G) parameters which are calculated using equations 1.18 and 1.19 respectively:

$$D = 10\log_{10}\frac{U}{U_0} \quad (dB), \quad \text{where} \quad U_0 = \frac{\text{total radiated power } (P_{rad})}{4\pi} \quad (W), \tag{1.18}$$

$$G = 10\log_{10}\frac{\max(U)}{U_0} \qquad (dB). \tag{1.19}$$

1.10.2 Implementation of Method of Moments to Dielectric Structures

The method of moments solution for dielectric materials can be obtained using the method of volume integral equation [60]. However, more efficient methods are normally utilized such as those described by Creticos et. al. [52] and Kulkarni et. al [61].

The volume SWG basis functions, introduced in [60], are very similar to the surface RWG basis functions. However, instead of two adjacent triangular patches sharing the common edge, we consider two adjacent tetrahedra sharing the common face (see Figure 1.17). For any two tetrahedra, T_n^+ and T_n^- as shown in Figure 1.17, having volumes V_n^+ and V_n^- and sharing the common face S_n, the basis function of n^{th} face discretized dielectric body becomes:

$$\mathbf{f_n}(\mathbf{r}) = \begin{cases} \dfrac{S_n}{3V_n^+}(\rho_n^+), & r \ in \ T^+ \\ \dfrac{S_n}{3V_n^-}(\rho_n^-), & r \ in \ T^- \\ 0 \quad , & otherwise \end{cases}$$

(1.20)

where, $\boldsymbol{S}$ = the face area

$\mathbf{V}$ = the volume of each adjacent tetrahedron

$\boldsymbol{\rho}^-$ and $\boldsymbol{\rho}^+$ = vectors that connect the free vertex of each tetrahedron to an arbitrary observation point.

The subsequent calculations are obtained through volume integral equations presented in [60], in a similar manner to that shown in section 1.10.1. However, this solution does not yield a complete result for the combined metal-dielectric structures.

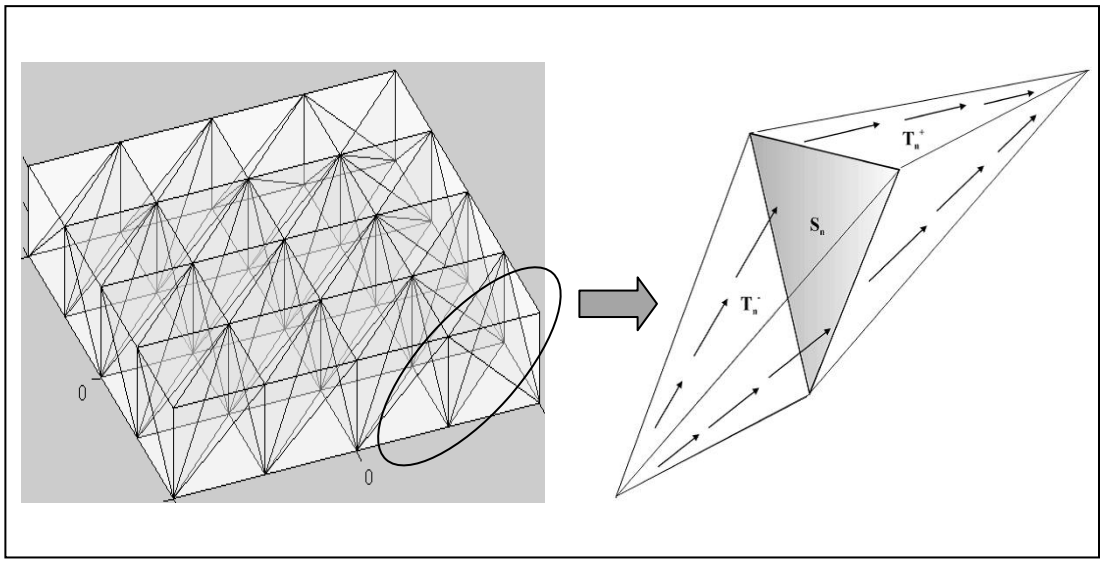

Figure 1-17 SWG basis with two adjacent tetrahedra, showing a volume of a conducting body divided into a tetrahedral mesh

1.10.3 Implementation of Method of Moments to Metals and Dielectrics Combined

Although the solution to SWG basis functions, as presented in [60] and explained in section 1.10.2, provides a number of advantages, such as the applicability to inhomogeneous dielectric materials as well as a potentially better accuracy at resonances, its main disadvantage is a rapid growth of computational complexity with increasing size of the volumetric grid [61].

A better solution, with respect to the computational efficiency of the SWG basis function, is the zeroth-order edge-based basis function presented by Kulkarni et. al. [61] and the rooftop basis functions defined over prism as presented by Carvalho et. al. [62]. Both methods were originally devised with aim to reduce the number of unknowns for modelling combined metal-dielectric resonators (eg. patch antennas) utilizing method of moments. The zeroth-order edge-based basis function provides approximately 40-50 % smaller number of unknowns [61]. In this technique, the metal surface is described in terms of the RWG basis functions [54], while the dielectric volume is described in terms of the zeroth-order, edge-based basis function originally introduced in [62].

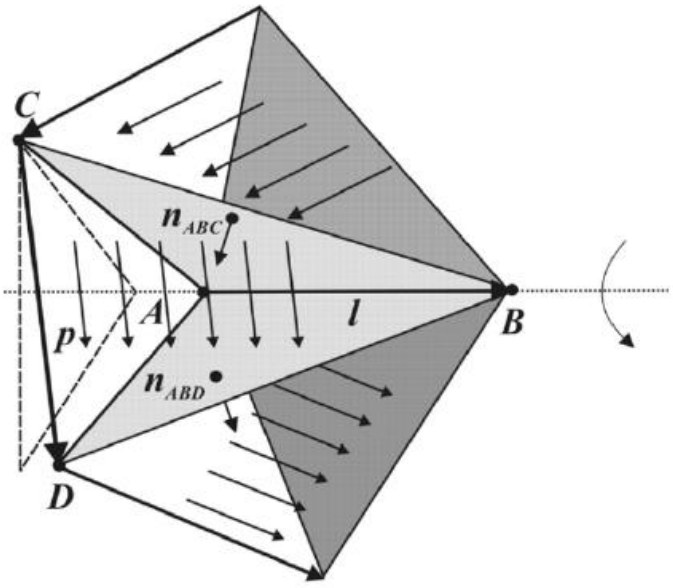

Figure 1-18 Edge-based basis function, showing three tetrahedra and two outer faces (dark gray) [61]

For a tetrahedral mesh, the edge-based basis function introduced in [61] and [62], is shown in Figure 1.18. The basis function for a tetrahedron $\Delta ABCD$ is defined by a vector of the edge $\overline{CD}$ which is opposite to the base edge $\overline{AB}$. With this tetrahedron $\Delta ABCD$, the basis function is a constant field given by equation 1.21:

$$\mathbf{f} = \frac{1}{\bar{\boldsymbol{l}} \times \bar{\mathbf{S}}} \times \boldsymbol{p} \tag{1.21}$$

where $\bar{\mathbf{S}}$ is the area of the projection of triangle ACD, or BCD, onto a plane perpendicular to the base edge [61], while $\boldsymbol{p} = \overline{CD}$, and $\bar{\boldsymbol{l}} = \overline{AB}$. If we assume a dielectric volume with M number of dielectric basis functions then the total electric flux $\boldsymbol{\Psi}(\mathbf{r})$ at some point **r** in the dielectric medium, can be obtained using:

$$\boldsymbol{\Psi}(\mathbf{r}) = \sum_{m=1}^{M} \Psi_m \, \mathbf{f_m}(\mathbf{r}), \tag{1.22}$$

where Ψ_m is the electric flux on boundary of each tetrahedron face. Consequently, the associated bound surface charge density $\boldsymbol{\sigma}_S(\mathbf{r})$ can be determined using equation 1.23:

$$\boldsymbol{\sigma_S}(\mathbf{r}) = \sum_{m=1}^{M} \mathbf{K}(\mathbf{r}) \boldsymbol{\Psi}_{\perp}(\mathbf{r}) = \sum_{m=1}^{M} \left\{ \sum_{q=1}^{Q} K_q \mathrm{f}_{\perp \mathrm{mq}}(\mathbf{r}) \right\} \Psi_m \tag{1.23}$$

where $\boldsymbol{\Psi}_{\perp}$ is the normal component of the total electric flux on the boundary of each tetrahedron; Q is the total number of faces between each tetrahedra; $K_q = K_+ - K_-$ is the differential contrast on face $\boldsymbol{q}$ between tetrahedra "+" and "−"; and $K_{\pm} = (\boldsymbol{\varepsilon}_{\pm} - \varepsilon_0)/\boldsymbol{\varepsilon}_{\pm}$ is the dielectric contrast, which is assumed constant within every tetrahedron [61].

When combined with the metal surface current density, given by equation 1.10, the coupled MoM equations for both the metallic and dielectric structures can be obtained

using the volume Electric Field Integral Equations (EFIE) for the dielectric, and the surface EFIE for the metallic sheets. The coupled MoM equations are then combined with the given integral equations as described by Sarkar et al [63]. These formulations portray the core theory used within MoMADT design tool.

Detailed derivation of the volume-surface integral equation (VSIE) methods based on edge-based basis function and its implementation to metal-dielectric structures is presented by Kulkarni et. al. [61], [64].

1.11 Objectives

The need to increase bandwidth of PAF technology has become significant in development of advanced radioastronomical instruments. Successful design of wideband and low noise operation requires that adequate polarization purity, directivity, gain, impedance and efficiency be obtained over the required frequency range and these parameters to be reliable as function of the FoV and phase.

The proposed aim of this project has been to investigate solutions to a wide bandwidth FPA receiver for reflector antennas to operate in the frequency range 500 to 1100 MHz and cover the bandwidth of one indicated SKA sensor technology discussed in section 1.1. Design solutions are to be considered utilizing appropriate modelling techniques via method of moments. Antenna parameters are to be studied in relation to structure, shape, element size, element spacing, ground plane distance, array configuration and overall array size. As a result, objectives of this project are outlined with a set of criteria to be followed during the time of the array design:

1) **Bandwidth** - The array and/or its elements must cover range of frequencies for required operation (500 to 1100 MHz), whilst providing adequate impedance match to the low noise amplifiers. The FPA system must have ability to cover bandwidth range of at least $\geq$ 2:1 for all desired scan angles, whilst sustaining directivity, gain and efficiency

parameters. Careful consideration must be given to array configuration, element spacing and mutual inductance effects between the array elements.

2) **Polarization** - The array and/or its elements must have ability to differentiate a range of polarization vectors of the incident focal field without the need of additional mechanics to rotate the array. As a result, the array must provide adequate polarization purity as function of the FoV and frequency. This characteristic is important for detection and tracing of magnetic fields during radio astronomical observations.

3) **Directivity** - Whilst generating multiple beams (phased beams) that operate at the required frequency range and provide polarisation diversity, the beams must also be unidirectional. This property requires that the specific type of radiator (the individual elements or the array itself) be unidirectional, or the system may require a ground plane. Two approaches are considered: Travelling wave structures and planar broadband arrays over a ground plane.

4) **Cost** - One of the most important parameters in designing FPAs is the production, maintenance and operational cost. These characteristics are usually related to the complexity of the system, such as the number of elements necessary for successful operation of the array. These conditions can be controlled by understanding the operating requirements of the array, its design, and providing constraints on the number of feeds (or ports) that will be necessary to operate the array. Another parameter that governs the cost is the Focal Plane Array size. The FPA size directly relates to the choice of F/D ratios, FoV and the overall starting point for system design [4].

1.12 Contributions

Whilst established designs in PAF technology are continuing to be tested and implemented by various organisations [22], [25], [28], [65] (see section 1.3), antenna types such as Vivaldi end-fire linearly polarized antennas as well as dipole and cross

dipole array structures (eg. Chequer board array and dipole arrays) have been intensively studied in various theoretical frameworks of physics, electrical engineering and astronomy. Practical significance of these structures has been identified and maximum bandwidth as function of the FoV and number of ports has been broadly determined. However, not all antenna types, structures and configurations have been considered for possible use in PAF technology. Furthermore, not all antenna types have been modelled accurately due to lack of computational resources and modelling efficiency.

Advanced modelling techniques via MoM were utilized in this research for modelling complex conductor-dielectric objects. Aim was to explore possible candidate structures that have not been previously identified and to determine if existing techniques in PAF technology can be further improved with a system that yields less demand on computational resources and offers wider bandwidth and reduced cost.

MoM modelling for conductor-dielectric objects was employed via the piecewise-constant edge basis function as described by [61], [62]. These basis functions form a full vector basis on volume tetrahedral meshes with a continuous normal component while at the same time they form a subset of the SWG basis functions [60] that do not possess the artificial volume charges. As a result, this technique enables the number of edge basis functions to be considerably reduced compared to the original SWG basis functions [61]. Contributions from current research to VSIE were directed in improvement to boundary conditions of the zeroth order edge basis function where the surface boundary condition of the electric field component must be extended into adjacent tetrahedra, improvement to matrix manipulation techniques, refinement to digitization procedure in Matlab and C++ and computational implementation of zeroth order edge based basis function in a 64 bit architectural environment.

Objective of this research was to investigate examples of a FPA system that generates extra-wide bandwidth characteristics through the analysis of planar antennas, while at the same time, minimize the number of feeds (or ports) necessary to operate the array. It was then determined that such a system was achievable only if the effective (conductive

surface) area of the array was considerably increased, while at the same time, the element spacing and the number of ports was kept to a minimum. To achieve this result, a FPA system whose elements consist of 3 polarization ports was designed, instead of 2, utilizing the diamond tripole strip antenna elements. Whilst tripole antennas and unloaded tripole arrays [31], [33], [36] have indeed previously been studied by numerous authors, the HDT array as derived in this work has not received much attention in the past. Results have shown that a 7×7 HDT array offers an operating frequency range 550 to 2100 MHz, providing bandwidth ratio of 3.8:1 with FoV of 8° at F/D ratio of 0.4, utilizing only 111 individual receiving ports. While the polarization can be distinguished by virtue of amplitude comparison at any angle about the axis normal to the antenna plane to within a maximum theoretical uncertainty of ± 2.2°. This is also true for any function of the FoV allowed by the surface area of the FPA.

To acquire the same receive characteristic, in terms of bandwidth, FoV and polarisation, the HDT array has shown to require considerably smaller number of ports compared to existing PAF designs [11], [25], [27]. The benefit of this allows the effective area of the FPA to be considerably increased at a reduced operational cost. It is concluded that the HDT array yields a promising solution to PAF technology for present and future design studies, with a system that offers potential for greater operational efficiency, robust and simple-to-manufacture structure and yields a relatively cost effective solution.

1.13 Summary

In this chapter, a broad section of relevant theoretical background was covered relating to the SKA and phased array feed technology, as well as a review to Method of Moments modelling procedures and related computational electromagnetic theory. Some important antenna parameters, describe the relationship of the focal field to that of the FoV. Understanding these parameters is important for successful design of wideband PAFs since the effects of mutual coupling and polarization purity is largely influenced by displacement and distribution of the focal field.

An introduction to Method of Moments Antenna Development Toolbox (MoMADT), software was also presented in this chapter. MoMADT software was developed during the course of this study under Matlab and C++. This software provides the ability to model antenna or electromagnetic structures via Method of Moments utilizing the Frequency Domain Integral Equation (FDIE) modelling techniques. MoMADT enables modelling of both metallic and dielectric materials with fields and currents that vary in three dimensional space. In addition, MoMADT provides versatile functions that enable the system to generate precise structures and yield accurate method of moments solutions.

The end of Chapter 1 describes the objectives and contributions of this project and outlines a set of criteria to be followed during the time of the array design.

CHAPTER 2

Chapter 2 - Design and Methodology

Chapter 2 begins by presenting an introduction to range of antenna and array structures investigated in this study. Following this, information relating to design and development of the three-axis antenna, specifically the diamond-tripole antenna, is presented. A general review is disclosed that clarifies the choice of designing the FPA that provides three vectors of polarization. Following this, information on the preliminary array design and modelling procedures are explained.

2.1 Antenna Structure and Polarization

The start of this project was established by investigating a range of antenna structures that exhibit wideband properties and provide desired impedance, directivity and gain parameters. Some examples of these structures are shown in Figure 2.1. Antennas were studied theoretically and computationally using appropriate modelling techniques, one of which is called method of moments [61] (see section 1.10 for more information). The most promising antennas were investigated both as single elements and arrays. Results were then compared with solutions obtained using commercially available software, called Ansoft HFSS. Proof of concept of the method of moments solver and its comparison with Ansoft HFSS are presented in Appendix A.

Due to large number of antennas investigated in this study, their modelling solutions will not be presented in this chapter, however, examples as well as the information relating to the modelling software, can be found in Appendix A and B.

		Pattern	Directivity	Polarization	Bandwidth	Comments
Patch		Broadside	Medium	Linear/Circular	Narrow	Easiest design
Slot		Broadside	Low/Medium	Linear	Medium	Bi-directional
Ring		Broadside	Medium	Linear/Circular	Narrow	Feeding complicated
Spiral		Broadside	Medium	Linear/Circular	Wide	Balun & Absorber
Bow-Tie		Broadside	Medium	Linear	Wide	Same as Spiral
TSA(Vivaldi)		Endfire	Medium/High	Linear	Wide	Feed transition
Yagi Slot		Endfire	Medium	Linear	Medium	Two layer design
Quasi Yagi		Endfire	Medium/High	Linear	Wide	Uniplanar, Compact
LPDA		Endfire	Medium	Linear	Wide	Balun, Two Layer
Leaky-Wave		Scannable	High	Linear	Medium	Beam-steering, Beam-tilting

Figure 2-1 Range of antenna structures investigated in this study

Antennas exhibit a specific radiation pattern. The overall radiation pattern changes when several antenna elements are combined in an array. This is due to the so called array factor [5], which quantifies the effect of combining radiating elements in an array without the element specific radiation pattern taken into account. Array factor depends on the number of elements, the element spacing, amplitude and phase of the applied signal to each element. The number of elements and element spacing determine the overall effective area of the structure. It is the task of the designer to ensure that components of the array do not cause excessive signal distortion. Often, it is important to measure how reflective a radiating element is to ensure that it absorbs energy efficiently. Measuring antenna match, in this case, is vital for successful array design.

Therefore, it is essential to understand the physical mechanisms of array elements; for example, the number of feeds they possess, type of polarisation they can detect, as well as their frequency response parameters. As explained in section 1.11, these variables are important in order to meet the requirements outlined under the objectives of this project.

2.1.1 Linearly Polarized Antennas

To categorize the polarization of received electromagnetic signals indicates that one must break down and identify the separate vector components of the incoming radiation. This immediately places constraints on the type of antenna structure that can be implemented in the design of the FPA system. For example, several scaled antenna structures that generally exhibit wide-band properties, such as spiral, ring or helical antennas, have limited ability to distinguish the separate polarisation vectors and provide appropriate element spacing to the array (see Appendix A.6 for results on modelling the spiral phased array antenna). These limitations show that spiral, ring or helical antennas are not the most ideal antennas to be used for developing PAFs for radio astronomy.

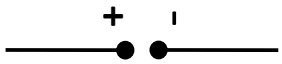

Figure 2-2 Dipole antenna

The FPA system must be configured to maximise polarization discrimination. Linearly polarized antennas, such as the dipole antenna shown in Figure 2.2, are generally practical for situations where electromagnetic waves (those incident or transmitted) are polarized along one axis. Thus, antenna arrays with elements aligned in the same direction, as shown in Figure 2.3a, yield a system with limited polarization diversity. This type of an array when packed tightly is referred to as the "gangbuster" surface [33], and has the benefit of providing increased bandwidth if the surface number of elements is increased. However, this system would require a mechanism to rotate the array during reception for radio astronomical observations, so that a range of polarization vectors could be identified. With careful consideration, linearly polarized antennas can be arranged in a cross-pole configuration for detecting electromagnetic (EM) waves polarized along two or more axes. However, such configurations must be uniformly distributed. Below we investigate some examples.

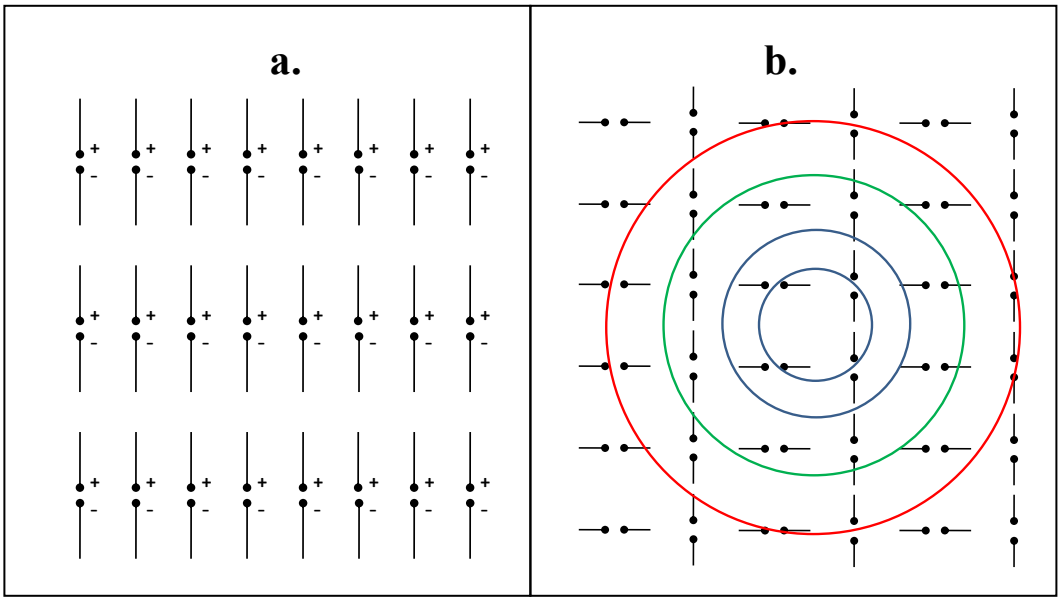

Figure 2-3 a) Array of linearly polarized antennas aligned in the same direction (also referred to as gangbuster array [33]); b) Array of 6 x 6 linearly polarized antenna elements arranged in a mutually perpendicular manner

Figure 2.3b shows an array of 6 x 6 small linearly polarized antenna elements arranged in a mutually perpendicular manner. This design relies upon one of the prototypes developed by Seavey Engineering Associates, Inc. Massachusetts [57]. This design (Figure 2.3b) is viable in situations where plane waves of uniform intensity are incident on the array, because in a reflector system the power density (Poynting vector normal to the focal plane) available for reception at the focal plane is an Airy pattern. Thus, linearly polarized elements aligned as shown in Figure 2.3b, would not be the most ideal configuration to be used at the focal plane of the radio dish, because the oppositely oriented elements would not be evenly illuminated by the focal field, especially at higher frequencies. This condition would evidently depend on the frequency, element spacing, number of elements and the overall array size.

Figure 2.4 shows yet another example, and the most common array pattern using the cross-dipole or quadra-pole antenna configurations. In Figure 2.4a, the linearly polarized elements are aligned in a uniformly perpendicular manner to cover two vectors of polarization. This type of element pattern is used in both Vivaldi FPA studied by

ASTRON [19] and DRAO [24] groups, as well as the chequer board array studied by the CSIRO group [14].

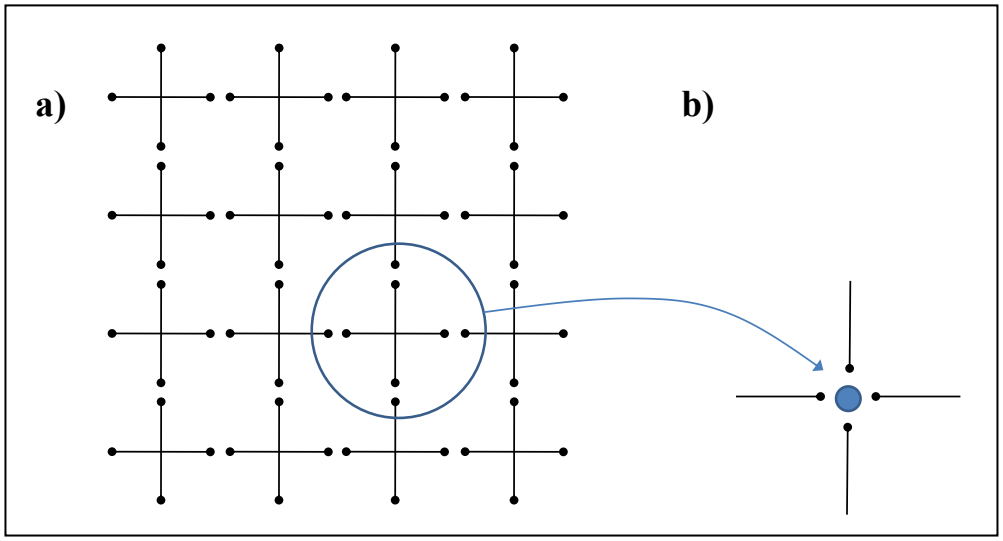

Figure 2-4 a) Linearly polarized elements arranged in a uniformly perpendicular manner; b) The equivalent cross-dipole configuration of this structure

In a cross-dipole antenna array (as seen in Figure 2.4a), incident signals polarized at angles other then vertical or horizontal can only be categorized if the phase of the respective signals is electronically matched (see Figure 2.5). While these techniques are well established in cross-dipole configurations [22], [25], [28], [65], polarization cross-talk due to mutual coupling effects between the oppositely oriented poles can occur, making determination of the true polarized vector more difficult [66].

Figure 2.5 shows assorted polarized EM waves (arrow lines) incident at the antenna plane of a cross-dipole antenna. The percentage values in Figure 2.5 represent the received amplitude coefficients at each of the terminals during reception, obtained via modelling using the MoMADT. Results show that EM waves polarized at angles other than vertical or horizontal (other than 0° or 90°), as shown in Figure 2.5b and 2.5c, cannot be appropriately categorized unless the phase of the respective signals is rotated and matched. This procedure requires that additional mechanics be implemented in the system thereby increasing the production and operational cost of the instrument.

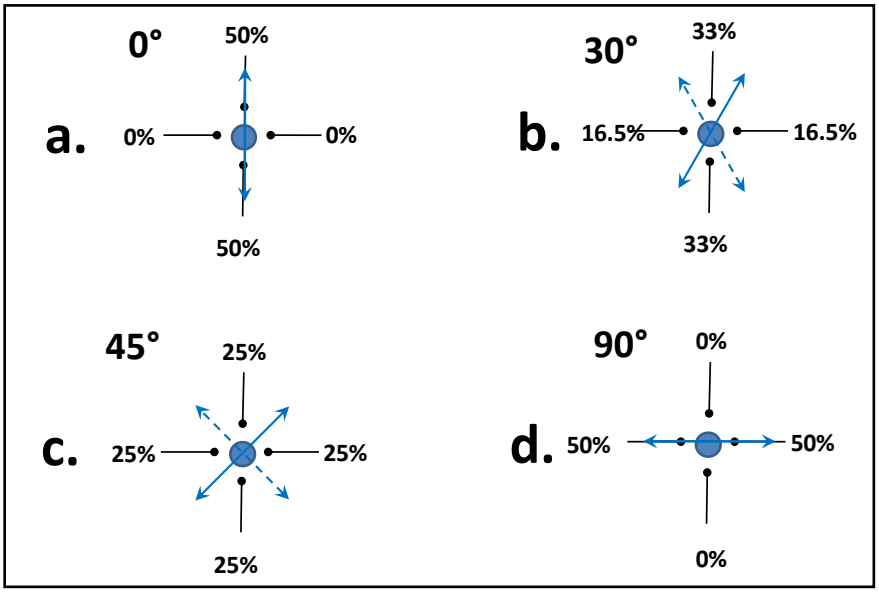

Figure 2-5 Received feed power (%) of a cross-dipole antenna calculated at varying angles of polarization (0°, 30°, 45°, 90°) during reception

Although cross-dipole antenna arrays are widely used despite some of the above drawbacks, one important limitation is that the physical length of the antenna generates restrictions on the minimum element spacing of the array, much similar to that of the spiral antenna discussed in Appendix A.6. Large element spacing deteriorates the gain and directivity of the array at higher frequencies, which results in reduced bandwidth. One obvious solution to this problem is to reduce the size of the elements and increase the size of the array; however increasing the size of the array introduces additional feeds and immensely increases the operational cost of the instrument.

In addition to the above, Pelton and Munk [36] show that reflection coefficient versus frequency of symmetrical crossed-dipole arrays can exhibit distinct resonances with nulls. This occurs when the dipole elements are on the order of a $\lambda/2$. It is demonstrated by [36] that the null phenomenon occurring from the cross-dipole array is caused by the presence of two distinct current components on the elements, each having different resonant frequencies. Munk [31] points out that the problem with double resonance can be avoided if an "unloaded tripole" element is used instead, in which case the two resonances degenerate into one [31].

2.1.2 Triple Polarized Antenna

An alternate solution to FPA systems would be to design an array that yields three vectors of polarization utilizing the "tripole" antenna [36], [67]. As stated by Munk [31], this system referred to as the "unloaded tripole array" [33], would enable the element spacing of the array to be considerably reduced compared to cross-dipole antenna arrays. Furthermore, polarization cross-talk due to coupling in a 3 port network is not feasible [67]. Munk [33] explains that the tripole array has a very attractive feature because the elements can be packed very tightly, thereby making the inter-element spacing small and bandwidth large, however, it can also suffer from nulls in the second harmonics [33].

The tripole antenna was first suggested by Kajfez 1969 [68]. The original design [68] consists of three distinct end-feed antenna elements connected to a separator network fed by three sources of electro-motive force (emf), see Figure 2.6a. This type of antenna was first developed for transmitting and receiving circularly polarized waves, where the three feed sources of equal amplitudes are phased by $2\pi/3$ degrees.

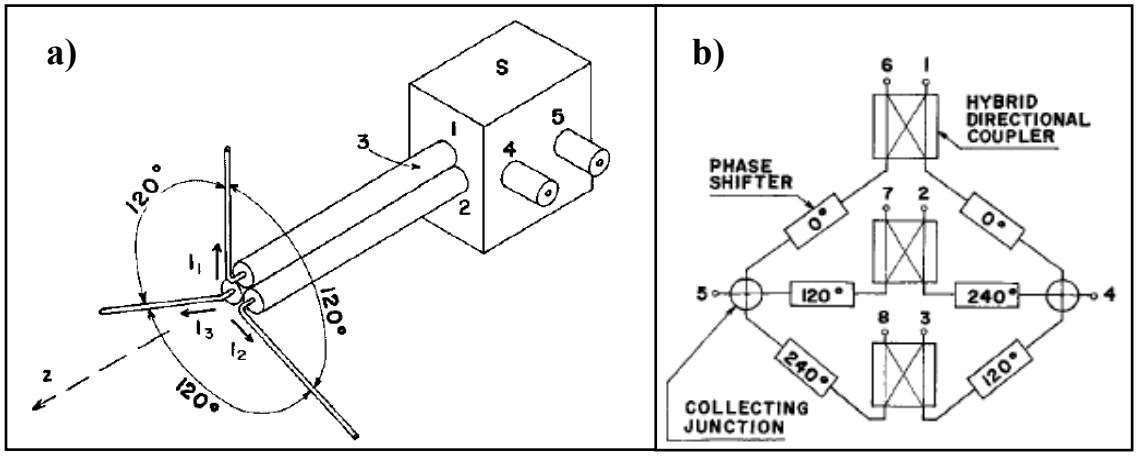

Figure 2-6 a) The Tripole antenna, b) The separator network for detecting circularly polarized waves. Image obtained from **[68]**

A three terminal antenna, as shown in Figure 2.6a, can also be used to differentiate linearly polarized signals at any angle about the axis normal to the antenna plane by

virtue of amplitude comparison (see Figure 2.7), provided that the appropriate feed network is supplied between the three terminals.

Figure 2.7 shows assorted polarized EM waves (arrow lines) incident at the antenna plane of the tripole antenna. The percentage values in Figure 2.7 represent the received amplitude coefficients at each port during reception, obtained via modelling using the MoMADT. Results show that EM waves polarized at angles 0°, 30°, 45° and 90° about the axis normal to the antenna plane, can indeed be categorized using the tripole antenna. In other words, when irradiated by an incident EM field, the three poles will be excited concurrently to generate a unique amplitude distribution coefficient between the three terminals that solely depend on the intensity and polarization of the incident EM field. In addition, as discussed above, the physical length and configuration of the tripole antenna would not generate restrictions on the element spacing of the array as obtained with the cross-dipole array in Figure 2.4a. This will be illustrated in chapter 3.

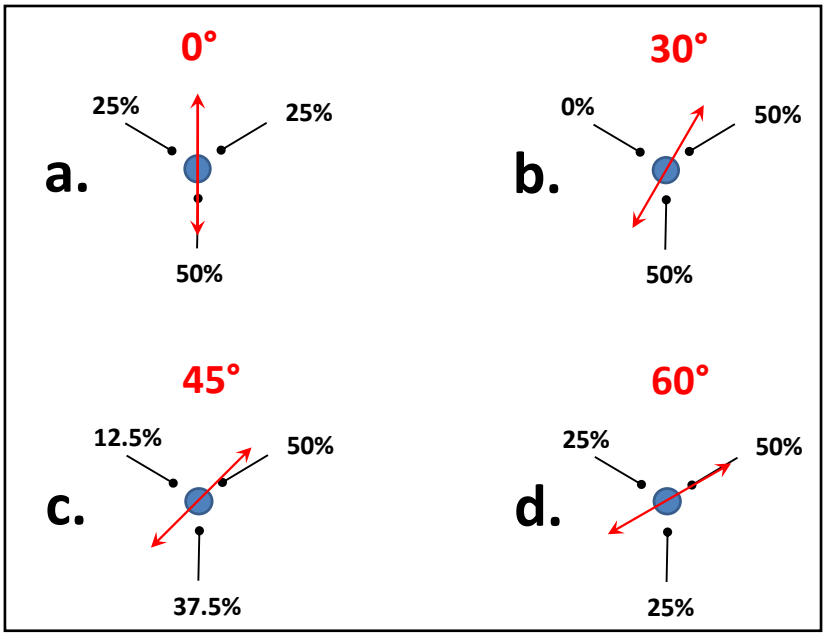

Figure 2-7 Received relative power (%) of a tripole antenna calculated at varying angles of polarization (0°, 30°, 45°, 90°) during reception

2.2 Antenna Design

During the course of this study, a decisive step was made to investigate the design of the FPA that provides three vectors of polarisation. The tripole antenna [33], [36], [67] was selected as the starting point of system design on to which the design concept of the "diamond" tripole antenna was derived.

2.2.1 Feed network

The "dipole" antenna is generally characterized with a Norton equivalent circuit shown in Figure 2.8a. This circuit can also be represented as a dual source circuit shown in Figure 2.8b provided that two separate sources in Figure 2.8b contain half the amplitude of the original source, and that they are in phase.

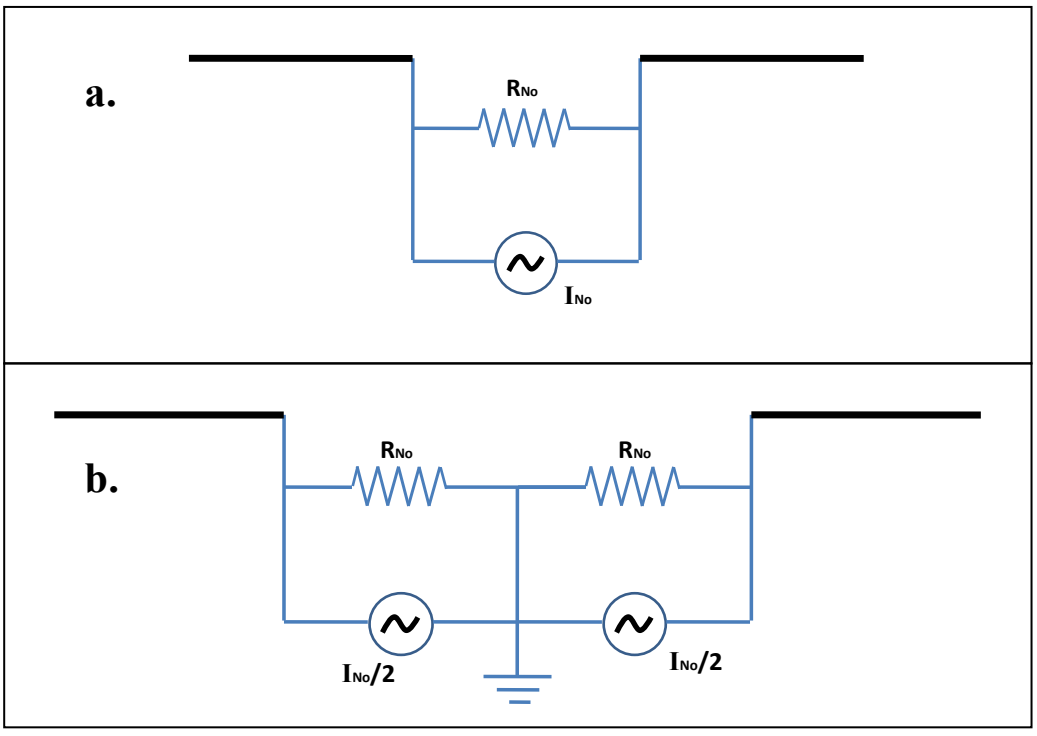

Figure 2-8 Norton equivalent circuits for a dipole antenna, showing: a) single source feed, and b) dual source feed.

In a three terminal antenna, each of the feeds can be treated as individual sources fed with respect to a common ground, generating an element with three unique radiating components, or three end-feed dipole antenna elements. In simplest case, the tripole circuit is a direct modification of the circuit shown in Figure 2.8b, in that it includes one additional source component, hence generating a three terminal structure as shown in Figure 2.9a and 2.9b.

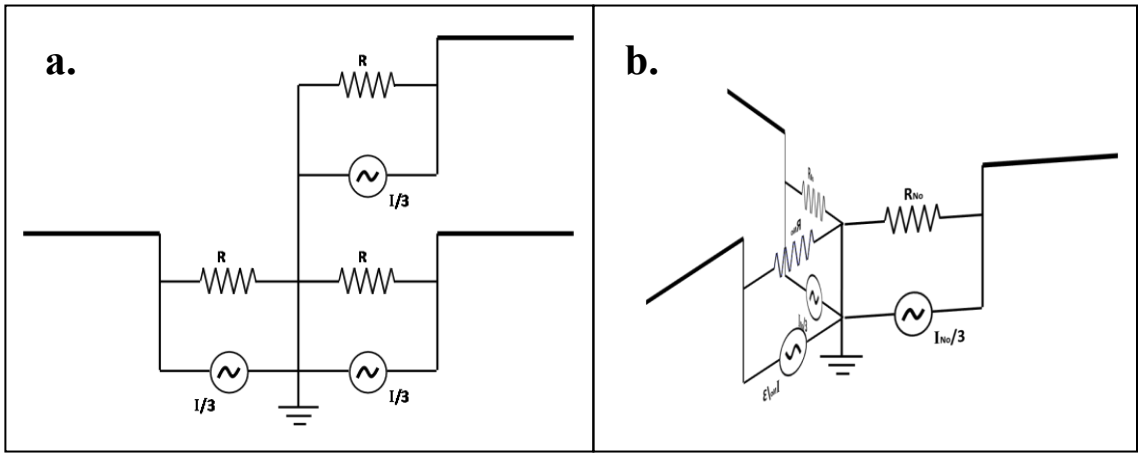

Figure 2-9 Norton equivalent circuits for the tripole antenna

Figure 2.9 represents the basic feed network of the tripole antenna. As mentioned previously, this type of antenna provides some advantages over the dual pole structures, however it remains to be seen if this structures can be implemented in an array and most importantly what measures must be introduced to attain frequency independence.

2.2.2 Frequency Independence

The tripole antenna was initially investigated in a range of structures, with terminals consisting of simple wire radiating components and those that may exhibit some form of frequency independence. Frequency independence is generally obtained from structures that are continuously scaled, such as conical antennas, planar equiangular antennas and the bowtie antenna. Other forms of frequency independent antennas are classified as

"self complementary" structures which are arbitrarily shaped antennas that constitute with half of an infinitely extended planar-sheet conductor such that $Z_{\text{CONDUCTOR}} / Z_{\text{SLOT}} = \eta^2/4$, where η is the vacuum impedance [69]. In the general case, the shape of the complementary structure is exactly identical with that of the original structure, with two terminals for the simplest case, as shown in Figure 2.10.

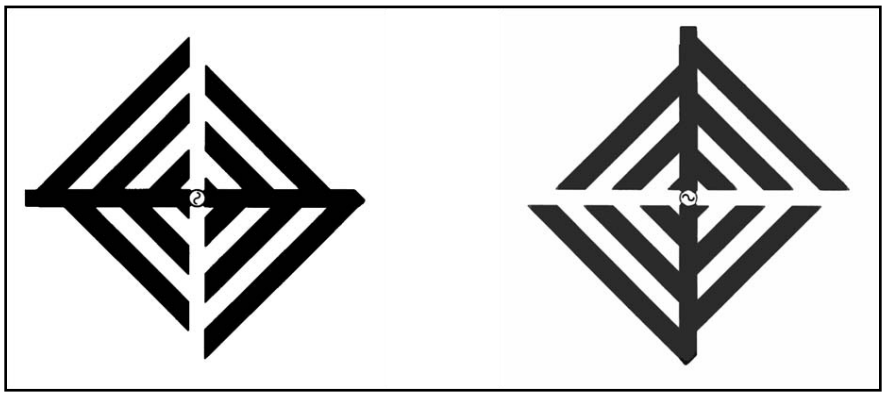

Figure 2-10 Self complementary two-terminal antenna structure

Another form of frequency independent structure is the log-periodic antenna, however it should be noted that log-periodic shape does not necessarily provide any broadband property to antennas. In fact, log-periodic antennas arranged in an anti-complementary manner do not have broadband property [70], see Figure 2.11.

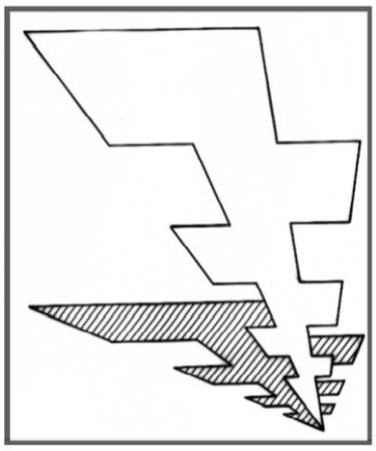

Figure 2-11 Anti-complementary Log periodic antenna - not a broadband antenna

In case of the tripole antenna, we are interested in a solution that can provide some form of broadband property. Given the nature of the tripole antenna and its orientation within the plane, the most ideal approach was implemented by introducing a scaled structure attached to individual poles, much similar to that of the bowtie antenna and diamond antenna (see Figure 2.12). This design was established by introducing a scaled planar equilateral-triangle structure, similar to design obtained by [71], and a scaled diamond structure as shown in Figure 2.12a and 2.12b, respectively. Other structures were also investigated during this study, including blade tripoles and droopy tripole antennas.

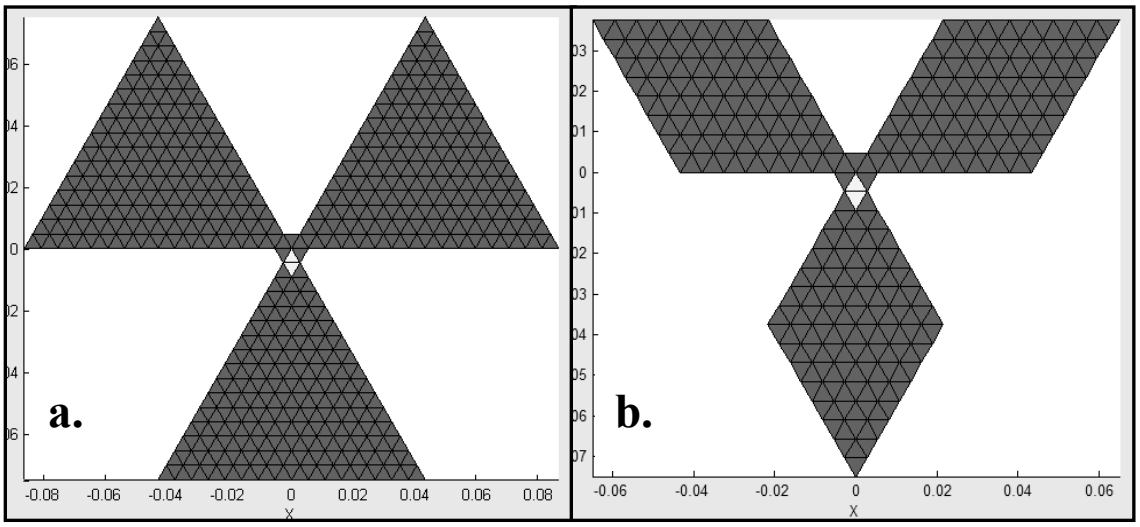

Figure 2-12 Showing the design of the scaled tripole antenna using, a) Equilateral triangle tripole structure **[71]**, and b) Diamond tripole structure

The planar equilateral tripole strip antenna shown in Figure 2.12a, can be directly related to the 60° bowtie antenna shown in Figure 2.13. Figure 2.13 briefly illustrates the surface current magnitudes of the bowtie and the equilateral tripole antennas calculated using method of moments modeling procedures during reception. Both structures are illuminated by a plane wave polarized in X axis (Figure 2.13a) and Y axis (Figure 2.13b) respectively. The size of the triangle poles between the tripole and bowtie antennas are identical, including the size of the feed edge. Figure 2.13 illustrates the basic behavior of the tripole and bowtie antennas during reception when signals are polarized in X and Y axes respectively. Note that brighter areas indicate higher surface current magnitudes (see grayscale bar in Figure 2.13).

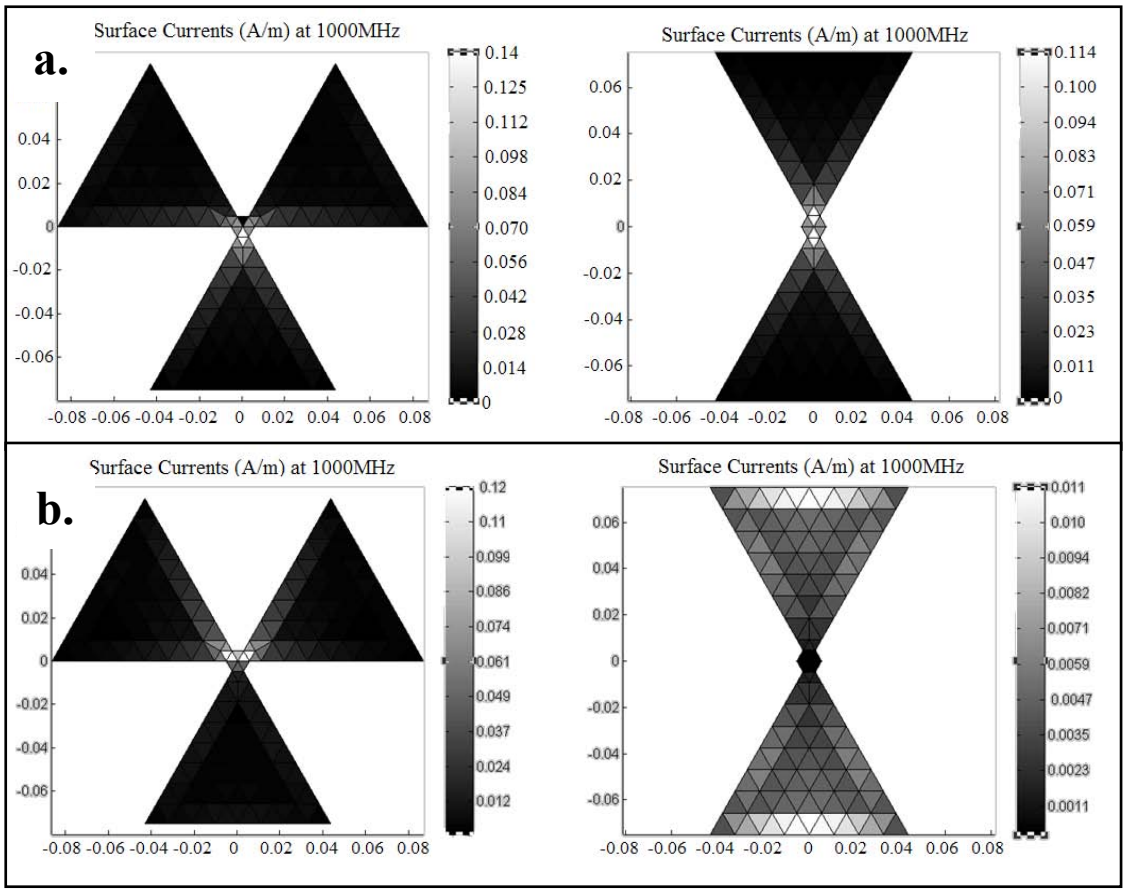

Figure 2-13 Tripole and 60° Bowtie antennas illuminated by a plane wave polarized in, a) Y axis, and b) X axis, showing surface current magnitude (A/m) at 1000 MHz.

Figure 2.14, on the other hand, shows the calculated impedance and reactance as function of frequency for the bowtie and the tripole antennas. As can be seen, the equilateral tripole antenna behaves similarly to the bowtie antenna and clearly illustrates broadband property, radiating most efficiently at frequency where reactance is minimal.

The "bowtie" antenna is normally considered to be a scaled structure that contains frequency independence. And like the equilateral tripole antenna in Figure 2.14b, the level of frequency independence is directly proportional to the size and scale of the structure. For example, if the structure is infinitely scaled, it would evidently become a well-matched structure for a very wide frequency range. However in reality, the bowtie and other scaled antennas alike are not infinitely long, as a result the transient responses

of the antenna are characterized by a number of small reflections that occur from the ends of the antenna, resulting in an erratic response long after the excitation pulse has ended [57]. These responses generate resonant modes with frequency, as shown in Figure 2.14, hence degrading the effects of the frequency independence. If compared to a "dipole" antenna, the reflections from the bowtie antennas-end are reduced significantly, which makes the bowtie essentially a non-resonant structure attractive for broadband applications [57, p. 169].

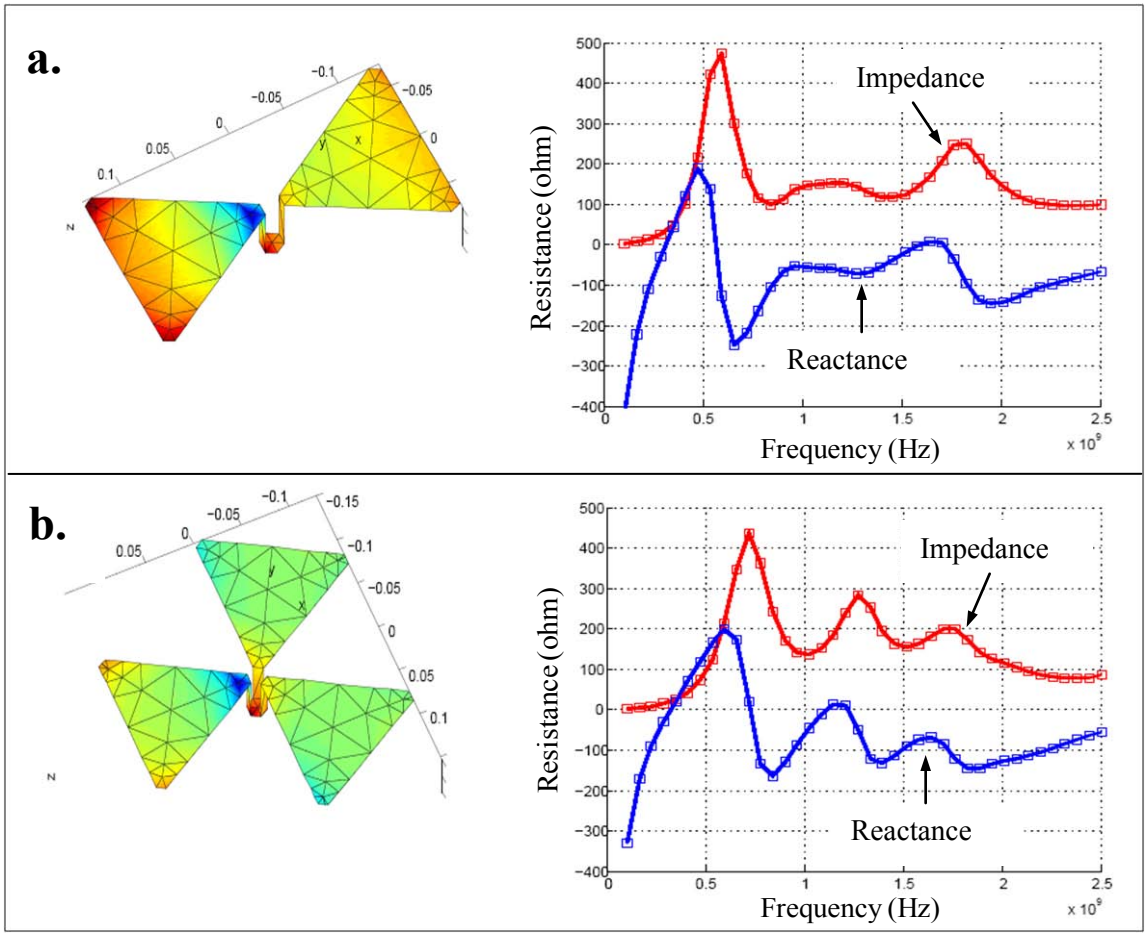

Figure 2-14 Impedance (red line) and reactance (blue line) as function of frequency for: a) Bowtie, b) Tripole antenna. This figure illustrates the similarities in the frequency response between the two antennas for frequency range 100 - 2500 MHz

Frequency independence is important for operation of wide bandwidth antennas since their input impedance must be matched to a low noise amplifier (LNA). One general approach to designing broadband non-resonant antennas is to introduce a variable internal resistance per unit length. This method involves the introduction of resistive, capacitive and/or inductive loads installed per unit length of the antenna, thereby altering the behaviour of the antenna by changing its resistivity as function of length and/or frequency. This technique is termed as antenna loading [57, p. 223]. Although the antenna loading can improve the impedance response of antennas, its main disadvantage is that the portion of the power is always lost across the load especially in the case of resistive loads. In the case of inductive or capacitive loads the reflection coefficient can be considerably altered in a way that changes the matching of the radiating system.

2.3 Preliminary Modelling Study

When designing phased arrays, it is important to ensure that the components of the array do not cause excessive signal distortion and reflections. In order to minimize these effects it is usually desirable that the element spacing of the array is maximized. However, to insure that the focal field is sufficiently sampled and that the appropriate beam shape and beam width is generated, the element spacing should not exceed half-wavelength of the upper operating frequency, and for these conditions to be met it is rather desirable that the element spacing be minimized. Therefore, it becomes a trade-off between sampling effectiveness and coupling. These components are further affected by impedance responses of the selected structure and the choice of element size. In this section we intend to discuss the preliminary array design and modelling procedures undertaken during the course of this study, outlining the three feed modelling technique.

2.3.1 Initial Array Design

The design of the FPA was first established by investigating a broadband array structure with 19 "equilateral tripole antenna" elements [71], arranged in a self-complementary

hexagonal manner shown in Figure 2.15. This array design was derived based on element presented by [71]. Other variations of tripole antennae were also studied such as blade tripoles and droopy tripoles, however they will not be addressed in this section. As can be seen, Figure 2.15 yields an array pattern that can be evenly illuminated by the focal field, especially since the centre of the array is perfectly covered by the first tripole element. Additionally, the oppositely oriented poles provide coverage of three vectors of polarization at the same point within the array plane. However, even though this structure is self complementary, elements spacing is restricted by the size of the element itself. This means that bandwidth will be restricted due to large element spacing.

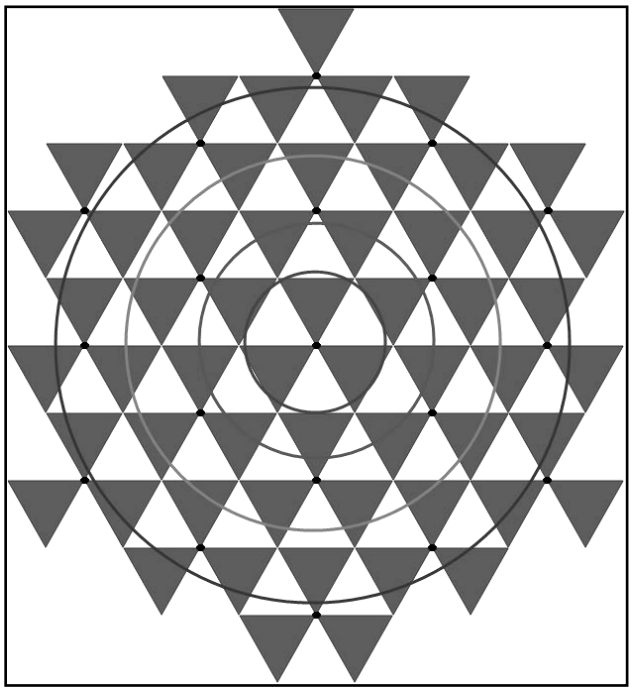

Figure 2-15 Self-complementary hexagonal tripole array (array design contains antenna element based on designs by **[71]**)

Figure 2.16 illustrates impedance response of the single equilateral tripole antenna and the 3x3 equilateral tripole array in transmit mode without the ground plane. Results are calculated for frequency range 300 to 3000 MHz using method of moments in transmit mode by supplying 1 V to a single terminal of each tripole antenna. Figure 2.16b shows that when the equilateral tripole antenna is utilized as a 3x3 hexagonal array, a sharp

resonance occurs at ~1450 MHz. This resonance is caused due to coupling effects between the elements at the frequency region where the wavelength is proportional to the antenna size and element spacing.

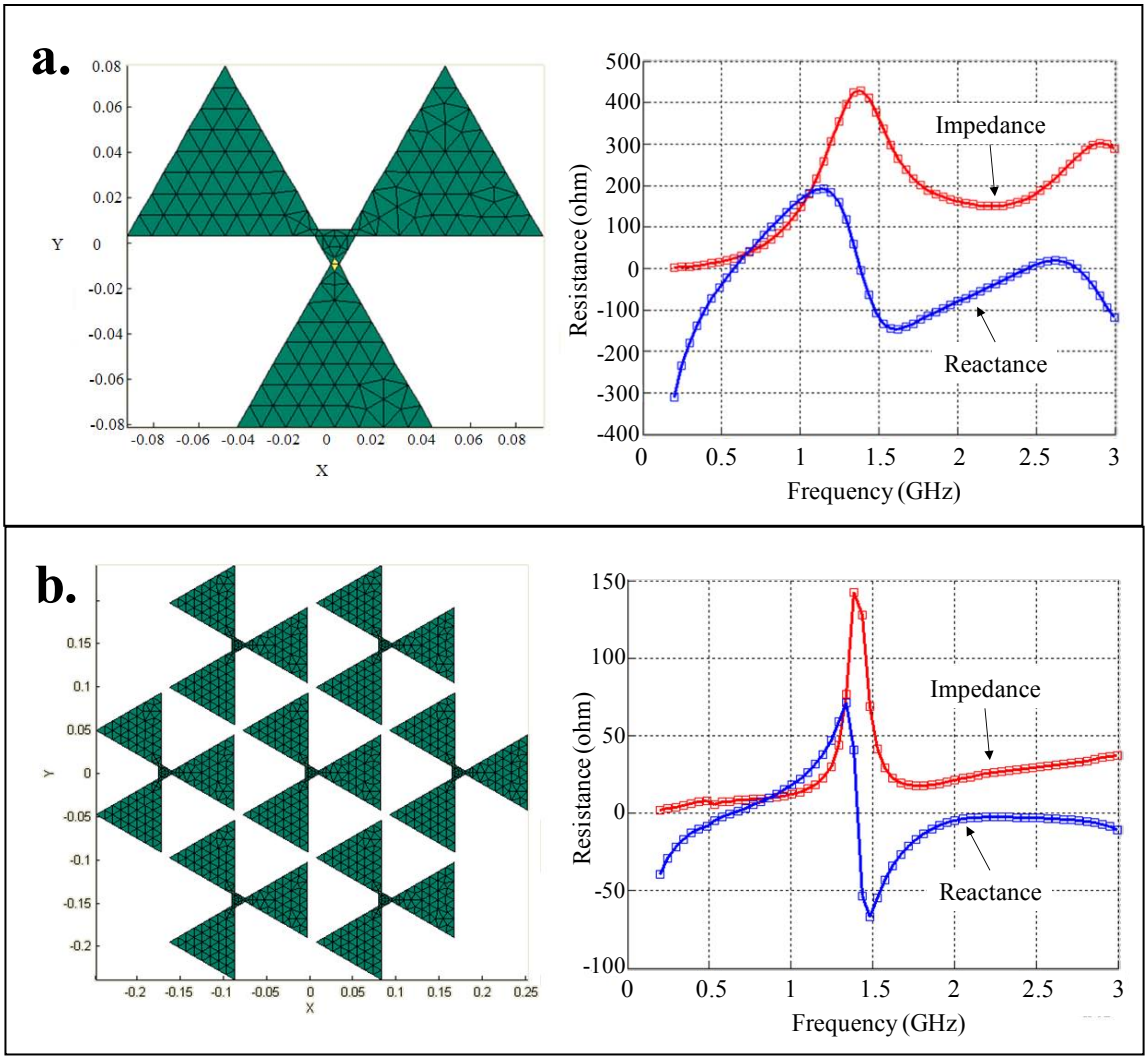

Figure 2-16 Plot of impedance and reactance versus frequency, showing: a) Single equilateral tripole element; b) 3 x 3 hexagonal equilateral tripole array. Figure illustrates variation of impedance as function of frequency when additional elements are added

The reactance curve in Figure 2.16b shows that the array will radiate most efficiently at regions where reactance is minimal, however the impedance will also vary considerably throughout this region. Figure 2.17 shows that by introducing a slot within each of the poles of the tripole antenna, the sharpness of the resonant mode (at ~1450 MHz) would

be significantly reduced (see Figures 2.16b and 2.17b). Thus, changing the shape and structure of the radiating components, changes the way in which the elements interact with each other and modifies the overall frequency response of the array.

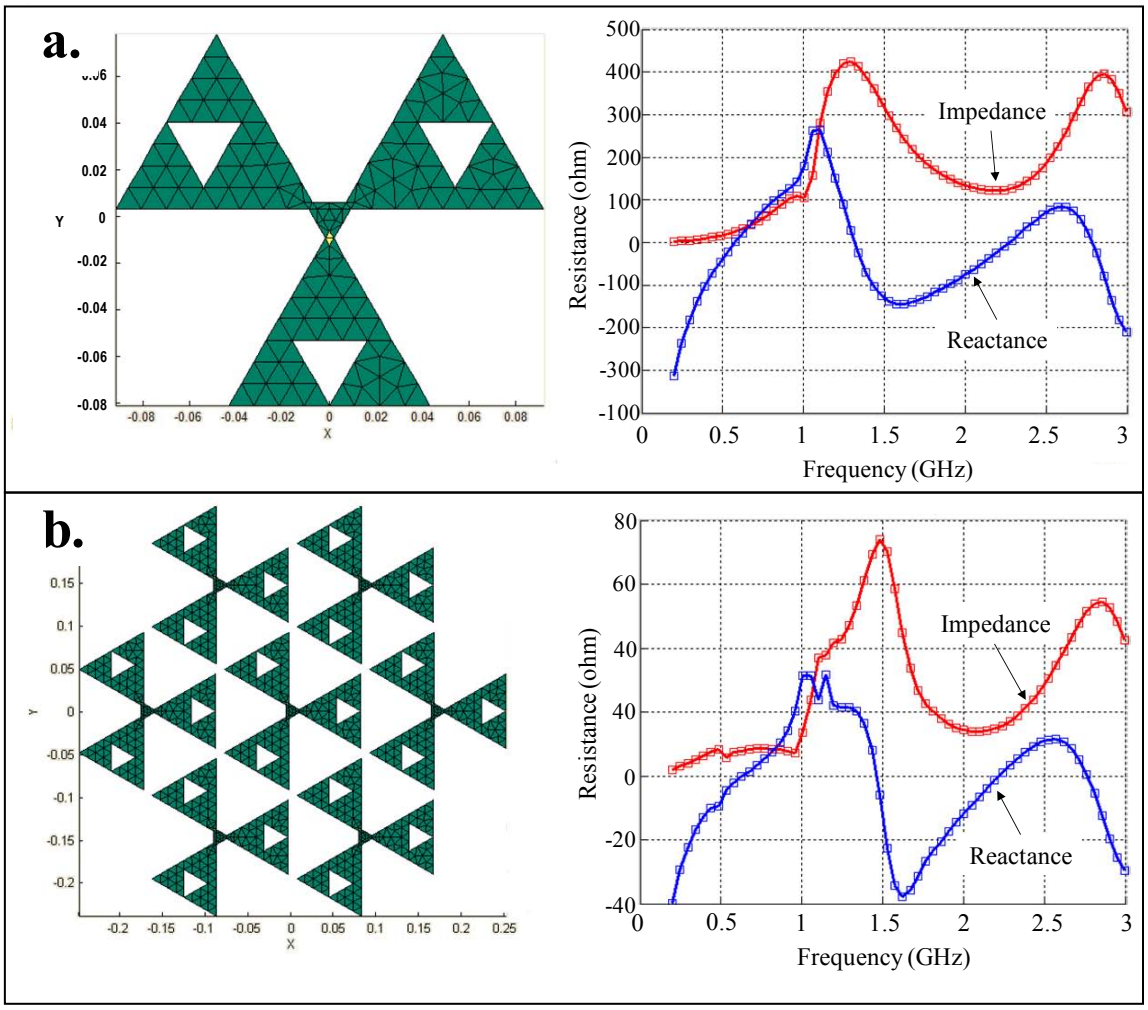

Figure 2-17 Plot of impedance and reactance versus frequency, showing: a) One single equilateral slot tripole antenna; and b) 3x3 slot tripole antenna array

2.3.2 Three Feed Modelling Technique

Results in Figures 2.16 and 2.17 were calculated using method of moments modelling technique in transmit mode. This process was established by exciting only "one" of the three terminals of each antenna with an applied voltage of 1 V. However, ideally, all

"three" terminals of the tripole antenna must be excited simultaneously. This means that amplitude coefficients and excitation phase of the three terminals must be arranged and split in order that depends on the polarization of the total electro-magnetic field. We can determine these excitation coefficients by examining how the tripole antenna behaves in receive mode, as illustrated in Figure 2.18.

If the tripole antenna, in Figure 2.18, is irradiated by an incident plane wave (say 1500 MHz polarized in Y axis), the received amplitude coefficients at each terminal would be split in order that depends on the polarization of the incoming electric field. Surface currents would be scattered in such a way that approximately 50 % (0.43×10^{-3} W) of the power is received at terminal A, while further 25 % is received at the terminal B and terminal C, respectively; as calculated using MoMADT (see calculated Feed Power values in Figure 2.18).

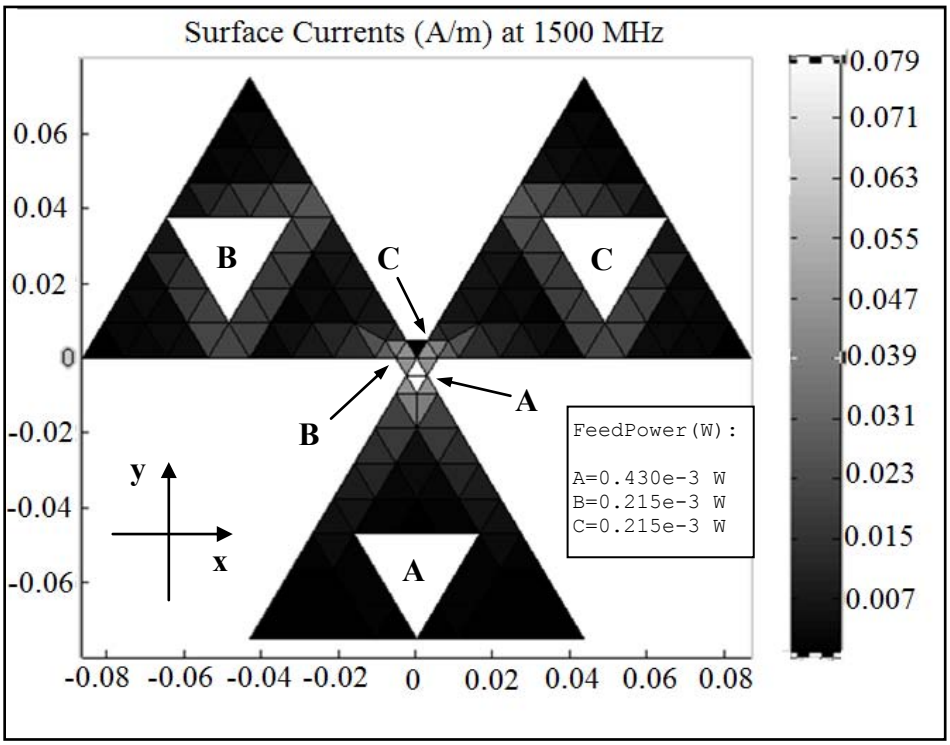

Figure 2-18 Receive mode solution for the equilateral slot tripole antenna showing surface current magnitudes (A/m) and feed power (W) through feed edges A, B and C of the tripole antenna when illuminated by an incident plane wave at 1500 MHz, polarised in Y axis.

If we consider reciprocity, then same can be concluded if the antenna was treated as a transmitter. In transmitting case, the tripole antenna must be excited so that terminal A is supplied with 50 % of the power, while terminal B and terminal C are excited with equivalent 25 % of the total transmitted power, see Figure 2.19. Furthermore, the applied excitations between the three terminals must be in phase, as indicated by the black arrow lines in Figure 2.19. This process would insure that the coupled radiated electric field is linearly polarized in Y axis. During this process, the central portion of the tripole antenna would be treated as a common ground. The MoMADT modelling tool enables us to implement and model these specific conditions, which makes possible to calculate terminal antenna parameters that relate to terminal impedances, terminal reflection coefficient (S11) and VSWR.

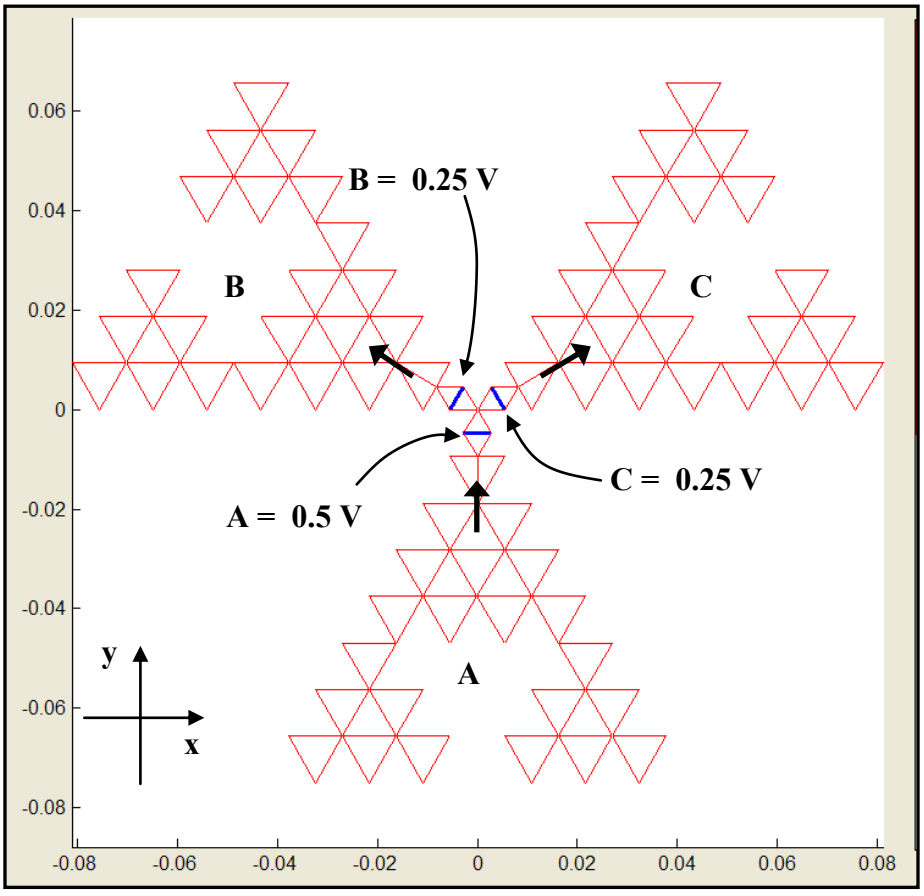

Figure 2-19 Excited terminals A, B and C of the modeled slot tripole antenna in transmit mode with assigned feed voltage values of A = 0.5 V, B = 0.25 V and C = 0.25 V applied on the three feed edges (blue edge lines)

Figure 2.20 shows the calculated terminal impedances, terminal VSWR and terminal reflection coefficient of the equilateral slot tripole antenna using the three feed modelling technique discussed above. Note how the impedance response for each terminal in Figure 2.20b agrees perfectly with that obtained in Figure 2.17a. In addition, the line plot for each terminal in Figure 2.20b completely overlap each other, which indicates that impedance, VSWR and S11 are identical for each of the three terminals. Results show that equilateral slot tripole antenna radiates best at the frequency region 1.5 to 2.5 GHz where VSWR $\leq$ 2:1, and the return loss of -10 dB is achievable, which constitutes approximately 11 % reflected power if normalized to 105 ohm.

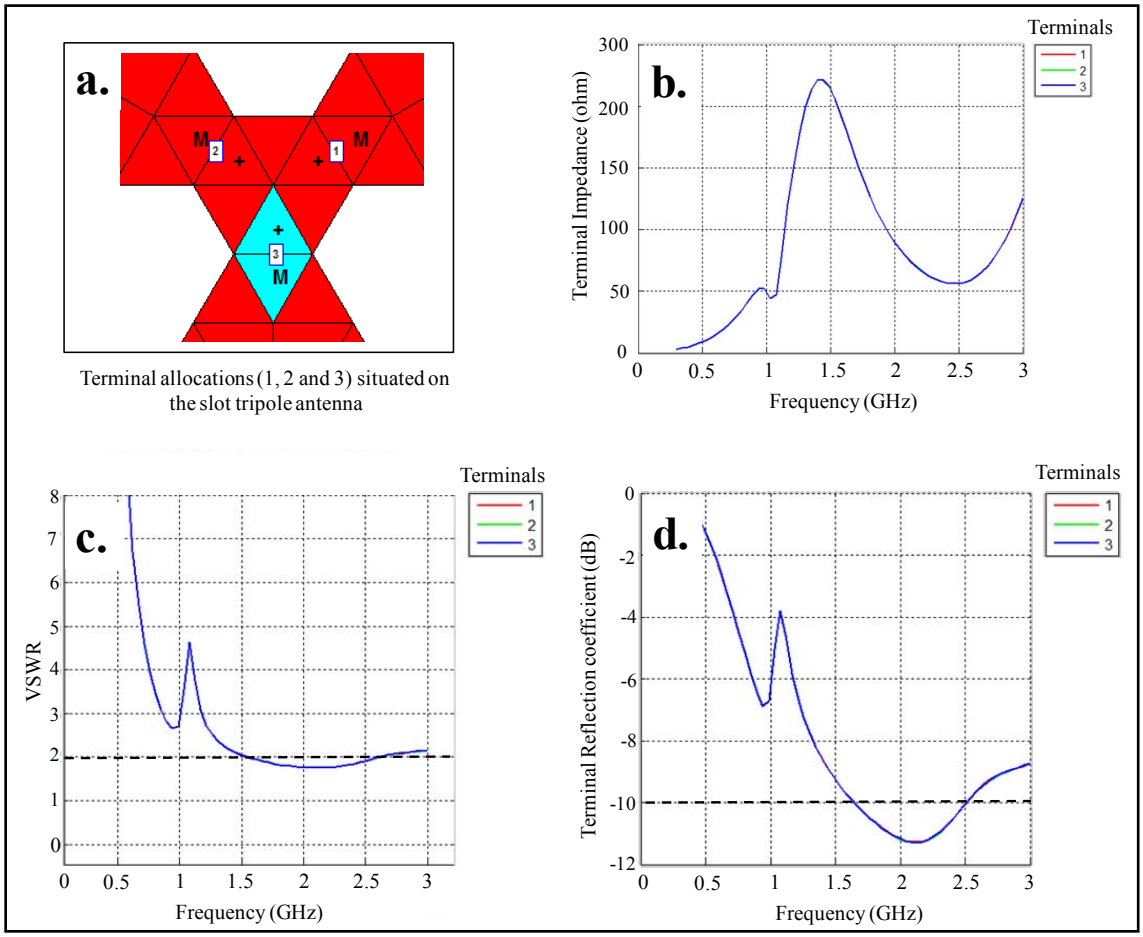

Figure 2-20 Three feed modeling solution of the slot tripole antenna in transmit mode, showing: a) Terminal feed edges 1, 2 and 3; b) Impedance vs frequency; c) Voltage standing wave ration (VSWR) vs frequency; and d) Reflection coefficient vs frequency for each terminal. The vertical scale 1, 2 and 3 shows the colour line plots for each terminal. Note that the three curves completely overlap each other.

Figure 2.20(c-d) shows that the equilateral slot tripole antenna does not radiate efficiently at frequencies less than ~1500 MHz, especially at the frequency region of 500 MHz, under which circumstance reflected power of well above 60% would be achieved if normalized to 105 ohm. In order for this to be corrected, normalization impedances would have to be modified, or the size of this antenna would have to be increased so that the impedance curves are shifted towards the lower frequencies. However, increasing the size of the antenna means that the element spacing of the array would also be increased and this would result in reduceed sampling effectiveness of the array at the upper operating frequency.

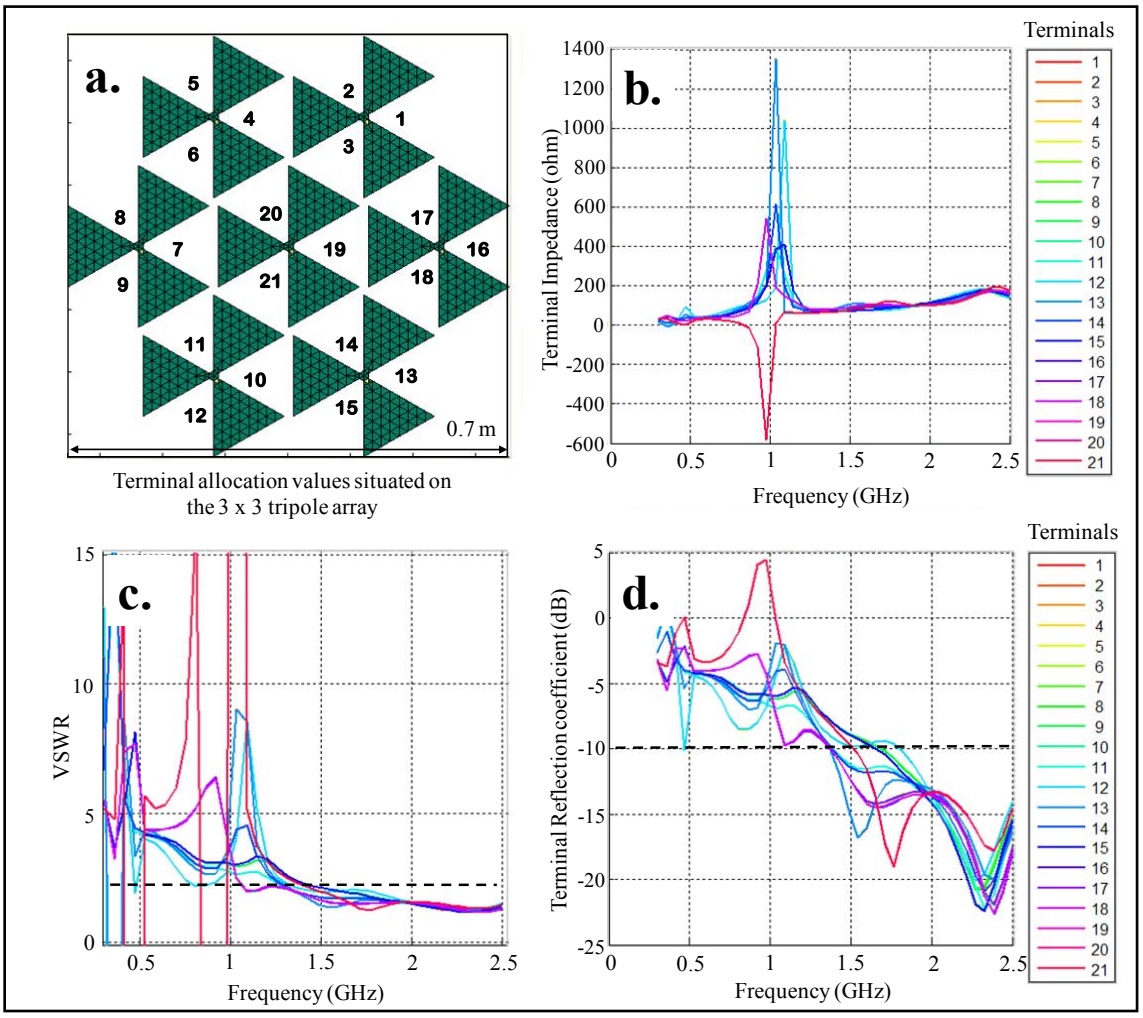

Figure 2-21 Three feed modeling solution of the 3×3 tripole array in transmit mode, showing: a) Terminal allocation values; b) Terminal impedance, c) VSWR and, d) Reflection coefficient, normalized to 150 ohm. Note that the element size has been increased to yield array diameter of 0.7 m, compared to Figure 2.17b

Figures 2.21 and 2.22 show what happens when the size of the element and the size of the array are increased. Figure 2.21 shows the three-feed transmit mode solution of the 3×3 equilateral tripole array with element size increased by 50 % compared to Figure 2.17, giving an array size diameter of 0.7 m. Conversely, Figure 2.22 shows the same calculation expect this time the element size has been increased by 125 %, giving an array size diameter of approximately 1.1 m. Both solutions are normalized to 150 ohm for self-complementary structures [72].

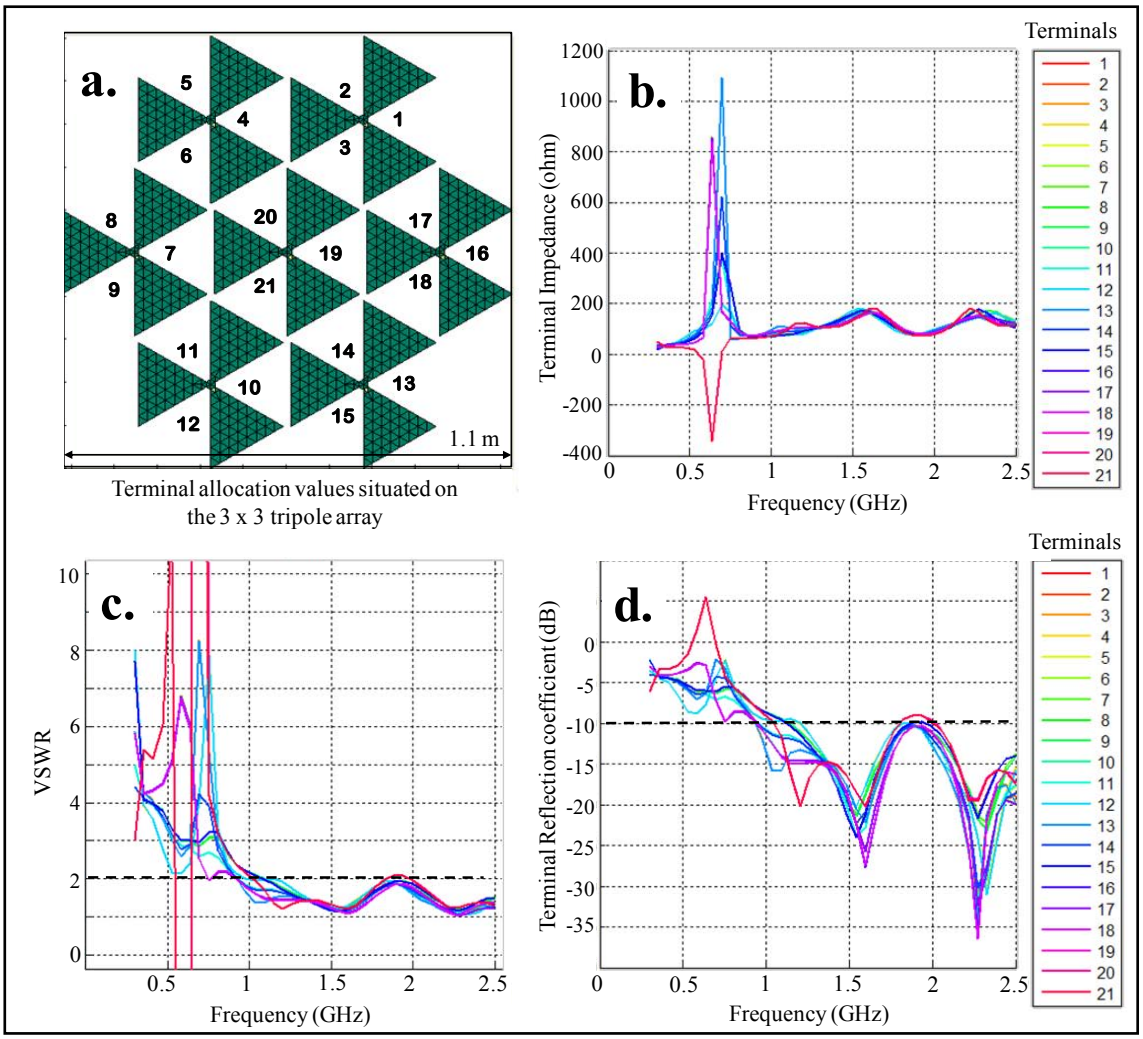

Figure 2-22 Three feed modeling solution of the 3×3 tripole array in transmit mode, showing: a) Terminal allocation values; b) Terminal impedance, c) VSWR and, d) Reflection coefficient as function of frequency, normalized to 150 ohm. Note that element size is increased to yield array diameter of 1.1 m

As can be seen in Figure 2.21 and 2.22, if the element size is increased, the terminal reflection coefficient of the array and its elements is improved towards the lower frequencies specifically at the region where VSWR ≤ 2:1 and the return loss of -10 dB is achievable, if normalized to 150 ohm. However, if the element size is increased, the element spacing of the array is also increased and becomes ≥ 0.16 m between centres of oppositely oriented terminals, which is considerably larger than the preferred "half wavelength" at the upper operating frequency, which at 1100 MHz is given to be $(3 \times 10^8)/(1100 \times 10^6)/2 = 0.136$ m.

The general conclusion from the modelling study of the equilateral tripole antenna [71] shows that, although this antenna can be used to design a relatively wideband array, the overall size and shape of the antenna creates limitations on the minimum element spacing which places basic limits on the size and operating frequency of the array.

An alternative solution to these problems would be to use the ***diamond tripole antenna*** shown in Figure 2.12b. An equivalent diamond tripole array does not generate sharp resonances, furthermore, the diamond tripole antenna provides an improved impedance response over the equilateral structure, and enables the element spacing of the array to be reduced without significant reduction to element size. These solutions will be presented in chapter 3.

2.4 Summary and Conclusions

In chapter 2, an important step was discussed through a review of various antennae and array structures that concludes to use of the tripole antenna [36], [67] and development of the focal plane array that provides three vectors of polarization. Following this, a series of frequency independent structures were investigated, results of which yield a design solution for the ***diamond*** tripole antenna and the ***equilateral*** tripole antennas.

The equilateral tripole antenna [71] was selected as the starting design onto which basic operations of the array were investigated. For example, the frequency response parameters were examined and compared against varying array sizes. It was found that although the equilateral tripole antenna exhibits wideband properties the overall size of the antenna creates limitations on the minimum element spacing of the array, which places basic limits on the overall size and operating frequency of the array and results in reduced bandwidth.

Throughout this chapter, number of preliminary array designs and basic modelling procedures were discussed; specifically outlining the three-feed modelling technique. An important concept of this technique illustrates that a tripole antenna must be modelled with the three feeds excited independently. This is also the case if the antenna is used in an array, under which circumstance all feeds of the array must be excited independently taking into consideration any phase variations applied between the respective elements of the array (see Appendix A 6). This technique enables the ability to model and observe terminal antenna parameters in transmit and receive modes, providing solutions on terminal impedance, terminal VSWR and terminal reflection coefficient as function of the frequency, polarization and phase.

CHAPTER 3

Chapter 3 - Modeling and Simulation

In Chapter 3, the full modelling implementation of the Hexagonal Diamond Tripole (HDT) FPA is discussed. Two distinct variations of the FPA (5×5 and 7×7 array) are presented utilizing the diamond planar strip antenna elements arranged to provide three vectors of polarization. Modelling of the array and its elements is derived via method of moments utilizing the MoMADT design tool, and offers solutions to both metallic and dielectric materials. All results include computations comprising mutual coupling effects with fields and currents that vary in three dimensional space. Section 3.1 presents the design concept of the diamond tripole antenna. Section 3.2 shows the design and modelling solutions of the 5×5 HDT array, while section 3.3 presents the design and modelling solutions of the 7×7 HDT array.

3.1 Diamond Tripole Antenna

Design of the diamond tripole antenna was established in this research through means and logical steps described in chapter 2. The "diamond tripole antenna" consists of three planar diamond structures over a ground plane with centre feeds, as shown in Figure 3.1. Dimensions of the antenna, such as element spacing, ground plane distance (from radiating terminals), as well as the feed line structure were carefully derived using modelling and simulation procedures via MoMADT. Detailed graphic representation of the diamond tripole antenna is shown in Figure 3.1 (note that although the balun circuit is not shown in Figure 3.1, it is indeed included in the system).

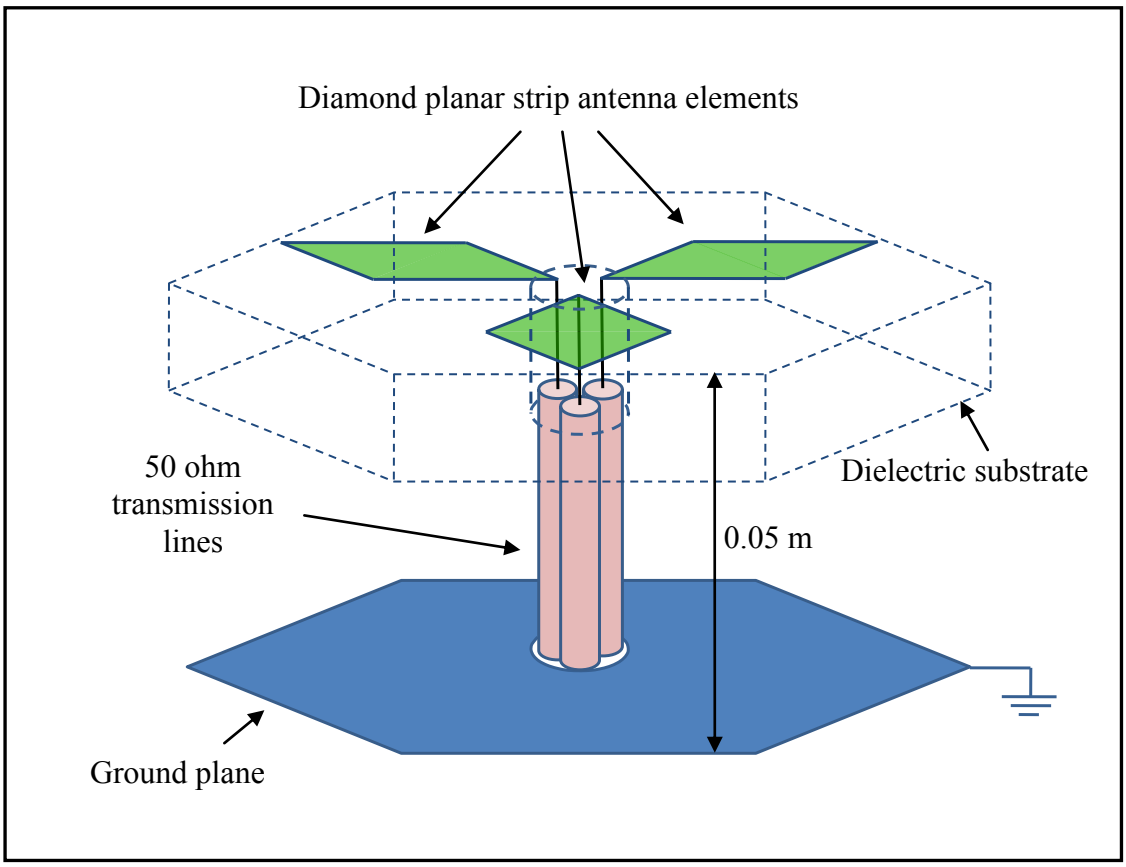

Figure 3-1 Graphic illustration of the diamond tripole antenna showing the relative components of the antenna including the ground plane, dielectric substrate layer, planar strip antenna elements and the transmission lines. Appropriate balun circuit is also required (not shown in the image).

As can be seen (Figure 3.1), the diamond tripole antenna consists of three distinct feeds sharing a common ground. The ground plane is represented by a metallic (conductive) sheet positioned beneath the radiating elements at a distance of 0.05 m, to ensure that unidirectional radiation is obtained. The transmission lines (subject to appropriate balun circuit being installed - ferrite beads are used in this study) pass through the ground plane and through the dielectric substrate to the feed port. The diamond planar antenna elements are positioned $2\pi/3$ degrees apart and printed onto a dielectric substrate of relative permittivity of $\varepsilon = 2.3$. The size of the elements was determined based on the element spacing, operating frequency, overall array size and the F/D ratio. Proportional dimension of the diamond tripole antenna is shown in Figure 3.2.

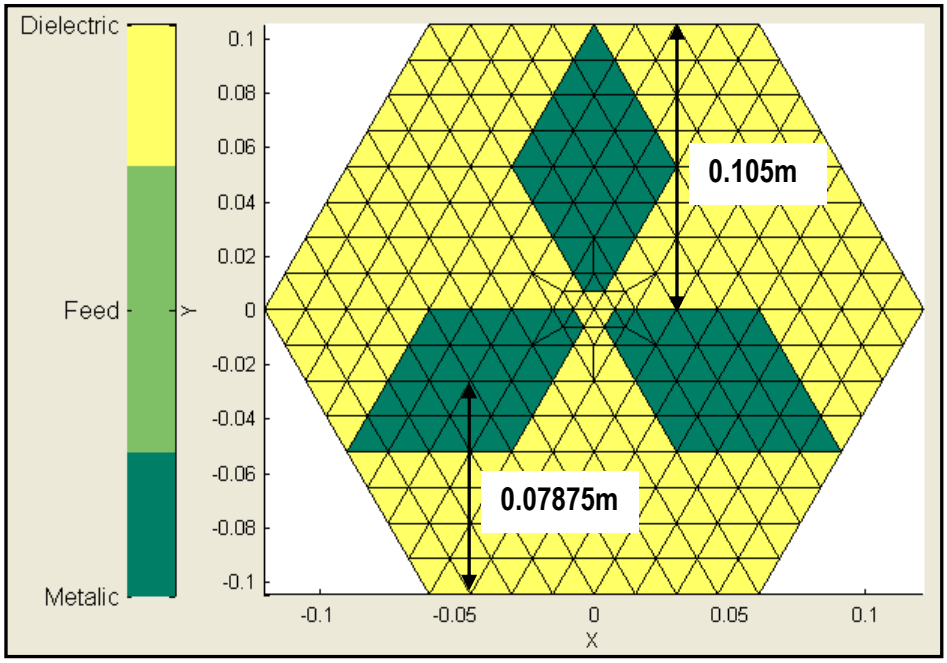

Figure 3-2 Proportional dimensions of the diamond tripole antenna to be used in a 5×5 array. The vertical bar represents the components of the system, showing the dielectric substrate (yellow), and metallic components (dark green) etched onto a dielectric substrate.

Figure 3.2 shows the modelling implementation of a single diamond tripole antenna and its respective dielectric substrate layer. The dielectric substrate plays a positive role in determining the overall impedance response of the antenna and the array. Figure 3.3 shows what happens when the dielectric substrate layer is included and removed from the system. Results illustrate the transmit mode solution of the diamond tripole antenna, with and without the 0.05 m dielectric substrate layer, revealing the "total" impedance and reactance as function of the frequency for the two cases.

Figure 3.3 shows that, if the dielectric substrate is included in the system, the antenna shifts the impedance curves towards the lower frequencies (see Figures 3.3a and 3.3b). In other words, the dielectric substrate acts as an inductive load to the antenna, effectively making the antenna longer than it physically is. It was determined that by changing the relative permittivity and the dielectric layer thickness, the amount of shift can be varied. However, much like the antenna loading, this feature comes at the cost of

return loss and efficiency. Hence, there is a trade off between relative permittivity, substrate layer thickness, resulting inductance and the efficiency of the radiating system. A relative permittivity of 2 - 3, and substrate layer thickness of 0.001 – 0.003 m was found to work effectively without any significant loss to efficiency.

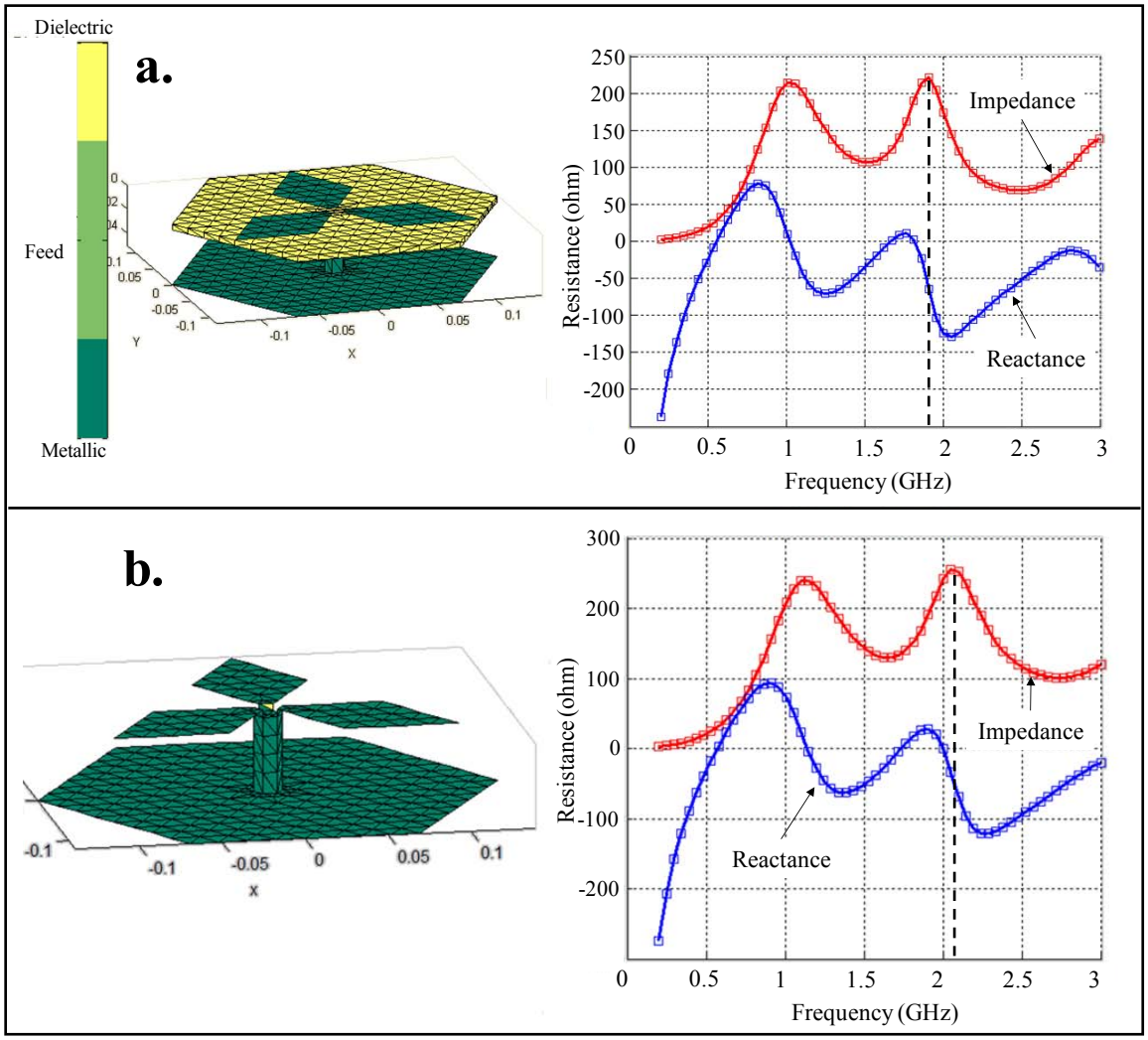

Figure 3-3 Transmit mode solution of the diamond tripole antenna, showing: a) impedance and reactance versus frequency with the 0.005 m dielectric substrate layer included; and, b) impedance and reactance versus frequency with the 0.005 m dielectric substrate layer removed. The broken line demonstrates the impedance shift towards the lower frequencies if dielectric substrate layer is used.

3.2 The 5x5 HDT Array

As briefly discussed in chapter 2, the planar diamond tripole antenna offers an improved impedance over the equilateral tripole structure (see Figure 3.3) and enables the element spacing of the array to be reduced without significant reduction to element size. In this section, we intend to demonstrate these advantages and reveal the operation of the 5×5 hexagonal diamond tripole (HDT) array. Solutions are obtained using MoMADT via receive and transmit modelling techniques, including procedures relating to scan and phase offsets.

As mentioned previously, the diamond tripole antenna was designed for its use in developing FPAs for radio astronomy, thus, antenna dimensions were selected based on array size and operating frequency of 500 to 1500 MHz. Ground plane distance (from radiating elements) was set to be 0.05 m, which is less than half wavelength of the upper operating frequency, to ensure that destructive interferences from the ground plane fall outside of the frequency of operation. Modelling implementation of the 5×5 HDT array, its elements and the ground plane is illustrated in Figures 3.4.

Figure 3.4a shows the top view of the 5×5 HDT array, while Figure 3.4b shows the side view of the 5×5 HDT array. Due to hexagon formation, the 5×5 HDT array consists a total of 19 tripole antennas, and a total of 57 individual terminals or ports. Successful operation requires that all 57 terminals of the 5×5 HDT array be excited (or matched) independently with appropriate amplitude coefficients and phases to insure that signals with unique beam displacements and polarizations are identified. These excitation conditions (amplitude and phase offsets) depend on the state of the transmitted or received EM field. Total diameter of the 5×5 HDT array was selected to be 0.8 m, while the ground plane is slightly wider and spans approximately 1.0 m for the reasons that will be explained later. The vertical colour bar in Figure 3.4a shows the individual components of the system, i.e. the dielectric substrate (yellow), feed edges (light green) and metallic components (dark green) etched onto a dielectric substrate. Note that feed edges are situated beneath the dielectric substrate and cannot be seen in the image.

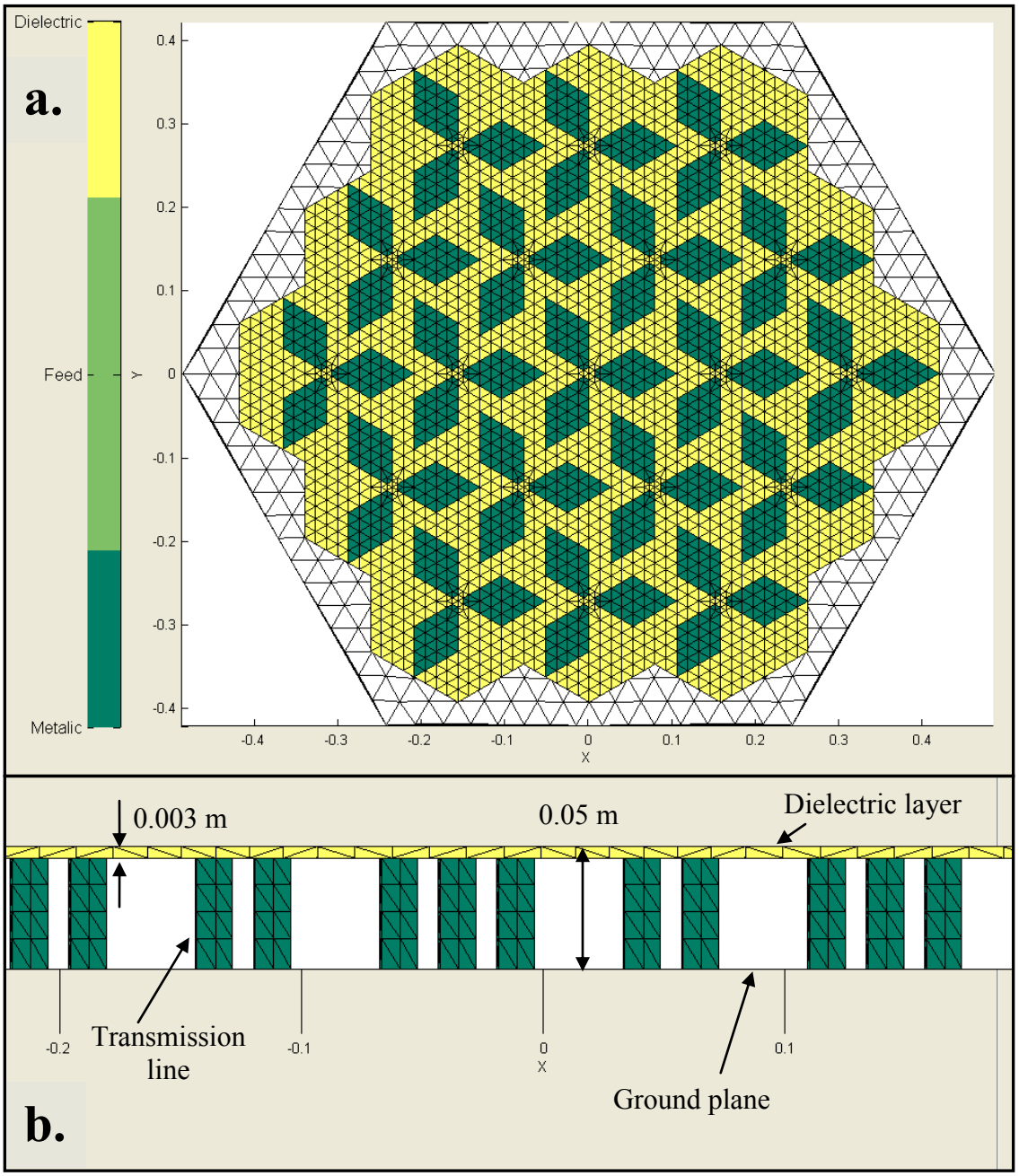

Figure 3-4 Modeling implementation of the 5×5 hexagonal diamond tripole (HDT) array, showing: a) Top view of the 5×5 HDT array revealing individual diamond tripole antenna components, their size and orientation within the plane; b) Side view of the 5×5 HDT array showing the ground plane, dielectric layer, transmission lines and vertical dimensions (note that the discretization resolution of the ground plane, although not shown in the image, is far less than λ/8)

3.1.2 Transmit mode solution of the 5×5 HDT array

In a classical phased steered array, all elements of the array are generally excited with equal or equivalent amplitude coefficients so that a beam of specified intensity, direction and polarization is generated. However, a FPA system does not operate in the same manner as a classical phase-steered array, because during reception the elements are conjugate matched to the focal plane field instead. In this section of the thesis we intend to investigate the operation of the 5×5 HDT array in transmit mode, by treating the array as a "classical phased steered" array. These solutions will enable us to investigate the impedance response of the system and determine the gain, efficiency and directivity parameters of the array. Results relating to phase offsets are explained in Appendix A.

Transmit mode solution of the 5×5 HDT array without phase offsets

When designing phased arrays, it is important to ensure that specific elements of the array do not cause excessive signal distortion and reflections. Most effective way to measure these parameters is to analyse the terminal frequency response factors of the array elements individually during reception and/or transmission operations. As explained in Chapter 2, these factors enable us to investigate terminal impedance, terminal VSWR and terminal reflection coefficient of the system. It is the objective of this research to investigate the frequency response of the antenna through modelling procedures of the 5×5 HDT array in both transmit and receive modes. The transmit mode solutions will be determined for all terminals simultaneously so that variations between the respective elements of the array can be visually observed.

Figure 3.5, 3.6 and 3.7 shows the terminal impedance, terminal VSWR and terminal reflection coefficient as function of frequency, calculated for each feed of the 5×5 HDT array between 400 to 2100 MHz (normalized to 80 ohm). These calculations were performed in transmit mode by supplying equivalent amplitude coefficients to all of the 57 terminals simultaneously, so that signals are polarized in X direction with zero phase

offset. Figure 3.5 shows that terminal impedance of the 5×5 HDT array is generally uniform between 400 to 1650 MHz for all terminals, except above 1650 MHz where number of resonances are generated. It was found that these resonances are caused by reflections between the elements at the frequency region where the element spacing starts to exceed half wavelength of the operating frequency. The element spacing is determined as the distance between the planar diamond strip antenna elements, given to be 0.07875 m in X-axis direction and 0.088 m in Y-axis direction. This equates to a frequency of 1900 MHz, and 1704 MHz. As expected, these resonances are perfectly visible in Figure 3.5.

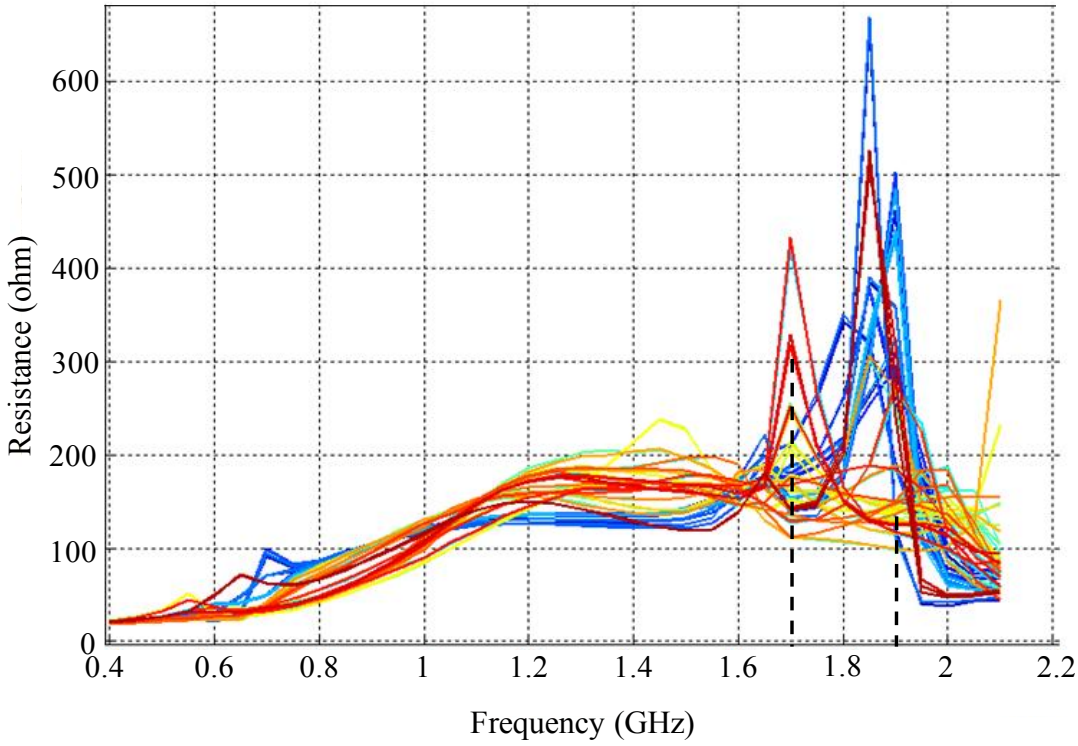

Figure 3-5 Terminal impedance versus frequency of the 5×5 HDT array, showing impedance curves for all 57 terminals calculated in transmit mode while supplying equivalent amplitude coefficients with zero phase. This figure illustrates the variation of impedance between terminals of the array. Broken lines indicate resonance modes due to element spacing at 1900 MHz and 1704 MHz

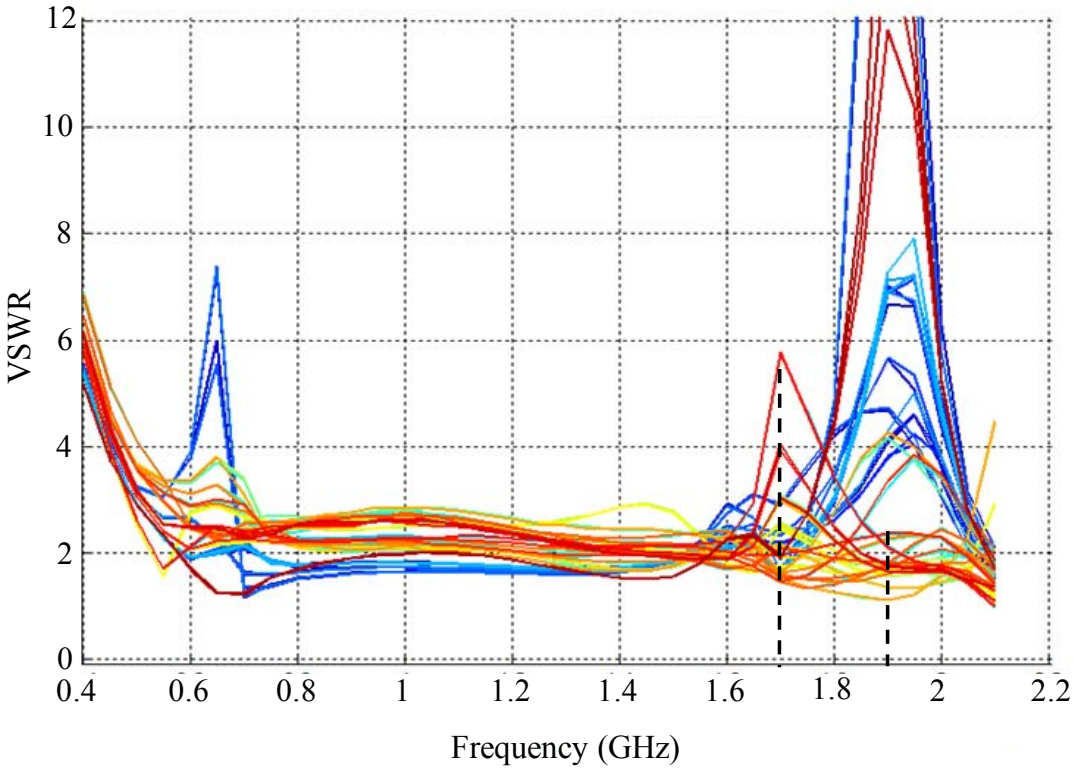

Figure 3-6 Terminal VSWR versus frequency for the 5×5 HDT array normalized to 80 ohm, showing plot of VSWR for all 57 terminals calculated in transmit mode while supplying equivalent amplitude coefficients with zero phase. This figure illustrates the variation of VSWR between terminals of the array normalized to 80 ohm. Broken lines indicate resonance modes due to element spacing which occurs at 1900 MHz and 1704 MHz. Resonance mode at 650-700 MHz is formed by the central terminals at the frequency region when array diameter becomes approximately two wavelengths long

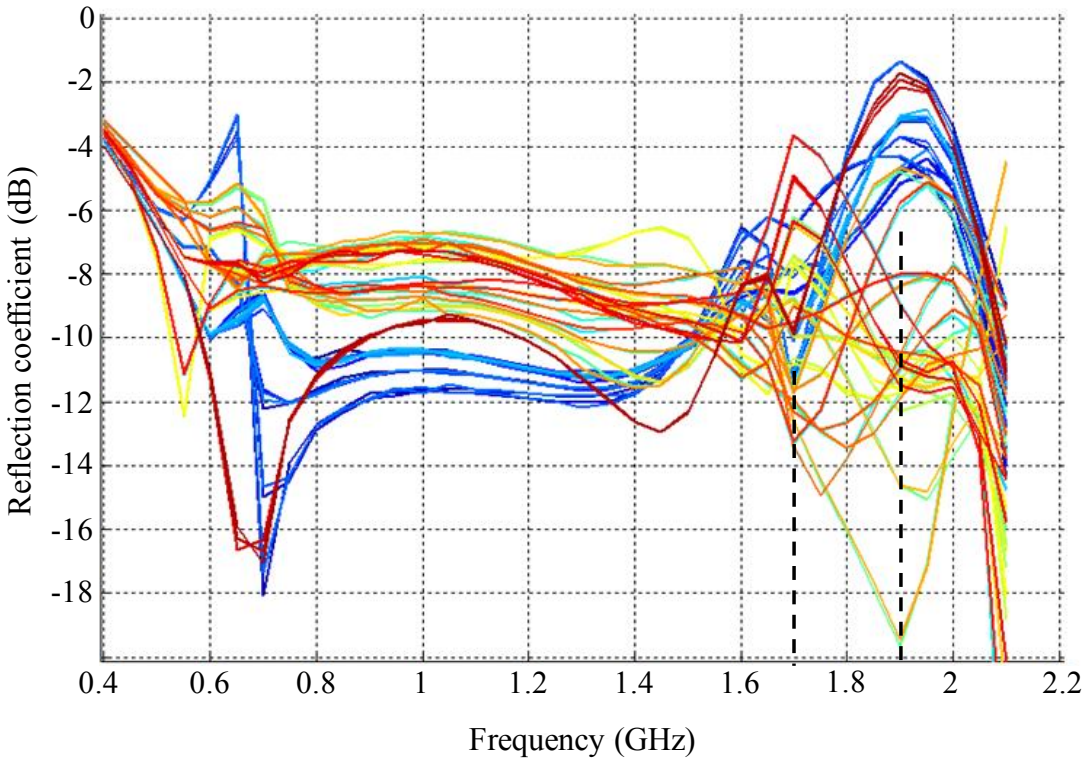

Figure 3-7 Terminal reflection coefficient versus frequency for the 5×5 HDT array normalized to 80 ohm, showing plot of reflection coefficient in transmit mode while supplying equivalent amplitude coefficients to all 57 terminals simultaneously with zero phase. This figure illustrates the variation of reflection coefficient between terminals of the array normalized to 80 ohm. Broken lines indicate resonance modes due to element spacing which occurs at 1900 MHz and 1704 MHz. Resonance mode at ~700 MHz is caused by the central terminals at the frequency region when array diameter becomes approximately two wavelengths long

Figures 3.6 and 3.7 show the terminal VSWR and reflection coefficient of the 5×5 HDT array, normalized to 80 ohm. As can be seen, the 5×5 HDT array yields a relatively uniform impedance across 500 to 1700 MHz for all 57 terminals, except at ~700 MHz where the array diameter becomes approximately two wavelengths long. When this occurs, a destructive interference is generated at the central terminals. This source of interference (~700 MHz) can be reduced by extending the array with addition of dummy antenna elements [73]. This procedure will be further explained in section 3.3.2.

Figure 3.8 shows the mean VSWR versus frequency of the 5×5 HDT array. As can be seen, an average VSWR of ≤ 2.2:1 can be achieved across 700 to 1700 MHz, which yields an average reflection coefficient of approximately ≤ -8.6 dB and total reflected power of 13.8% and transmission loss of 0.65 dB if normalized to 80 ohm. However, below 700 MHz, impedance mismatch is increased. At 550 MHz VSWR of 2.7:1 is obtained which yields total reflected power 20.8 % if normalized to 80 ohm. This reflected power can be improved if the normalization impedance is reduced, or a resistive load is applied on the feed. However, applying a resistive load at the feed would reduce the radiation efficiency of the system especially at lower frequencies.

Figure 3.9 shows the total radiation efficiency versus frequency for the 5×5 HDT array. This plot describes the ratio between **total** feed power and **total** radiated power during this modelling procedure, which illustrates that the radiation efficiency of the 5×5 HDT array is well above 77 % for all frequencies between 500 to 1700 MHz, which is considered to be good. But what can be said about the gain and directivity? We investigate these in Figures 3.10 and 3.11.

Figures 3.10 and 3.11 show the directivity patterns (offset by 20 dB) for the 5×5 HDT array obtained in transmit mode by supplying equivalent amplitude coefficients to all 57 terminals simultaneously in order to polarize the signal in X-axis direction. The viewing angles are given in the XZ plane (Figure 3.10) and YZ plane (Figure 3.11) respectively.

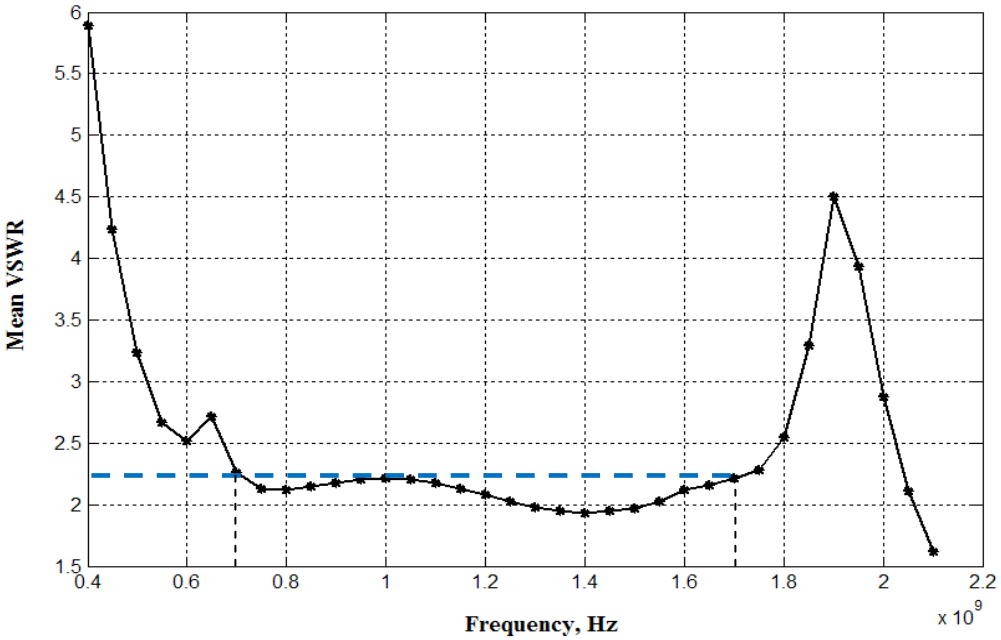

Figure 3-8 Total VSWR versus frequency of the 5×5 HDT array for all elements combined

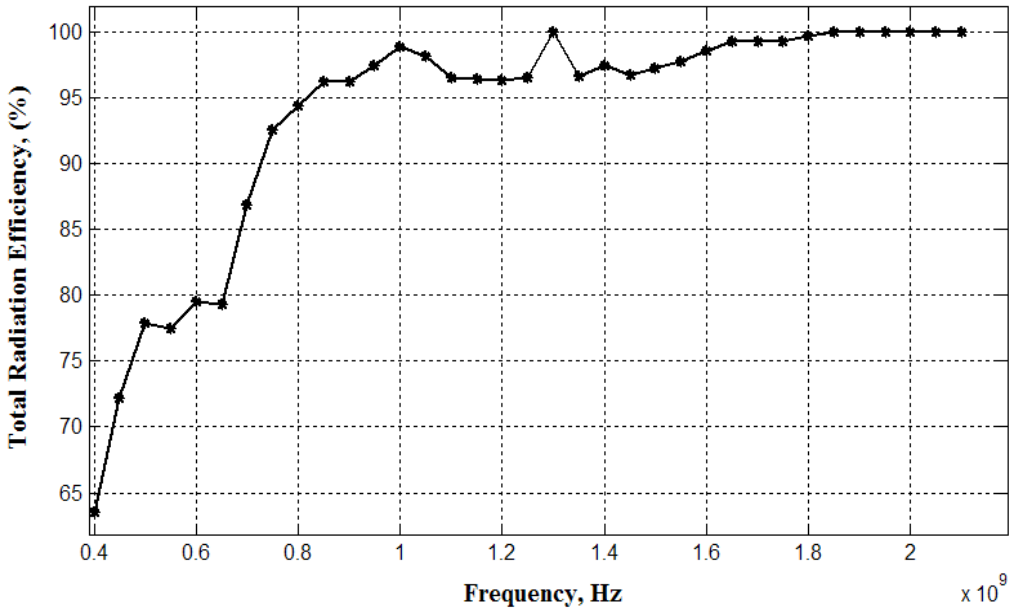

Figure 3-9 Total radiation efficiency versus frequency for the 5×5 HDT array

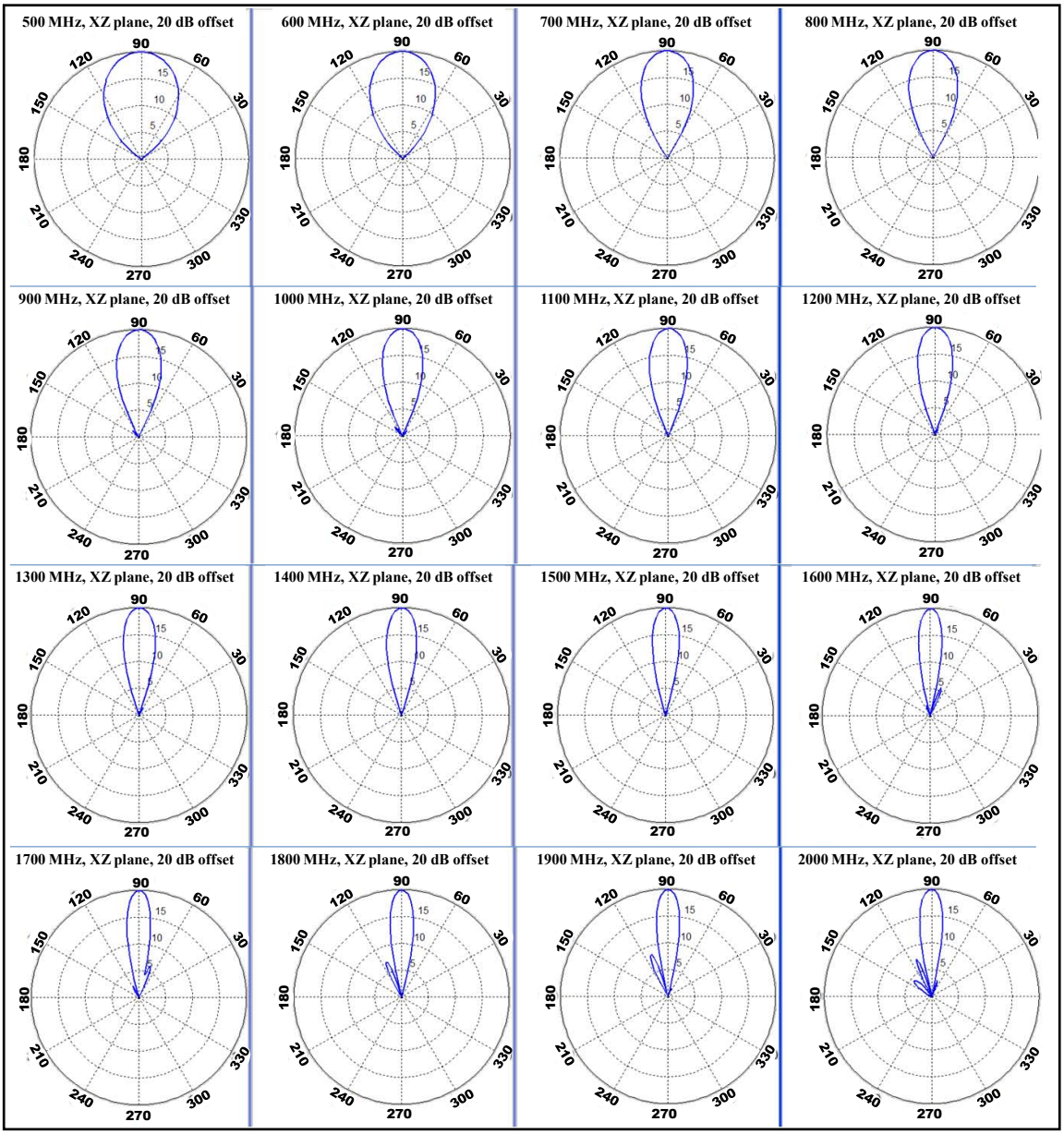

Figure 3-10 Directivity pattern of the 5×5 HDT array in XZ plane (offset by 20 dB) for the frequency range 500(100)2000 MHz

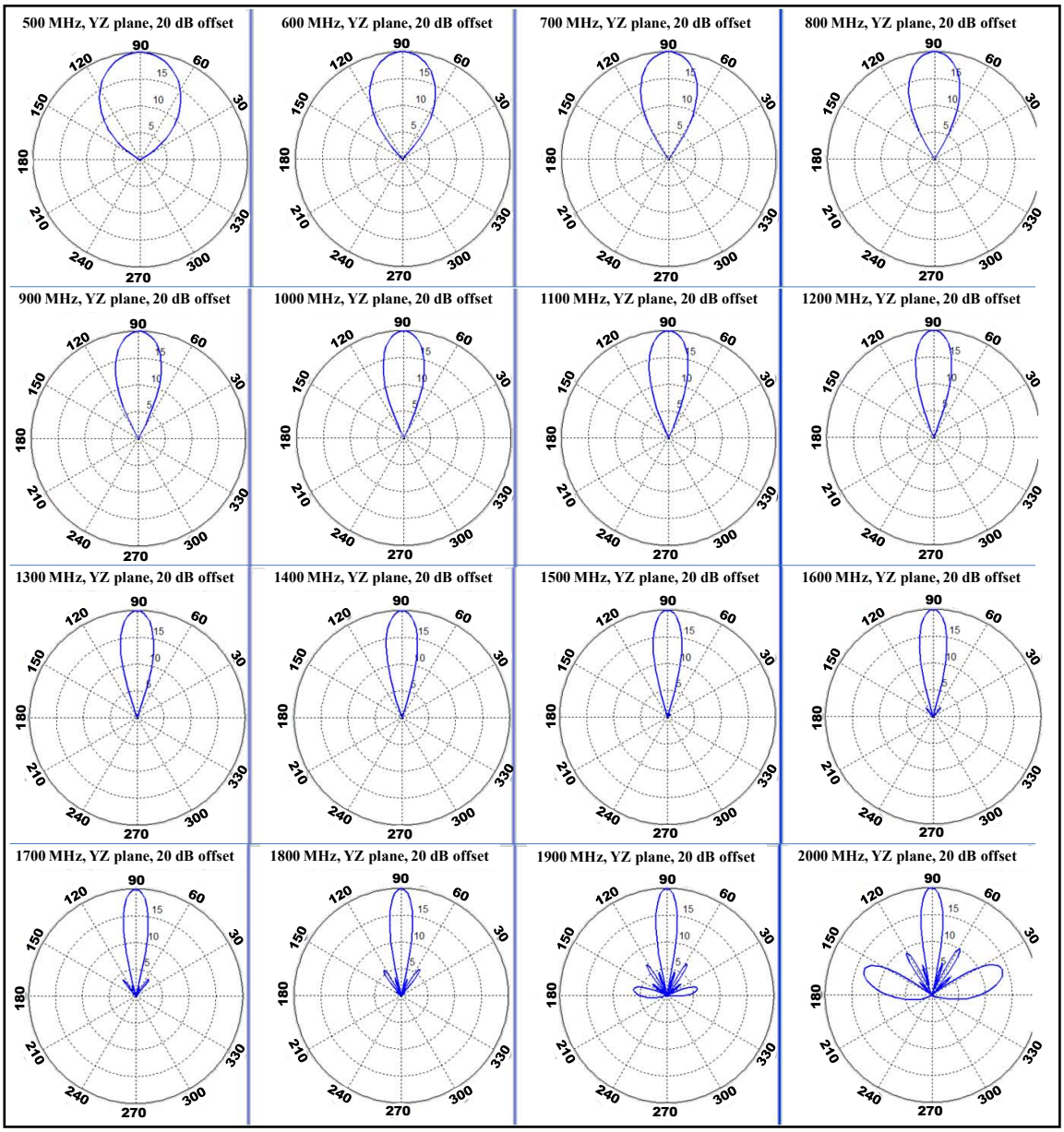

Figure 3-11 Directivity pattern of the hexagonal 5×5 HDT array in YZ plane (offset by 20 dB) for the frequency range 500(100)2000 MHz

As can be seen in Figures 3.10 and 3.11, the directivity patterns of the 5×5 HDT array are relatively uniform across 500 to 1700 MHz, however when frequency exceeds ~1700 MHz, additional beams start to form. This result indicates that the gain deteriorates above 1700 MHz as we would expect due to the element spacing effect discussed above. Once again, we can confirm this by looking at the total linear gain and total logarithmic gain plots in Figure 3.12.

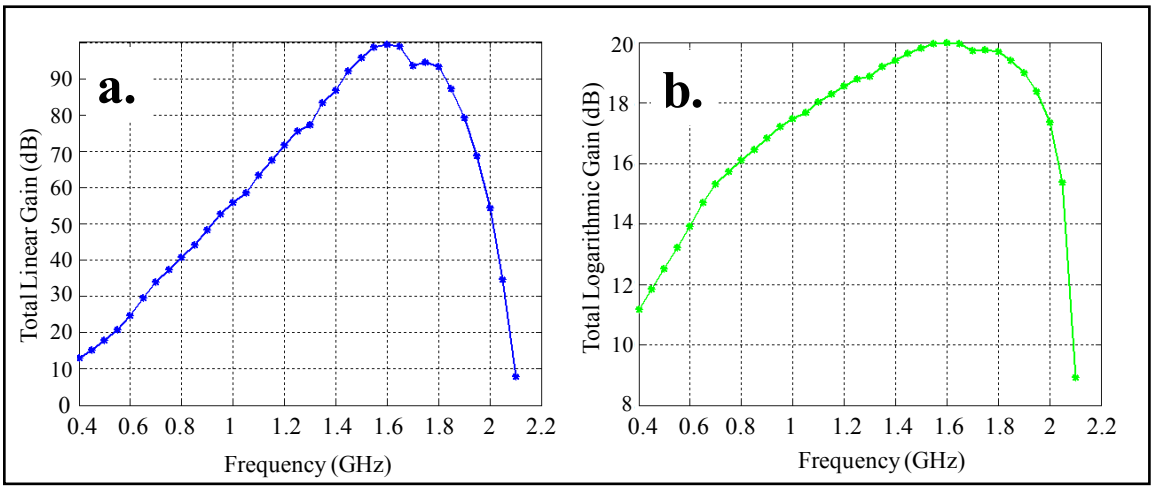

Figure 3-12 a) Total linear, and b) total logarithmic gain, versus frequency for a 5×5 HDT array in transmit mode

The conclusion from the modelling study of the 5×5 HDT array in transmit mode, shows that a relatively good directivity and efficiency in the frequency region 500 to 1700 MHz can be obtained, with a peak logarithmic gain of 20 dB, if all terminals are excited with equivalent amplitude coefficients. Furthermore, a quite acceptable impedance match can be achieved across the indicated frequency range for all terminals if the ports are normalized to 80 ohm.

Transmit mode solution of the 5×5 HDT array with phase offsets

It now remains to be seen how the 5×5 HDT array behaves when phase offsets between the respective elements of the array are introduced. By introducing phase shifts, we can

effectively change the direction of the main beam, as would be expected with a classical phased steered array. Details behind the modelling processes of phase shifts, using the MoMADT, are discussed in Appendix A.

Figures 3.13 - 3.15 show the modelling solutions of the 5×5 HDT array using phase alterations between the elements in transmit mode. Results are calculated via three feed modelling technique utilizing all 57 terminals simultaneously for frequencies 400 MHz, 500 MHz, 800 MHz, 1000 MHz, 1200 MHz and 1400 MHz respectively. Transmitted signal is polarized in X-direction for each case in Figures 3.13 - 3.15, with a maximum beam displacement of 30°.

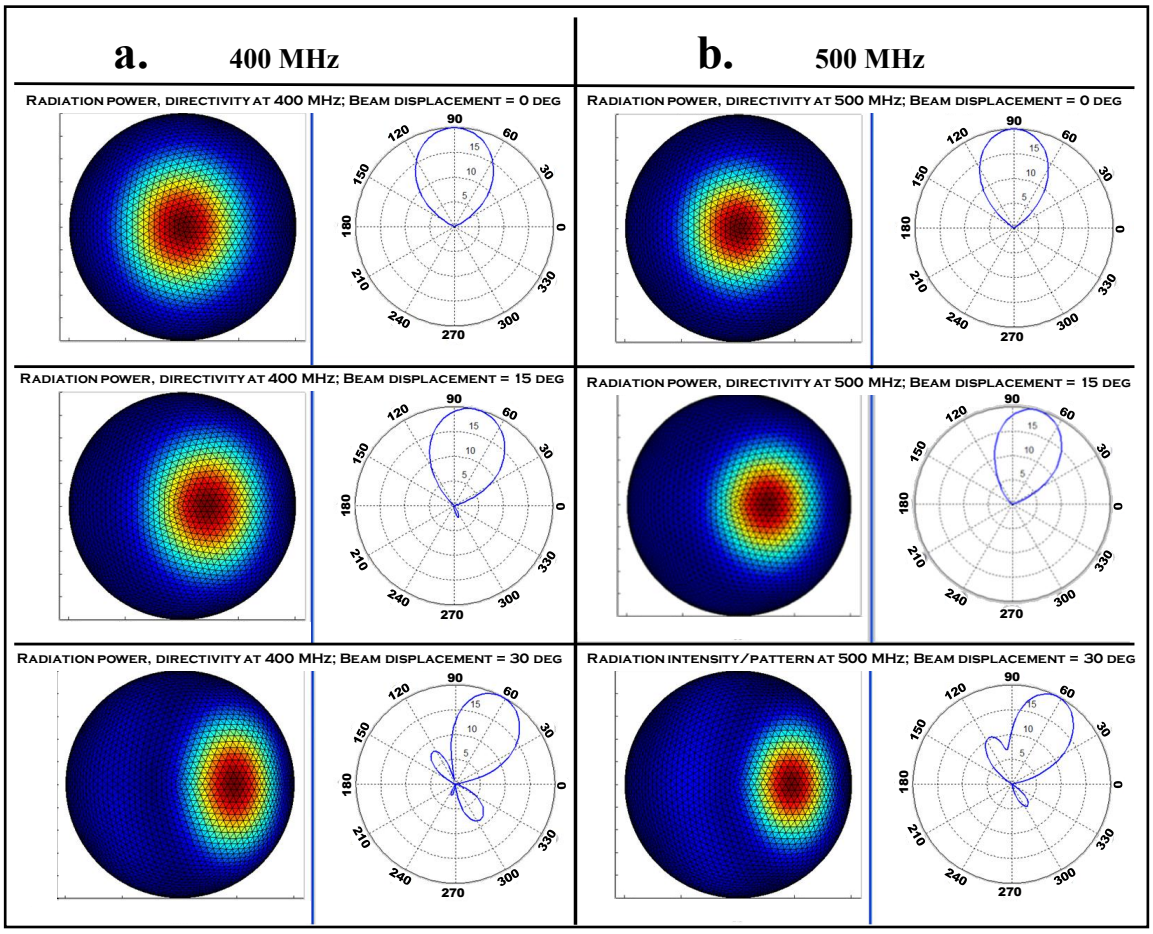

Figure 3-13 Radiation intensity and directivity patterns in transmit mode of the 5×5 HDT array at 1000 m away from the source, with phase offsets added between the respective elements in X direction with beam displacements of 0°, 15° and 30°, showing: a) phase offsets at 400 MHz; and b) phase offsets at 500 MHz

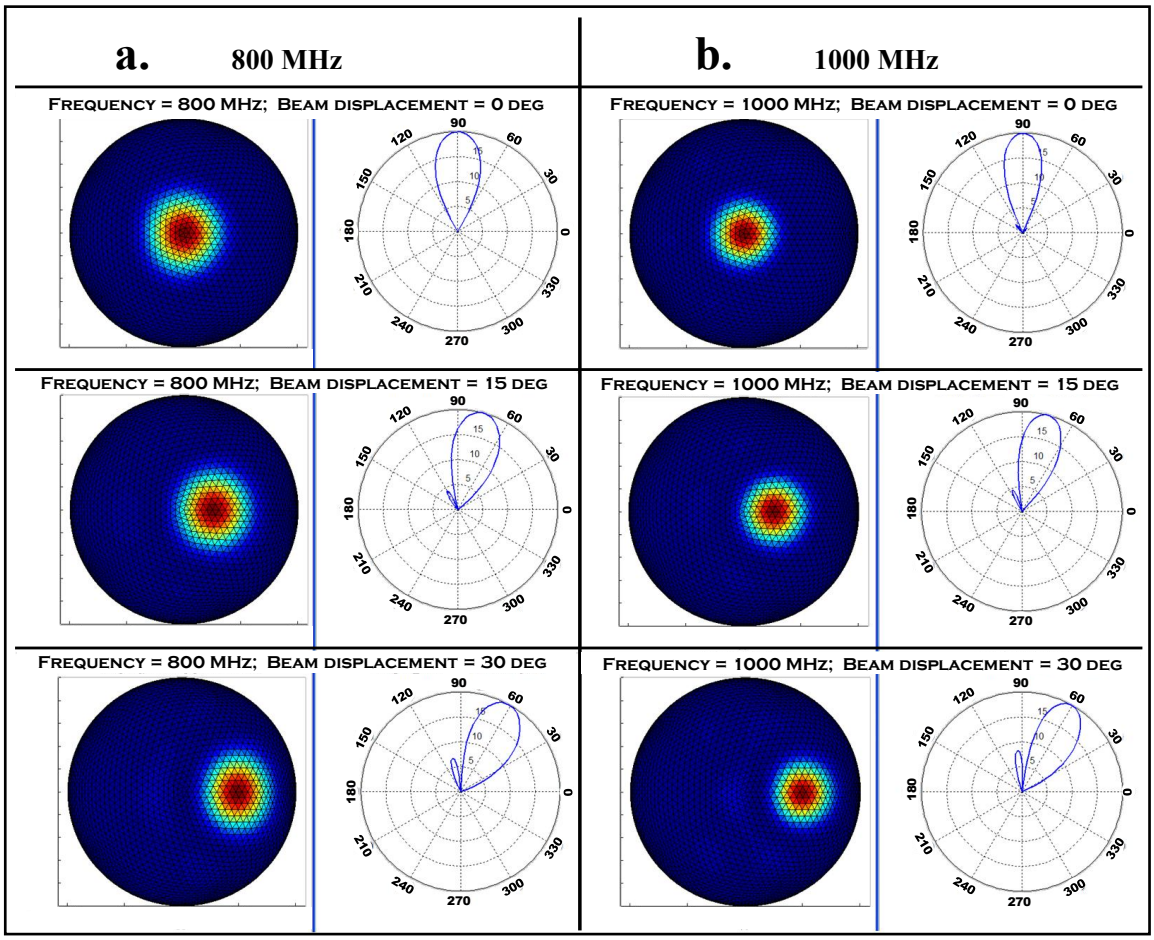

Figure 3-14 Radiation intensity and directivity patterns in transmit mode of the 5×5 HDT array at 1000 m away from the source polarized in X-axis, with phase shifts added between the elements in X direction, showing: a) phase offsets at 800 MHz; and b) phase offsets at 1000 MHz. Results illustrate radiation intensity and directivity patterns for three beam displacements 0°, 15° and 30°

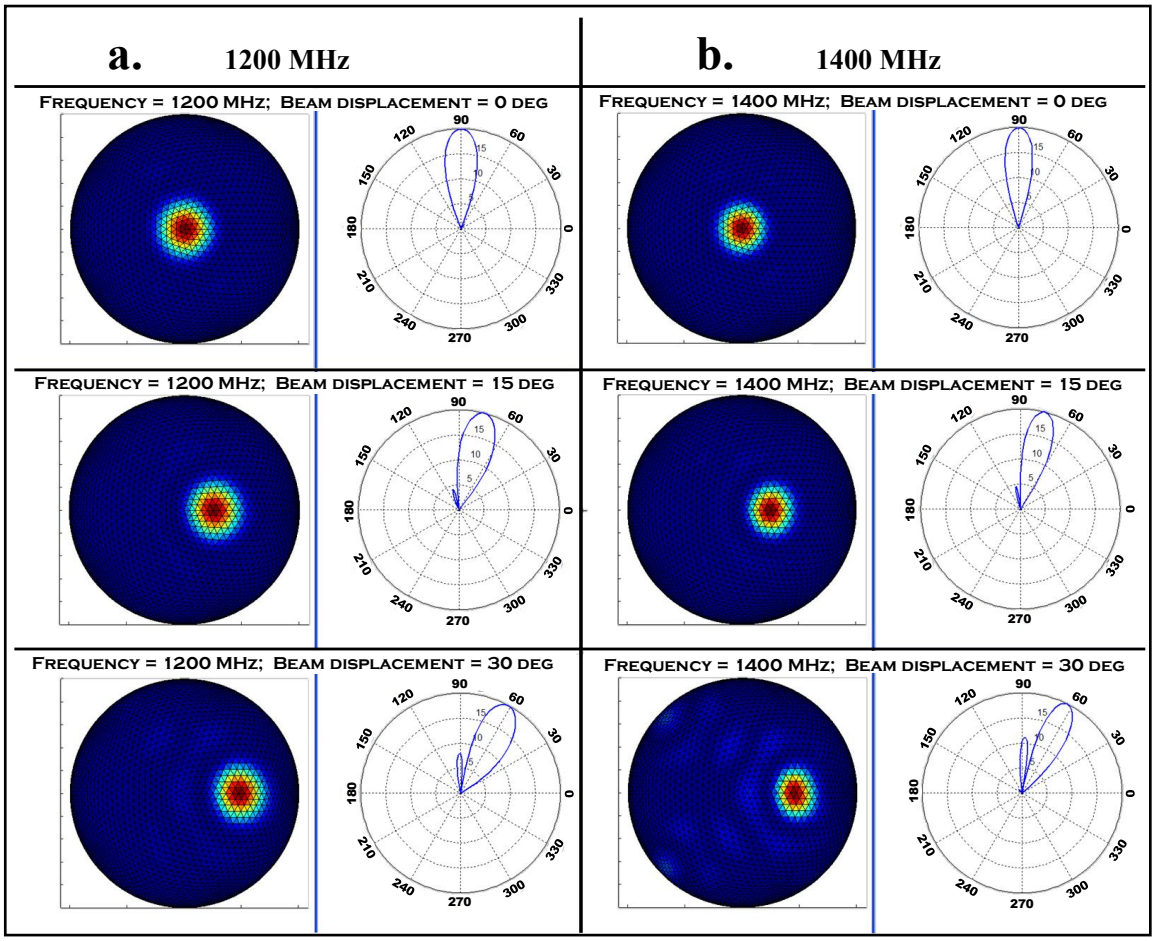

Figure 3-15 Radiation intensity and directivity patterns in transmit mode of the 5×5 HDT array at 1000 m away from the source polarized in X-axis, with phase shifts added between the elements in X direction, showing: a) phase offsets at 1200 MHz; and b) phase offsets at 1400 MHz. Results illustrate radiation intensity and directivity patterns for three beam displacements 0°, 15° and 30°

Results in Figures 3.13 - 3.15 clearly show that when the array is treated as a classical phased steered array, introduction of phase offsets for frequencies 400 to 1400 MHz yields a very coherent beam. These modelling solutions show that the array does not generate excessive side-lobes or deterioration of the main beam for the indicated frequency range. Furthermore, additional modelling analysis has revealed that these results hold for all angle between -30° to 30°, applied at any directions about the axis normal to the antenna plane with range of polarization vectors. Although these results are ideal, it is important to investigate how the array behaves in receive mode since the FPA is primarily used as a receiver.

3.1.2 Receive mode solution of the 5×5 HDT array

Unlike with classical phased steered arrays, FPA feeds are conjugate matched to the focal plane field from many overlapping beams. If the frequency of the incident field changes, or is increased, the shape of the focal field scattered from the parabolic reflector is altered. In addition the focal field is displaced off centre as function of the field of view (see section 1.8 for more information). Thus, it is relatively challenging to design a broadband array to cover all fields, while at the same time, sustain its ability to distinguish the polarization vectors and provide for all objective properties discussed in section 1.11. In spite of these challenges, the HDT array has been derived to provide exactly that, as will be illustrated in subsequent sections.

Receive mode solution of the 5×5 HDT array illuminated by an on-axis focal field

In this section of the thesis, we intend to investigate the receive mode solution of the 5×5 HDT array when irradiated by the focal field at zero scan angle, for frequencies 400 to 1600 MHz. In other words, the array will be irradiated by an on-axis focal beam resulting from a plane wave incident normal onto a parabolic reflector, as illustrated in Figure 3.16. Figures 3.20 - 3.24 shows the surface current magnitude and received terminal power of the 5×5 HDT array in receive mode by illuminating the array with an on-axis focal field between 400 to 1600 MHz, polarized in X direction.

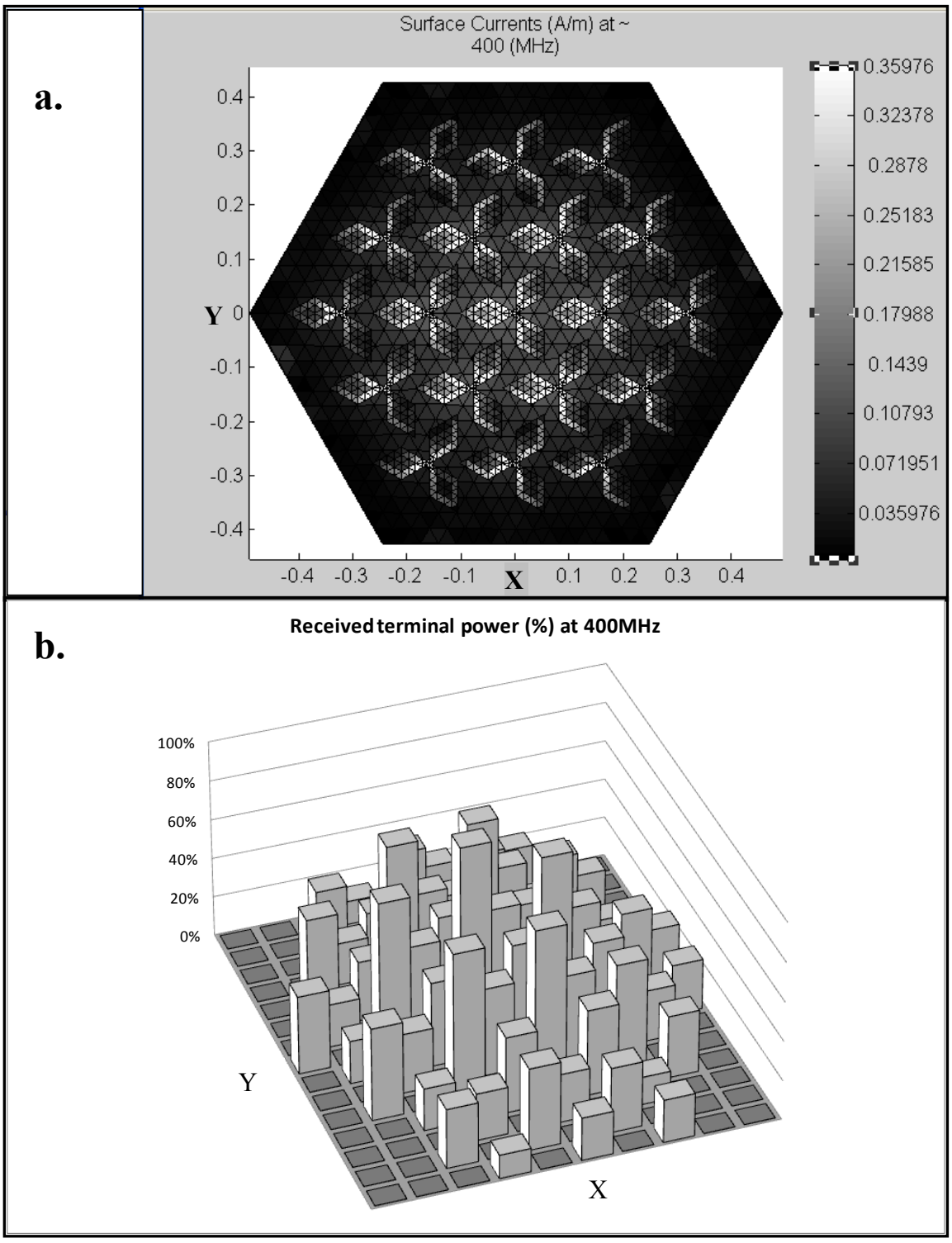

Figure 3-16 Receive mode solution of the 5×5 HDT array illuminated by the focal field at 400 MHz polarized in X-axis, showing: a) surface currents (A/m) in grayscale, and b) relative terminal power (%) received at each port

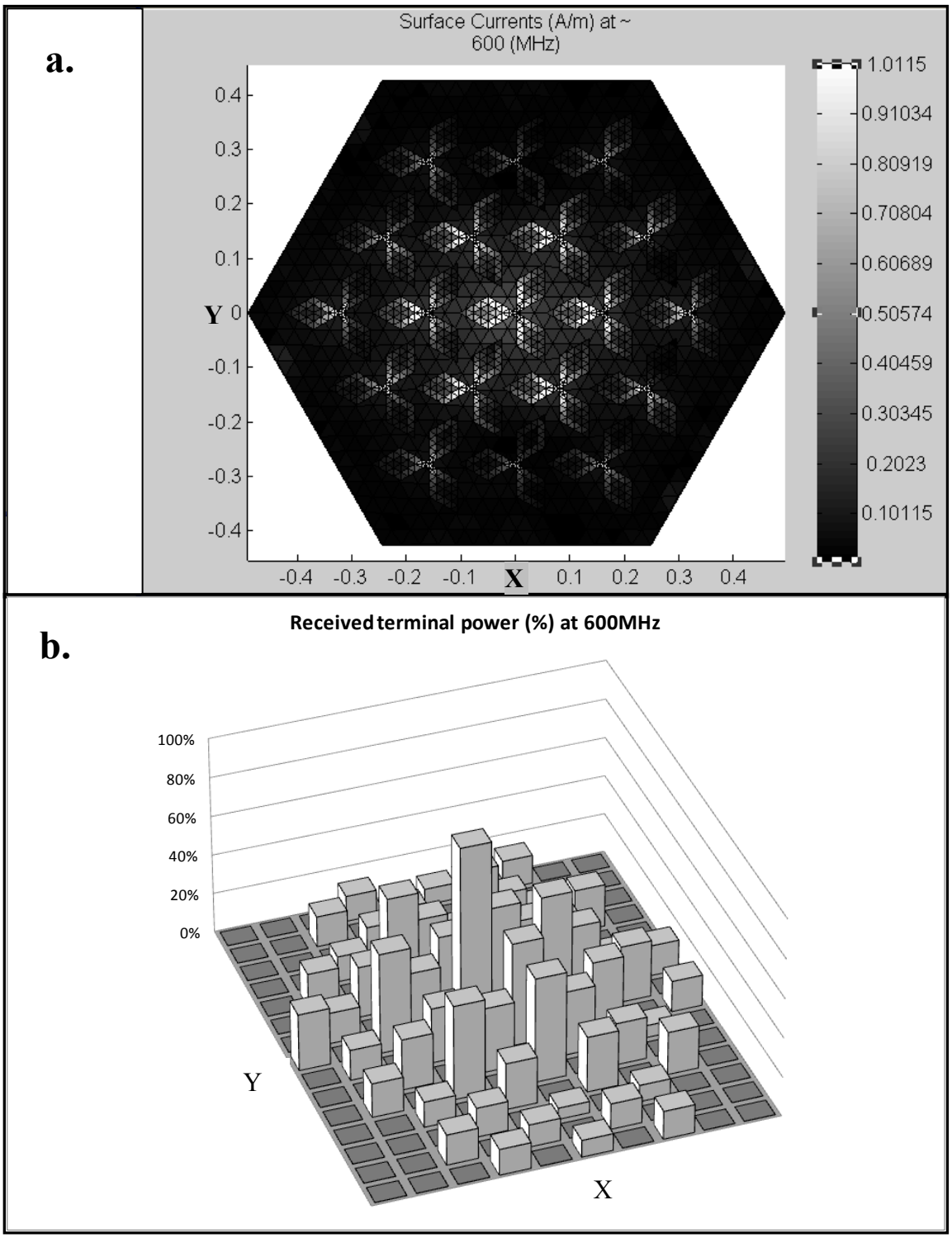

Figure 3-17 Receive mode solution of the 5×5 HDT array illuminated by the focal field at 600 MHz polarized in X-axis, showing: a) surface currents (A/m) in grayscale, and b) relative terminal power (%) received at each port

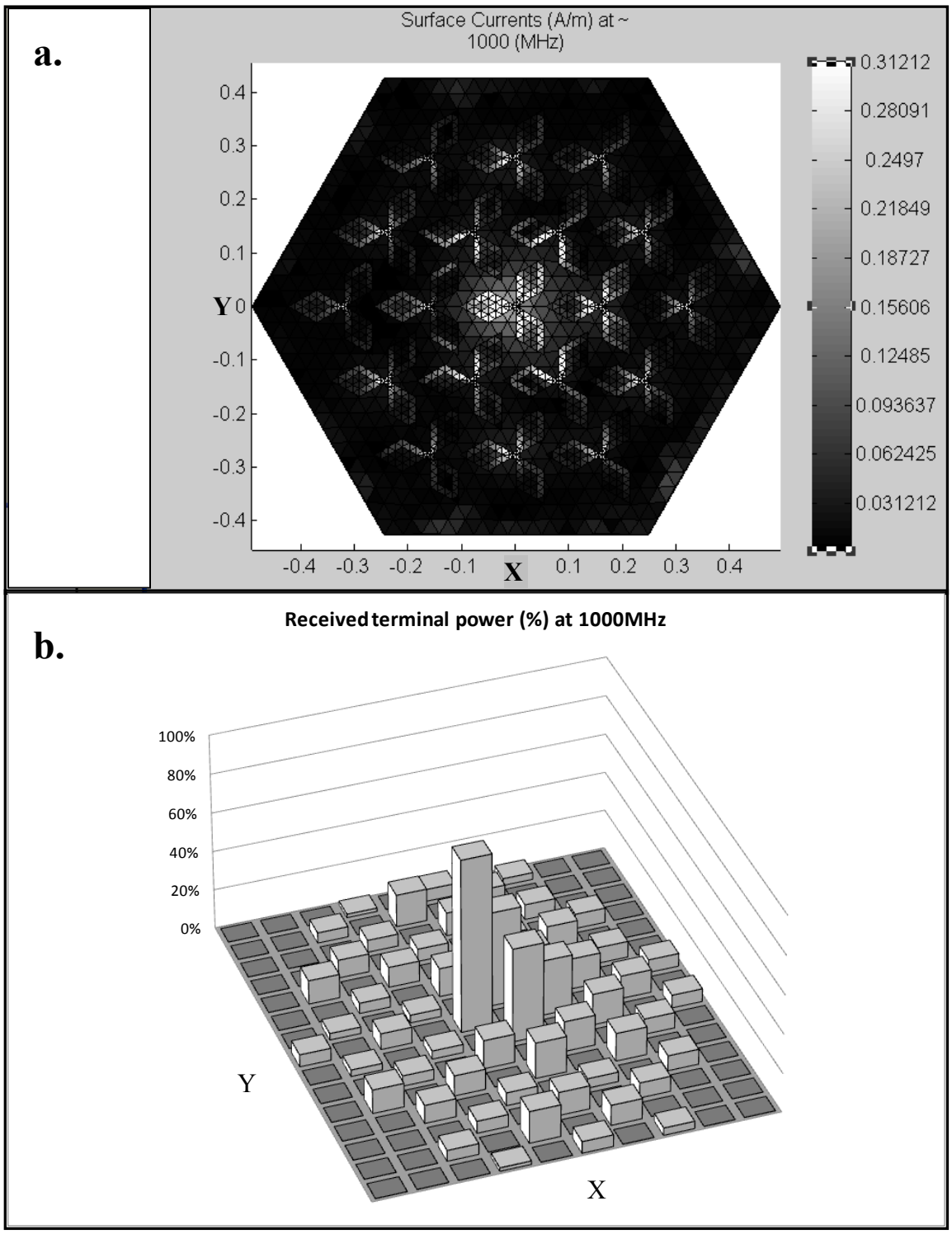

Figure 3-18 Receive mode solution of the 5×5 HDT array illuminated by the focal field at 1000 MHz polarized in X-axis, showing: a) surface currents (A/m) in grayscale, and b) relative terminal power (%) received at each port

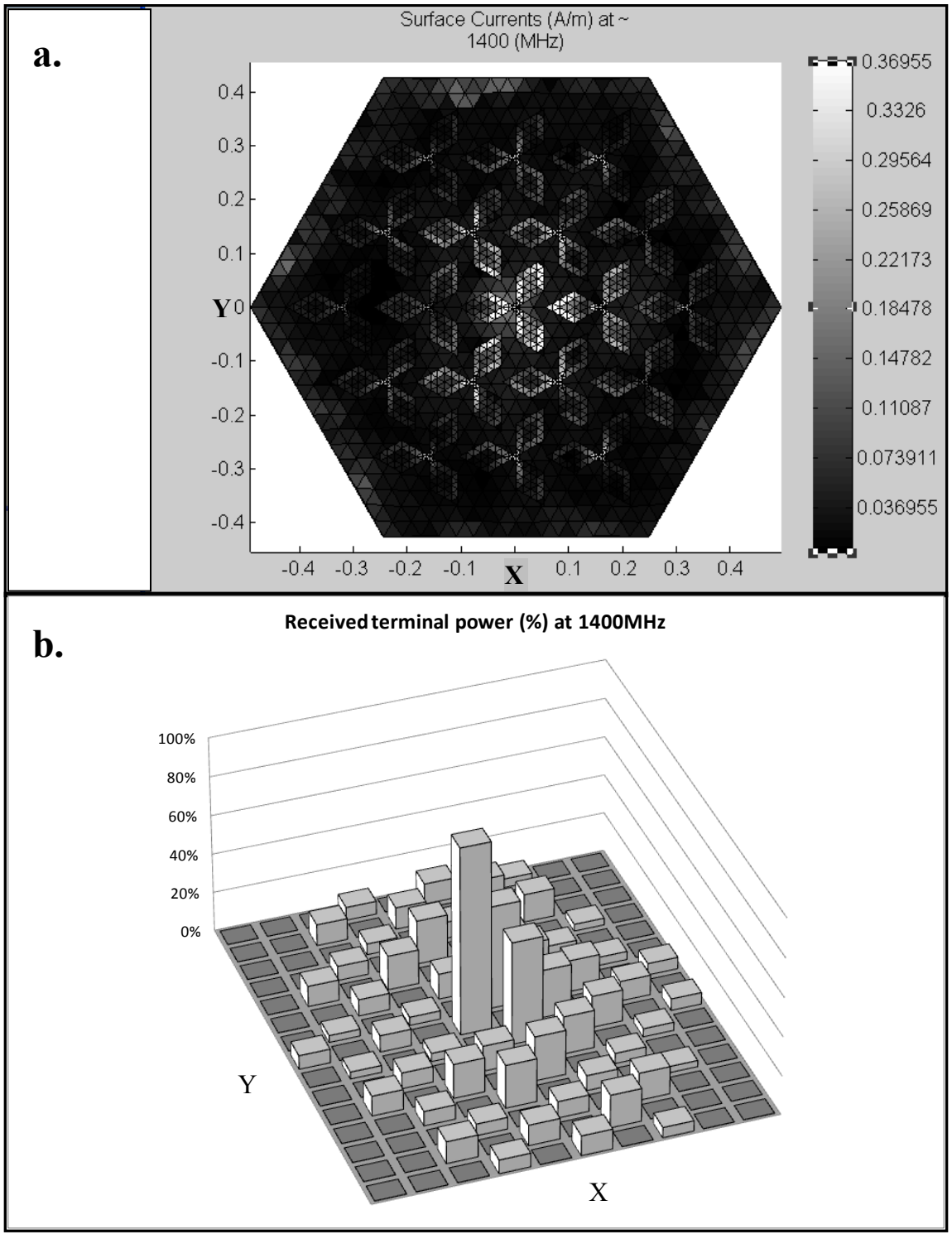

Figure 3-19 Receive mode solution of the 5×5 HDT array illuminated by the focal field at 1400 MHz polarized in X-axis, showing: a) surface currents (A/m) in grayscale, and b) relative terminal power (%) received at each port

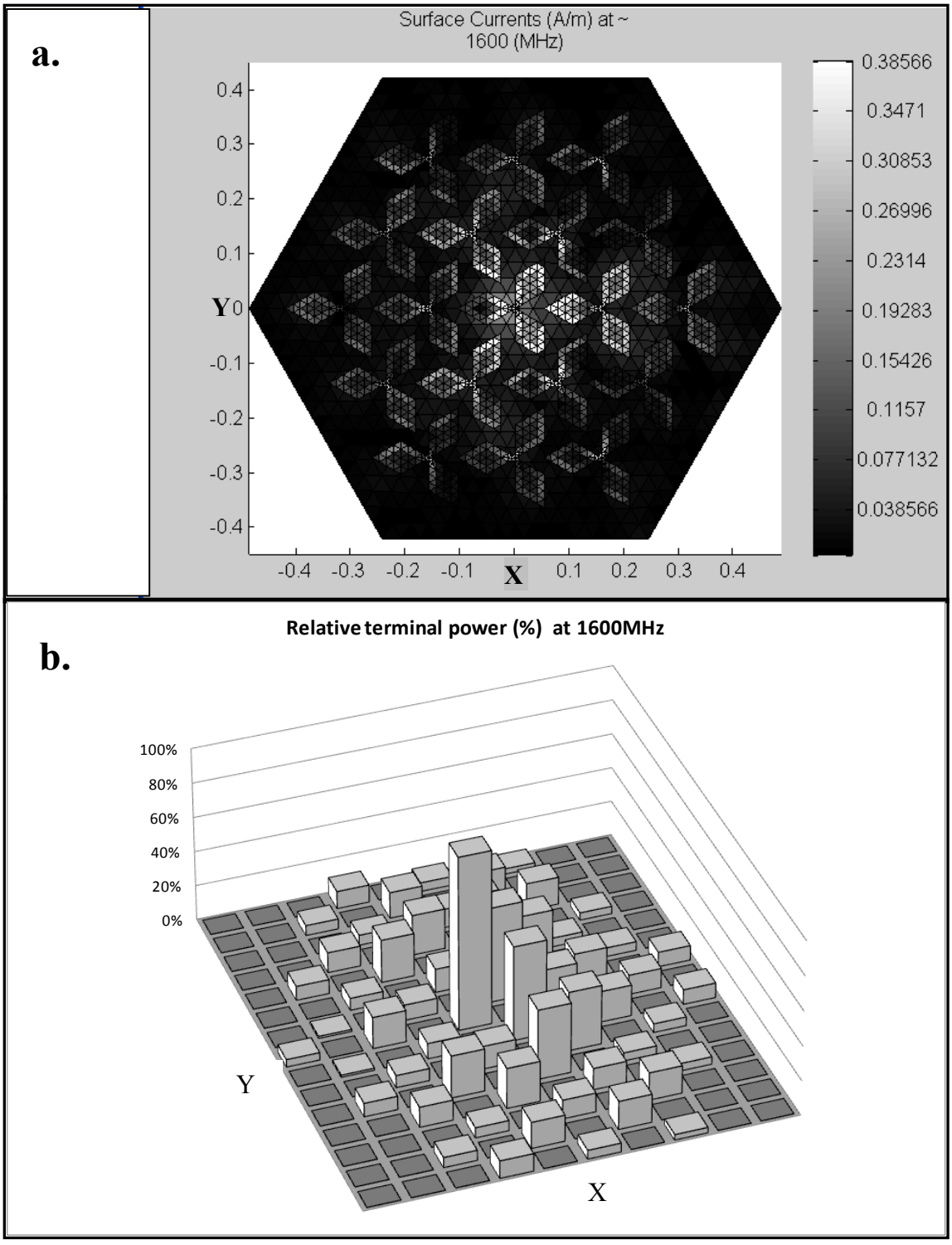

Figure 3-20 Receive mode solution of the 5×5 HDT array illuminated by the focal field at 1600 MHz polarized in X-axis, showing: a) surface currents (A/m) in grayscale, and b) relative terminal power (%) received at each port

Figures 3.20 - 3.24 show the surface current magnitudes and terminal power relative to maximum power received at each port of the 5×5 HDT array, during reception. Results illustrate an ideal solution for the surface current distribution, because the relative amplitude coefficients clearly follow the trend of the focal field for all indicated frequencies. The surface currents are distributed based on the focal field, resonant properties, characteristic modes and mutual coupling effects between all neighbouring conductive bodies. It is evident that these effects change as function of the frequency and yield currents that are uniquely scattered through the conducting terminals.

The question that remains is can we differentiate the polarization vector from such a large scattering of surface currents through the array, especially if the focal field is displaced off axis? As we will discover in the subsequent sections, the answer to that question is yes!

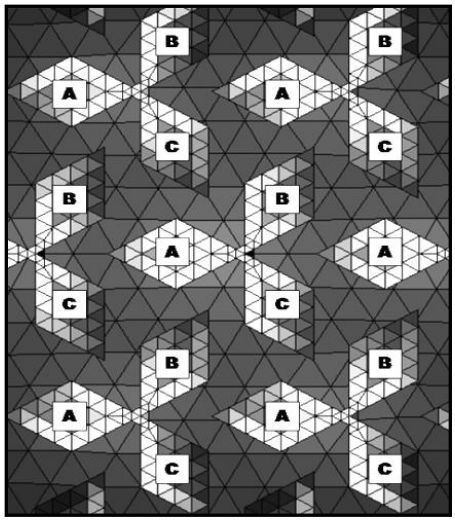

Figure 3-21 Terminals arranged into respective polarization groups A, B and C

Polarization vector can be determined using an amplitude comparison approach. If we arrange all received conjugate matched signals into three distinct polarization groups, group A, B and C, as shown in Figure 3.25, the mean amplitude coefficients received at each group can be extrapolated from the results obtained in Figures 3.20b - 3.24b, using equation 2.1.

```
MeanPowerA = sum(FeedPower(Terminals A))/19;
MeanPowerB = sum(FeedPower(Terminals B))/19;
MeanPowerC = sum(FeedPower(Terminals C))/19;

RelativePowerA = MeanPowerA/(MeanPowerA+MeanPowerB+MeanPowerC)*100
RelativePowerB = MeanPowerA/(MeanPowerA+MeanPowerB+MeanPowerC)*100
RelativePowerC = MeanPowerA/(MeanPowerA+MeanPowerB+MeanPowerC)*100
```

(2.1)

Since there are a total of 57 terminals in a 5×5 HDT array, each terminal "group" contains a total of 19 feeds. Thus, equation 2.1 shows that the mean power for each terminal group can be calculated as the sum of all amplitudes coefficients for that group, divided by 19. These calculations were performed with solutions obtained in Figures 3.20b - 3.24b, and are displayed in Table 3.1.

Table 3-1 Mean relative power induced onto each terminal group of the 5×5 HDT array during reception from an incident focal field polarized in X direction (0°)

Frequency	Polarization Group	Mean relative terminal power (%) received
400MHz	**Group A**	**47.74 %**
	Group B	26.13 %
	Group C	26.12 %
600MHz	**Group A**	**44.28 %**
	Group B	27.84 %
	Group C	27.88 %
1000MHz	**Group A**	**45.95 %**
	Group B	26.97 %
	Group C	27.08 %
1400MHz	**Group A**	**43.46 %**
	Group B	28.26 %
	Group C	28.28 %
1600MHz	**Group A**	**43.41 %**
	Group B	28.32 %
	Group C	28.26 %

As can be seen from Table 3.1, the mean relative amplitude coefficient for each terminal group clearly shows that the incident focal filed is polarized along the X-axis, with group A terminals having the largest current amplitude coefficients for each frequency. This is true because terminal A is parallel with X-axis (as obtained in Figures 3.20 -

3.24), thus the mean of all currents from terminals oriented in X-axis (group A) yields a received power that is much larger than the remaining two groups (B and C) for each frequency; which agrees in accordance with the expected values described in Figure 2.7. Furthermore, groups B and C are almost identical in each case, with relative amplitude coefficients ranging between 26 – 28 % depending on the frequency. In fact, this relationship closely follows the 50 %, 25 %, 25 % three-feed reception rule discussed in section 2.3.1, with some differences caused due to the shape of the focal field. These differences indicate that a consistent deviation of the received signal exists away from the forward terminal group (Group A), relative to the direction of polarization, which varies between 2 - 6 % depending on frequency (see Table 3.1). Nonetheless, results show that group terminals B and C are identical (to within a theoretical uncertainty), which can only be possible if signals are polarised in X direction. What remains to be seen, however, is what happens if the signal is polarized at X = Y direction? We investigate this below.

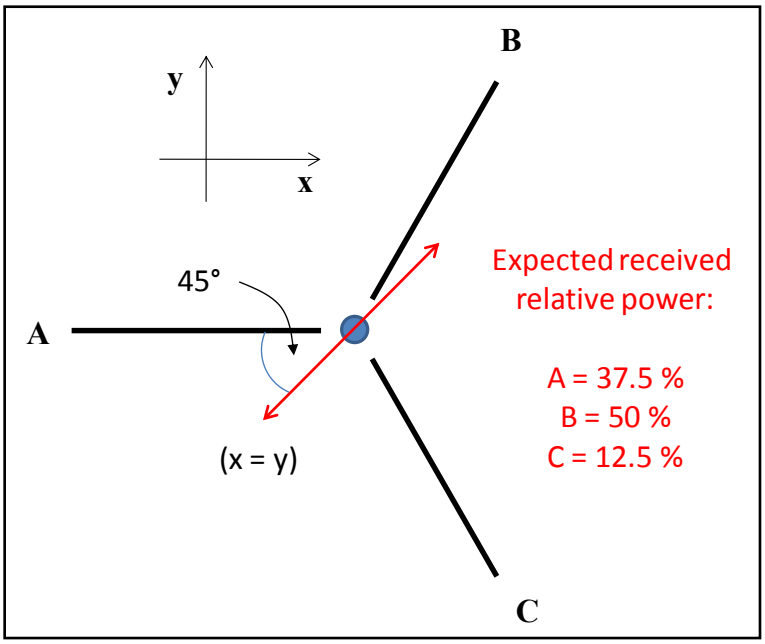

Figure 3-22 Figure shows three terminals A, B and C of the tripole antenna illuminated by an incident planewave polarized in X = Y direction (red arrow line). The relative power received at each terminal of the tripole antenna (as modeled using MoMADT) yields a value A = 37.5 %, B = 50 % and C = 12.5 %

If the incident focal field was polarized in X = Y direction, instead of X-axis as obtained earlier in Figures 3.20 - 3.24, then the relative power expected at each terminal group of the 5×5 HDT array should yield a value very similar to the tripole antenna shown in Figure 3.26, where A = 37.5 %, B = 50 % and C = 12.5 %. At least that is what we would expect, although it is not guaranteed as the overall result purely depends on the total coupling effects between all neighbouring conductive bodies of the array.

Table 3.2 shows the calculated mean relative power induced onto each terminal group of the 5×5 HDT array during reception, when focal field is polarized in X = Y direction. Calculations were obtained using MoMADT in the same manner as obtained in Figures 3.20 - 3.24 and Table 3.1.

Table 3-2 Mean relative power induced onto terminal group A, B and C of the 5×5 HDT array during reception illuminated by the focal field polarized in X = Y direction (45° with respect to X-axis)

Frequency	Polarization group	Mean relative terminal power (%) received	Difference between group A and C (%)
400MHz	Group A	38.71 %	25.02 %
	Group B	**47.64 %**	
	Group C	13.69 %	
600MHz	Group A	40.43 %	25.01 %
	Group B	**44.20 %**	
	Group C	15.42 %	
1000MHz	Group A	39.59 %	24.99 %
	Group B	**45.91 %**	
	Group C	14.60 %	
1400MHz	Group A	40.84 %	25.04 %
	Group B	**43.41 %**	
	Group C	15.80 %	
1600MHz	Group A	40.83 %	25.02 %
	Group B	**43.39 %**	
	Group C	15.81 %	

Table 3.2 shows that group terminal B has the largest amplitude coefficient, followed by group terminals A and C, respectively. This result indicates that polarization can indeed

be determined by noting that the mean relative terminal power between group terminals A and C differ with respect to each other by approximately 25.00 ± 0.05 %, for all frequencies. In other words, this deviation can only be mathematically possible if the incident focal field is polarised in X = Y direction.

Therefore, calculating the mean amplitude coefficients between the three respective polarization groups, in this manner, can indeed help us determine the polarization state from waves that are originally incident onto a parabolic reflector. However, it remains to be seen if this result can be reproduced when the focal field is displaced off axis? We investigate this in the subsequent section.

Receive mode solution of the 5×5 HDT array illuminated by an off-axis focal field

As explained in section 1.7 and 1.8, when the focal field is displaced off-axis, a portion of the central power flux density is transferred to the forward rings with respect to the direction of the displaced field. Depending on the scan angle, this portion of the power can be spilled outside of the surface area of the focal plane array. Furthermore, the unique shape and position of the focal field generates characteristic modes which result in spurious scattering of surface currents through the array.

In this section of the thesis we intend to investigate how the 5×5 HDT array behaves when the incident focal field is displaced off-axis using a focal field displacement angle of -3° in X and Y direction. We measure this behaviour for frequencies 400 MHz, 600 MHz, 1000 MHz, 1400 MHz and 1600 MHz, and we investigate the surface current magnitude and the relative terminal power (%) received at each port.

Solutions for this modelling study are illustrated in Figures 3.27-3.31. Note that the off-axis beam angle was selected to be -3° in X and Y direction for all frequencies, respectively, using an F/D ratio of 0.4 and a 12 m parabolic reflector.

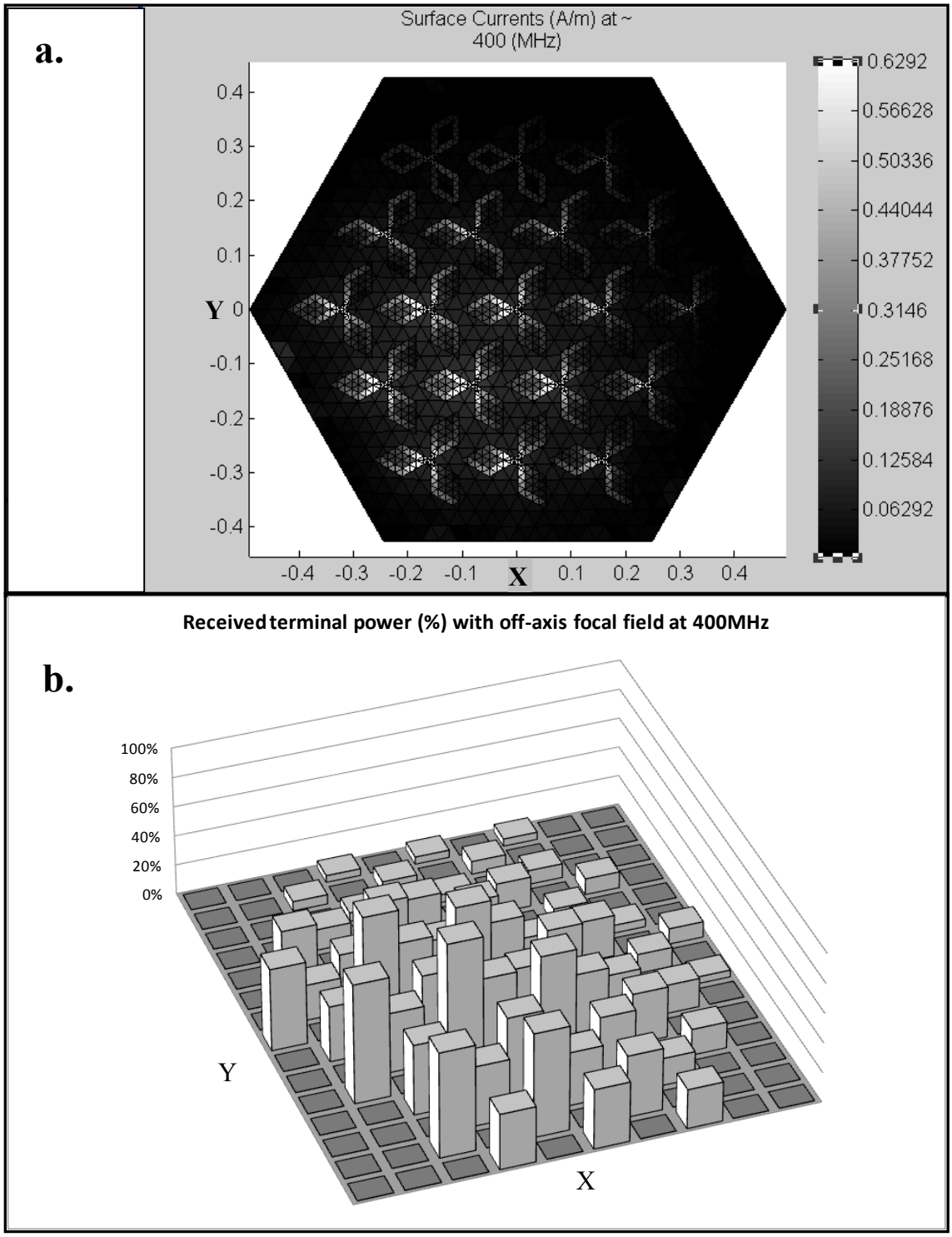

Figure 3-23 Receive mode solution of the 5×5 HDT array illuminated by an off-axis beam (-3° in X and Y direction) at 400 MHz polarized in X axis, showing: a) surface currents (A/m) across the array (see grayscale vertical bar) , and b) relative terminal power received at each port

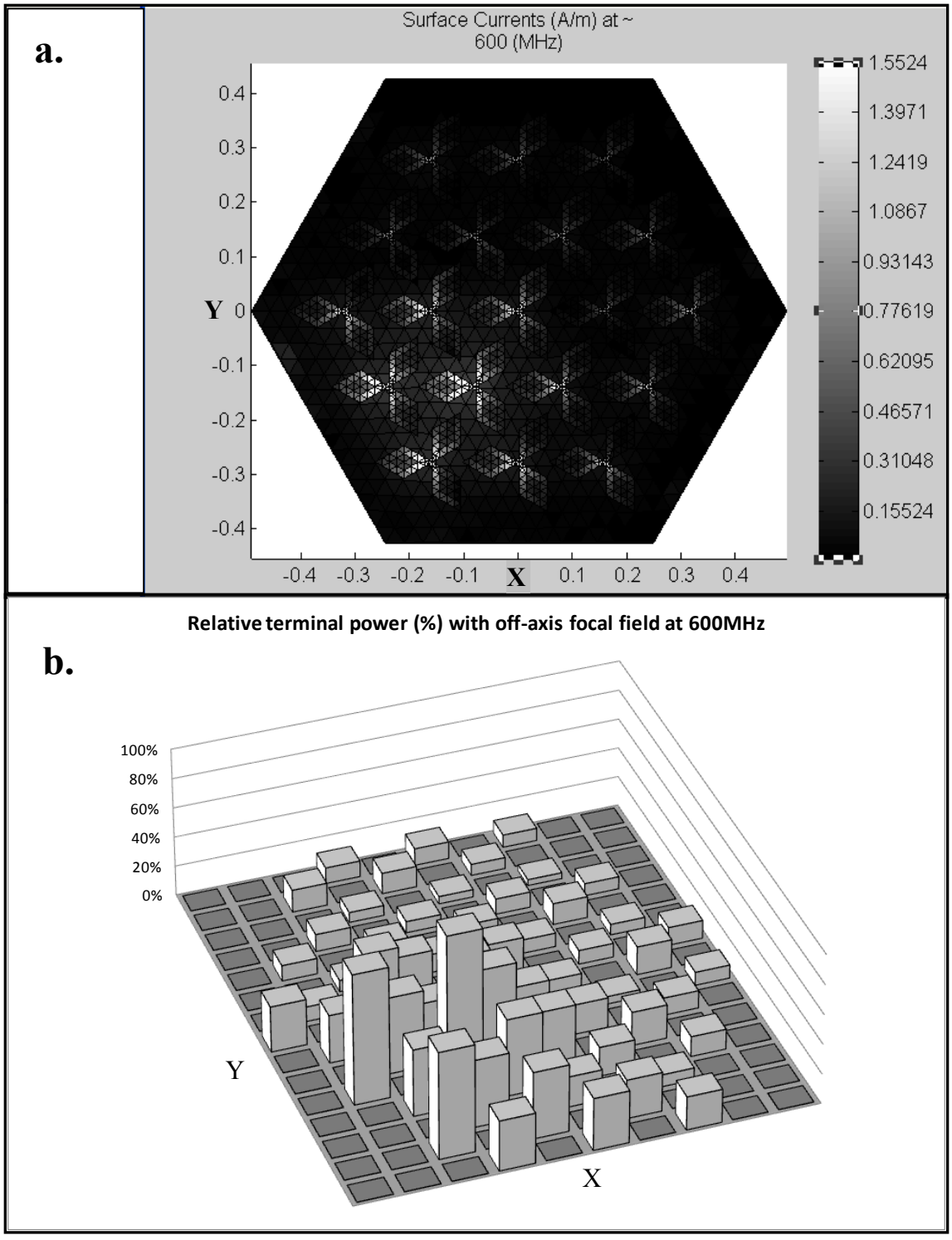

Figure 3-24 Receive mode solution of the 5×5 HDT array illuminated by an off-axis beam (-3° in X and Y direction) at 600 MHz polarized in X axis, showing: a) surface currents (A/m) across the array (see grayscale vertical bar) , and b) relative terminal power received at each port

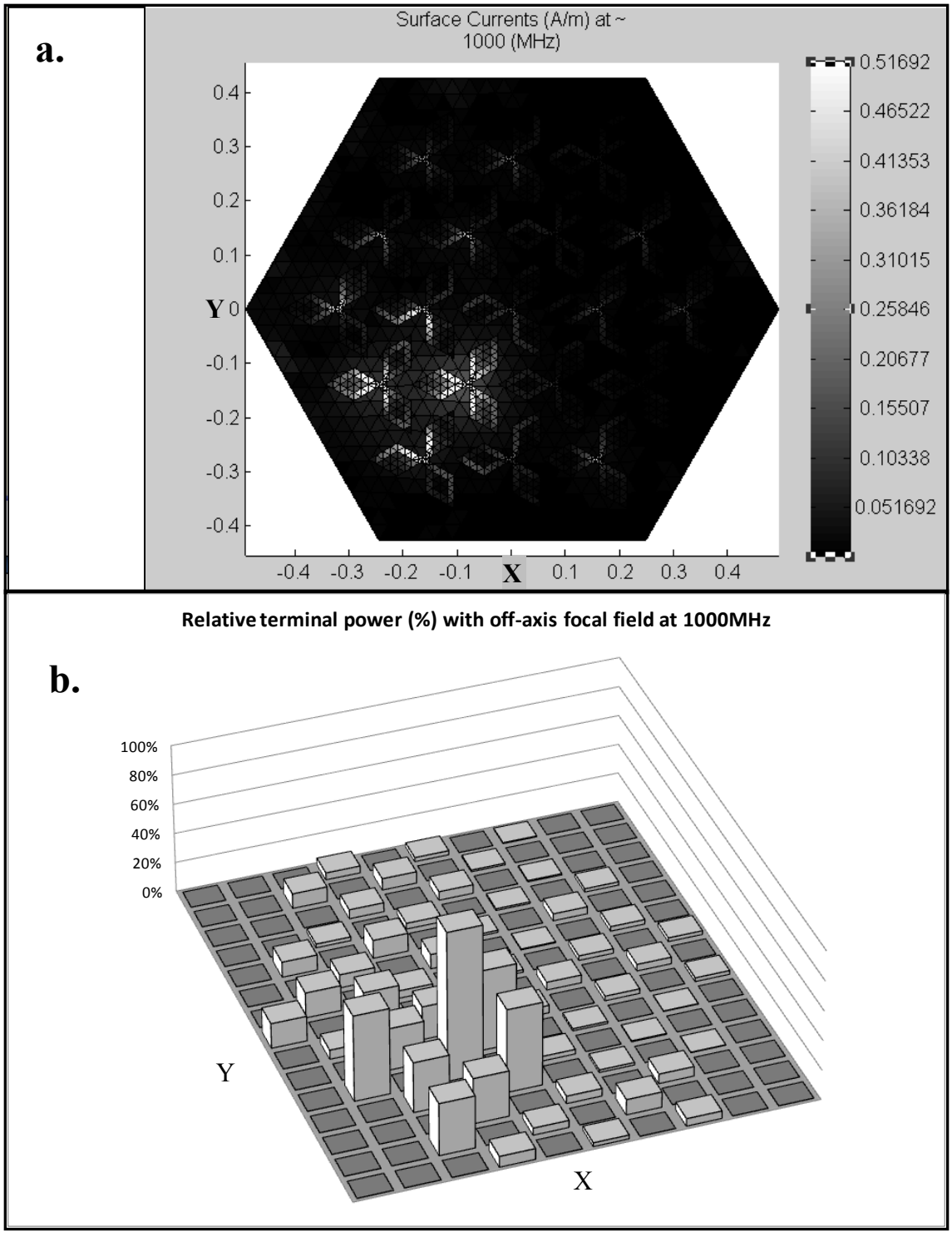

Figure 3-25 Receive mode solution of the 5×5 HDT array illuminated by an off-axis beam (-3° in X and Y direction) at 1000 MHz polarized in X axis, showing: a) surface currents (A/m) across the array (see grayscale vertical bar) , and b) relative terminal power received at each port

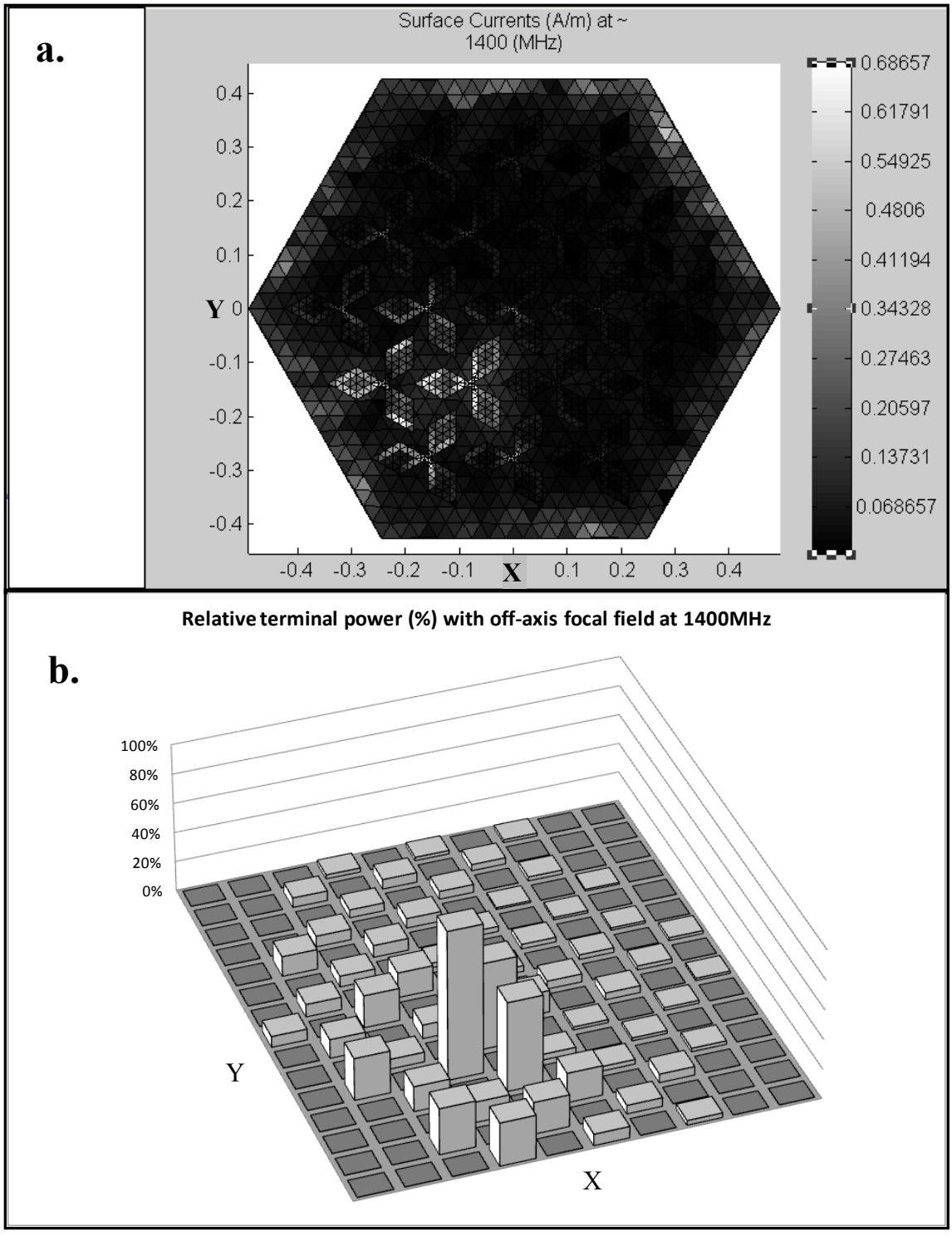

Figure 3-26 Receive mode solution of the 5×5 HDT array illuminated by an off-axis beam (-3° in X and Y direction) at 1400 MHz polarized in X axis, showing: a) surface currents (A/m) across the array (see grayscale vertical bar) , and b) relative terminal power received at each port

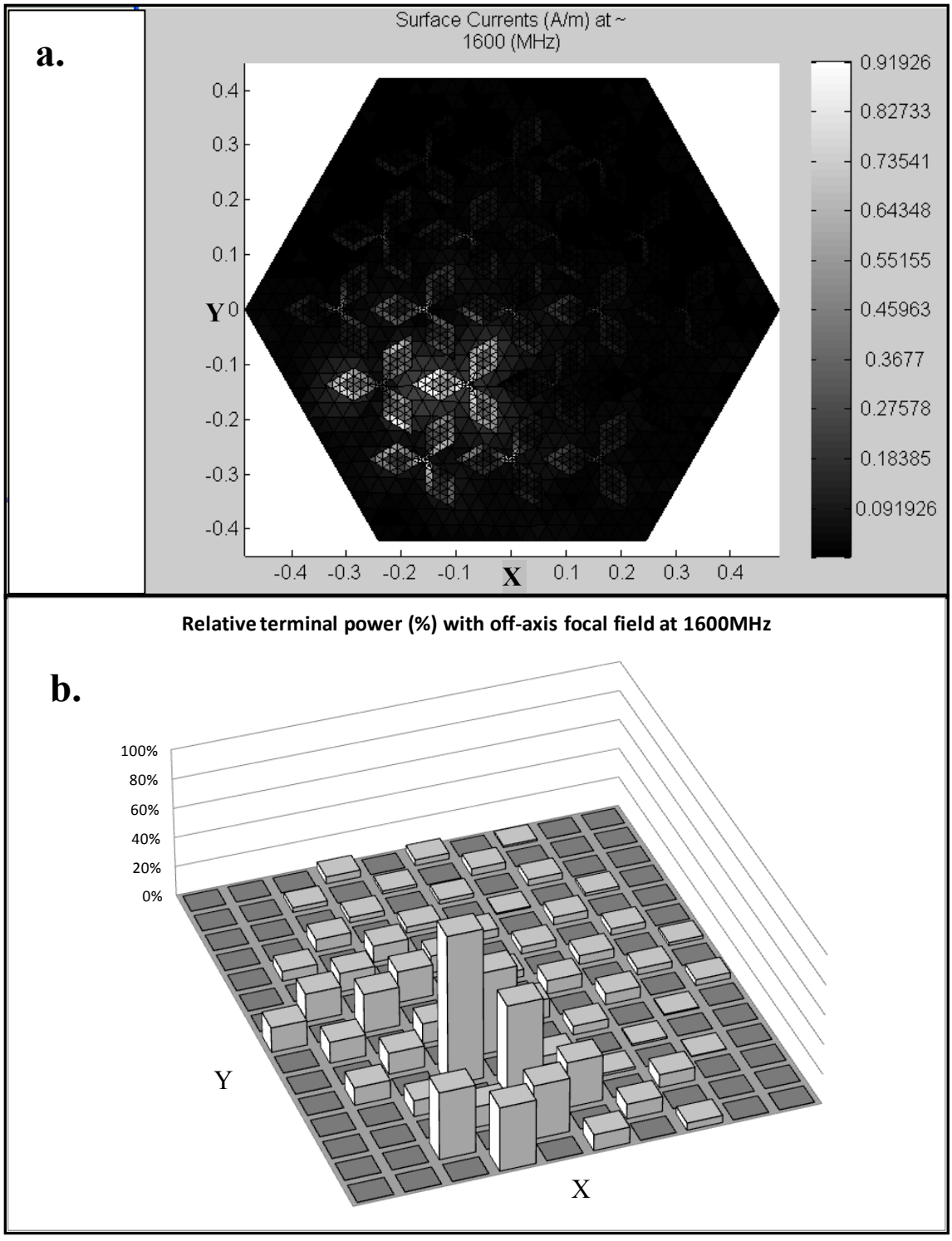

Figure 3-27 Receive mode solution of the 5×5 HDT array illuminated by an off-axis beam (-3° in X and Y direction) at 1600 MHz polarized in X axis, showing: a) surface currents (A/m) across the array (see grayscale vertical bar) , and b) relative terminal power received at each port

Note how the surface currents in Figures 3.27-3.31 are displaced off-axis, and again follow the trend of the focal field. Once again, the relative amplitude coefficients can be calculated using equation 2.1 and are displayed in Table 3.3. As can be seen, the mean relative terminal power received between the three terminal groups can indeed help us distinguish the polarization of the incident focal field, even when the focal field is displaced off-axis (see Table 3.3). Moreover, this is also true even if the signals are polarized in X = Y direction, as show in Table 3.3 (note how the difference between group A and C varies by 25.0 ± 0.4 % for each frequency). However, it is observed that a small deviation occurs between terminal groups B and C for higher frequencies 1400 MHz and 1600 MHz, where terminal group C reads a higher value compared to terminal group B. It was found that this deviation is caused due to the position and shape of the focal field, as well as the proximity of the ground plane edge.

Table 3-3 Mean relative power induced onto terminal group A, B and C of the 5×5 HDT array during reception illuminated by an off-axis focal filed (-3° in X and Y direction). Table shows the relative power (%) received at each terminal group for signals polarized in X direction and signals polarized in X = Y direction. Results also illustrate the difference between group A and C for signals polarized in X = Y direction

Frequency	Polarization group	Received relative power (%) for signals polarized in X direction	Received relative power (%) for signals polarized in X = Y direction	Difference between group A and C for signals polarized in X = Y direction (%)
400MHz	Group A	**47.39 %**	38.86 %	25.03 %
	Group B	25.88 %	**47.29 %**	
	Group C	26.73 %	13.83 %	
600MHz	Group A	**45.71 %**	40.53 %	25.05 %
	Group B	27.14 %	**44.00 %**	
	Group C	27.14 %	15.48 %	
1000MHz	Group A	**47.06 %**	39.89 %	25.08 %
	Group B	25.90 %	**45.31 %**	
	Group C	27.04 %	14.81 %	
1400MHz	Group A	**44.54 %**	40.86 %	24.64 %
	Group B	26.96 %	**42.90 %**	
	Group C	28.50 %	16.22 %	
1600MHz	Group A	**42.32 %**	41.01 %	24.62 %
	Group B	28.39 %	**42.59 %**	
	Group C	29.28 %	16.39 %	

As seen in Table 3.3, when the focal field is displaced off axis, group terminal C records a higher amplitude coefficient by approximately 1.6 % compared to group terminal B, at 1400 MHz and 1600 MHz, which yields a swing of about 0.8 %. Reason for this is that the portion of the central power flux density, transferred to the forward rings, is induced onto group terminal C. In addition, the central power flux density and the resulting scattered fields, become closer to the edge of the ground plane. The resulting effect is that characteristic modes from the ground plane edge are induced back onto the radiating terminals. Similar situation occurs for signals polarized in X = Y direction. Thus, depending on the shape, size and distance of the ground plane edge, characteristic modes can result in mutually coupled interference that can cause further loss of polarization.

Therefore, it is important to make the correct choice regarding the size of the ground plane. If the ground plane diameter is matched to that of the array, its edge would be close to the radiating terminals. If, on the other hand, the ground plane diameter is more than one wavelength wider compared to the array diameter, a surface area of the ground plane that hangs outside of the elements would be directly exposed to the incident field. It was determined in this study, that the ground plane diameter should not exceed more than $1 \times \lambda_{MIN}$ of the array diameter, where λ_{MIN} is the wavelength of the upper operating frequency. In the case of the 5×5 HDT array, the ground plane diameter was selected to be approximately 10 - 15 % larger than the array diameter.

We now complete our theoretical and modelling analysis of the 5×5 HDT array and conclude that this array provides good directivity with peak logarithmic gain of 20 dB, efficiency above 77 %, and relatively consistent VSWR and reflection coefficient for frequencies 500 to 1700 MHz if normalized to 80 ohm, which enables a bandwidth ratio of ~3.4:1. Furthermore, additional modelling analysis has revealed that polarization can be determined at any angle about the axis normal to the antenna plane using techniques described above to within a theoretical uncertainty that varies as function of frequency by a maximum of ± 0.8 % (± 3.0°). This uncertainty shows to be greater at higher frequencies. However, it was also discovered that a correction factor can be devised in the calculations to correct for some of these variations.

3.2 The 7x7 HDT Array

In this section of the thesis we intend to investigate the operation of the diamond tripole array by increasing the density of the array elements to a 7×7 HDT array (see Figure 3.32). When density of array elements is increased, resolution of the array can be improved considerably. Furthermore, since the array contains a larger number of elements, there is an option of increasing the array size, which in turn provides larger fields of view. However, there is also the flexibility of choosing the upper operating frequency limit for as long as the element spacing is less than or equal to half wavelength of the upper operating frequency.

Even though these choices seem quite practical, increasing the number of elements of the array also increases the operating cost of the instrument. In other words, number of feeds, LNAs and the beam-former configuration change and yields a more computationally and productively expensive instrument. In this section, we intend to demonstrate the operation of the 7×7 HDT array.

3.2.1 Transmit mode solution of the 7×7 HDT array

When the diamond tripole antenna is arranged in a 7×7 hexagonal array pattern, system yields a total of 37 tripole antenna elements and a total of 111 individual receiving ports, as illustrated in Figure 3.32. Diameter of the 7×7 HDT array was selected to be the same as the 5×5 HDT array presented in section 3.1, so that array operation at higher frequencies can be achieved. This means that element size and element spacing of the array will be reduced compared to the 5×5 HDT array presented in section 3.1. The proportional size and dimensions of the 7×7 HDT array are displayed in Figure 3.32.

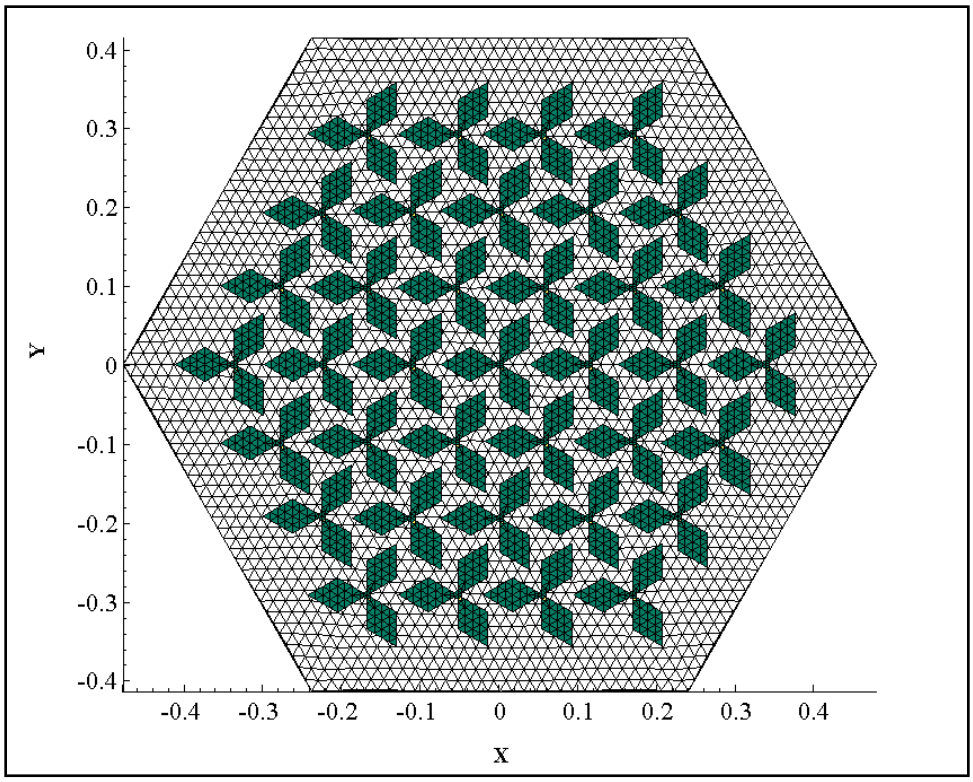

Figure 3-28 7x7 hexagonal diamond tripole array

Figure 3.33 shows the terminal impedance as function of frequency, calculated for the 7×7 HDT array between 400 to 2100 MHz in transmit mode. These calculations were performed by supplying equivalent amplitude coefficients to all of the 111 terminals simultaneously, in order to polarize the signals in X direction with zero phase. As can be seen, unlike with the 5×5 HDT array (see Figure 3.5), the impedance of the 7×7 HDT array shows to be quite uniform for the entire frequency range 400 to 2100 MHz without interferences caused due to the element spacing. However, number of small resonances is still present at approximately 850 MHz. It was found that resonances at 850 MHz are caused at the frequency region where array diameter becomes approximately two wavelengths long. This source of interference can be reduced (or shifted to lower frequencies) by extending the diameter of the array with addition of dummy antenna elements, hence generating a 9×9 HDT array.

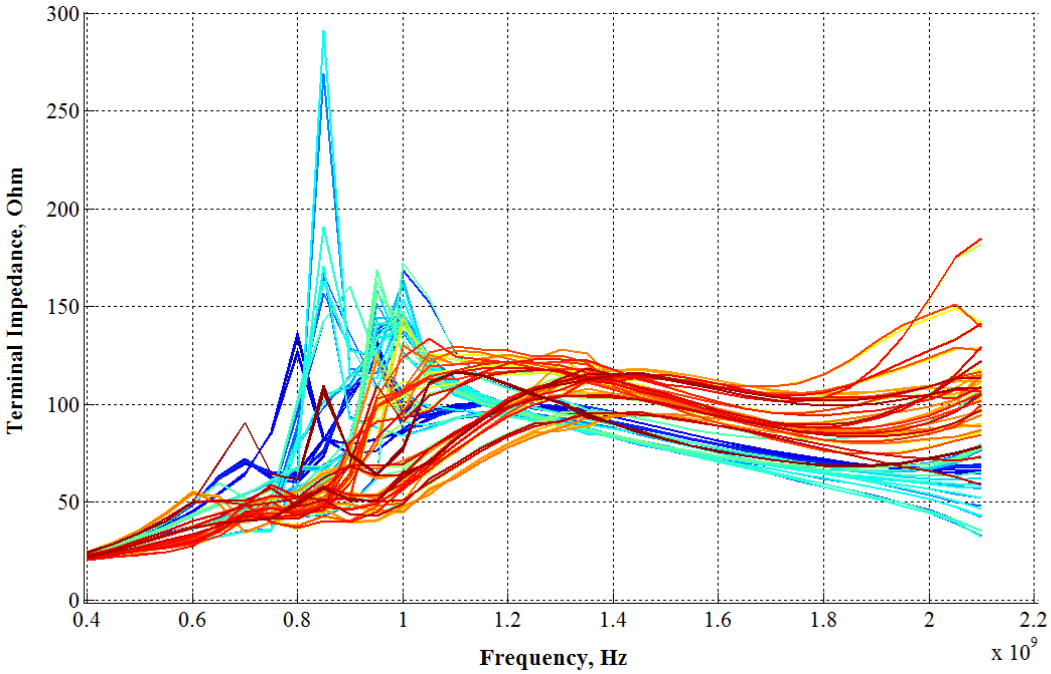

Figure 3-29 Terminal impedance versus frequency for the 7x7 hexagonal diamond tripole array

Dummy antenna elements generally behave like ordinary antenna elements with regards to scattering when irradiated by the focal field. However, dummy elements are not connected to a feeding network as is the case with the ordinary antenna elements; hence this setup generates a partially sparse array with the outer elements turned off [73]. However in this study, array solutions are presented without addition of dummy antenna components because the resonances occurring at 850 MHz do not cause excessive signal distortion. Furthermore, at 850 MHz the size of the central power flux density of the focal field is much smaller compared to the array diameter, preventing the array from being evenly illuminated by the focal field.

Figures 3.34 and 3.35 show the terminal VSWR and terminal reflection coefficient of the 7×7 HDT array normalized to 70 ohm. Figures 3.36 and 3.37 show the total VSWR and the total reflection coefficient normalized to 70 ohm.

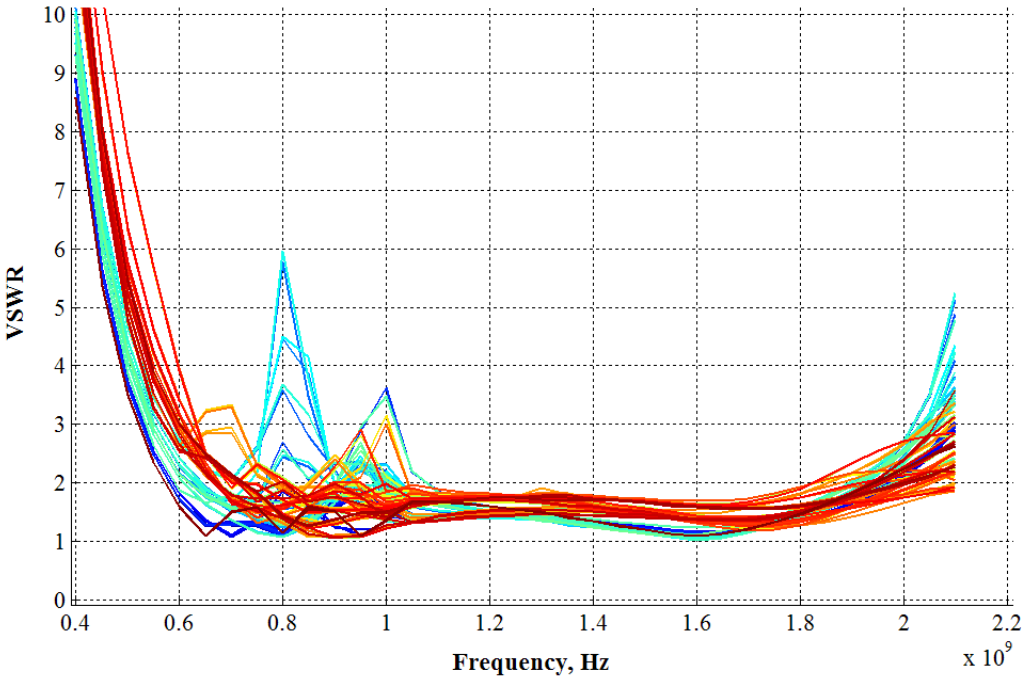

Figure 3-30 Terminal VSWR versus frequency for the 7×7 HDT array, normalized to 70 ohm

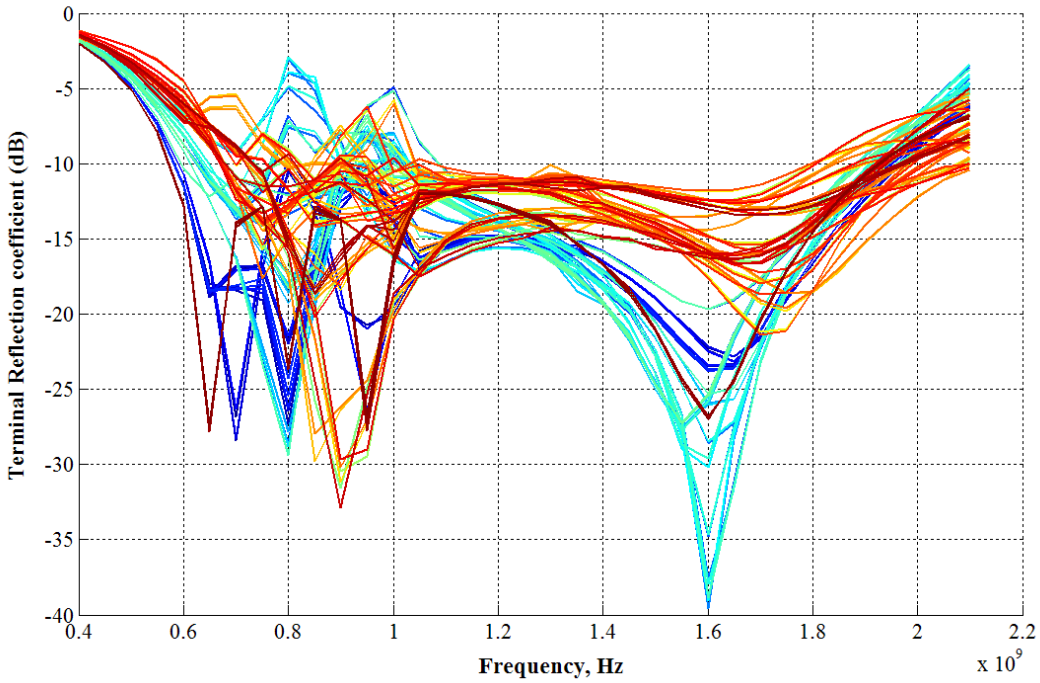

Figure 3-31 Terminal reflection coefficient versus frequency for the 7×7 HDT array, normalized to 70 ohm

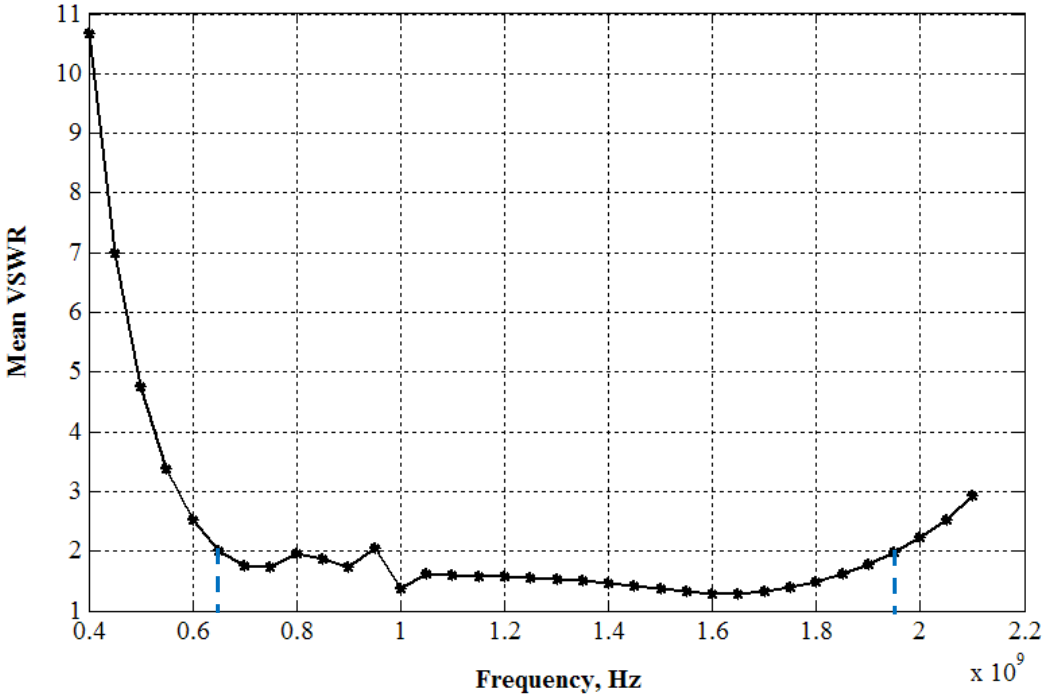

Figure 3-32 Total VSWR versus frequency for the 7×7 HDT array, normalized to 70 ohm

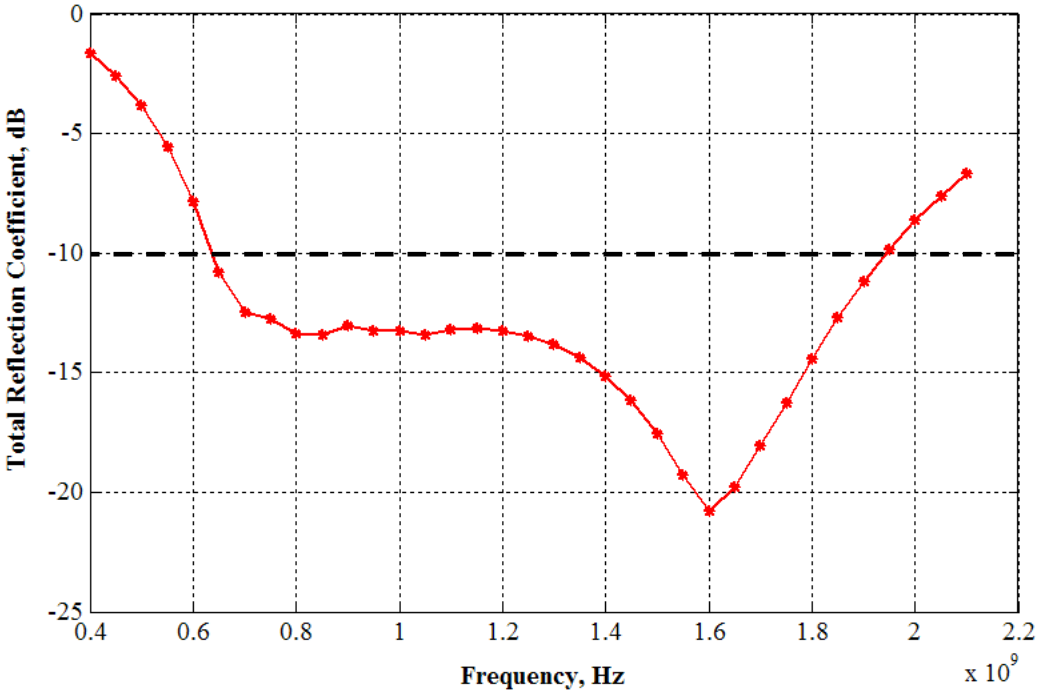

Figure 3-33 Total reflection coefficient versus frequency for the 7×7 HDT array, normalized to 70 ohm

As can be seen in Figures 3.36 and 3.37, an average VSWR of ≤ 2:1, and reflection coefficient of approximately ≤ -10 dB can be achieved across 650 to 1950 MHz if each port is normalized to 70 ohm. This relates to a total reflected power of 11% and transmission loss of 0.5 dB. This is considered to be very good.

Below 650 MHz, and above 1950 MHz impedance mismatch is increased. At the frequency of 600 MHz and 2050 MHz, total VSWR of ≤ 2.5:1 and total reflection coefficient of approximately ≤ -7.3 dB can be achieved, which constitutes 18 % reflected power and transmission loss of 0.88 dB and is considered to be acceptable. However, at 550 MHz, VSWR of 3.3:1 is obtained which yields total reflected power 27.9 % if normalized to 70 ohm.

Figures 3.38 and 3.39 show the directivity patters of the 7×7 HDT array, calculated in transmit mode between 500 to 2000 MHz with signals polarized in X-axis with zero phase. Results show directivity in XZ (Figure 3.38) and YZ (Figure 3.39) planes respectively.

As can be seen, directivity patterns are relatively steady for the entire frequency range 500 to 2000 MHz, which clearly suggests that no specific distortions are present and the array does not generate excessive side-lobes or deterioration of the main beam for the indicated frequency range. Once again, this can be confirmed by looking at the total linear and total logarithmic gain versus frequency shown in Figure 3.40. If the frequency exceeds 2000 MHz gain starts to decrease, which suggests that additional beams are likely to form due to restrictions in the element spacing.

Finally, Figure 3.41 shows the plot of radiation efficiency versus frequency, which describes the relationship between the total feed power and total radiated power of the system. As can be seen, a radiation efficiency of well above 70 % can be achieved for frequencies 600 to 2000 MHz, whereas at 550 MHz radiation efficiency of approximately 65 % is achieved.

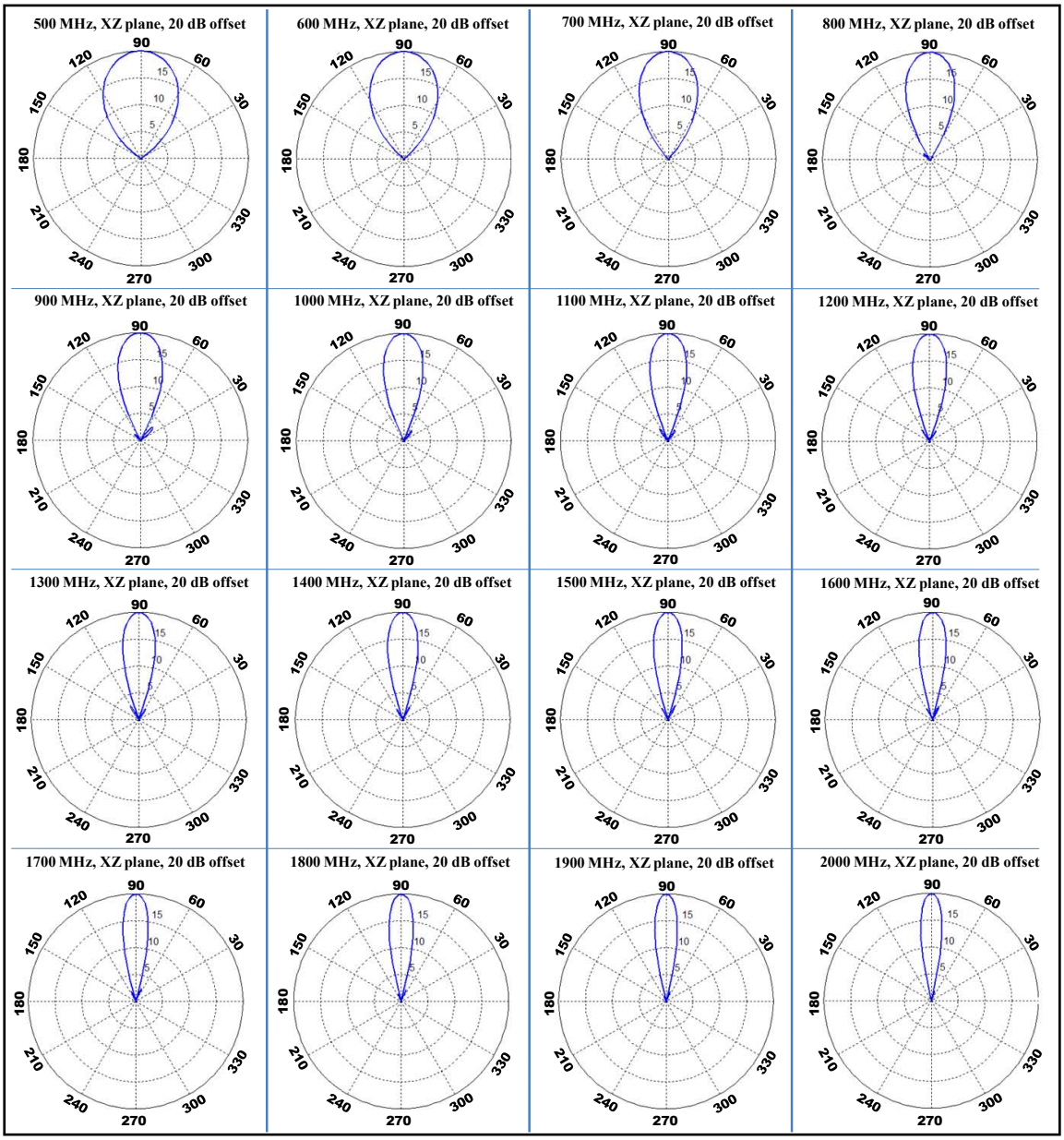

Figure 3-34 Directivity pattern of the 7×7 HDT array in XZ plane (offset by 20 dB) for the frequency range 500(100)2000 MHz

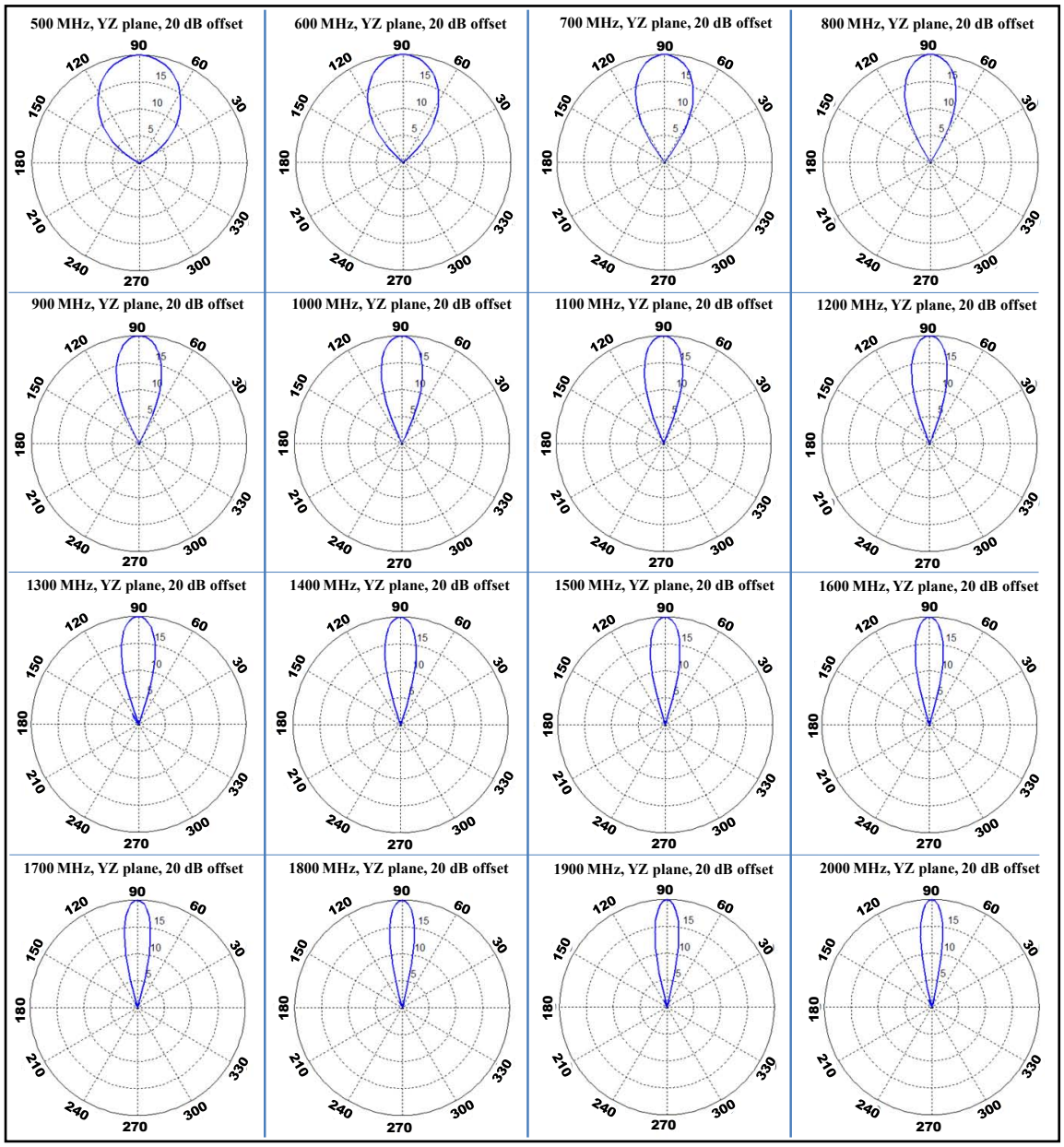

Figure 3-35 Directivity pattern of the 7×7 HDT array in YZ plane (offset by 20 dB) for the frequency range 500(100)2000 MHz

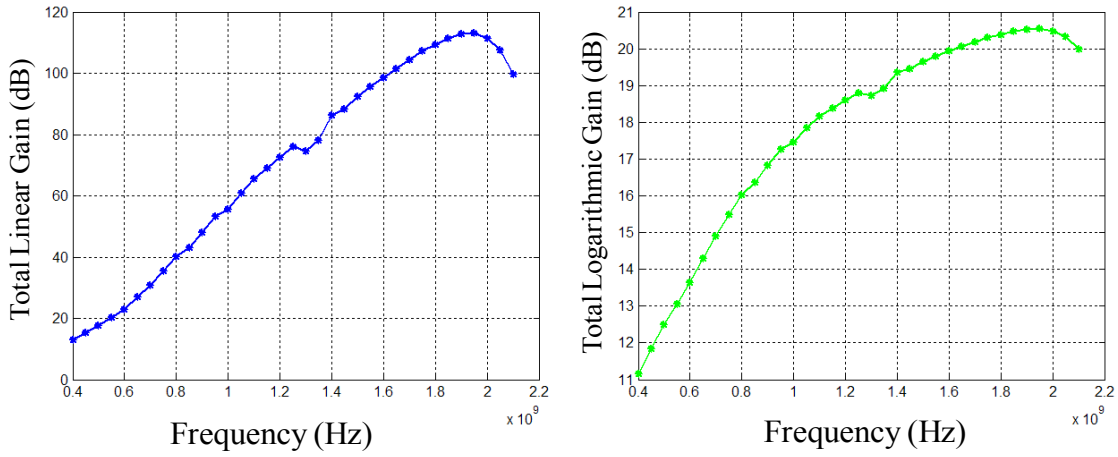

Figure 3-36 Total linear gain and total logarithmic gain of the 7×7 HDT array

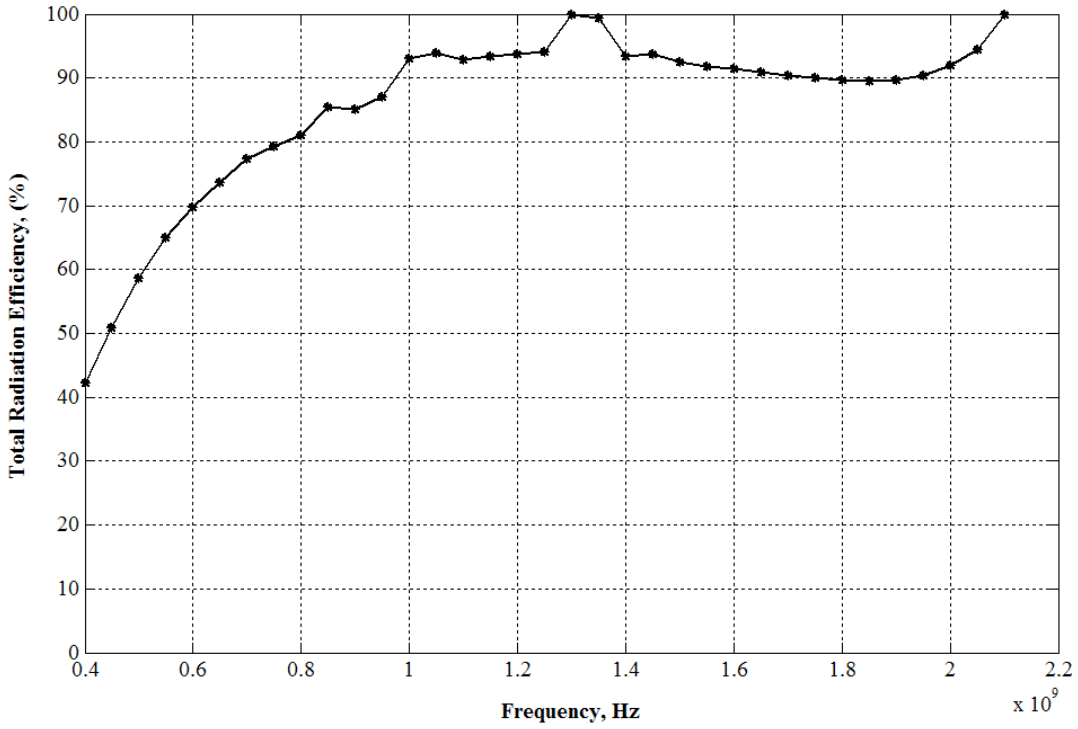

Figure 3-37 Radiation efficiency of the 7×7 HDT array

The modelling study of the 7×7 HDT array has shown that a relatively good directivity and efficiency in the frequency region 550 to 2100 MHz with a peak logarithmic gain of 20.5 dB can be achieved. Furthermore, a relatively acceptable impedance match can be obtained across the indicated frequency range for all terminals if the ports are normalized to 70 ohm.

3.2.2 Receive mode solution of the 7×7 HDT array

Receive mode solution of the 7×7 HDT array illuminated by an on-axis focal field

In this section of the thesis we intend to investigate the receive mode solution of the 7×7 hexagonal diamond tripole (HDT) array when irradiated by the focal field with zero scan angle, between 500 to 2100 MHz. This means that the array will be irradiated by the on-axis central beam as shown earlier in Figure 3.16.

Figures 3.42-3.46 show the surface current magnitude (A/m) and relative terminal power (%) received at each port of the 7×7 HDT array when illuminated with the focal field polarized in X direction at frequencies 500 MHz, 900 MHz, 1300 MHz, 1900 MHz, and 2100 MHz respectively. Once again, results indicate an ideal solution for the surface current distribution, because the relative amplitude coefficients follow the shape and size of the focal field. Furthermore, currents are strongest at terminals that are parallel to the polarization vector.

We can confirm this by calculating the average relative terminal power received at each terminal group of the 7×7 HDT array, by finding the mean of all terminal amplitude coefficients that share the same group as obtained earlier with the 5×5 HDT array using equation 2.1 (see section 3.3.1). The only difference this time, is that the 7×7 HDT array contains a total of 111 individual receiving ports.

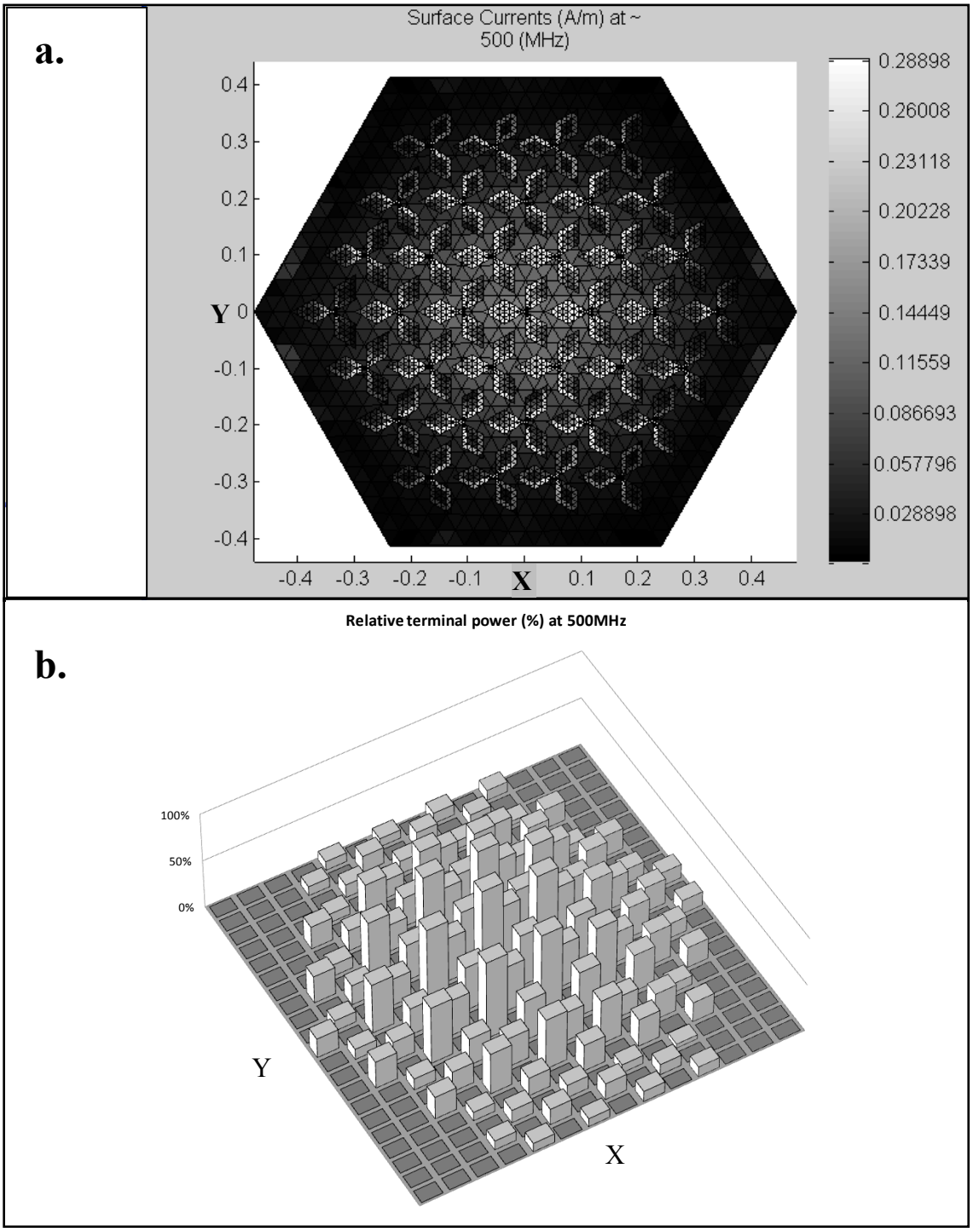

Figure 3-38 Receive mode solution of the 7×7 HDT array irradiated by the focal field at 500 MHz polarized in X, showing: a) surface currents, and b) Relative terminal power received at each port.

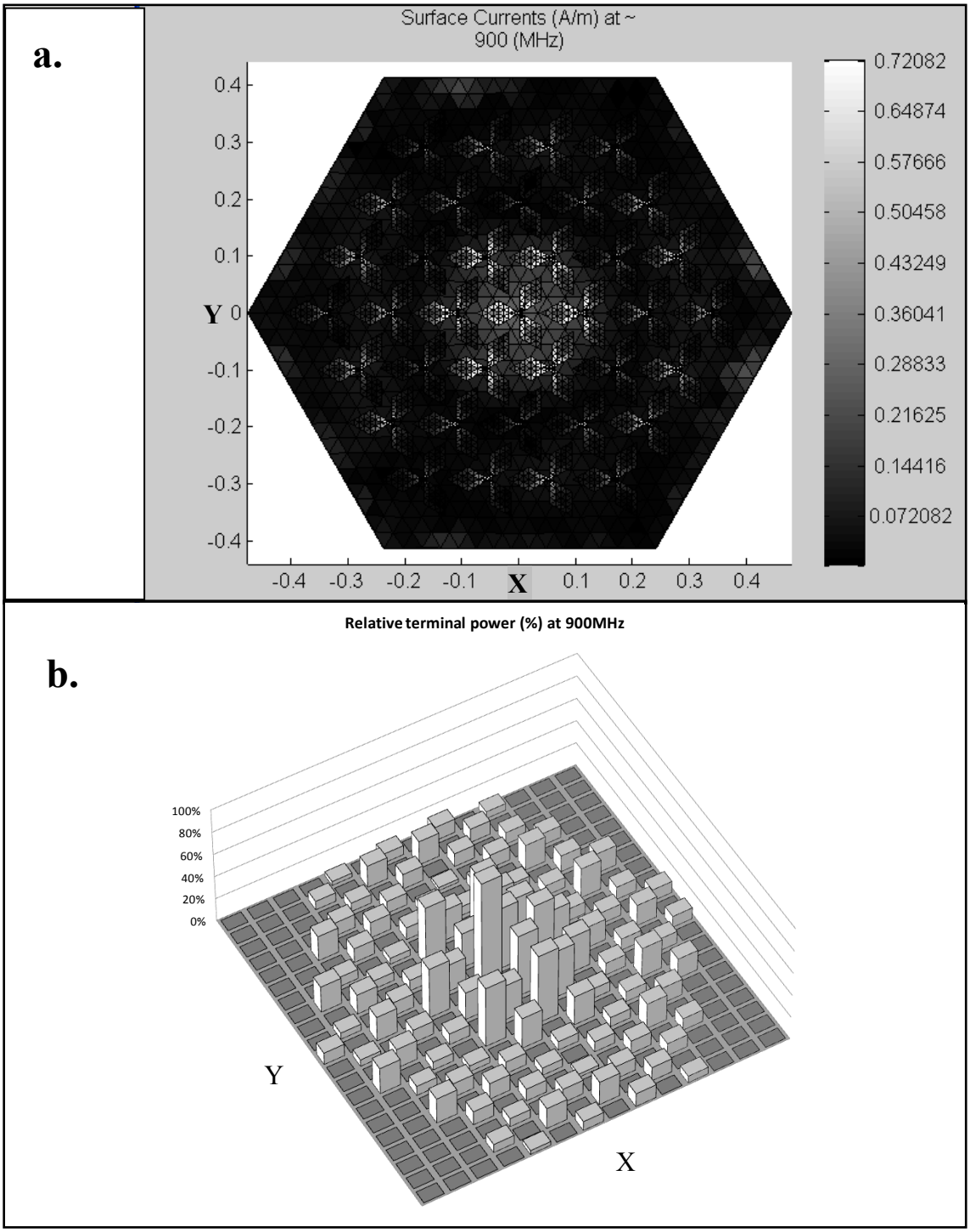

Figure 3-39 Receive mode solution of the 7×7 HDT array irradiated by the focal field at 900 MHz polarized in X, showing: a) surface currents, and b) Relative terminal power received at each port.

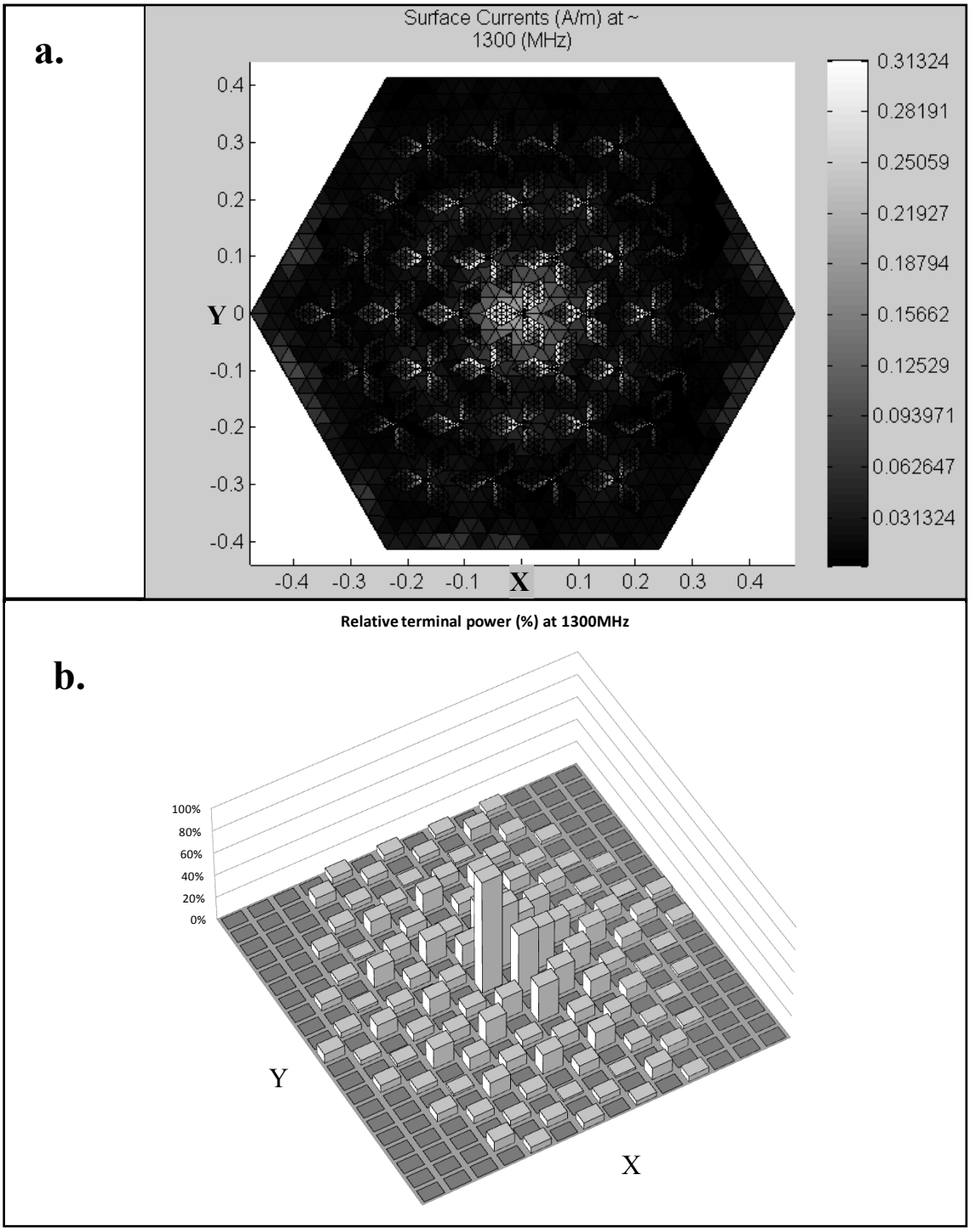

Figure 3-40 Receive mode solution of the 7×7 HDT array irradiated by the focal field at 1300 MHz polarized in X, showing: a) surface currents, and b) Relative terminal power received at each port.

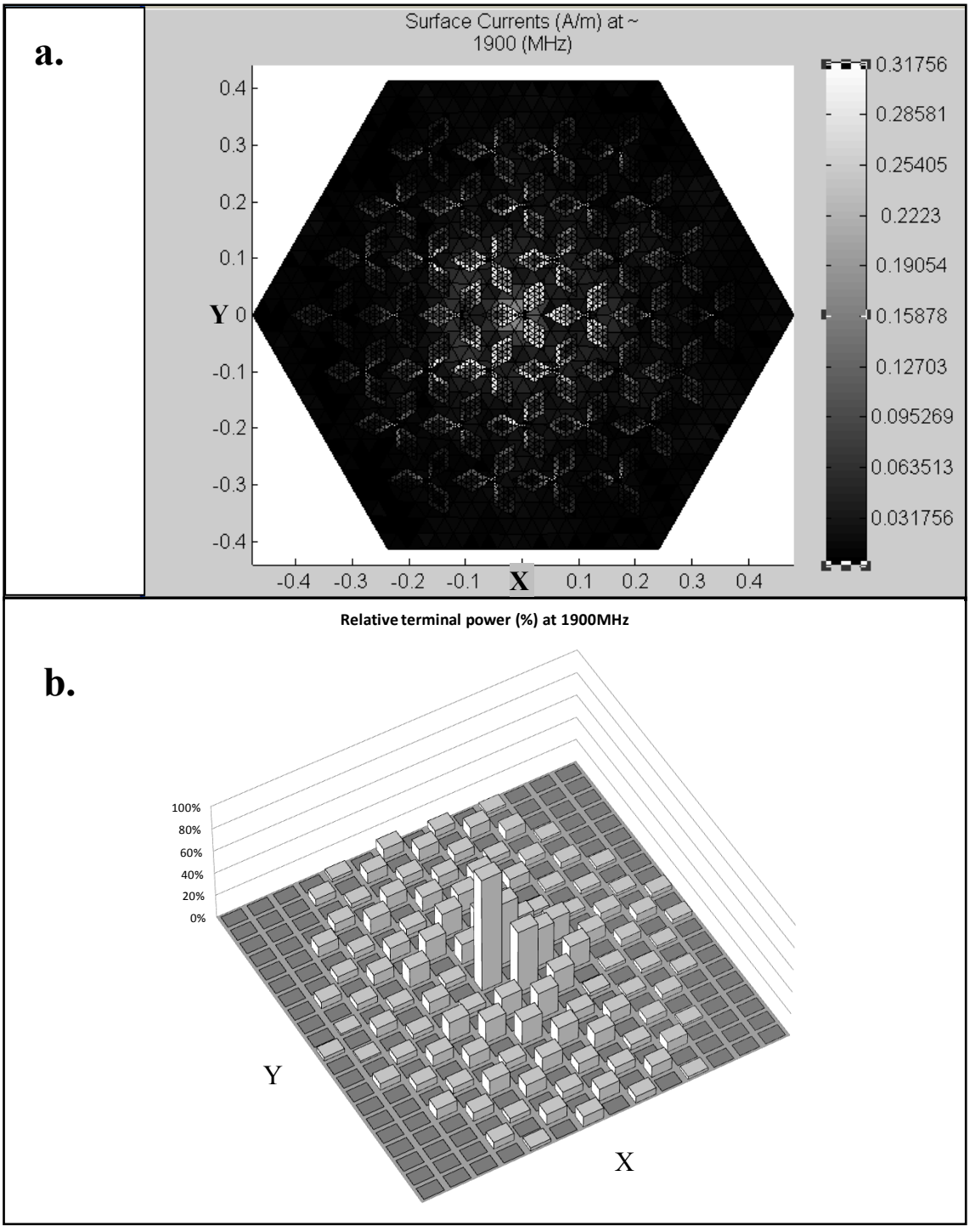

Figure 3-41 Receive mode solution of the 7×7 HDT array irradiated by the focal field at 1900 MHz polarized in X, showing: a) surface currents, and b) Relative terminal power received at each port.

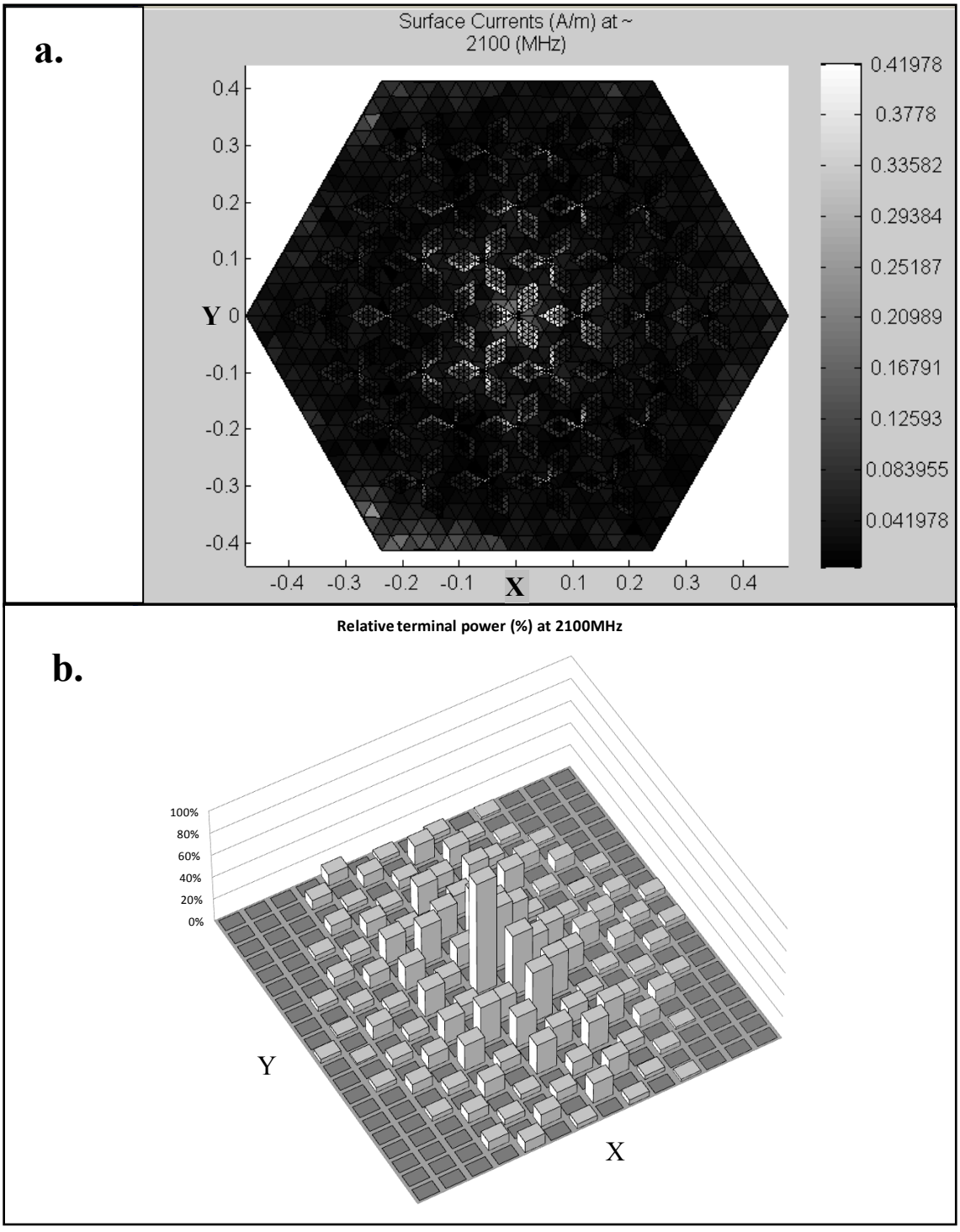

Figure 3-42 Receive mode solution of the 7×7 HDT array irradiated by the focal field at 2100 MHz polarized in X, showing: a) surface currents, and b) Relative terminal power received at each port

Table 3.4 shows the relative power induced onto each terminal group of the 7×7 HDT array when irradiated by an on-axis focal field polarized in X-axis direction for frequencies 500 to 2100 MHz.

Table 3-4 Relative power induced onto terminal groups A, B and C of the 7×7 HDT array when irradiated by an on-axis focal field polarized in X-axis direction

Frequency	Polarization group	Received relative power (%) for signals polarized in X direction
500MHz	**Group A**	**47.74 %**
	Group B	26.13 %
	Group C	26.12 %
900MHz	**Group A**	**44.28 %**
	Group B	27.84 %
	Group C	27.88 %
1300MHz	**Group A**	**45.95 %**
	Group B	26.97 %
	Group C	27.08 %
1900MHz	**Group A**	**41.64 %**
	Group B	29.19 %
	Group C	29.17 %
2100MHz	**Group A**	**42.36 %**
	Group B	28.85 %
	Group C	28.79 %

As can be seen, the mean relative power received at each terminal group of the 7×7 HDT array clearly shows that the incident focal filed is polarized in X-axis, with group A terminals having the largest current amplitude coefficients at each frequency while groups B and C are almost identical in each case. However, as obtained earlier with the 5×5 HDT array, results indicate that a continuous deviation (swing) of the received signal away from the leading terminal group (Group A) is present, which varies between 2 - 9 % depending on frequency (see Table 3.4).

Table 3.5 shows the calculated mean relative power induced onto terminal groups A, B and C of the 7×7 HDT array, for frequencies 500 to 2100 MHz, when the focal field is

polarized in X = Y direction. As can be see, Table 3.5 indicates that group terminal B has the largest amplitude coefficient, followed by group terminals A and C, respectively. Once again, difference between group terminals A and C shows to be approximately 25.0 ± 0.1 % for all frequencies, which is only possible if signals are polarised in X = Y direction.

Table 3-5 Mean relative power induced onto terminal group A, B and C of the 7×7 HDT array during reception illuminated with a focal field polarized in X = Y direction (45° with respect to X-axis)

Frequency	Polarization group	Received relative power (%) for signals polarized in X = Y direction	Difference between group A and C (%)
500MHz	Group A	38.71 %	25.02 %
	Group B	**47.70 %**	
	Group C	13.69 %	
900MHz	Group A	40.40 %	24.93 %
	Group B	**44.23 %**	
	Group C	15.47 %	
1300MHz	Group A	39.56 %	24.90 %
	Group B	**45.95 %**	
	Group C	14.67 %	
1900MHz	Group A	41.76 %	25.08 %
	Group B	**41.58 %**	
	Group C	16.69 %	
2100MHz	Group A	41.40 %	25.06 %
	Group B	**42.35 %**	
	Group C	16.35 %	

Receive mode solution of the 7×7 HDT array illuminated by an off-axis focal field

In this section, we intend to investigate the behaviour of the 7x7 HDT array when the focal field is displaced off-axis at an angle -3° in X and Y direction. We measure this behaviour for frequencies 500 MHz, 1033 MHz, 1566 MHz and 2100 MHz, and we investigate the surface current distribution and the relative amplitude coefficient received at each port. Results are illustrated in Figures 3.47 - 3.50.

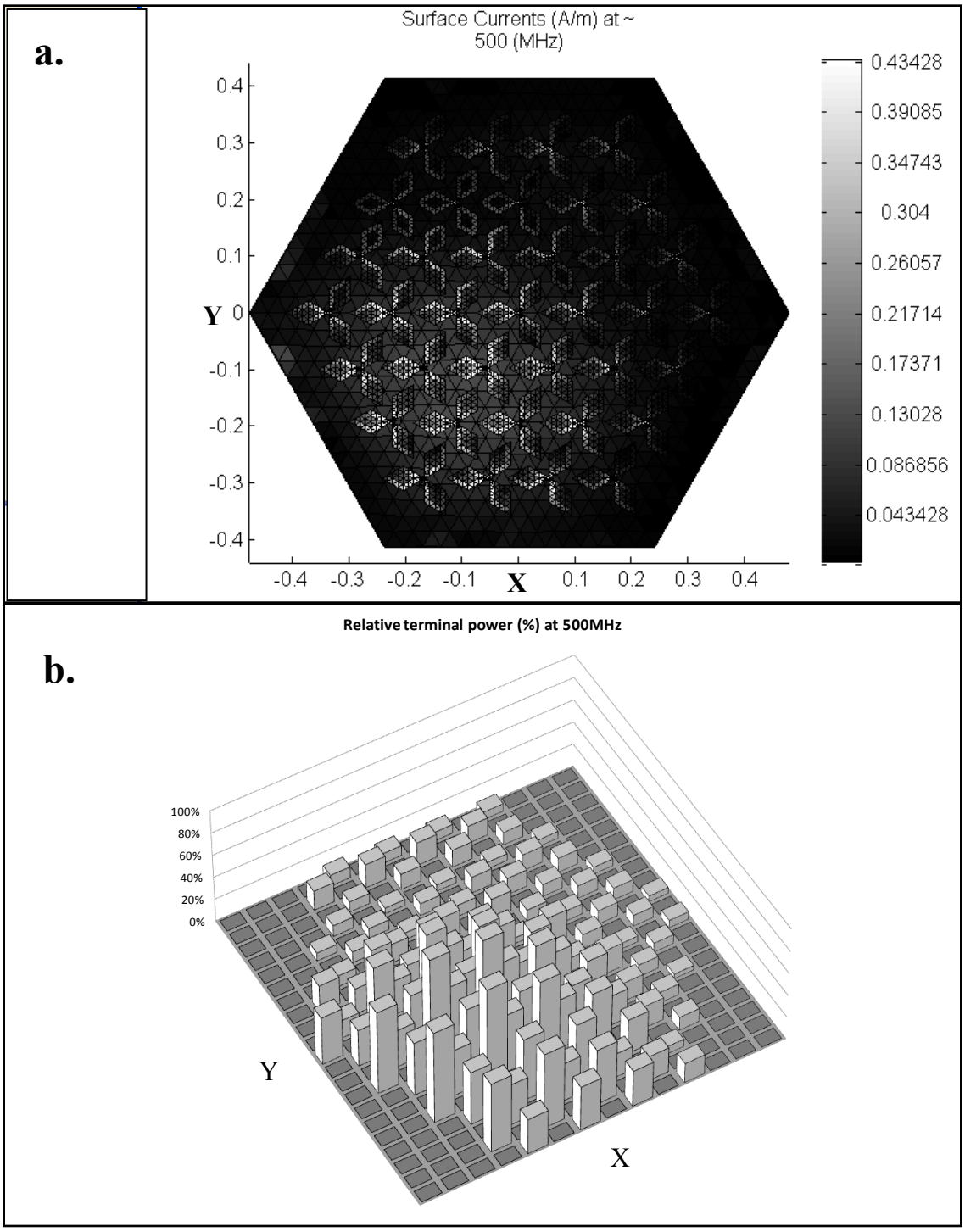

Figure 3-43 Receive mode solution of the 7×7 HDT array illuminated by an off-axis beam (-3° in X and Y direction) at 500 MHz polarized in X axis, showing: a) surface currents (A/m) across the array (see grayscale vertical bar) , and b) relative terminal power received at each port

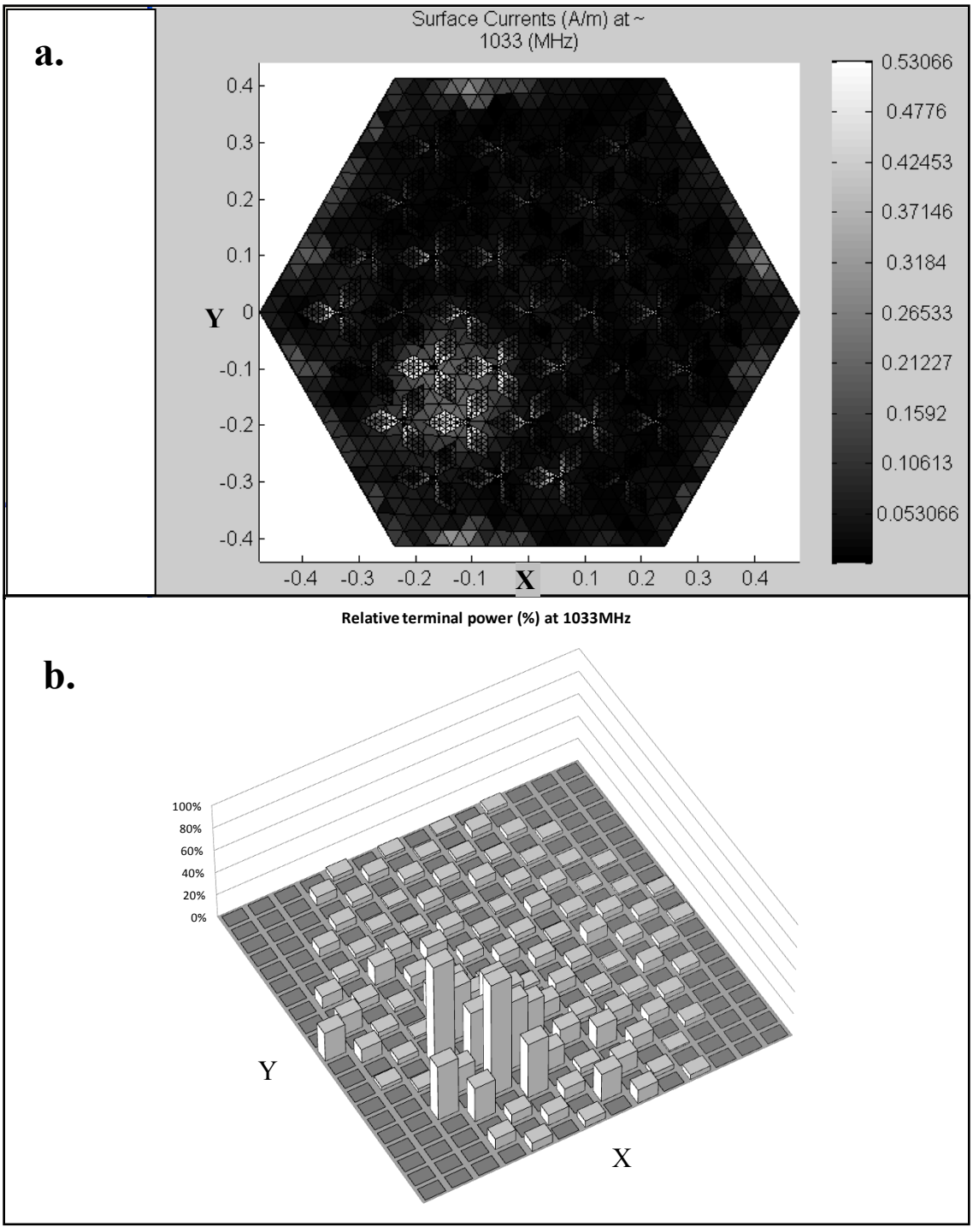

Figure 3-44 Receive mode solution of the 7×7 HDT array illuminated by an off-axis beam (-3° in X and Y direction) at 1033 MHz polarized in X axis, showing: a) surface currents (A/m) across the array (see grayscale vertical bar) , and b) relative terminal power received at each port

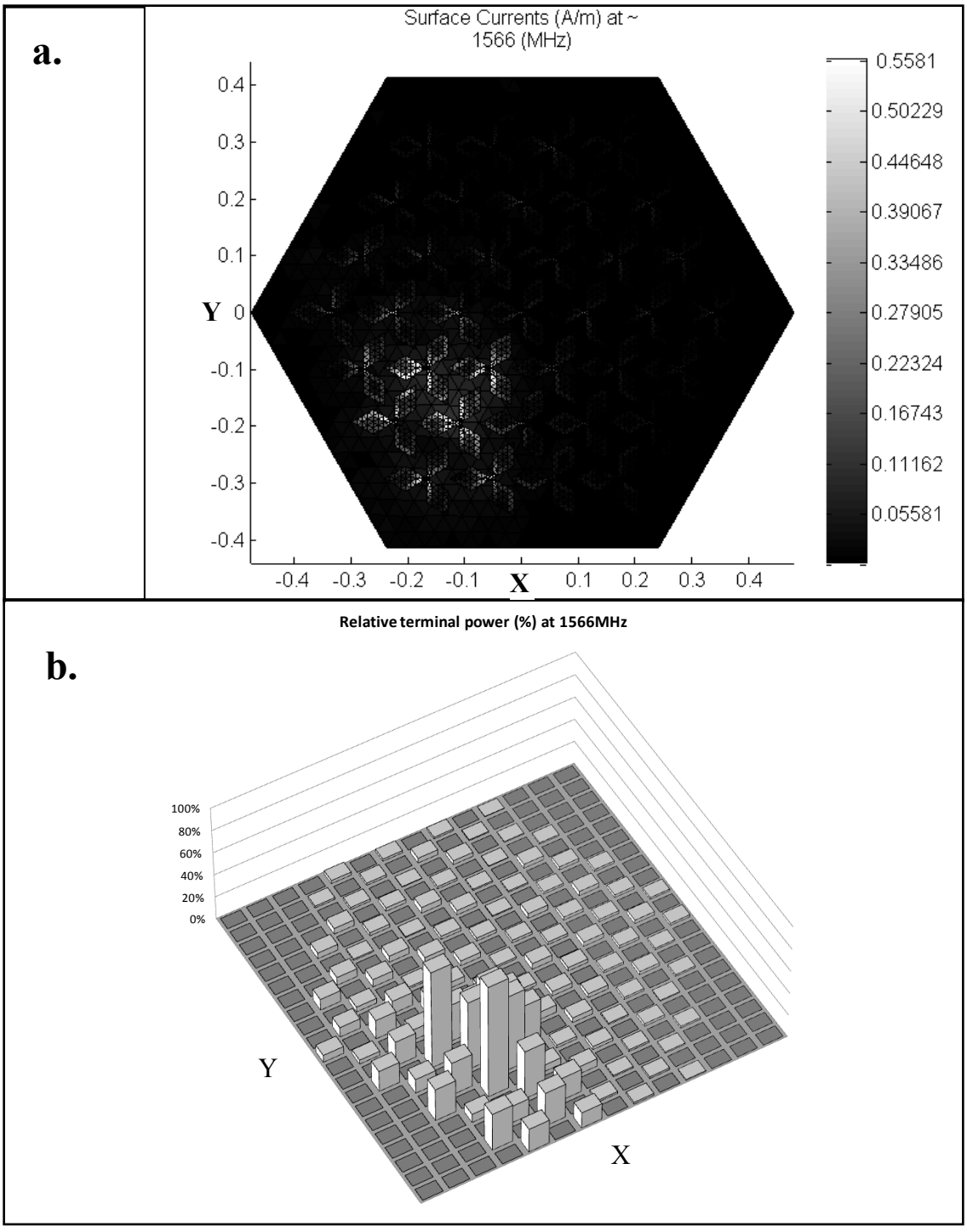

Figure 3-45 Receive mode solution of the 7×7 HDT array illuminated by an off-axis beam (-3° in X and Y direction) at 1566 MHz polarized in X axis, showing: a) surface currents (A/m) across the array (see grayscale vertical bar) , and b) relative terminal power received at each port

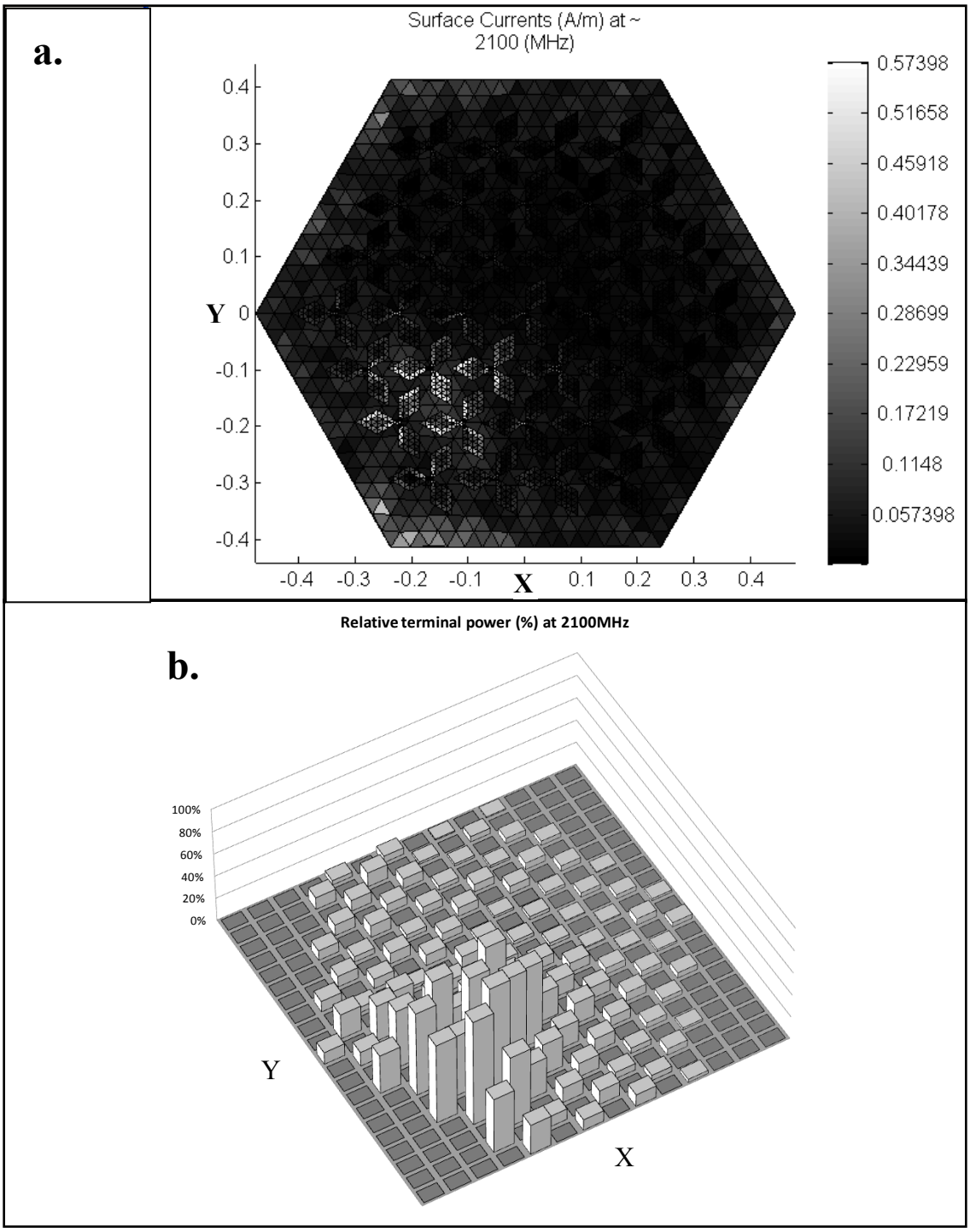

Figure 3-46 Receive mode solution of the 7×7 HDT array illuminated by an off-axis beam (-3° in X and Y direction) at 2100 MHz polarized in X axis, showing: a) surface currents (A/m) across the array (see grayscale vertical bar) , and b) relative terminal power received at each port

Table 3.6 shows the calculated mean relative terminal power received between the three terminal groups A, B and C of the 7×7 HDT array, with signals polarized in X direction, and X = Y direction. Note that the off-axis beam angle was selected to be the same as previously obtained using the 5×5 HDT array, set to be -3° in X and Y direction, using an F/D ratio of 0.4 and a 12 m parabolic reflector.

Table 3-6 Mean relative power induced onto terminal group A, B and C of the 7×7 HDT array during reception while illuminated by an off-axis focal filed (-3° in X and Y direction). Results show relative power (%) received at each terminal group for signals polarized in X direction, and signals polarized in X = Y direction. Table also indicates the difference between group A and C for signals polarized in X = Y direction

Frequency	Polarization group	Received relative power (%) for signals polarized in X direction	Received relative power (%) for signals polarized in X = Y direction	Difference between group A and C for signals polarized in X = Y direction (%)
500MHz	Group A	**46.95 %**	38.99 %	24.87 %
	Group B	26.48 %	**46.93 %**	
	Group C	26.61 %	14.11 %	
1033MHz	Group A	**46.44 %**	39.31 %	24.90 %
	Group B	26.75 %	**46.41 %**	
	Group C	26.81 %	14.41 %	
1566MHz	Group A	**45.75 %**	39.88 %	25.36 %
	Group B	27.28 %	**45.69 %**	
	Group C	26.97 %	14.51 %	
2100MHz	Group A	**41.62 %**	41.40 %	24.32 %
	Group B	28.89 %	**41.57 %**	
	Group C	29.52 %	17.08 %	

As can be seen, the mean relative terminal power received between terminal groups A, B and C can indeed help us distinguish the polarization of the incident focal field, even when the focal field is displaced off-axis (see Table 3.6). Moreover, this is also true when the signals are polarized in X = Y direction, as show in Table 3.6. However, once again a deviation of approximately 1.2 %, occurs between terminal groups B and C at higher frequencies (1566 MHz and 2100 MHz), which yields a swing of about 0.6 %.

These variations are caused due to the distribution of the focal field and proximity of the ground plane edge.

We now complete our theoretical and modelling analysis of the 7×7 HDT array and conclude that this array provides good directivity with peak logarithmic gain of 20.5 dB, efficiency well above 65%, and relatively consistent VSWR and reflection coefficient for frequencies 550 to 2100 MHz, which enables a bandwidth ratio of ~3.8:1. Furthermore, additional modelling analysis has revealed that polarization can be determined at any angle about the axis normal to the antenna plane using techniques described above to within a theoretical uncertainty that varies as function of frequency by a maximum of ± 0.6 % (± 2.2°). In addition, it was discovered that this result holds for all functions of FoV allowed by the surface area of the FPA across the indicated frequency range.

3.3 Summary

In this chapter, the full modelling implementation of the three axis hexagonal diamond tripole (HDT) FPA was revealed. Two distinct variations of the FPA (5×5 and 7×7 arrays) were presented utilizing the diamond-tripole planar strip antenna elements.

The modelling of the array and its elements were derived via method of moments utilizing the MoMADT design tool, providing solutions to both metallic and dielectric materials. Results were obtained by employing both transmit and receive modelling techniques and include computations comprising mutual coupling effects with fields and currents that vary in three dimensional space.

Modelling results of the 5×5 HDT array have revealed that this array provides good directivity with peak logarithmic gain of 20 dB, efficiency above 77 %, and relatively consistent VSWR and return loss for frequencies 500 to 1700 MHz, provided that each port is normalized to 80 ohm, which enables a bandwidth ratio of ~3.4:1. Conversely,

the 7×7 HDT array has shown to yield good directivity, with peak logarithmic gain of 20.5 dB, efficiency well above 65 %, VSWR of ≤ 2.5:1, and reflection coefficient of approximately ≤ -7.3 dB for frequencies 550 to 2100 MHz, if normalized to 70 ohm. This provides a bandwidth ratio of ~3.8:1.

Important lessons acquired from the modelling study of the HDT-FPA has shown that the 5×5 and 7×7 arrays can be used to distinguish the polarization of the incident focal field at numerous angles about the axis normal to the antenna plane, using an amplitude comparison approach described above. Two modelling techniques were used to demonstrate this operation with signals polarized in X direction and X = Y direction, during which the focal field was altered in size as function of frequency and displaced off centre as function of the FoV. It was found that polarization vectors were achievable to within a theoretical uncertainty of ± 3.0° for the 5×5 HDT array, and ± 2.2° for the 7×7 HDT array and vary as function of frequency. Due to the symmetry of the HDT-FPA, including additional modelling analysis, it is concluded that these results hold for any angle of polarization for the indicated frequency range, to within a theoretical uncertainty value described above.

CHAPTER 4

Chapter 4 - Measurements and Analysis

Chapter 4 presents number of experimental measurement cases of the diamond tripole antenna and the 7×7 HDT prototype array developed during the course of this study. Measurements are performed using a network analyser and include the magnitude of scattering or S-parameters, reflection and transmission coefficients between the incident and reflection waves which describes the device's behaviour under linear conditions at the microwave frequency range, specifically for frequencies 400 to 2200 MHz.

4.1 S-Parameters

Scattering or S-parameters are variables that describe the input-output relationship between ports (or terminals) of an electrical system. If we consider a two port network, as illustrated in Figure 4.1, the scattering parameter "S12" effectively represents the power transferred from Port 1 to Port 2. While S21 represents the power transferred from Port 2 to Port 1. In general, S_{NM} is a scattering parameter that represents the power transferred from Port N to Port M in a multi-port network [69].

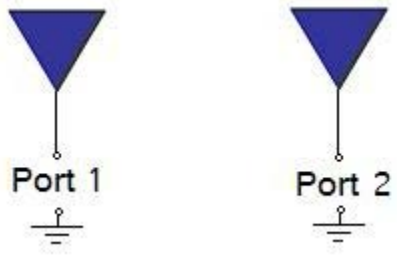

Figure 4-1 Two port electrical network

If the ports in Figure 4.1 are treated as antenna elements, then S21 would effectively describe the power received at antenna 2 relative to the power input to antenna 1. For instance, if S21=0 dB this implies that all of the power delivered to antenna 1 ends up at the terminals of antenna 2 (which is not physically possible). If, on the other hand, S21=-10 dB, this implies that 1 W delivered to antenna 1 (or 0 dB), ends up as -10 dB at antenna 2, or 0.1 W.

In practice, the most commonly quoted parameter in regards to antennas is S11. S11 describes how much power is reflected from the antenna when excited by a random source or excitation. If the measured variable S11= 0 dB, this would imply that all of the power is reflected from the antenna and nothing is radiated. If S11=-10 dB, this implies that if 3 dB of power is delivered to the antenna, then -7 dB is the reflected power and the rest was "accepted" by the antenna. This accepted power is either radiated or absorbed as losses within an antenna. However, since antennas are typically designed to be low loss, the majority of the power delivered to the antenna is radiated.

The scattering parameters S21 and S11 are generally measured using a device called the network analyser. To further clarify the meaning of these measurements, we consider the plot of S11 in Figure 4.2.

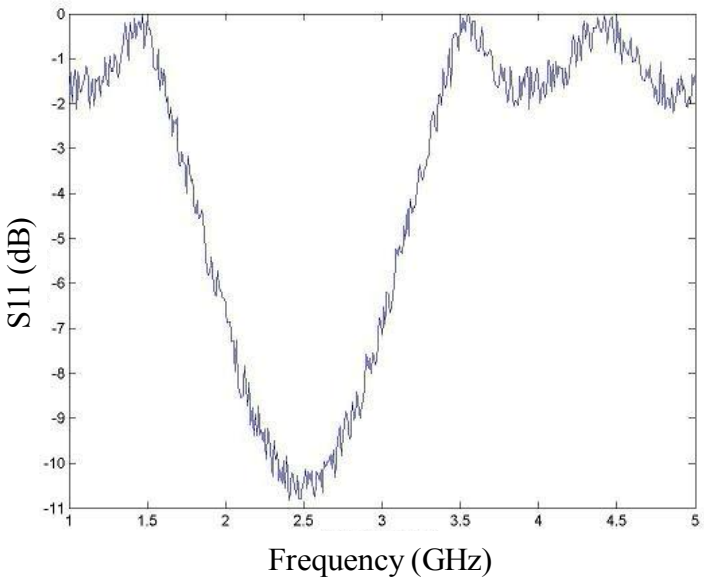

Figure 4-2 Plot of S11 measured from an arbitrary antenna

Figure 4.2 shows the plot of S11 measured from an arbitrary antenna using a network analyser. The results indicate that the antenna in question radiates best at 2.5 GHz, where S11=-10 dB. Furthermore, at 1.5 GHz the antenna will radiate virtually nothing, since S11 is close to 0 dB. From these measurements, the bandwidth of the antenna can also be determined. For example, if the acceptable range of S11 is given to be <-6 dB, then the bandwidth would roughly equate to 1 GHz, with 3 GHz at the high end and 2 GHz at the low end of the band, which yields a bandwidth ratio of 1.5:1.

4.2 Measurements of the Diamond Tripole Antenna

In this section, a direct comparison between theory and measured data of the diamond tripole antenna are presented. An ELAD SNA2550 scalar network analyser (see Appendix C) is used to measure the reflection coefficient (S11 in dB) and VSWR of the diamond tripole antenna normalized to 50 ohm. The experimental setup of the diamond tripole antenna is illustrated in Figure 4.3.

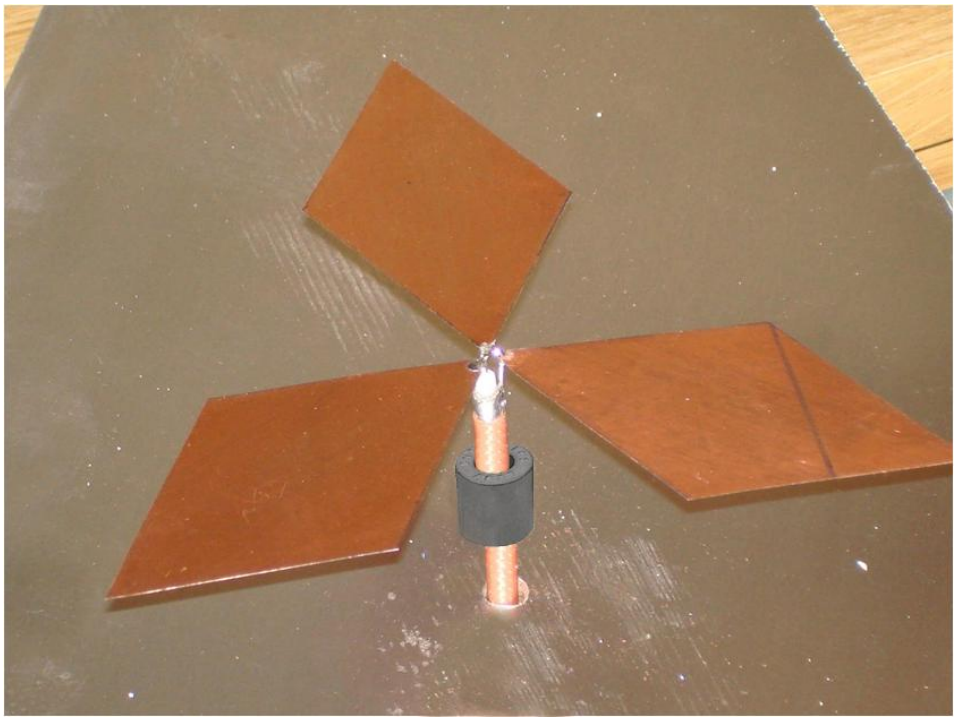

Figure 4-3 Experimental setup of the diamond tripole antenna positioned 0.065 m above the ground plane

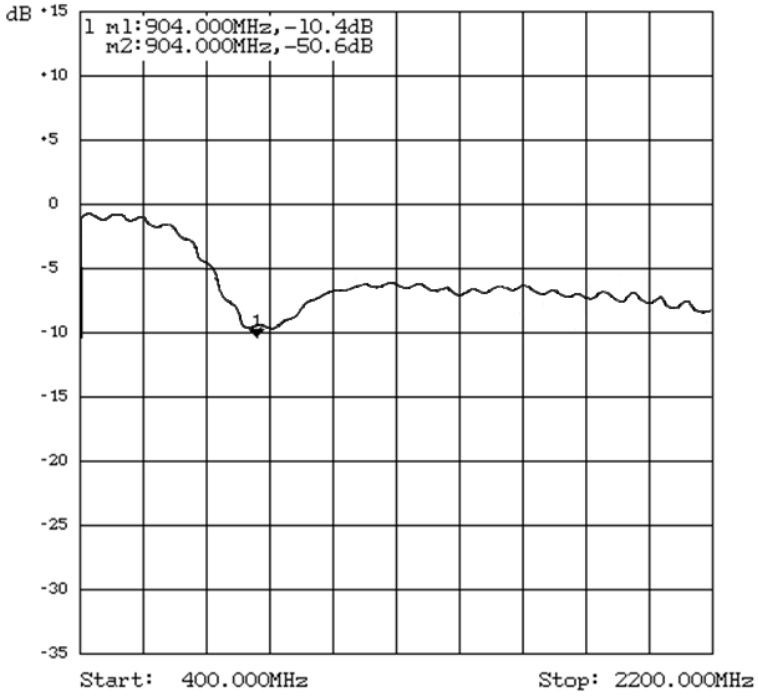

a) Measured

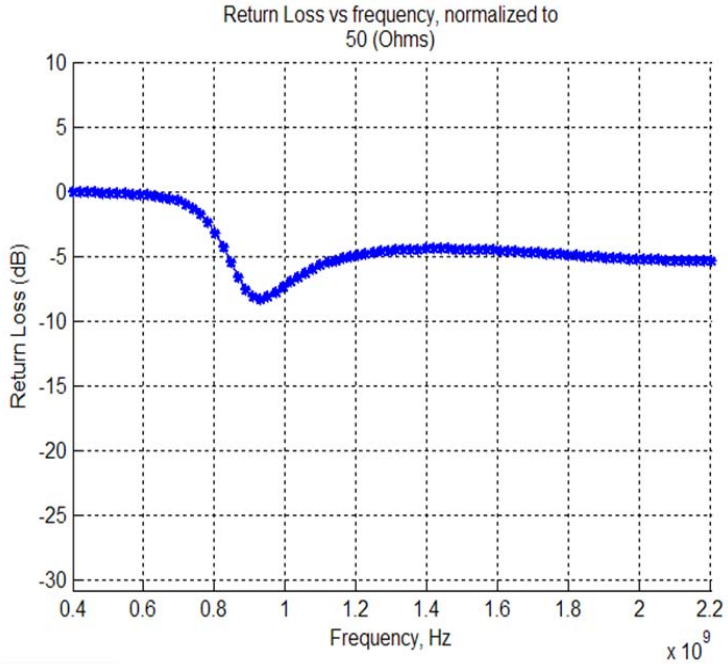

b) Theory

Figure 4-4 Reflection coefficient (S11) versus frequency for the diamond tripole antenna showing: a) Measured, and b) Theory

Figure 4.3 shows the fabricated diamond planar strip antenna elements arranged in three distinct axes constructed from a thin copper sheet material above a ground plane. A ferrite bead is used as a temporary choke balun. The test antennae were constructed by the author and all measurements performed by the author. The ground plane is made up from a 3 mm thick aluminium plate and separation distance set to 0.065 m below the radiating elements. Direct comparison between the measured and theoretical data for the magnitude portion of S11 is shown in Figure 4.4. As can be seen, Figure 4.4 shows that the measured and theory data agree relatively well. However a slight noise variation is present within measured data. The residual noise present in Figure 4.4 was identified due to absence of a Type III balun circuit. A more appropriate balun would be a Type III balun as discussed in section 1.6. Nonetheless, results show to be in good agreement. It is also useful to note that these solutions differ from those calculated in chapter 3 because impedances are normalized to 50 ohm instead of 70 ohm as obtained in chapter 3. Consequently, slightly higher reflections are observed for frequencies above 1GHz.

4.3 Measurements of the 7x7 HDT Array

As discussed in section 4.1, the scattering parameters S21 and S11 are generally measured using a two port network analyser. In this section the scattering measurements are carried out on the 7×7 HDT prototype array developed during the course of this study, using the SNA2550 network analyser (see Appendix C). The measured data are then compared with theoretical solutions obtained using method of moments. Figures 4.5-4.7 shows the 7×7 HDT prototype array constructed during the course of this study. As can be seen, the array was manufactured from a series of materials in a four layer formation. The diamond planar strip antenna elements were fabricated from a thin copper sheet material, effectively bonded onto a 3 mm polycarbonate dielectric substrate of relative permittivity 2.9, while the ground plane was manufactured from a 3 mm aluminium plate. Contained within, is sandwiched foam of 0.06 m thickness between the ground plane and the radiating elements whose relative permittivity is very close to that of air. The overall system forms a robust and simple-to-manufacture structure.

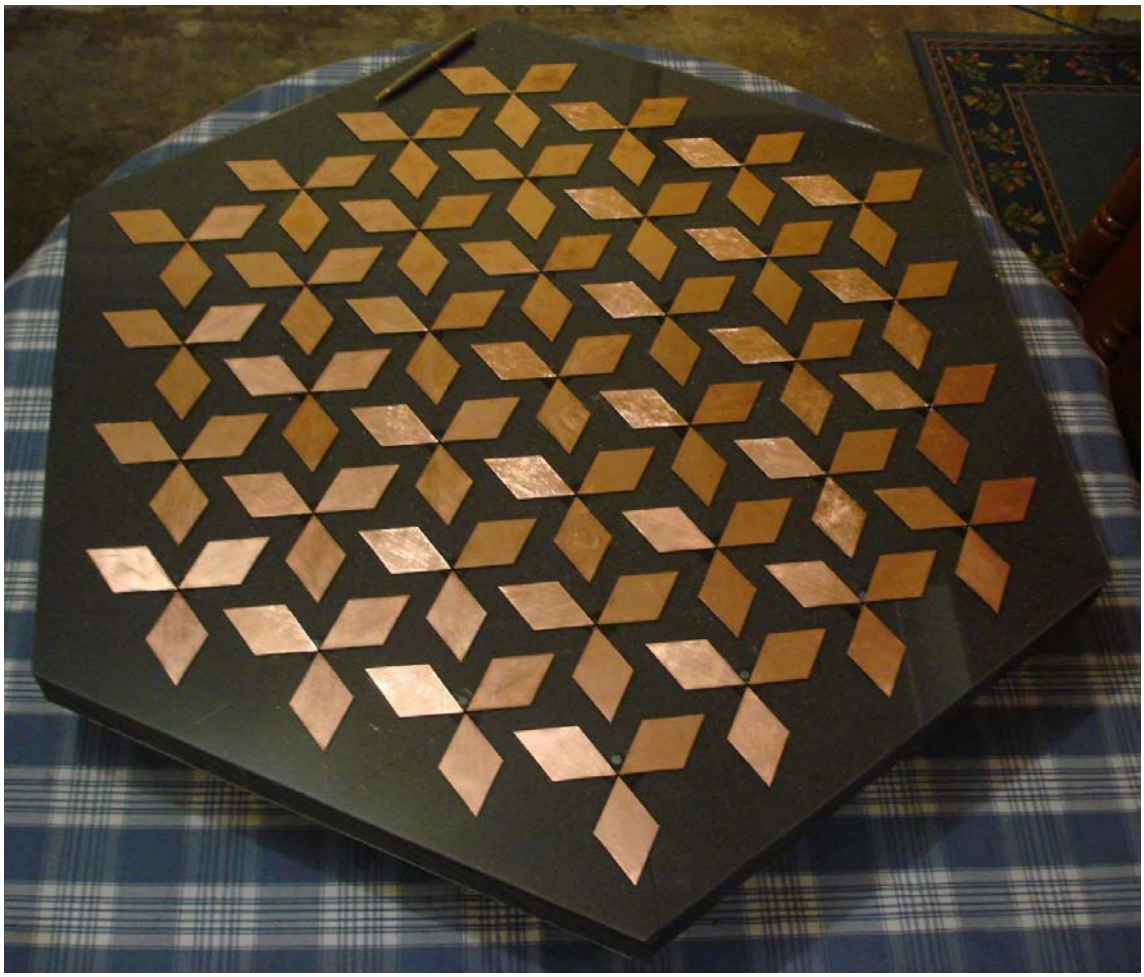

Figure 4-5 Prototype 7×7 HDT array developed in this study

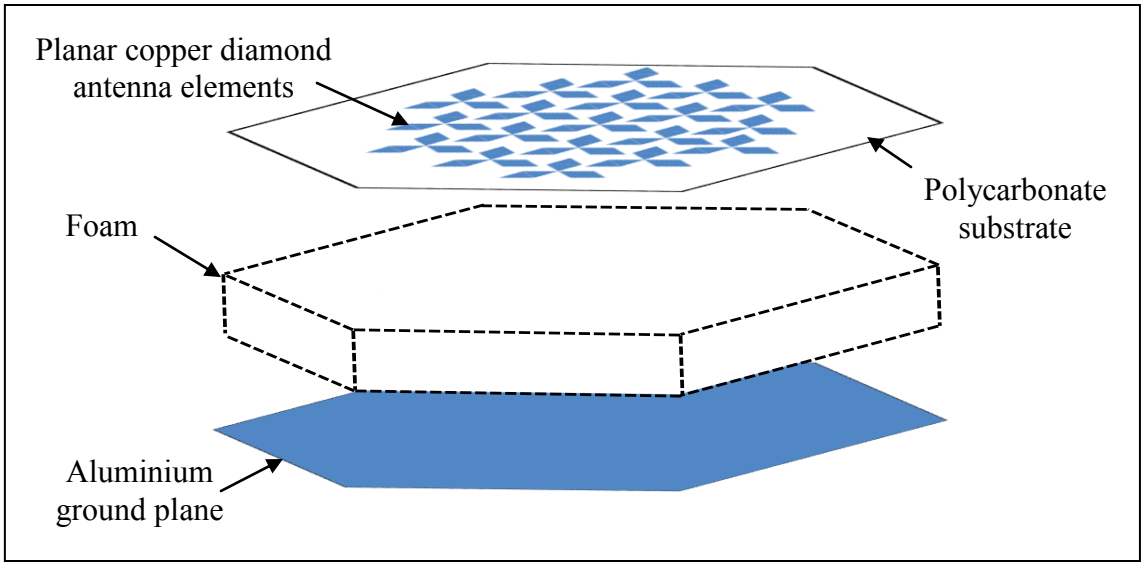

Figure 4-6 Graphic representation of the HDT array showing material structure

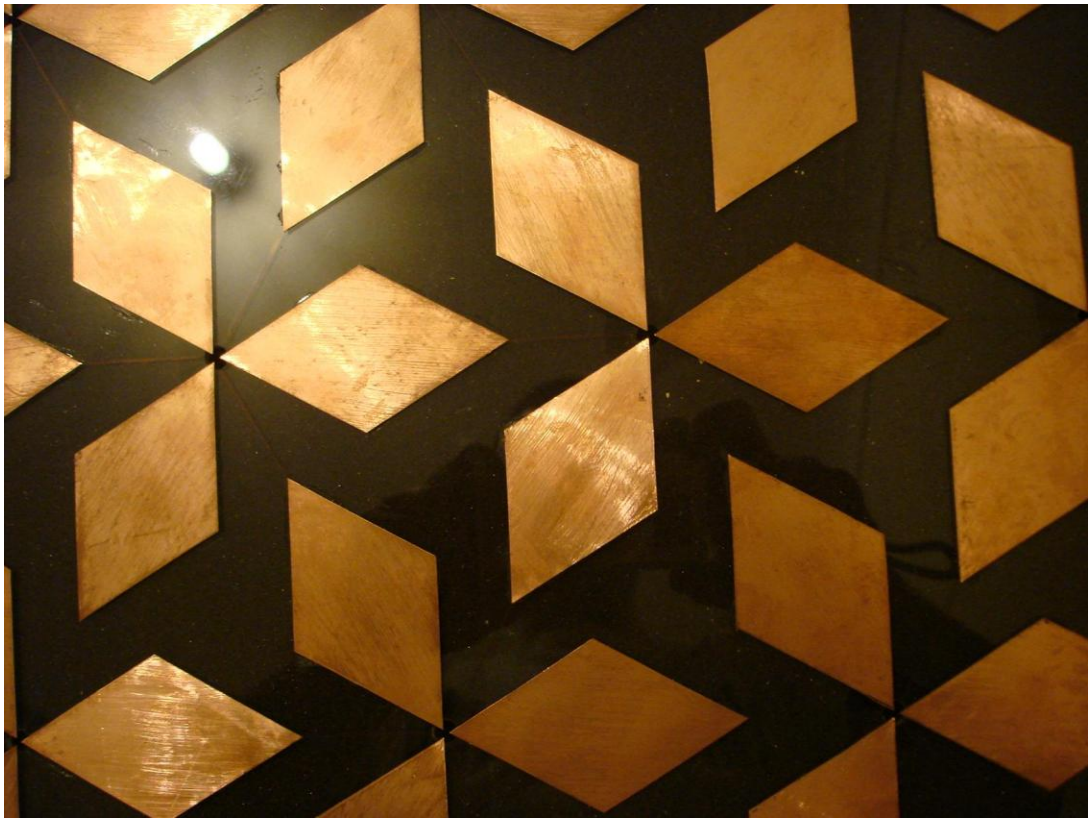

Figure 4-7 Top view of the 7×7 HDT prototype array manufactured by the author, showing the diamond planar strip antenna elements bonded on polycarbonate substrate

It is worth noting that the polycarbonate dielectric material (normally very lossy) was chosen in this study for testing purposes. Alternatively, more suitable material would be to use a printed circuit board (PCB).

4.3.1 S-Parameter Measurements

Given the symmetry of the 7×7 HDT array, the scattering measurements of the array were carried out along one line of the array plane as shown in Figure 4.8. This measurement procedure proved to be sufficient to ensure that the basic interactions and scattering effects between the elements of the array were understood. In order to perform such measurements a total of 12 diamond strip antenna elements were selected and three distinct set of measurements performed by alternating the polarization terminals A, B and C, between the tripole antennas marked as 1, 2, 3 and 4, illustrated in Figure 4.8.

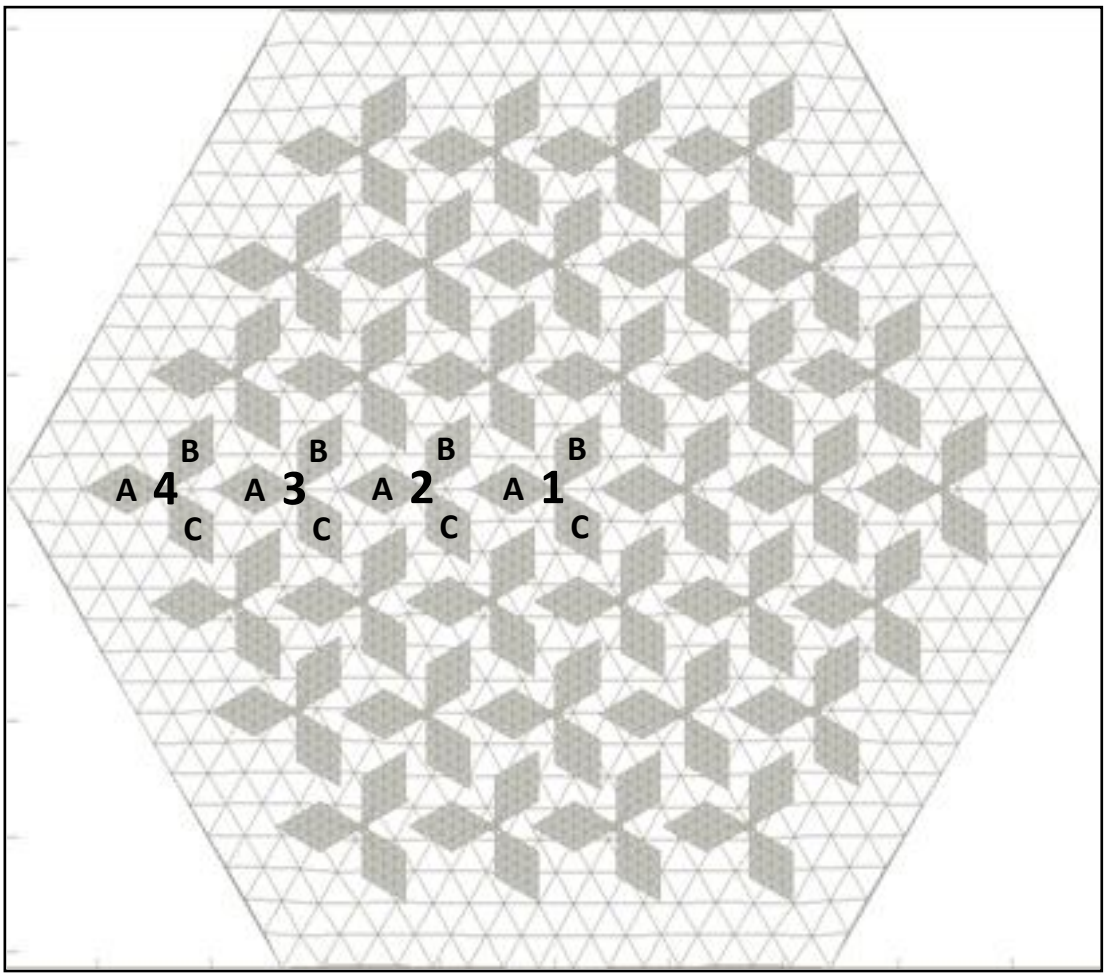

Figure 4-8 Port number allocation for scattering parameter measurements (note: the above image is for schematic purposes and does not reflect the precise geometry)

To begin the procedure, the output of the SNA2550 network analyser was fed into terminal 1A, as seen in Figure 4.8, supplying a power of 95 dBμV. During this time, the insertion loss "S21" (in dB) was individually measured at ports 2A, 2B, 2C, 3A, 3B, 3C, 4A, 4B and 4C, as illustrated in Figure 4.8. For the duration of the measurement procedure, all remaining ports (except the two ports in use) were terminated with a 70Ω balanced load (determined through modelling) [14]. This measurement procedure was performed on the 7×7 HDT prototype array which provided direct observation of power received at each terminal, due to the power delivered to terminal **1A**. This technique essentially describes the reflection coefficient and insertion loss effects between the two ports of the 7×7 HDT array. Results are illustrated in Figures 4.9, 4.10 and 4.11.

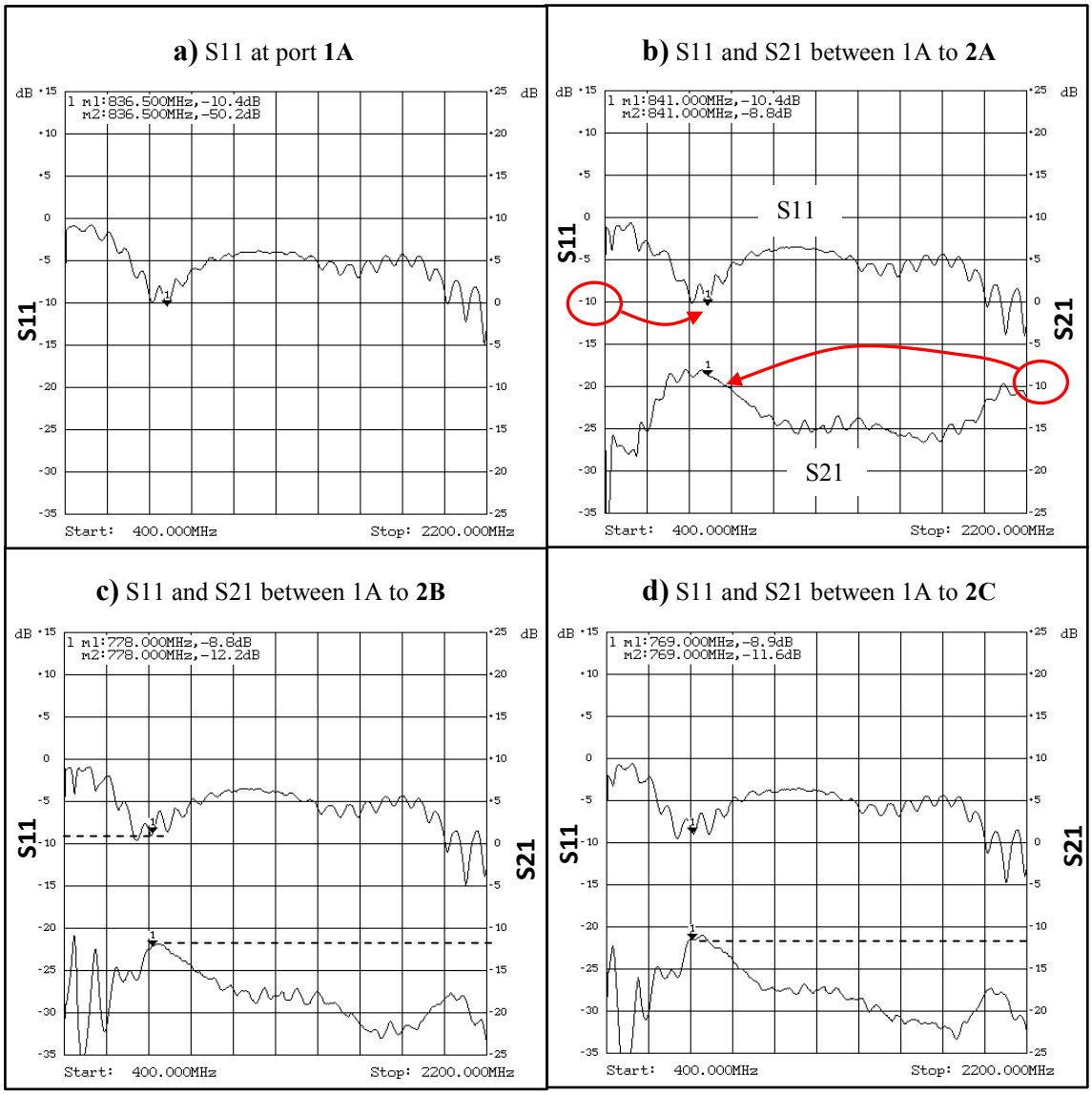

Figure 4-9 Scattering parameters S11 and S21 measured using a two port SNA2550 network analyzer between terminals 1 and 2 of the 7x7 HDT array, showing: a) S11 at port 1A, which describes the return loss; b) S11 at port 1A and S21 at port 2A, which describes both the return loss and insertion loss between the two ports; c) S11 at port 1A and S21 at port 2B; d) S11 at port 1A and S21 at port 2C. All measurements are performed for frequencies 400-2200 MHz.

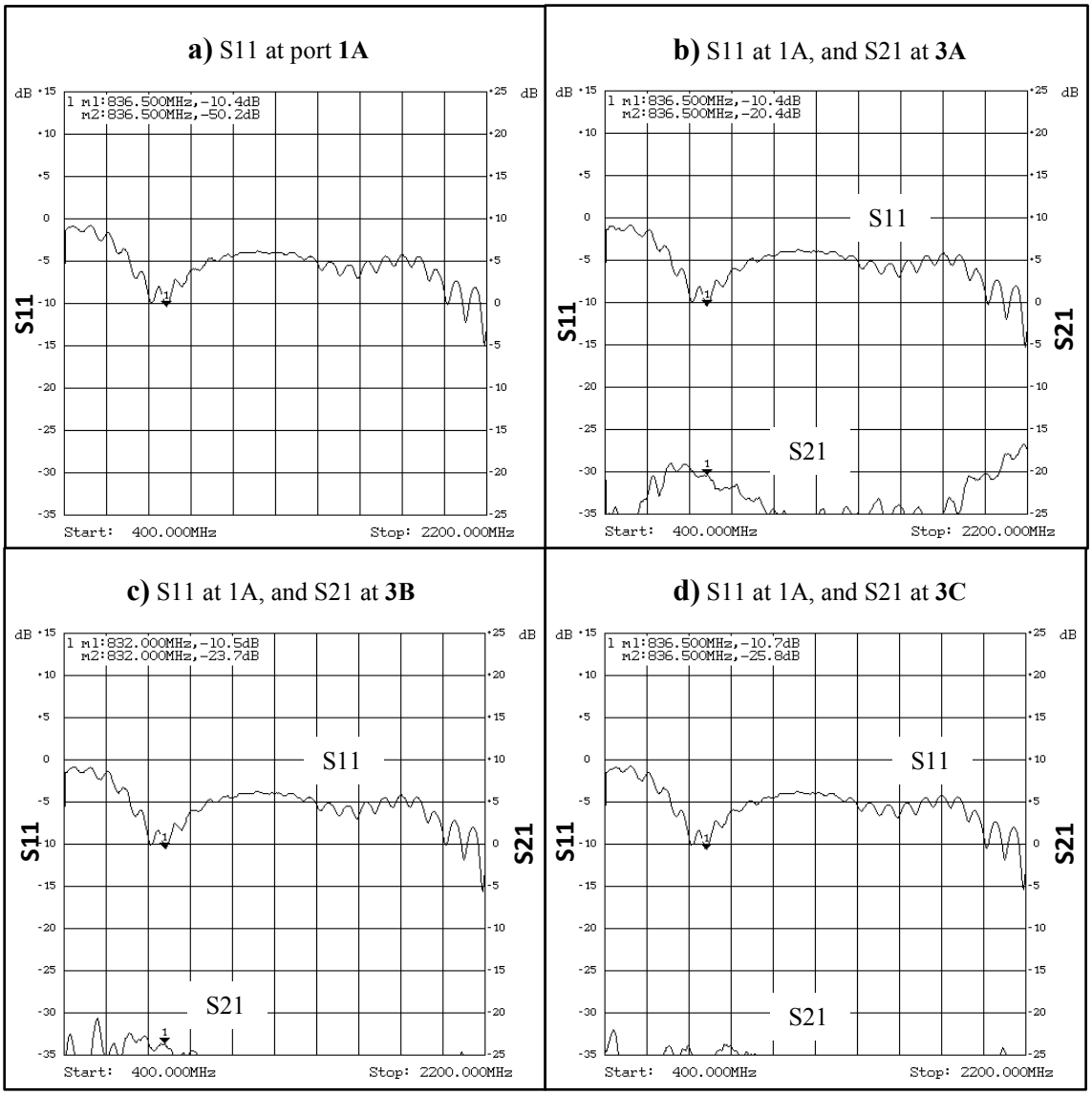

Figure 4-10 Scattering parameters S11 and S21 measured using a two port SNA2550 network analyzer between terminals 1 and 3 of the 7x7 HDT array, showing: a) S11 at port 1A, which describes the return loss; b) S11 at port 1A and S21 at port 3A, which describes both the return loss and insertion loss between the two ports; c) S11 at port 1A and S21 at port 3B; d) S11 at port 1A and S21 at port 3C. All measurements are performed for frequencies 400-2200 MHz.

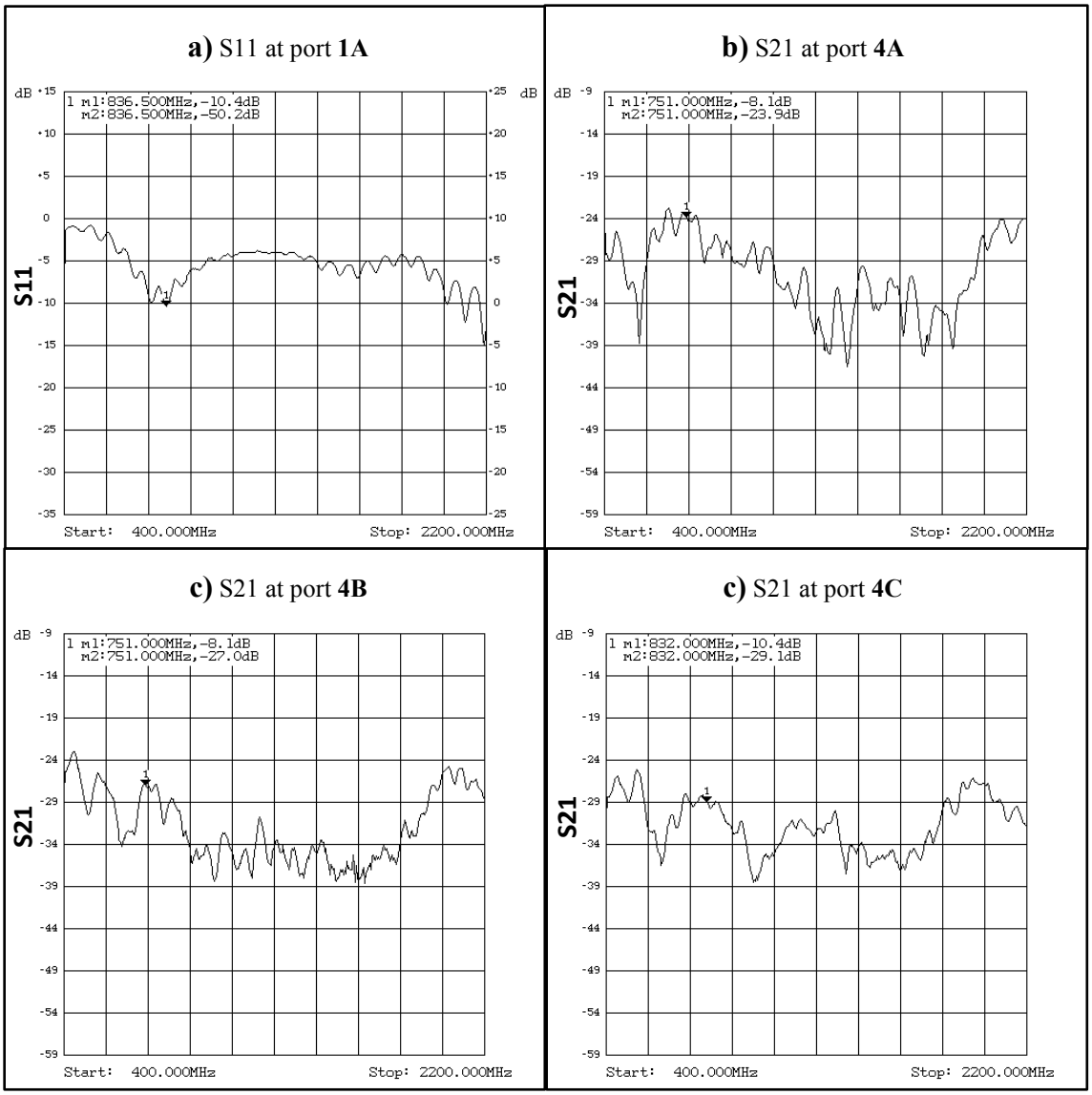

Figure 4-11 Scattering parameters S11 and S21 measured using a two port SNA2550 network analyzer between terminals 1 and 4 of the 7x7 HDT array, showing: a) S11 at port 1A; b) S21 at port 4A; c) S21 at port 4B; d) S21 at port 4C. All measurements are performed for frequencies 400-2200 MHz.

Figures 4.9-4.11 shows the scattering parameter measurements performed on the 7×7 HDT prototype array. In each Figure, a total of four graphs are displayed representing the respective scattering parameter "S11" and "S21" in dB, measured between two ports. During each measurement procedure, the reference port (excited port) was selected to be the same, being the network port **1A** as illustrated in Figure 4.8.

Results illustrate that the most critical scenario can be seen in Figure 4.9, which shows that the maximum power transfer occurs between ports 1A and 2A, being the closest equally aligned elements. For example, at ~840 MHz, Figure 4.9b shows that S21 = -9dB. This implies that if a relative power of 1 W was deliver to antenna 1A, approximately 0.126 W would be received at antenna 2A, which constitutes approximately 1/8 or 12 % of the power. Furthermore, no significant polarization cross talk would be generated, because ports 2B and 2C are induced by the same amount with S21 = -12 dB for each case, as seen in Figure 4.9b and 4.9c, which constitutes approximately 6 % of the transferred power. Furthermore, this solution clearly demonstrates the 50 %, 25 %, 25 % reception rule discussed in section 2.3.2.

For terminals 3 and 4, as shown in Figure 4.8, 4.10 and 4.11, the scattering is relatively minor with S21 = -20 dB for port 3A which constitutes transferred power of only 1 %, and S21 = -24 dB for port 4A which constitutes maximum transferred power of only 0.4%. In addition, both terminal groups 3B, 3C and 4B, 4C are induced by the same amount respectively, with total power transferred well below -24 dB.

It is important to note that the normalization impedances from this measurement study differ from those applied during the modelling calculations in chapter 3, being 70 ohm for the modelling solutions and 50 ohm for the measurement study. However, if the normalization impedances are matched, the modelling solution yields a result shown in Figure 4.12. In other words, Figure 4.12 shows the equivalent theoretical solutions of this measurement study obtained using method of moments normalized to 50 ohm.

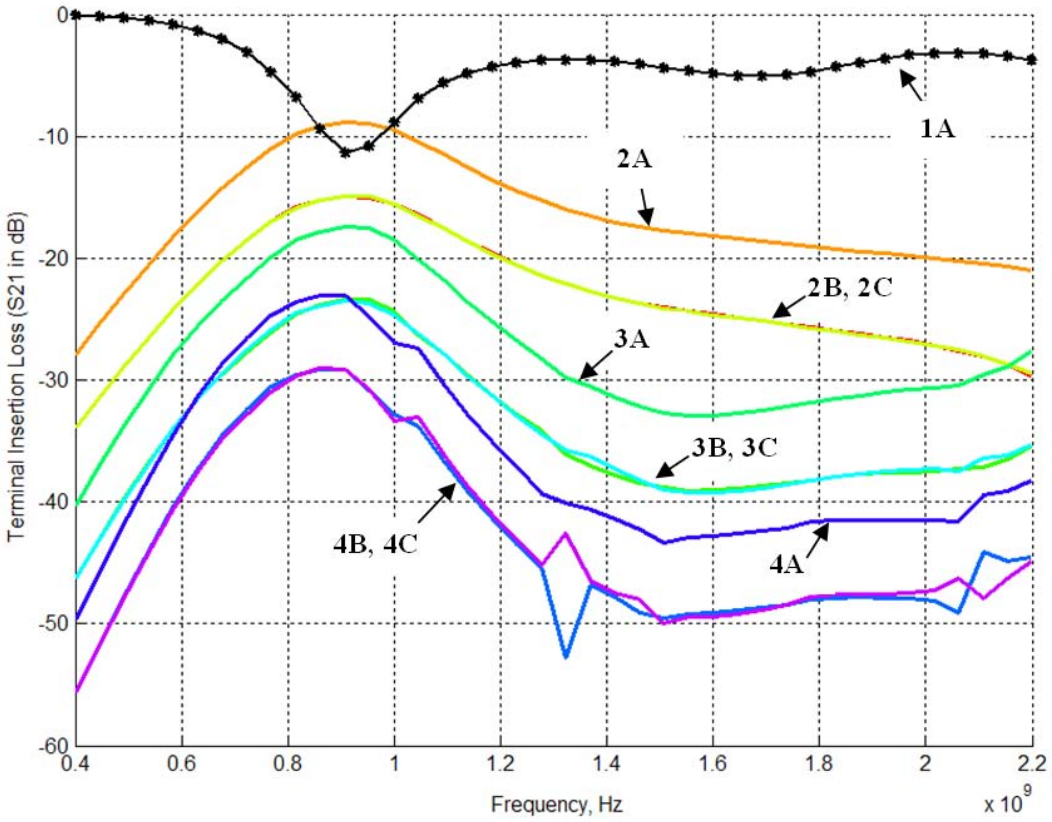

Figure 4-12 Modeled scattering parameters of the 7x7 HDT array, showing S11 in dB for port 1A, and S21 in dB for ports 2A, 2B, 2C, 3A, 3B, 3C, 4A, 4B and 4C, normalized to 50 ohm

As can be seen, the theoretical solutions in Figure 4.12 are in good agreement with the measured data obtained in Figures 4.9-4.11, except at the frequency region where additional noise is present due to the coax cable at ~ 2100 to 2200 MHz resulting from lack of proper balun circuit. It was found in this research that these differences are caused as a result of the transmission line and lack of appropriate balun circuit, as the ferrite beads used were not sufficient to cover the given frequency bands during the measurement procedure. Nonetheless, the study has shown that the measured and theoretical results are in good agreement, specifically in terms of the scattering magnitudes, which indicates that the amount of power transferred between the ports is matched between the theory and measured data.

Further testing of the FPA was limited by the available resources. The full antenna test would require design and implementation of a Type III balun as suggested by [42], integration of LNAs and testing of the prototype array in combination with the beam former and receiver as an optimized integrated unit. The ultimate goal of which would be to demonstrate acceptable efficiency, low system temperature and noise, low sidelobes and multiple beams that can be steered smoothly.

4.4 Summary

In this chapter, number of experimental measurement cases was presented for the diamond tripole antenna and the 7×7 HDT prototype array developed during the course of this study. Measurements were performed using the SNA2550 two port network analyser and include the magnitude of scattering or S-parameters, reflection and transmission coefficients between the incident and reflection waves for frequencies 400 to 2200 MHz.

The objective of this exercise was to compare the measured and theoretical data for the diamond tripole antenna and the 7×7 HDT array, outlining the scattering parameters which describe the quantity of power transferred between neighbouring elements of the array during operation. Results have shown that the measured and theoretical solutions are in good agreement. Furthermore, the scattering parameters of the 7×7 HDT array have shown to be within acceptable levels and constructive to reception of signals in a manner that conserves the polarization.

CHAPTER 5

Chapter 5 - Conclusion and Recommendations

A solution to wide bandwidth FPA receiver for reflector antennas that operates in the frequency range of 550 to 2100 MHz has been identified. Two unique design techniques, of varying size (5×5 and 7×7 arrays), were investigated utilizing the diamond planar strip antenna elements arranged to provide three vectors of polarization (triple-polarized FPA). The most promising FPA has been identified using the 7×7 Hexagonal Diamond Tripole (HDT) array designed specifically in this study. The 7×7 HDT-FPA comprises 37 planar three-axis antenna elements and yields a total of 111 individual receiving ports, providing a bandwidth ratio of 3.8:1 for frequencies 550 to 2100 MHz. While the 5×5 HDT array contains a total of 57 individual receiving ports and offers bandwidth ratio of 3.4:1 for frequencies 500 to 1700 MHz. The choice of array size, number of elements, as well as the configuration of the antenna has shown that the system provides a robust and simple-to-manufacture structure, and yields a relatively cost effective solution. It was found that varying choice of PAF size provides the possibility of increasing the upper operating frequency limit or field of view, for as long as the element spacing of the array is less than or equal to half wavelength of the upper operating frequency. It is evident that an array with larger number of elements (i.e. 7×7 HDT array) yields a better solution than the 5×5 array. However, increasing the number of elements also increases the production and operating cost of the instrument.

The preliminary FPA design procedure was carried out through a study of various antennae and array structures. The main goal was to investigate examples of a FPA system that generates extra-wide bandwidth characteristics and reduced operational cost. It was then determined that such a system was achievable if the effective area of the array was considerably increased, while at the same time, the element spacing and

number of ports was kept to a minimum. To achieve this effect, a FPA system whose elements consist of 3 polarization ports was designed, instead of 2. Antenna parameters were studied in relation to structure, shape, element size, element spacing, ground plane distance, array configuration and overall array size. These characteristics were compared against directivity, gain, polarization purity and bandwidth of the antenna. It was found that for wideband operation, some common scaled planar structures such as bowtie, spiral, square and equilateral-triangle planar antennas require that the antenna be of appropriate size and length and wide enough for operation at lower frequencies. While these structures may exhibit wideband properties, when used in arrays they generate large element spacing. It was shown that large element spacing deteriorates the gain and directivity of the array at higher frequencies which, in turn, results in reduced bandwidth. In addition, it was discovered that polarization purity of the array is highly influenced by mutual coupling between the oppositely oriented elements.

A large portion of the design work was achieved through modelling carried out using numerical computational electromagnetic methods (CEM) with fields and currents that vary in three dimensional space. The Frequency Domain Integral Equation model was used via Method of Moments (MoM) technique for simulation and modelling of the FPA utilizing surface and volume integral equations by treating the array as, both, a focal plane array and a classical phased steered array. The "Method of Moments Antenna Development Toolbox" (MoMADT), a 64 bit version of the modelling software, was developed specifically in this study by the author for building and modelling of complex antenna structures. Thus, design of the HDT-FPA was derived via modelling utilizing the MoMADT design tool. Preliminary assessment of the behaviour of the 7×7 HDT array and its elements was demonstrated through application of physical measurements. A number of experimental measurement cases was presented for the diamond tripole antenna and the 7×7 HDT prototype array developed during the course of this study. Measurements were performed using the SNA2550 two port network analyser and include the magnitude of scattering or S-parameters, reflection and transmission coefficients between the incident and reflection waves for frequencies 400 to 2200 MHz. Results have shown that the measured and theoretical data are in good agreement, while

the magnitude of the scattering measurements have revealed to be constructive to reception of signals in a manner that conserves the polarization.

The overall performance of the HDT array has been demonstrated through series of factors relating to bandwidth, directivity, efficiency, polarization and cost. It was found that the 7×7 HDT array offers an operating frequency range much larger than originally proposed for the parabolic reflectors with Phased Array Feeds (500 to 1100 MHz). This research has shown that the HDT array offers optimized efficiency and adequate impedance match. Further, it allows the polarization to be distinguished at multiple angles about the axis parallel to the antenna plane, without the need of additional mechanics to rotate the array. Appropriate modelling techniques were used to demonstrate this operation with signals polarized in X direction and X = Y direction, during which time the focal field was altered in size as function of frequency and displaced off centre as function of the FoV. It was found that polarization accuracy was achievable to within a theoretical uncertainty of ± 2.2° for the 7×7 HDT array, and ± 3.0° for the 5×5 HDT array. This is also true for any function of the FoV allowed by the surface area of the FPA.

It may be that the most important long term benefit of this research, in relation to the design of the HDT array, are the options to polarization diversity for radioastronomical observations, which provides the possibility of the system to be used for detecting and classifying circularly polarized waves based on the methods originally proposed by Kajfez [68]. However, it is concluded here that a more stringent measurements process is required in order to determine the optimal array operation and array size in combination with the receiver and low noise amplifiers as an optimized integrated unit. Further work is suggested in testing of the prototype array with addition of a rolling edge and corrugation of the ground plane and testing in combination with the beam former and the relevant electronics, the ultimate goal of which is to demonstrate acceptable efficiency, low system temperature and noise, low sidelobes and multiple beams that can be steered smoothly.

References

[1]. *The Square Kilometre Array.* **Dewdney, P. E., et al.**, Proceedings of the IEEE, August 2009, Vol. 97, pp. 1482-1496.

[2]. *Science with the Square Kilometre Array.* **Carilli, C. and Rawlings, S.,** Elsevier - New Astronomy Reviews, 2004, Vol. 48.

[3]. **Thompson, A. R., Moran, J. M. and Swenson, G. W.** *Interferometry and Aperture Synthesis in Radio Astronomy.,* Wiley, 1986.

[4]. *A measurement of excess antenna temperature at 4080 MHz.* **Penzias, A. A. and Wilson, R. W.,** Astrophysics Journal, 1965, Vol. 142, pp. 419-421.

[5]. *Standard Definitions of Terms for Antennas.* **Budnar G. D., et al.,** New York : Institute of Electrical and Electronics Engineers, 1993. IEEE Std. 145-1993.

[6]. **Kraus, J. D. and Marhefka, R. J.,** Antenna Temperature, Remote Sensing and Radar Cross Section. *Antennas: For All Applications.* New York : McGraw-Hill, 2002, pp. 401-427.

[7]. **Kouyoumjian, R. J.** [book auth.] J. D. Kraus. *Antennas: For all applications, 2nd ed.* New York : McGraw-Hill, 1988, pp. 791-797.

[8]. *Highlights of Antenna History.* **Ramsay, J.,** IEEE Antennas and Propagation Society Newsletter, 1981, Vol. 23, pp. 7-20.

[9]. **Visser, Hubregt J.** *Array and Phased Array Antenna Basics.* Chichester : John Wiley & Sons Ltd., 2005.

[10]. **Kraus, J. D. and Marhefka, R. J.** Phased Arrays. *Antennas: For All Applications 3rd ed.* New York : McGraw-Hill, 2002, pp. 572-576.

[11]. *A way to improve the field of view of the radiotelescope with a dense focal plane array.* **Ivashina, V. M. and van Anderne, A. J. D. B.,** Proc. 12th Int. Conf. Microwave and Telecomunication Technology, 2002. pp. 278-281.

[12]. *Experimental Demonstration of Focal Plane Array Beamforming in a Prototype Radiotelescope.* **Hayman, D. B., et al.,** IEEE Transactions on Antennas and Propagation, June 2010, Vol. 58.

[13]. *Focal Plane Array Architectures: Horn vs. Phase-Array Techniques.* **Veidt, B.,** International Square Kilometre Array Steering Committe, 2006. SKA Memo . Vol. 71.

[14]. *Focal plane array development for ASKAP (Australian SKA Pathfinder).* **Hay, S. G., et al.,** Edinburgh : Proc.of 2nd Euro. Conf. on Antennas and Propagation, 2007.

[15]. *Australian SKA Pathfinder: A High-Dynamic Range Wide-Field of View Survey Telescope.* **DeBoer, D., et al.,** Proceedings of the IEEE, August 2009, Vol. 97.

[16]. *Phased Array Feeds.* **Fisher, J. Richard, et al.,** The SAO/NASA Astrophysics Data System, Astro2010 Technology Development White Paper, 2009, Vol. 31.

[17]. *Summary of the second SKA Design Convergence Workshop.* **Schilizzi, R. T. and Hall, P. J.,** International SKA Project Office, 2004. SKA Memo. Vol. 53.

[18]. *Non-planar Log-periodic Antenna Feed for Integration with a Cryogenic Microwave Amplifier.* **Engargiola, G.** San Antonio Texas : in New Frontiers in Antennas and Propagation for a Wireless World, IEEE Symposium Digest, 2002.

[19]. *Decoupling Efficiency of a Wideband Vivaldi Focal Plane Array Feeding a Reflector Antenna.* **Ivashina, M. V., et al.,** IEEE Transactions on Antennas and Propagation, February 2009, Vol. 57.

[20]. *Computation of Finite Array effects in the framework of the square kilometer array project.* **Craeye, C., et al.,** Manchester : Proc. Inst. Elect. Eng. Int. Conf. on Antennas and Propagation (ICAP), 2001. Vol. 1, pp. 298-301.

[21]. *Design of a focal plane array system at Cryogenic temperatures.* **Simons, J., et al.,** Nice : Proc. Eur. Conf. on Antenna and Propagation (EuCAP), 2006. pp. 1-6.

[22]. *Apertif, a focal plane array for the WSRT in the evolution of galaxies through the neutral hydrogen window.* **Verheijen, W. M. A., et al.,** Am. Inst. Phys. Conf. Proc. series, 2008. Vol. 1035, pp. 265-271.

[23]. *Decoupling efficiency of a wideband Vivaldi focal plane array feeding a reflector.* **Ivashina, V. M., et al.,** IEEE Transactions on Antennas and Propagation, Feb 2009, Vol. 57, pp. 373-382.

[24]. *A phased-array feed demonstrator for radio telescopes.* **Veidt, B. and Dewdney, P.,** Proc. URSI General Assembly, 2005.

[25]. *The DRAO phased array feed demonstrator: Recent results.* **Veidt, B., et al.,** Banff : Proc. ANTEM Symposium, 2009. pp. 1-4.

[26]. *Beamforming and imaging with the BYU/NRAO L-Band 19-element phased array feed.* **Warnick, K. F., et al.,** Proceedings of the ANTEM/URSI International Symposium on Antenna Technology and Applied Electromagnetics, 2009.

[27]. *Encircled Power Study of Focal Plane Field for Estimating Focal Plane.* **Hayman, D. B., et al.,** Washington DC : 2005 IEEE AP-S INTERNATIONAL SYMPOSIUM, 2005.

[28]. *Australian SKA Pathfinder: A high-dynamic range wide-field of view survey telescope.* **Ball, L., et al.,** Proc. IEEE, Aug. 2009, Vol. 97, pp. 1507-1521.

[29]. *Focal plane array beam-formaing and spill-over cancellation using vivaldi antennas.* **Brisken, W. and Craeye, C.,** National Radio Astronomy Observatory, 2004. EVLA Memo. Vol. 69.

[30]. *Optimal noise matching for mutually coupled arrays.* **Warnick, K. F. and Jensen, M. A.,** IEEE Transactions on Antennas and Propagation, June 2007, Vol. 55, pp. 1726-1731.

[31]. **Munk, B. A.,** Frequency Selective Surfaces and Periodic Structures. [book auth.] J. D. Kraus and R. J. Marhefka. *Antennas: For All Applications 3rd ed.* New York : McGraw-Hill, 2002, pp. 636-658.

[32]. *Slot aerials and their relation to complementary wire aerials (Babinet's Principle).* **Booker, H. G.,** J. Inst. Electr. Eng. (IEE), 1946, pp. 620-626.

[33]. **Munk, B. A.,** *Frequency Selective Surfaces, Theory and Design.* New York : Wiley, 2000.

[34]. **Vardaxoglou, J. C.,** *Frequency Selective Surfaces.,* Research Studies Press Ltd, 1997.

[35]. **Wu, T. K.** *Frequency Selective Surface and Grid Array.* New York : Wiley, 1995.

[36]. *Scattering from Periodic Arrays of Crossed Dipoles.* **Pelton, E. L. and Munk, B. A.,** IEEE Transactions on Antennas and Propagation, May 1979, Vol. 27, pp. 323-330.

[37]. **Kraus, J. D. and J., Marhefka R.** Horizontal Antennas Above a Plane Ground. *Antennas: For All Applications 3rd ed.* New York : McGraw-Hill, 2002, pp. 555-566.

[38]. **Kraus, J. D. and J., Marhefka R.** Array of 2 driven lambda/2 elements end-fire case. *Antennas: For All Applications.* New York : McGraw-Hill, 2002, pp. 539-544.

[39]. **Kraus, J. D. and J., Marhefka R.** Vertical Antennas Above A Plane Ground. *Antennas: For All Applications.* New York : McGraw-Hill, 2002, pp. 566-570.

[40]. **Kraus, J. D. and J., Marhefka R.** Embedded Antennas. *Antennas: For All Applications.* New York : McGraw-Hill, 2002, pp. 784-785.

[41]. *Designing Embedded Antennas for Bluetooth Protocol.* **Perez, R.,** ACES Jour., November 2000, Vol. 1, pp. 152-158.

[42]. **Munk, B. A.** Baluns, etc. [book auth.] J. D. Kraus and Marhefka R. J. *Antennas: For All Applications.* New York : McGraw-Hill, 2002, pp. 803-825.

[43]. *Design of Ultra-wide band antennas using Characteristic Modes.* **Ferrando, M., et al.,** Berlin : Cost 284 Meeting, Dto. Comunicaciones, 2003.

[44]. *Theory of Characteristic Modes for Conducting Bodies.* **Harrington, R. F. and Mautz, J. R.,** IEEE Transactions on Antennas and Propagation, 1971, Vol. 19, pp. 622-628.

[45]. *Computational Electromagnetics-A review.* **Rao, S. M. and Balakrishnan, N.,** IAS - Current Science, November 1999, Vol. 77.

[46]. **Rao, S. M.** *Time Domain Electromagnetics.* New York : Academic Press, June, 1999.

[47]. *Electromagnetics: computational methods and considerations.* **Volakis, J. L. and Kempel, L. C.,** IEEE Computational Science and Engineering, 1995, Vol. 2, pp. 42-57.

[48]. *Microstrip antenna technology.* **Carver, K. R. and Mink, J. W.,** IEEE Transacitons on Antennas and Propagation, Jan 1981, Vol. 29, pp. 2-24.

[49]. *Integral equation formulation of microstrip antennas.* **Bailey, M. and Deshpande, M. D.,** IEEE Trans. Antennas Propag., July 1982, Vol. 30, pp. 651-656.

[50]. *Experimental verification of the 2-d rooftop approach for modeling microstrip patch antennas.* **York, R. A., Compton, R. C. and Rubin, B. J.,** IEEE Trans. Antennas Propag., May 1991, Vol. 39, pp. 690–694.

[51]. *Efficient prism modeling for arbitrary-shape antennas printed on finite-size dielectric substrate in efie analysis.* **Poey, P., Thiam, C. and Begaud, X.,** Microwave Opt. Technol. Lett., Apr 1998, Vol. 17, pp. 370–375.

[52]. *Electromagnetic Scattering by Mixed Conductor-Dielectric Bodies of Arbitrary Shape.* **Creticos, J. P. and Schaubert, D. H.,** IEEE Transactions on Antennas and Propagation, August 2006, Vol. 54, pp. 2402-2407.

[53]. *Improved Impedance Matrix Localization Method.* **Canning, X. F.,** IEEE Transactions on Antennas and Propagation, May 1993, Vol. 41, pp. 659-667.

[54]. *Electromagnetic scattering by surfaces of arbitrary shape.* **Rao, S. M., Wilton, D. R. and Galisson, A. W.,** IEEE Trans. Antenna and Propagation, 1982, Trans. Antennas and Propagation, Vol. 30, pp. 409-418.

[55]. *MoM antenna simulations with Matlab: RWG basis functions.* **Makarov, S. N.,** IEEE Antennas and Propagation Magazine, 2001, Vol. 43, pp. 100-107.

[56]. **Peterson, A. F., Ray, S. L. and Mittra, R.** *Computational Methods for Electromagnecits.* Piscataway : IEEE Press, 1998.

[57]. **Makarov, S. N.** *Antenna and EM Modeling with Matlab.* New York : John Wiley and Sons, Inc,, 2002.

[58]. *Triangular patch modelling of bowtie antennas: Validation against Brown and Woodward.* **Leat, C. J., Shuley, N. V. and Stickley, G. F.,** IEE Proc. Microwave Antennas Propagation, 1998, Vol. 145, pp. 465-470.

[59]. **Balanis, C. A.** *Antenna theory Analysis and Design.* New York : John Wiley and Sons, Inc., 1982.

[60]. *A tetrahedral modeling method for electromagnetic scattering by arbitrarily shaped inhomogeneous dielectric bodies.* **Schaubert, D. H., Wilton, D. R. and Glisson, A. W.,** IEEE Trans. Antennas and Propagation, January 1984, Vol. 32, pp. 77-85.

[61]. *MoM Volume Integral Equation Solution for an Isolated Metal-Dielectric Resonator With the Edge-Based Basis Functions.* **Kulkarni, S., et al.,** IEEE Transactions on Antennas and Propagation, April 2005, Vol. 53, pp. 1566-1571.

[62]. *Scattering of EM waves by inhomogeneous dielectrics with the use of the method of moments and the 3-D solenoidal basis functions.* **Carvalho, S. A. and Mendes, L. S.,** Microwave and Optical Technology Letters, October 1999, Vol. 23, pp. 42-46.

[63]. *Electromagnetic Scattering and Radiation from Finite Microstrip Structures.* **Sarkar, T. K., M., Rao S. and R., Djordjevic A.,** IEEE Transactions on Microwave Theory and Techniques, November 1990, Vol. 38, pp. 1568-1575.

[64]. **Kulkarni, S.** *MoM Modeling of Metal-Dielectric Structures via Volume Integral Equation (Master thesis).* Worcester : Worcester Polytechnic Institute, 2004.

[65]. *Recent focal plane array developments for the Australian SKA Pathfinder.* **O'Sullivan, J., et al.,** International Symposium on Microwave and Optical Technology, 2007.

[66]. *Wideband directional base-station antenna with dual-linear and circular-polarization capabilities.* **Leon-Lerma, F., et al.,** ISSC Dublin Institute of Technology, 2006. pp. 253-256.

[67]. *Electric Tripole Antenna for Circular Polarization.* **Kajfez, D., Harrison, M. G. and Sterling, C. E.,** IEEE Transactions on Antennas and Propagation, September 1974, Vol. 22, pp. 647-650.

[68]. *Three-phase seperator for Circular Polarization.* **Kajfez, D.,** IEEE Transactions on Microwave Theory and Techniques, 1969, Vol. 17, pp. 726-727.

[69]. **Stutzman, W. L.** *Antenna Theory and Design.* New York : John Wiley and Sons, 1981.

[70]. *Self-complementary antennas.* **Mushiake, Y.,** IEEE Antennas and Propagation Magazine, 1992, Vol. 34, pp. 23-29.

[71]. *Circularly polarised equilateral triangular patch array antenna for mobile satellite communications.* **Sumantyo, J. T. S. and Ito, K.,** IEE Proc.-Microw. Antennas Propag., December 2006, Vol. 153.

[72]. **Gustafsson, M.** *Broadband array antennas using a self-complementary antenna array and dielectric slabs.* Lund : Department of Electroscience Electromagnetic Theory Lund Institute of Technology Sweden, 2004. LUTEDX/(TEAT-7129).

[73]. *Pattern Synthesis of Sparse Phased Array Antenna Using Genetic Algorithms.* **Han, R.,** Modern Applied Science, September 2009, Vol. 3, pp. 91-94.

[74]. *A broadband stripline array element.* **Lewis, L. R., Fasset, M. and Hunt, J.,** IEEE Ant. and Prop. Sym., 1974. pp. 335-337.

[75]. **Schaubert, D. H. and Chio, T.** *Wideband Vivaldi Arrays for Large Aperture Antennas.* s.l. : Netherlands Foundation for Res. in Astronomy, 1999.

[76]. **Harrington, Roger F.** *Field Computation by Method of Moments.* New York : IEEE Press, 1993.

[77]. **Kraus, J. D.** *Antennas.* New York : McGraw Hill, 1950.

[78]. **Pozar, David M.** *Mocrowave Engineering 2nd Ed.* New York : John Wiley and Sons, Inc., 1998.

[79]. **Stratton, J. A.** *Electromagnetic theory.* New York : IEEE Press, McGraw-Hill, 1941.

[80]. **Chandran, S.** *Adaptive Antenna Arrays.* Berlin : Springer, 2004.

[81]. **Kraus, J. D. and Marhefka, R. J.** *Antennas: For All Applications, 3rd ed.* New York : McGraw-Hill, 2002. pp. 401-429.

APPENDIX A

Appendix A - MoMADT Software

In this section of the thesis, the Method of Moments Antenna Development Toolbox (MoMADT) software developed during the course of this study is discussed. Several fundamental operations are explained relating to the construction and modelling of antenna and array structures. In addition, details behind the modelling processes of phases, for one and two dimensional arrays, are also presented. Following this, the proof of concept for the MoMADT is revealed through comparison with Ansoft HFSS software.

A.1 Introduction

MoMADT software was developed under Matlab and C++ as part of the research work by the author and collaboration work with the antenna research group from Worcester Polytechnic Institute (WPI), Massachusetts. MoMADT is a 64bit application used for designing, building and modelling of EM and antenna structures. MoMADT currently contains two unique MoM solvers which can be accessed from within the MoMADT main interface (see Figure A.1). These solvers are termed as "MoM2D" and "MoM3D".

The "MoM2D" solver calculates method of moments solutions using surface integrals only on structures that consist of conductive surfaces. These structures may be 2-dimensional or 3-dimensional in nature, but do not contain dielectrics (dielectrics are ignored). Theory used within the MoM2D solver is described in section 1.10.1 of this dissertation.

The "MoM3D" solver, on the other hand, calculates combined volume and surface elements that include antenna/EM structures with metallic and dielectric materials combined, such as patch antennas, dielectric resonators or antennas with dielectric layers. These objects are generally referred to as mixed conductor-dielectric (MCD) resonators.

Analysis of electromagnetic scattering by MCD resonators has applications in a variety of areas including conformal antennas, radome covered antennas, planar microstrip and stripline antennas and radar cross section prediction. Of the various subclasses of conductor-dielectric problems, planar microstrip and stripline antennas have received the most attention in modelling technique development [48], [49], [50], [51]. Modelling of the combined conductor-dielectric objects are typically performed using the finite element method (FEM), the finite-difference time-domain method (FDTD), and the method of moments (MoM). Of the three methods, the MoM is the only one free of the requirement that the modelling environment be closed, either naturally or artificially [52]. The piecewise-constant edge basis function used within the MoM3D was employed as described by [61], [62]. These basis functions form a full vector basis on volume tetrahedral meshes with a continuous normal component while at the same time they form a subset of the SWG basis functions [60] that do not possess the artificial volume charges. As a result, the number of these edge basis functions is considerably reduced. For these basis functions, the tangential electric field for all tetrahedra in contact with metal faces is set to zero [61], to ensure continuity. This tangential field is then eliminated from the VIE, using a projection operation performed on the original equation. However, the normal field for tetrahedra in contact with metal faces is retained as required by the boundary condition [61]. This operation is simple but yields effective method to improve the convergence rate. Full theoretical derivation of the MoMADT is presented in section 1.10.1-1.10.3 of this dissertation.

One of many useful features in MoMADT is the development of the parameterized “2D Object generator” (2DOG). 2DOG initializes parameterized objects in Mesh Generator application to provide functions for building accurate triangular meshes (or two

dimensional projections of tetrahedral meshes) for any given 2D structure initialized using 2DOG, which is an important and integral part of generating method of moments solutions (see section 1.10.1-1.10.3 for more information). The Mesh Generator function utilizes number of command line functions that are similar to Matlab's PDE toolbox to generate a mesh and characterize the boundary conditions of objects, such as initmesh, decsg, jigglemesh, however, the Mesh Generator itself is a standalone distinct application and does not require nor depend on PDE toolbox.

Numerous types of 2D objects, including parametric objects, can be initialized with 2DOG and Mesh Generator application and can be assembled in an array formation. Most importantly, all structures initialized in Mesh Generator are done so with accurately displaced and precise dimensions. These objects are subsequently used for building antennas, EM structures or resonators on to which MoM solutions can be applied. The mesh data is extracted directly from memory into MoMADT interface and 3D structures such as patch antennas, antennas with dielectric layers or arrays can be created. Any structure created with MoMADT can be modified in various ways and settings.

MoMADT provides number of advanced functions for modifying and editing antenna and EM structures. For example, the “3D+” option found within MoMADT interface (see Figure A.1) enables any 2D or 3D structure to be reconfigured in a conical, concave, convex or hyperboloid arrangement. Separate layers within an existing structure can be reconfigured in separate ways. The user may also combine separate antenna components or include a ground plane or a reflector antenna. These configurations, including those consisting of dielectric components, can be assembled in an array discretely with axial, skewed or circular formations. This option is useful for creating antenna arrays or phased array systems and can be accessed via the “ARRAY” function from within the MoMADT interface. The work on MoMADT and its solvers is ongoing as part of the research by the author.

A.2 Interface

MoMADT interface consists of several function buttons and a workspace figure window, the main goal of which is to provide functions to build a desired EM structure and to apply a desired solver. The function buttons are therefore arranged in groups (see Figure A.1). Function buttons under "**Build structures**" group, are solely used for designing and building antenna or EM structures. These functions grant the ability to accurately define, generate and mesh the given structure and specify the structure attributes such as the feed, relative permittivity, dielectric loss tangent and other necessary antenna characteristics.

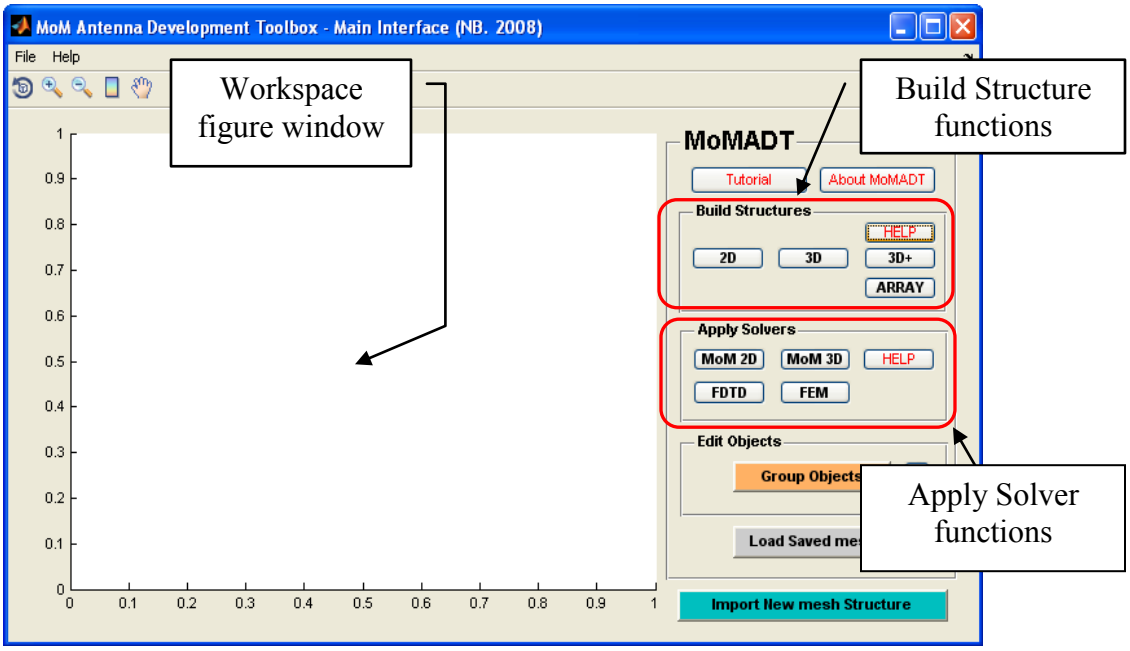

Figure A- 1 MoMADT main interface

"**Apply solver**" functions are used for applying the necessary calculations on the given structure and obtaining the necessary EM solutions. As mentioned above two unique method of moment solvers are available in MoMADT, called MoM2D and MoM3D.

A.3 2D Object Generator

The primary process of building antenna structures is initialized by opening a utility called the "2D Object Generator" (2DOG) from within the "Build Structure" functions of the MoMADT interface. This function is used for building a two dimensional antenna structures or a 3D projection. A 3D projection is a method of mapping three-dimensional points to a two-dimensional plane. This process allows the user to accurately define the feed components, the mesh type and assign the number of objects that may exist in the same plane, or in a layer formation.

2DOG draws 2D objects in “Mesh Generator” application, which provides the ability for creating diverse structures with accurately displaced and precise dimensions (see Figure A.2)

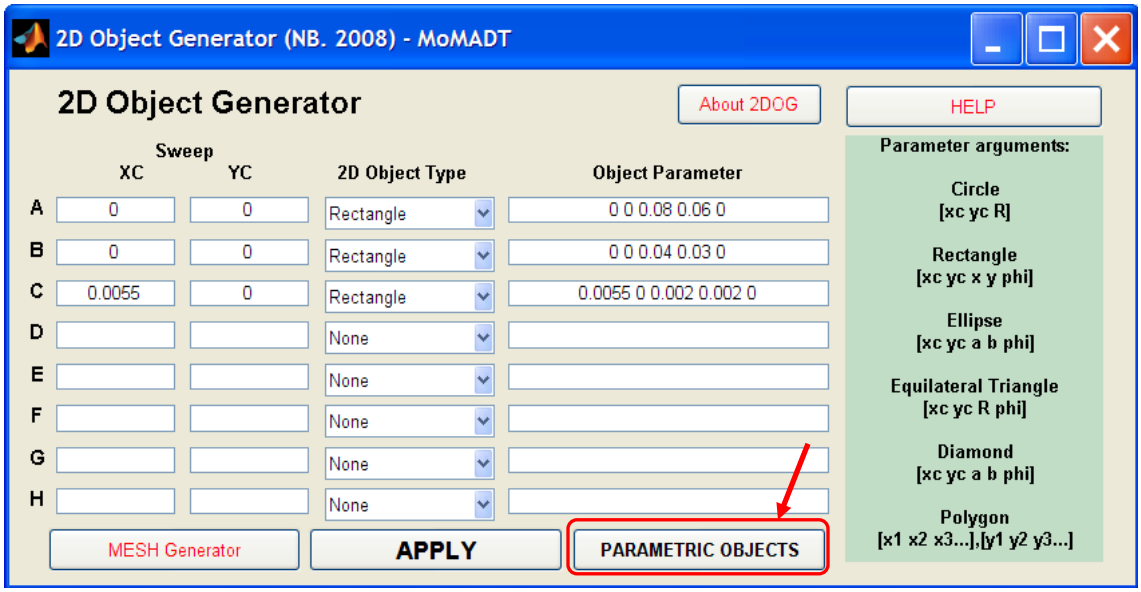

Figure A- 2 2D Object Generator

2DOG also offers a function for initializing **Parametric Objects**. These objects are surfaces bound by parametric curves and this feature is available via the “Parametric Objects” function within the 2DOG interface (see Figure A.2). Parametric objects button

opens a new interface for initializing parametric objects in Mesh Generator application (see Figure A.3).

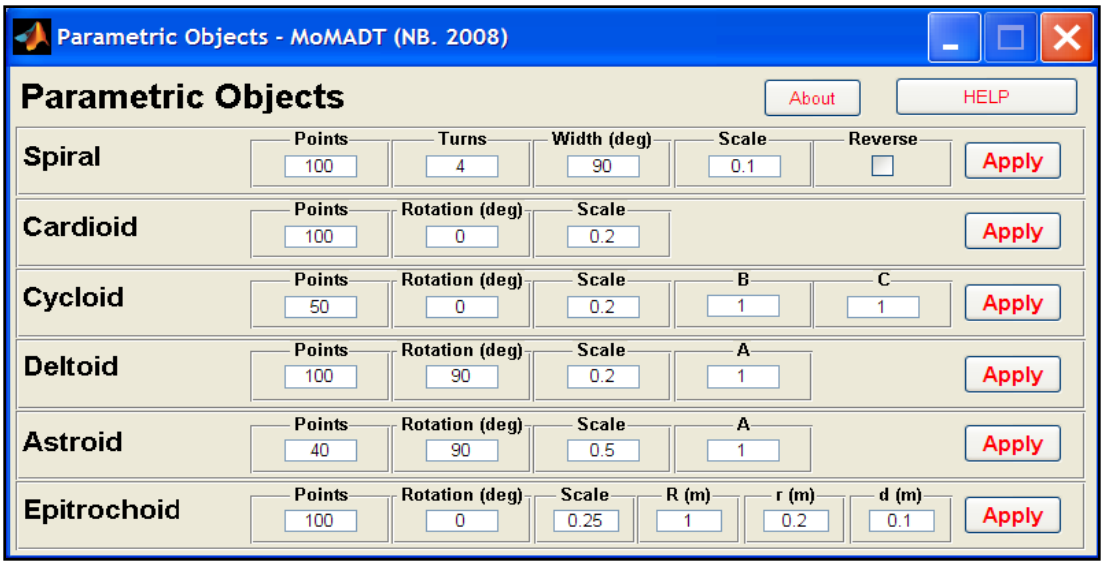

Figure A- 3 Interface for creating Parametric Objects

The Parametric Objects interface (Figure A.3) offers several parametric objects to be initialized in Mesh Generator, given as Spiral, Cardioid, Cycloid, Deltoid, Astroid, and Epitrochoid. Each of the parametric objects is supplied with default base values which can be modified by the user. Modification of these values will customize the function in various ways to yield a variety of surfaces. In order to clarify the meaning of some of these operations, we will present an example for generating a Spiral antenna and a Conical spiral antenna array in the subsequent sections.

A.4 Example1: Spiral and Conical Spiral Antenna

In this section, an example for generating an Archimedean spiral and conical Archimedean spiral antennas is presented. The spiral antenna is etched onto a dielectric substrate with centre feed. These examples follow some preliminary designs carried out during the course of this study, using references [59] and [69].

The Spiral object is constructed using an equation for Archimedes spiral curve. The Parametric function draws two curves and closes them to create a surface strip. The width of the strip is governed by the offset angle between the two spiral curves, as illustrated in Figure A.4. The "**Width**" for the spiral is therefore given in degrees as shown in Figure A.3, default being 90°. The "**Turns**" parameter for the spiral governs the number of turn of the spiral and its default is 4 turns. The "**Scale**" parameter, on the other hand, scales the size of the original object, in this case the spiral whose maximum radial distance is always 2π (m) regardless of the number of turns (provided that Scale = 1). Thus, if scale is given by some value S, the resulting maximum radial distance of the spiral will become $S \times 2\pi$ (m). The "**Points**" parameter for the Spiral in Figure A.3 specifies the resolution of the object, in this case the spiral. These parameters can in turn affect the mesh resolution when applying Delaunay triangulation in Mesh Generator.

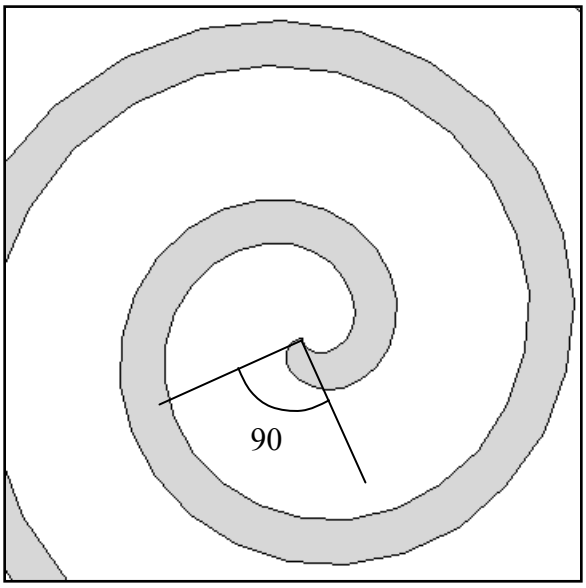

Figure A- 4 Archimedes spiral object drawn using MoMADT

For this example, we wish to create an Archimedes spiral antenna with maximum radial distance of 0.1 m and a centre feed, etched onto a dielectric substrate. As a result, we must generate 2 spiral strips that are reversely proportional with respect to each other. This can be achieved by selecting the "**Reverse**" checkbox when drawing the second spiral strip as seen in Figure A.3. When appropriate spiral parameters are specified the

Parametric function immediately draws the selected objects in Mesh Generator, as shown in Figure A.5.

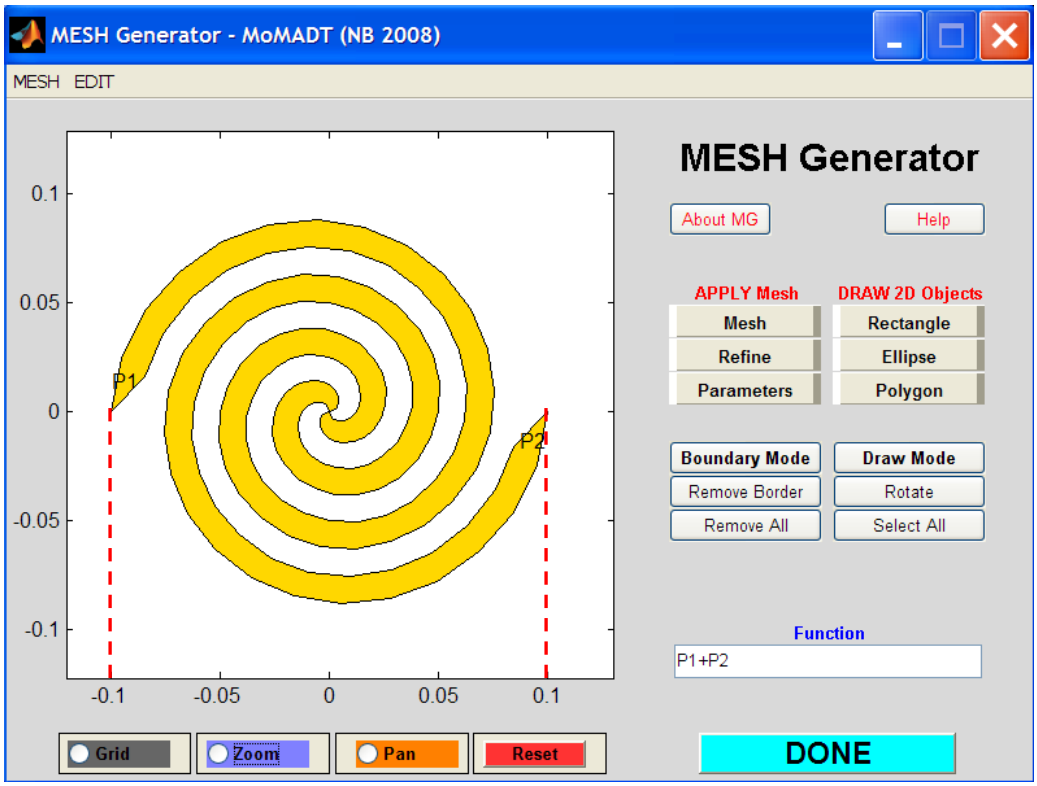

Figure A- 5 Two Archimedean spiral objects drawn in Mesh Generator

The resulting object in Figure A.5 is a self complementary Archimedean spiral. However, in order to simulate an Archimedean spiral antenna printed onto a dielectric substrate we need to add an additional object to represent the edge of the substrate layer. It is probably most ideal to chose a Circular object with R=0.11 m. We can initialize this object using the standard "2D Object Generator" Circle function, or we can use the Epitrochoid function from within the Parametric interface. In either case a circular object is drawn around the existing spiral objects, in which the Mesh Generator can be finally used to initialize a discretized mesh using a process called Delaunay triangulation, as shown in Figure A.6. Upon executing the mesh, the "DONE" button will immediately import the newly generated structure into MoMADT workspace figure window, as shown in Figure A.7.

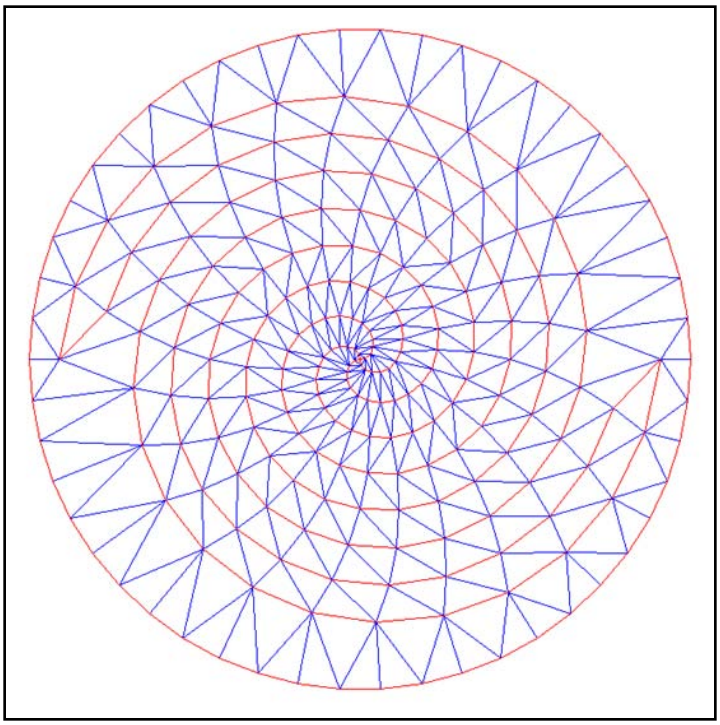

Figure A- 6 Discretized 3D projection of an Archimedian spiral antenna

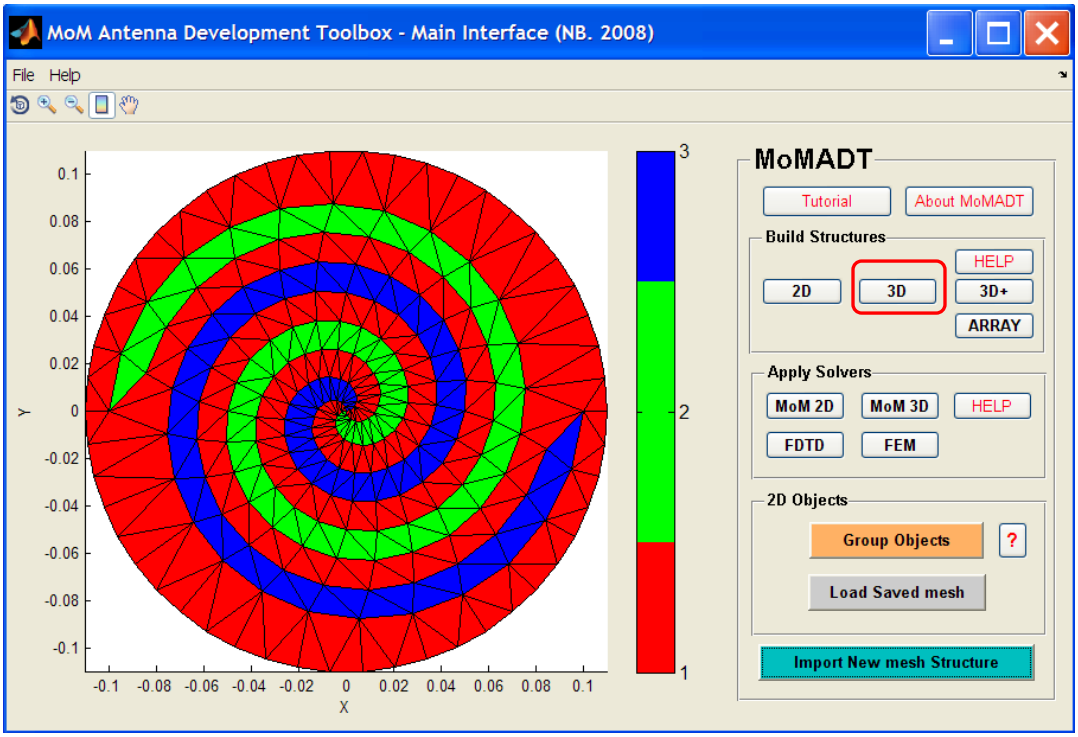

Figure A- 7 Discretized 3D projection of an Archimedian spiral antenna

At this stage, MoMADT can be used to further modify this object in order to select the dielectric and metallic components and transform the object into a volumetric mesh using a process called Delaunay tessellation. This procedure is initialized via the "3D" button from within the MoMADT interface, as shown in Figure A.7. The "3D" function enables the user to convert any two dimensional structure into a three dimensional object in order to specify the relative permittivity, dielectric loss tangent of the dielectric substrate, as well as the feed edges and termination edges, if any exist. Once the objects are converted the appropriate method of moments solver can be applied. The final Archimedean Spiral antenna structure is shown in Figure A.8.

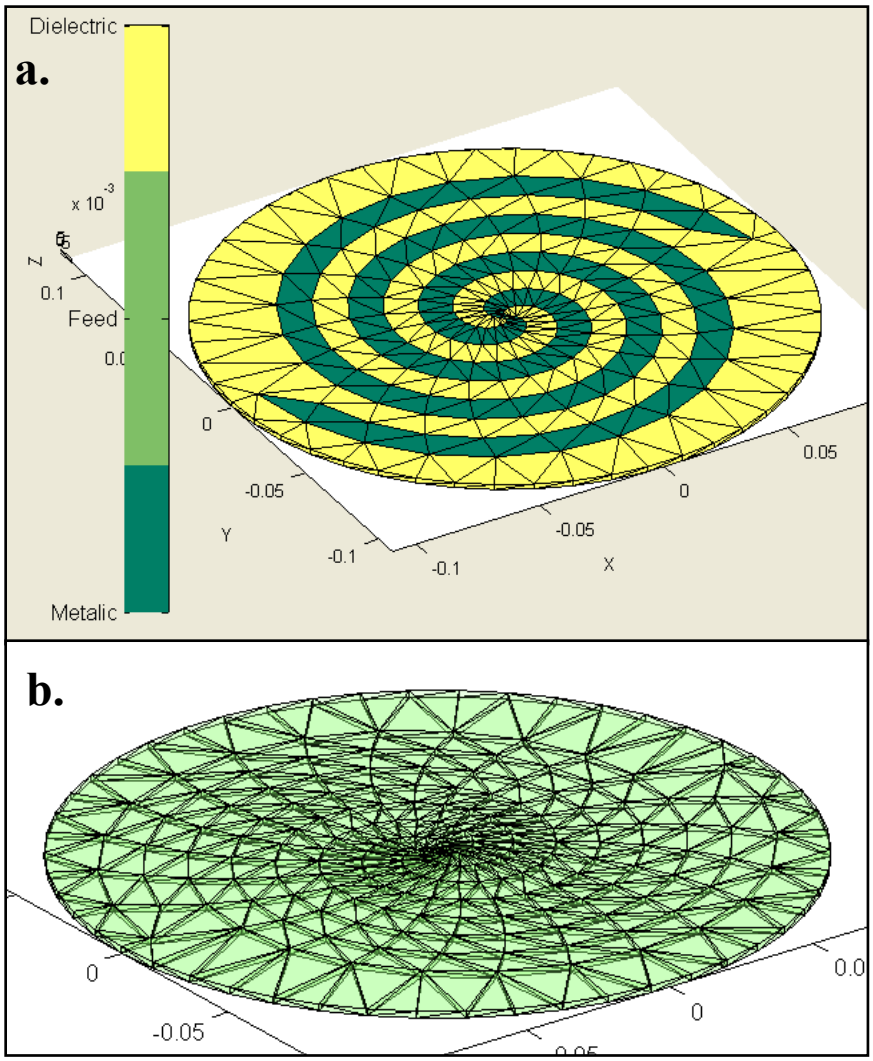

Figure A- 8 Completed Archimedean spiral antenna showing : a) Metallic and dielectric components, and b) Dielectric substrate layer - tetrahedra

To illustrate some additional operations of the MoMADT design tool, the above Archimedean spiral antenna can also be converted into a conical spiral antenna using the "3D+" function found within the MoMADT main interface (see, Figure A.9). As mentioned previously the “3D+” function enables any 2D or 3D structure to be reconfigured in a conical, concave, convex or hyperboloid arrangement.

Figure A.9 shows the conical spiral antenna created using the 3D+ Editor function and Figure A.10 shows the resulting MoM3D solution performed on the given structure, showing resistance as function of frequency (red line), and reactance as function of frequency (blue line). We can see that the modelling solution for the conical spiral antenna shows that the input impedance becomes very flat when frequency exceeds approximately 0.5 GHz. This input resistance varies around 188.5 Ω, which agrees with the theoretical prediction for self complementary structures.

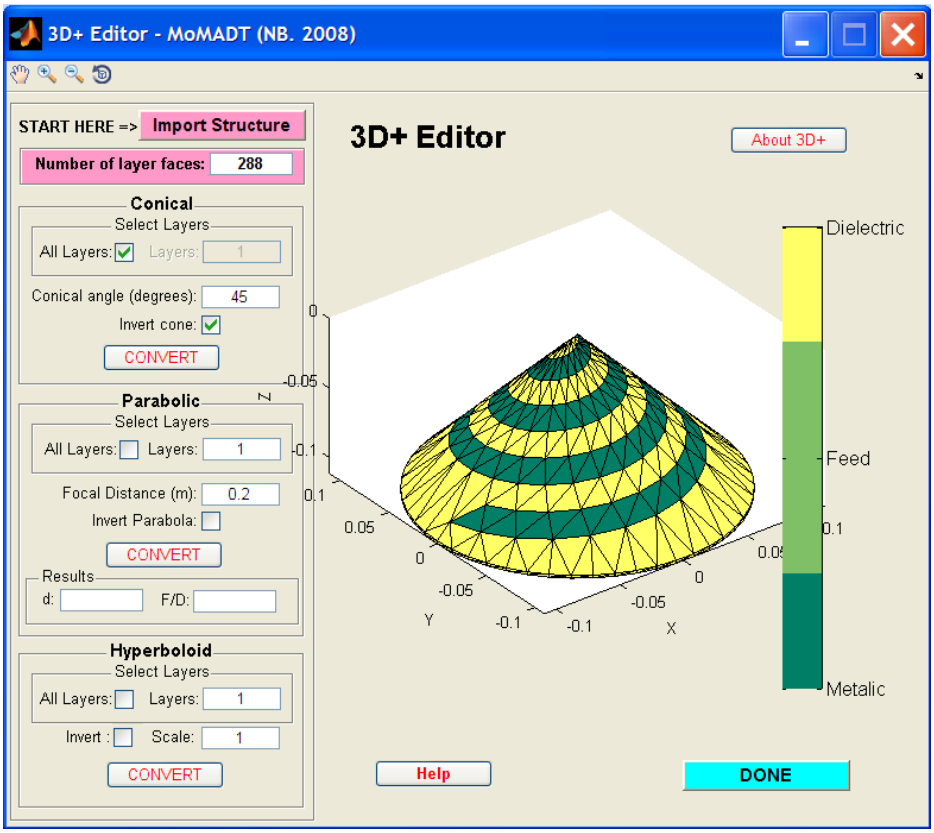

Figure A- 9 Conical spiral antenna created using the 3D+ Editor function

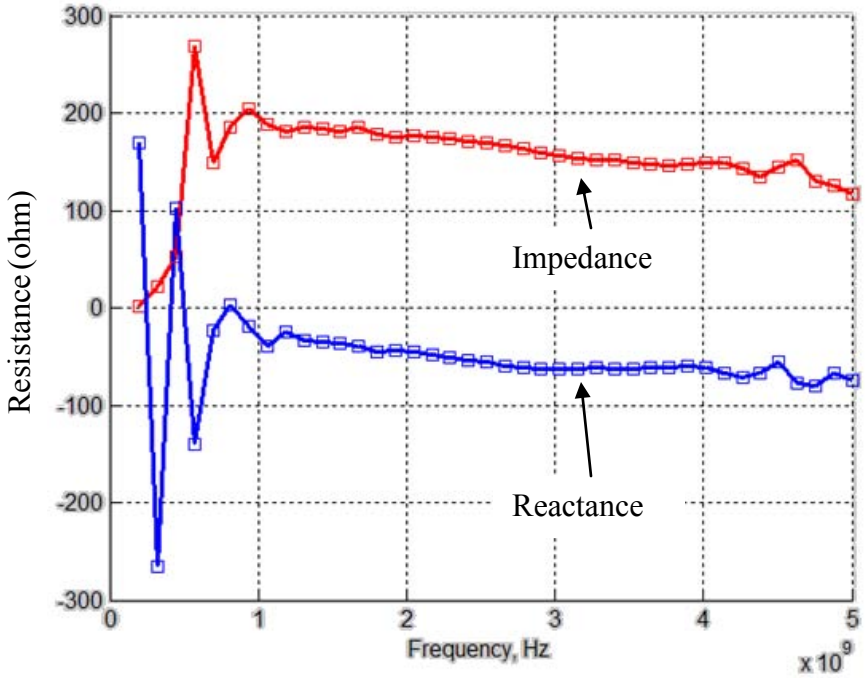

Figure A- 10 Impedance vs frequency solution for the conical spiral antenna using the MoM3D solver

A.5 The Array Editor

In addition to modifying antenna structures via the 3D+ function, the MoMADT enables the user to construct an "array" of antenna element using the "ARRAY" Editor function found within the MoMADT interface (see Figure A.11).

Figure A.11 shows the function description and Table A.1 shows the parameter accessibility of the ARRAY Editor. As can be seen, the ARRAY Editor consists of several parameter functions and a workspace figure window. The parameter functions describe all parameters that can be specified by the user. The input parameters are classified in groups as Array type, Array size, Element Spacing, Element Orientation and the Ground Plane functions (see Figure A.11).

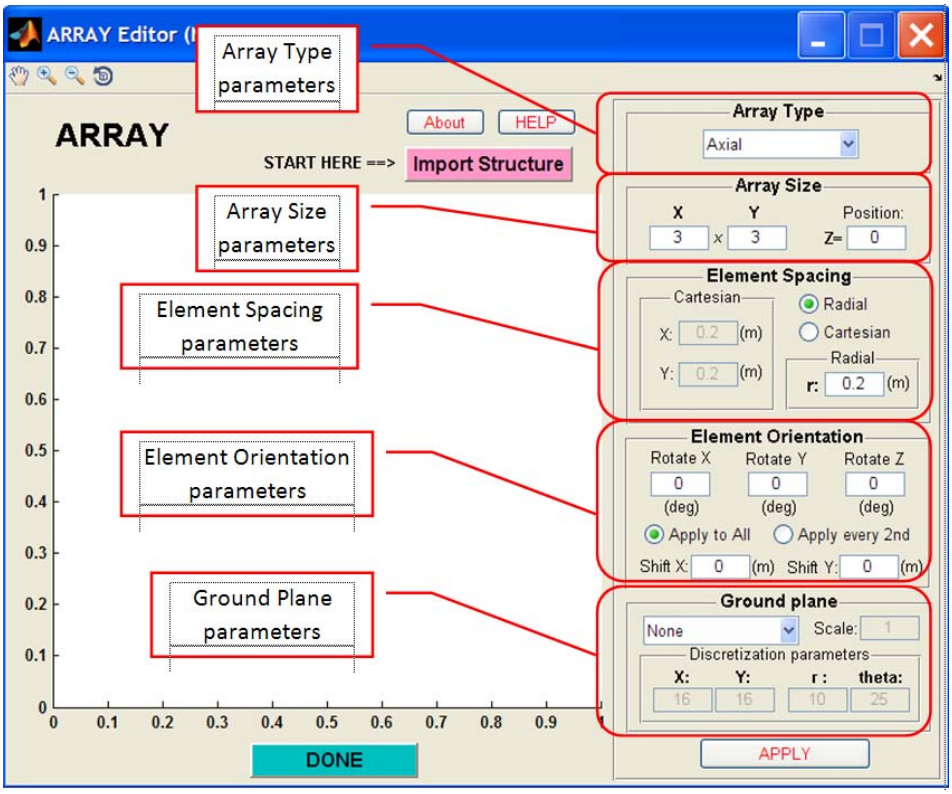

Figure A- 11 Array Editor function for building antenna arrays or phased array antenna structures

Table A- 1 Array Editor parameters

Parameters	**Array Type**		
	Axial	**Skewed**	**Circular**
Array Size	**X × Y** Any variation of array size is possible. Eg. 1x2, 2x2, 3x3, 4x2, 8x1, 10x5, 12x14... etc.	**X × Y** Only odd number of equal **X** x **Y** dimensions is possible. Eg. 1x1, 3x3, 5x5, 7x7, 9x9...etc.	**R** × **theta.** **r** = number of circles. **theta** = number of elements around the 1st circle. Eg. 1x2, 1x3, 1x4, 2x2, 2x7, 3x5...etc.
Element spacing	Both radial and Cartesian element spacing is possible.	Both radial and Cartesian element spacing is possible.	Both radial and Cartesian element spacing is possible.
Element Orientation	Any variation is possible	Any variation is possible	Any variation is possible
Ground Plane	Any Ground-plane is possible	Any Ground-plane is possible	Any Ground-plane is possible

The “ARRAY" Editor enables the user to modify any 2D, 3D, 3D+ or even an existing ARRAY structure into a new array. This function works for elements that consist of dielectric, pure metallic components or a combination of either properties. The ARRAY Editor immediately recognises the structure type and clones the elements according to input parameters specified by the user. In addition, the ARRAY Editor function can also be used to modify a single element, such as the element orientation or attach a ground plane, a conductive layer or additional objects to a single structure. The user can also create a unique cluster of array elements, by creating an array of the structure that is already in an array formation.

Three types of array structures can be generated using the ARRAY Editor given as Axial, Skewed and Circular. However an even larger range of array formations is possible by exploiting the Shift X and Shift Y variables, as well as the ability to import existing arrays. The ARRAY application is extremely useful for creating antenna arrays as it allows the user to assign the element orientation, type of element spacing, array size, and attach additional objects, and a ground plane as either a square plate, circular plate or hexagonal plate, at some position and scale size specified by the user.

Table A.1 shows the category of array parameters possible with each Array Type. For example, with **axial array** the user can specify any variation of array dimension given by X × Y, where X is the number of elements in the X-axis and Y is the number of elements in the Y-axis. **Axial array** is therefore a rectangular planar array. The position given by Z= 0 (default) is the end location of the array plane in Z-axis. Both Radial and Cartesian element spacing are possible with the Axial array as well as any variation of element orientation (including the shift feature) and ground plane. These options enable the user to arrange the elements in various formations, orientations and settings.

Skewed array, on the other hand, can only have an odd number of X and Y dimensions. Skewed array is a hexagonal shape planar array with offset element positions, as a result only odd numbers of equal dimensions are possible. However one can change the X and Y element spacing since both Radial and Cartesian element spacing is possible. In

addition, a range of orientation parameters can also be specified such as Shift X and Shift Y.

Circular array dimension parameters are given by "r" and "theta". As explained in Table A.1, "r" represents the number of circles and "theta' represents number of elements around the first circle. If say r = 3, and theta = 5, then the first circle will have 5 elements, the 2nd circle will have 10 and 3rd circle will have 15 elements, a total of 30 elements will be present in a 3x5 circular arrangement array.

In the case of dielectric resonators the generation of arrays is not a straight forward process of cloning, since the metallic and tetrahedral faces need to be appropriately reassembled in a given order as well as the basis functions recalculated for any new given structure. The Array Editor thus enables us to perform these modifications.

A.6 Example2: Conical Spiral Phased Antenna Array

In this section we will illustrate an example for creating a conical spiral antenna array using the ARRAY Editor, and will explain some basic operations of phase steering for two dimensional arrays using the MoM2D solver. This example follows on from the conical spiral structures created in section A.3.

In order to create an array of conical spiral antennas the ARRAY Editor was used with parameters illustrated in Figure A.12. The element spacing of the array structure was selected randomly (0.25 m) because we wish to observe the behaviour of this array for a range of frequencies. However, the element spacing is generally an important aspect of any array design and is selected precisely for a chosen frequency range and beamwidth.

When this array is complete as seen in Figure A.12, we can immediately proceed to apply the MoM2D solver. The MoM2D solver is initiated by selecting the "MoM2D" button from within the MoMADT main interface (see section A.2 for more information).

Note how the structure in Figure A.12 contains dielectric components beneath each of the spiral elements, this dielectric medium will be ignored by the MoM2D solver and the structure will be treated as though it contains only the metallic components (which is fine with us). When the MoM2D solver is initiated, we must first specify the structure type and feed edges.

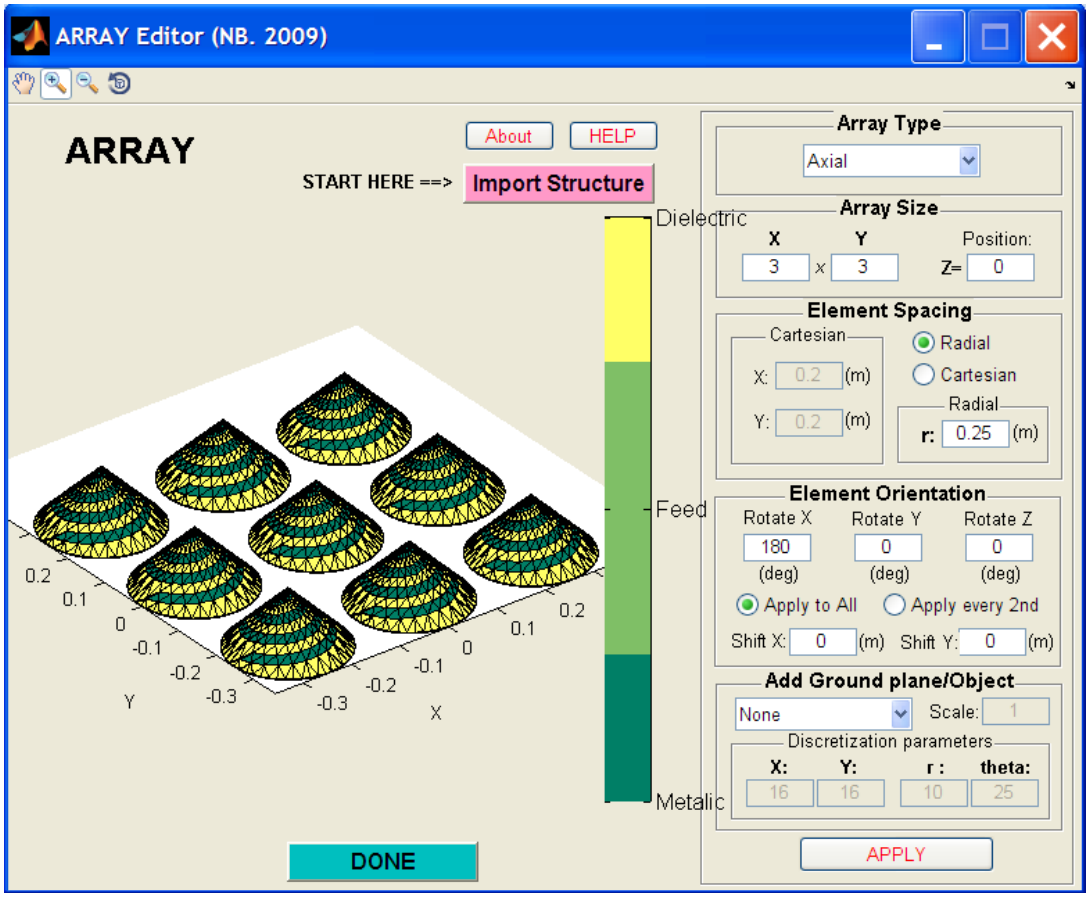

Figure A- 12 Conical spiral antenna array created using the Array editor

The process for selecting the feed edges for our conical planar array is shown in Figure A.13. For this step, the user is required to "Zoom in" to the feed region of each element and manually select the required feed edge with the mouse pointer. The user can also rotate the image to make sure that the selected feed edges are indeed correct. When this operation is complete, the user must click "DONE" button at the interface in Figure

A.13. This process immediately saves the feed edges in the original structure file, and prompts the MoM2D solver to begin calculations.

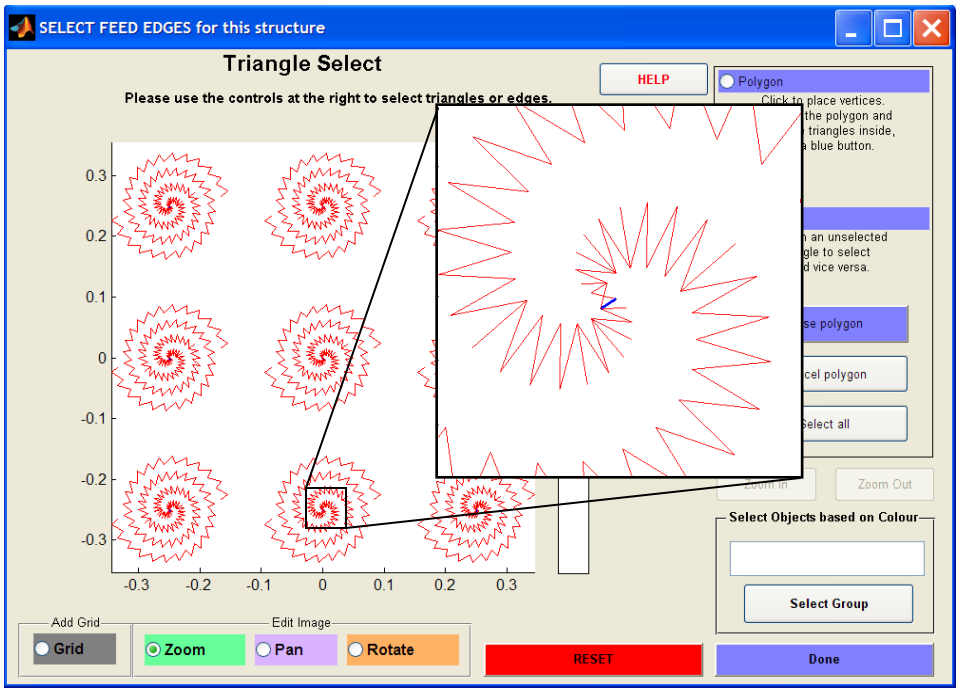

Figure A- 13 Selecting feed edges for the conical spiral array

The next step requires the user to specify the MoM2D solver parameters (see Figure A.14).

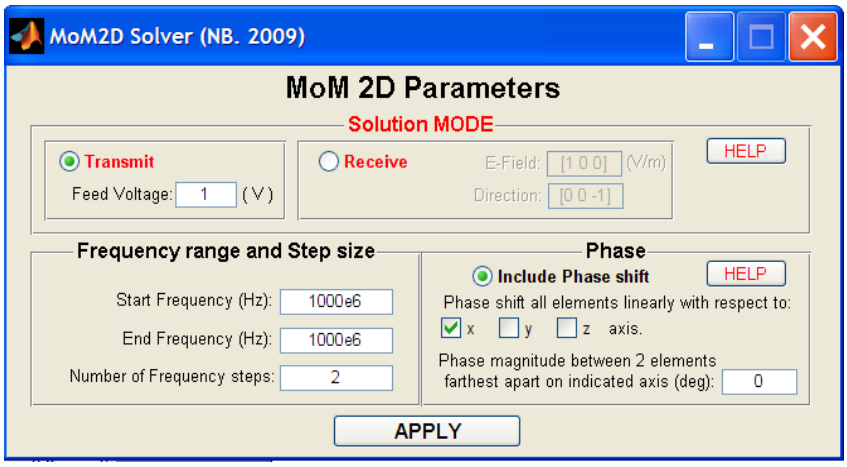

Figure A- 14 MoM2D solver Parameters interface

We will perform several solutions for this array at 1000 MHz in the transmit mode by varying the phases between all elements of the array. When phase alterations between elements of the array are specified, the calculations are obtained as shown in Figure A.15.

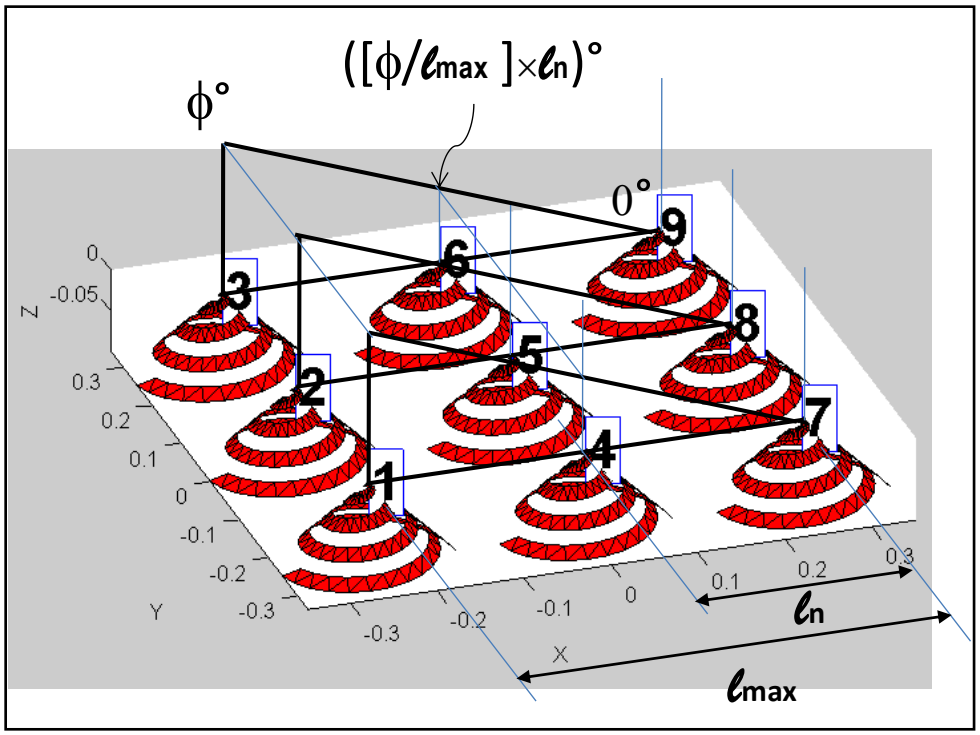

Figure A- 15 Calculation of phase difference between the respective elements of the 3×3 conical spiral array

Figure A.15 shows the calculation processes undertaken when the phase is applied in X-axis. If the phase between two elements farthest apart on the indicated axis is given by some value Φ, then the synchronized phase of the remaining elements in between (if any exist) is automatically calculated by the MoM2D solver using the following equation:

$$([\phi/\ell_{max}]\times\ell_n)^\circ . \tag{A.1}$$

We can also rotate the array about the Z-axis, using the ARRAY Editor, and perform phase calculations along any line of the array plane. However, for now we wish to

generate a radiation pattern and radiated field solutions at 1000 MHz by varying the phase from 0° to 270° between elements farthest apart along the X- axis. Note that the element spacing for this 3x3 conical spiral array was selected to be 0.25 m along the X and Y axis, which yields 0.353 m diagonally.

Figure A.16 shows the radiation pattern and radiated field of the conical spiral array at 1000 MHz by varying the phase from 0° - 270° along the x-axis. The phase "Φ" in Figures A.16 indicates the applied phase shift between elements furthest apart in X-axis as illustrated in Figure A.15.

It is important to note that all phases performed with the MoM2D solver are applied in the frequency domain and are relative to the frequency. This means that the pattern displacement (or pattern shift) is therefore much greater with the solutions performed in the lower frequency. This is expected because the time delay for phase change in each frequency is dissimilar due to the difference in the wavelength of the signal. In practice, phases are generally applied in time domain, where all signals between elements are delayed with equal time for all frequencies. These delays are most commonly produced electronically using analog phase shifters or using analog delay lines. Recent studies have also shown that it is possible to perform time delays digitally using high speed ADCs called digital beam-formers such as field programmable gate arrays (FPGA).

It is often useful to observe the radiation pattern directed in the same point in space for two or more frequencies. We can calculate analytically the phases required for two frequencies to produce the same pattern displacement (or the same pattern shift). This can be achieved using the following equation:

$$\frac{phase(A)}{A} = \frac{phase(B)}{B}, \tag{A.2}$$

where A and B are frequencies and phase (A) and phase (B) are the relative phases applied for each frequency using the MoM2D solver.

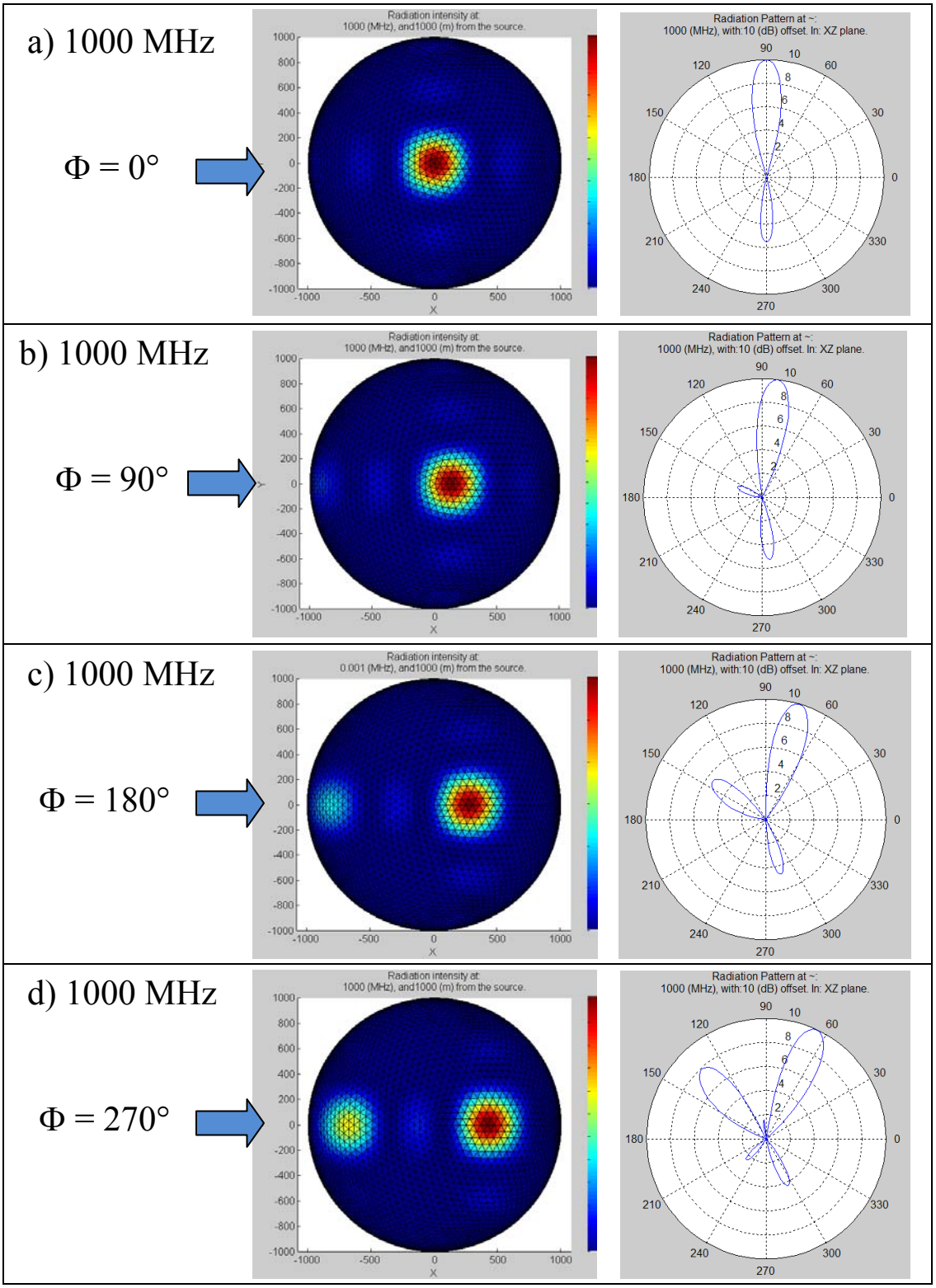

Figure A- 16 Radiation pattern of the 3×3 conical spiral array with phase alterations between 0-270°

Figure A.17 shows the radiation pattern of the 3×3 conical spiral array at 750 MHz and 180° phase difference between the outermost elements of the array.

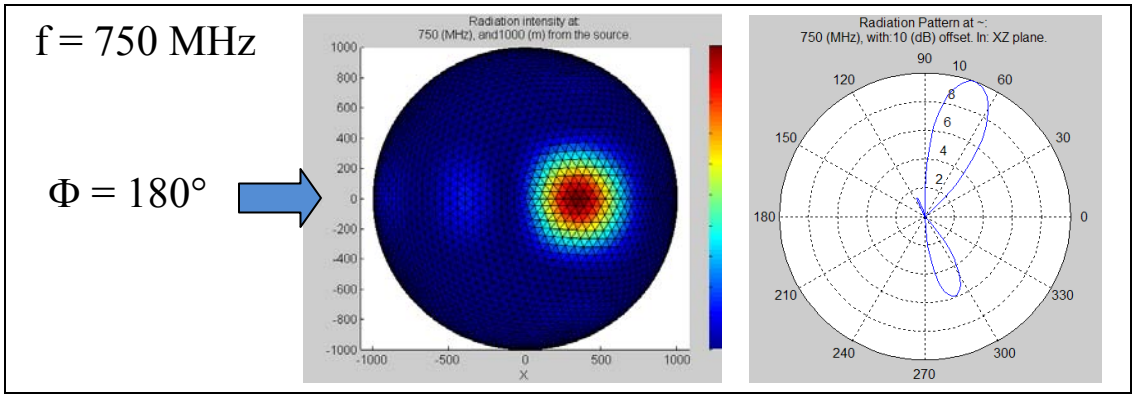

Figure A- 17 Radiation pattern of the 3×3 conical spiral array at 750MHz and 180° phase shift

From Figures A.16 and A.17, we can see that the side lobes are significantly increased as the main beam is displaced off-axis for this spiral array. And this effect is more prominent at higher frequencies provided that the element spacing remains the same. In order to acquire a reduction in the side lobes at higher frequencies, the element spacing of this array would have to be significantly reduced. However, there is maximum minimum space that can be acquired beyond which the spiral antennas would have to be overlapped, however this would result in increased coupling effects and reduced bandwidth of the array. Generally, numerous planar antennas suffer from this condition, and extensive studies are being carried out in the design of phased arrays for military, communication and astronomical purposes to reduce the degrading effects of side lobes.

A.7 Example3: Vivaldi Antenna

In this section we will introduce an example for generating the Vivaldi endfire tapered slot antenna. Originally this type of antenna was first proposed by Lewis et.al. [74]. The antenna is formed from two copper-clad substrates bonded together with a stripline conductor in the middle and ground planes having flared slots on the outer surfaces [75]. This example follows number of preliminary designs carried out during the course of this study. Several variations of the Vivaldi antenna are shown in Figure A.18.

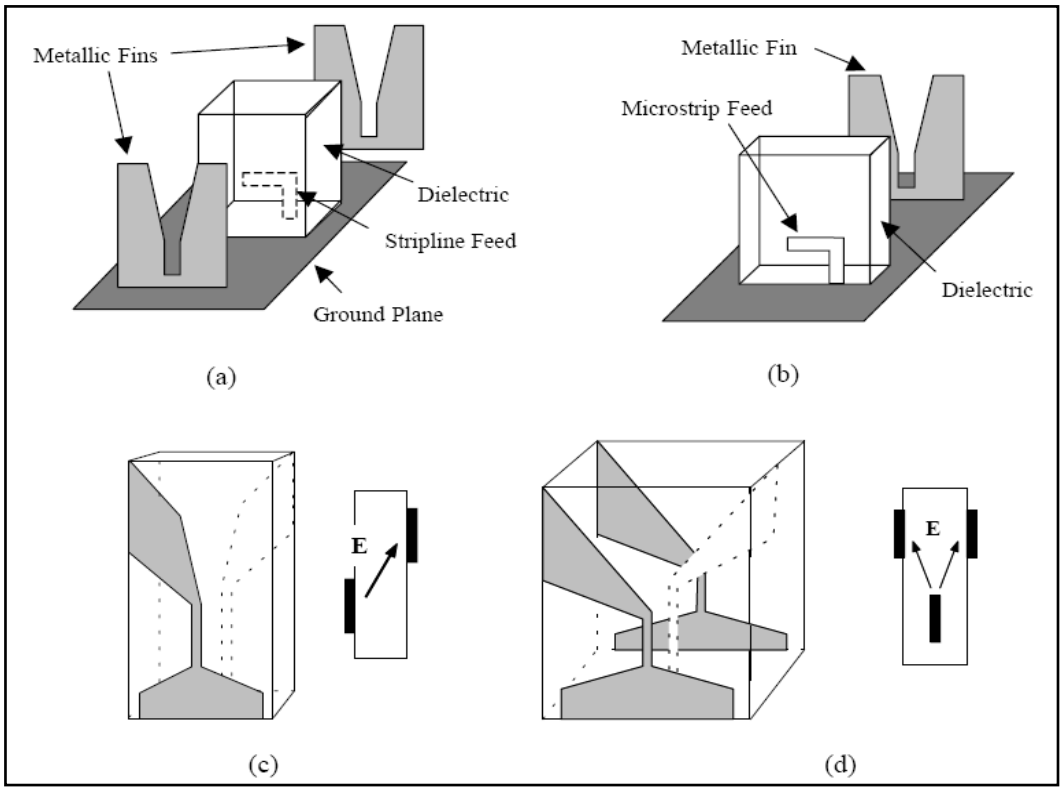

Figure A- 18 Variations of Vivaldi tapered slot antenna: Image taken from **[75]**

In this section we wish investigate the antenna structure shown in Figure A.18b, which is a microstrip version consisting of one substrate, with a ground plane on one side and a microstrip conductor on the other.

When Vivaldi endfire slot antennas are used in wide-band phased arrays, they must be smaller than 1/2 wavelength at the highest operating frequency to insure that the individual elements are small enough to fit into the required array spacing [75]. We will therefore design our Vivaldi antenna based on this rule, with the assumption that we will use the element to build an array. We wish the highest frequency of operation to be 1500 MHz, this means that the maximum size of the element must be less than or equal 1/2 wavelength which is 0.1 m. Dimensions of this Vivaldi structure is shown in Figure A.19.

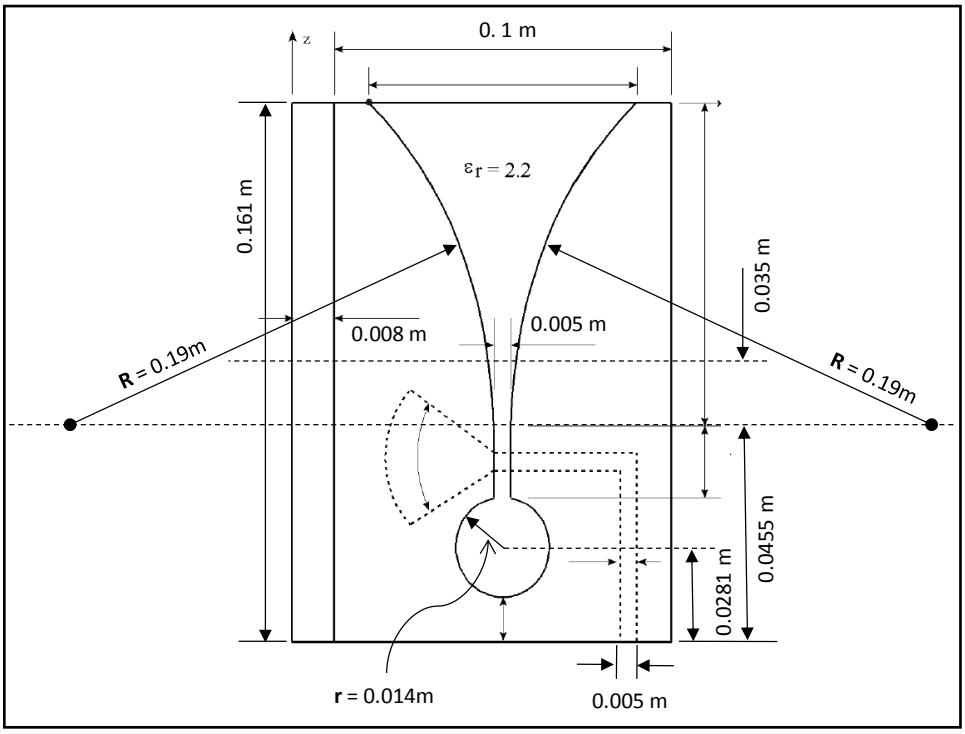

Figure A- 19 Dimensions of the Vivaldi antenna

The following structure can be created using the 2DOG and the Mesh generator functions. The object parameters required to build the Vivaldi antenna structure is shown in Figure A.20.

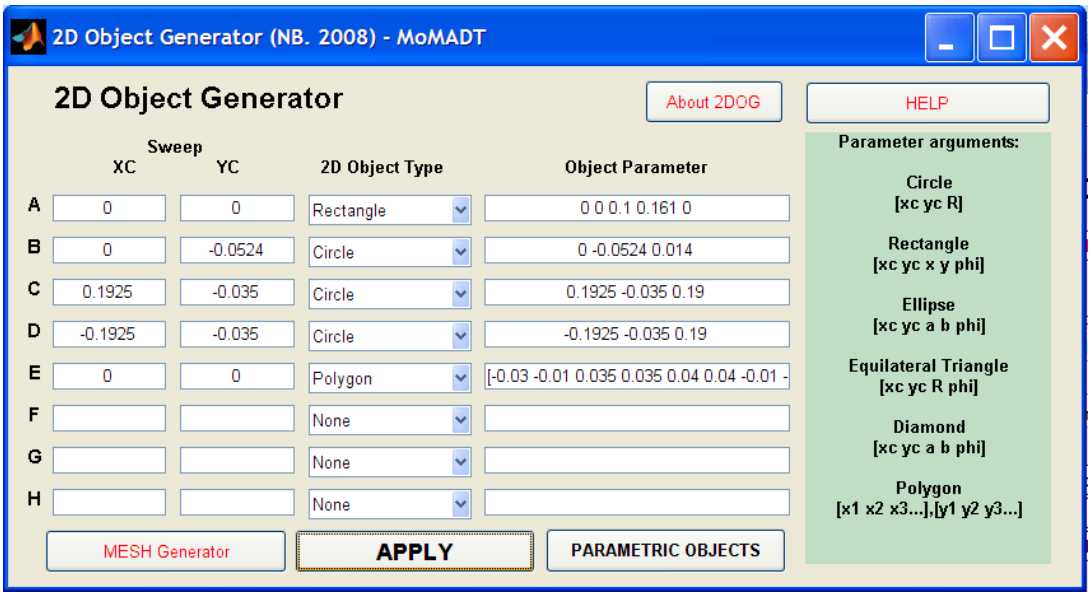

Figure A- 20 2DOG object parameters for building Vivaldi tapered slot microstrip antenna

When appropriate object parameters are set, as shown in Figure A.20, 2DOG can immediately initialize these objects in Mesh Generator application upon request. From this structure a triangularly discretized two dimensional structure can be generated as shown in Figure A.21, using a process called Delaunay triangulation.

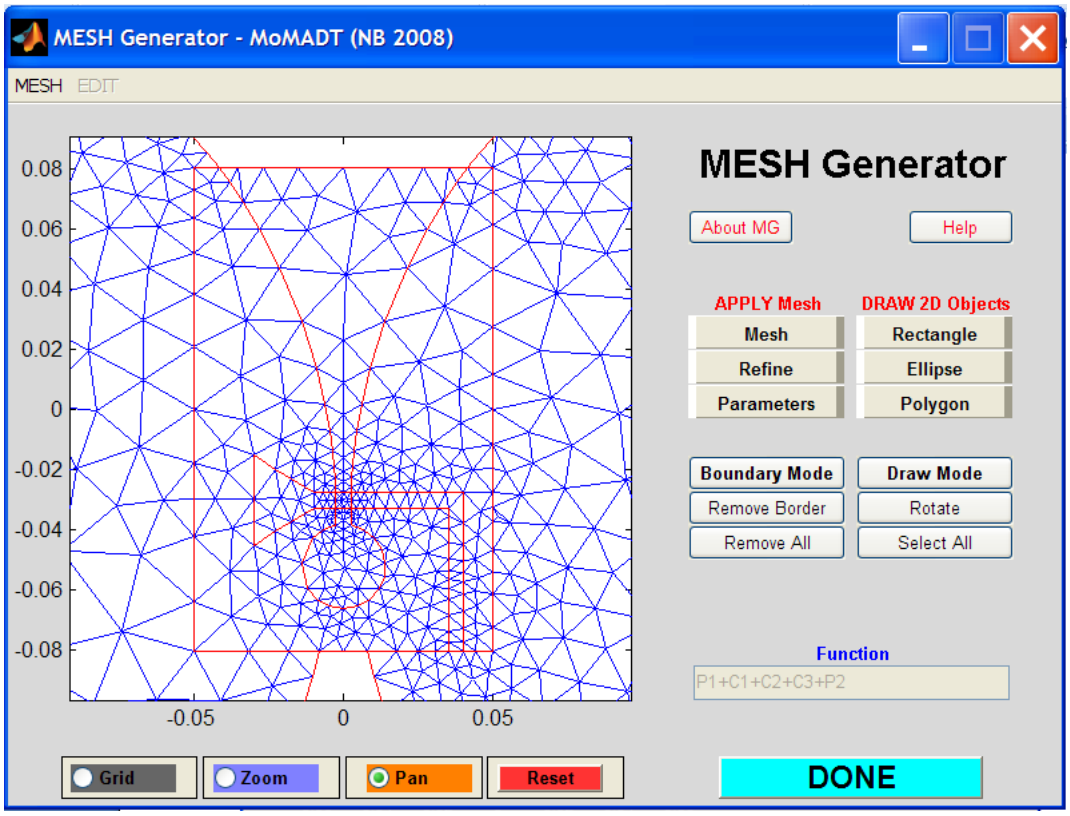

Figure A- 21 Delaunay triangulation applied on the Vivaldi 2D structure

Figure A.21 shows the final configuration of the 2D Vivaldi structure with mesh applied. It is also possible to modify the Mesh Parameters in order to reduce the number of triangle elements. This can be achieved by modifying the mesh parameters within the Mesh Generator interface.

We can now proceed to the next stage of building a 3D structure using the 3D function from within the MoMADT interface. The final structure of the Vivaldi antenna is shown in Figure A.22.

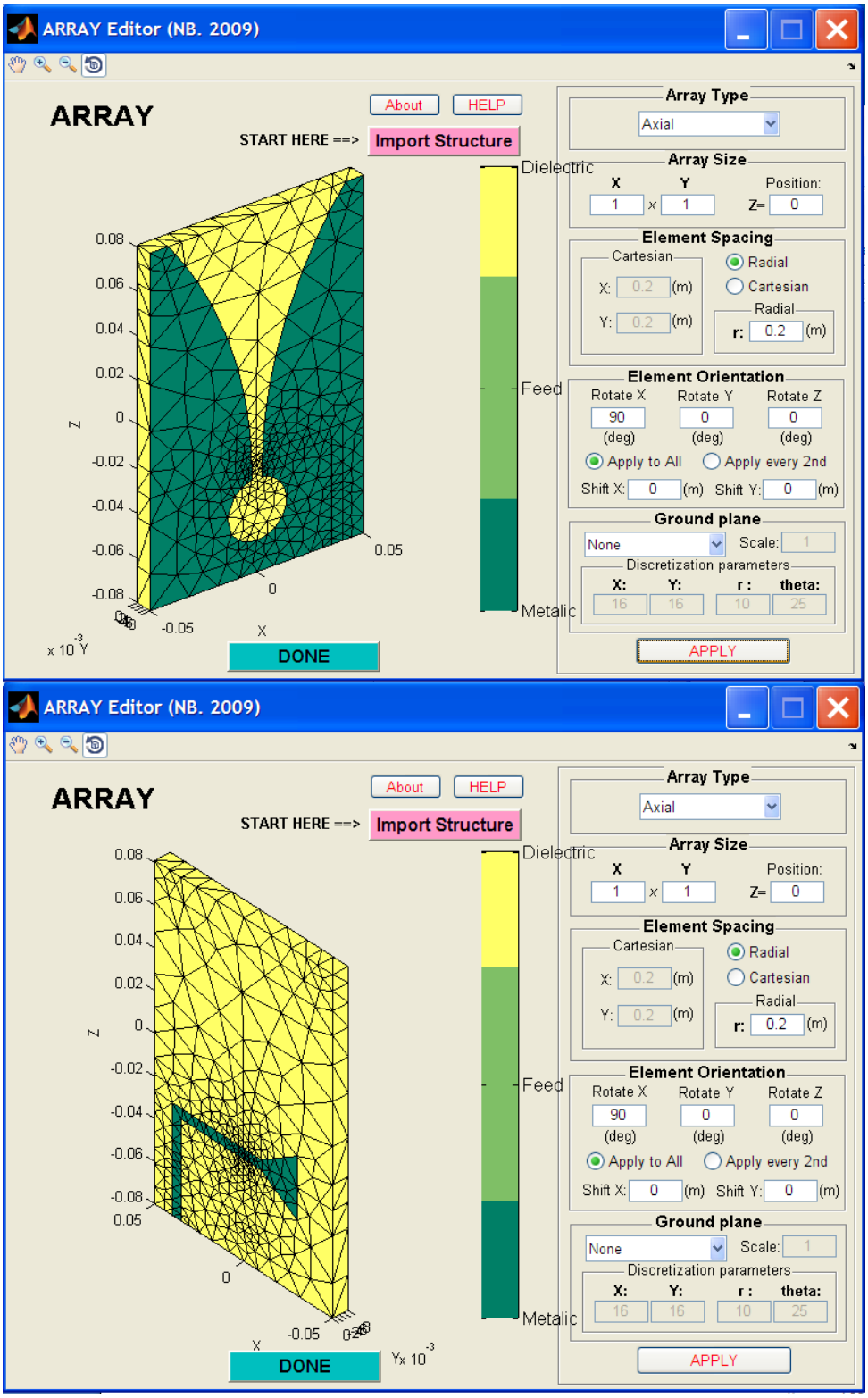

Figure A- 22 Final Vivaldi antenna structure rotated using the Array Editor function

Figure A.23 shows the impedance versus frequency solution for the Vivaldi antenna calculated using the MoM3D solver with frequency range 200 MHz-2500 MHz and 100 frequency steps. The figure clearly illustrates that although the Vivaldi antenna relies on electrical length to produce unidirectional radiation, the length of the structure causes sharp resonances, leading to large variations in the input impedance as previously explain in section 1.2.

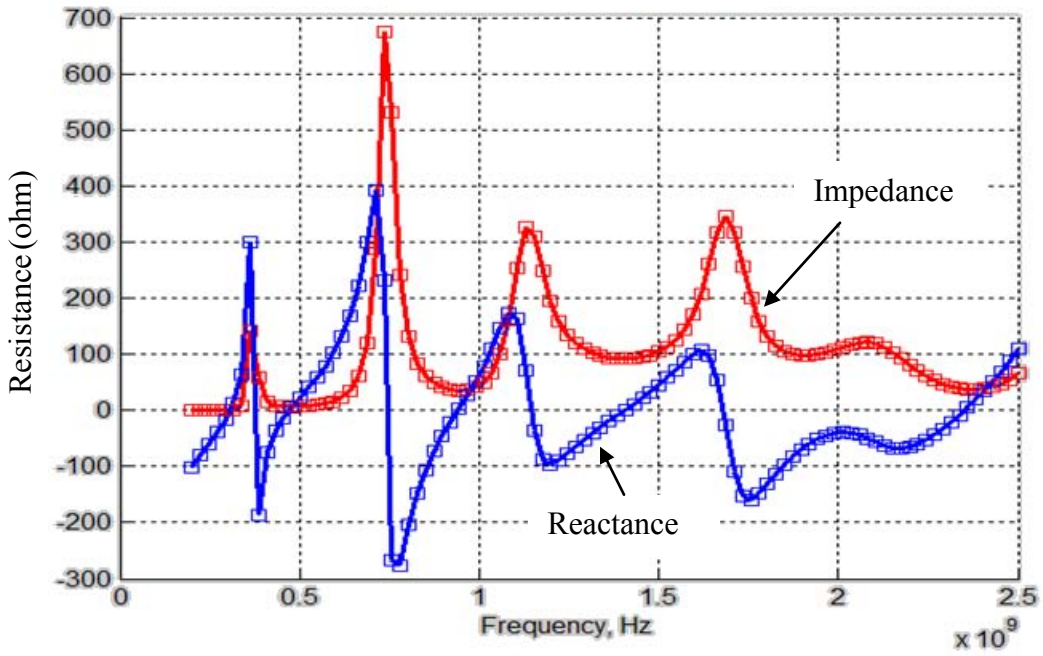

Figure A- 23 Impedance and reactance versus frequency for the Vivaldi antenna calculated suing the MoM3D solver

We can use the 3D function and the ARRAY functions to generate a variation of Vivaldi antennas, and build these antennas into an array. Figure A.24a shows an alternate variation of the Vivaldi antenna, and Figure A.24b shows the Vivaldi Antenna array developed using the Array Editor function.

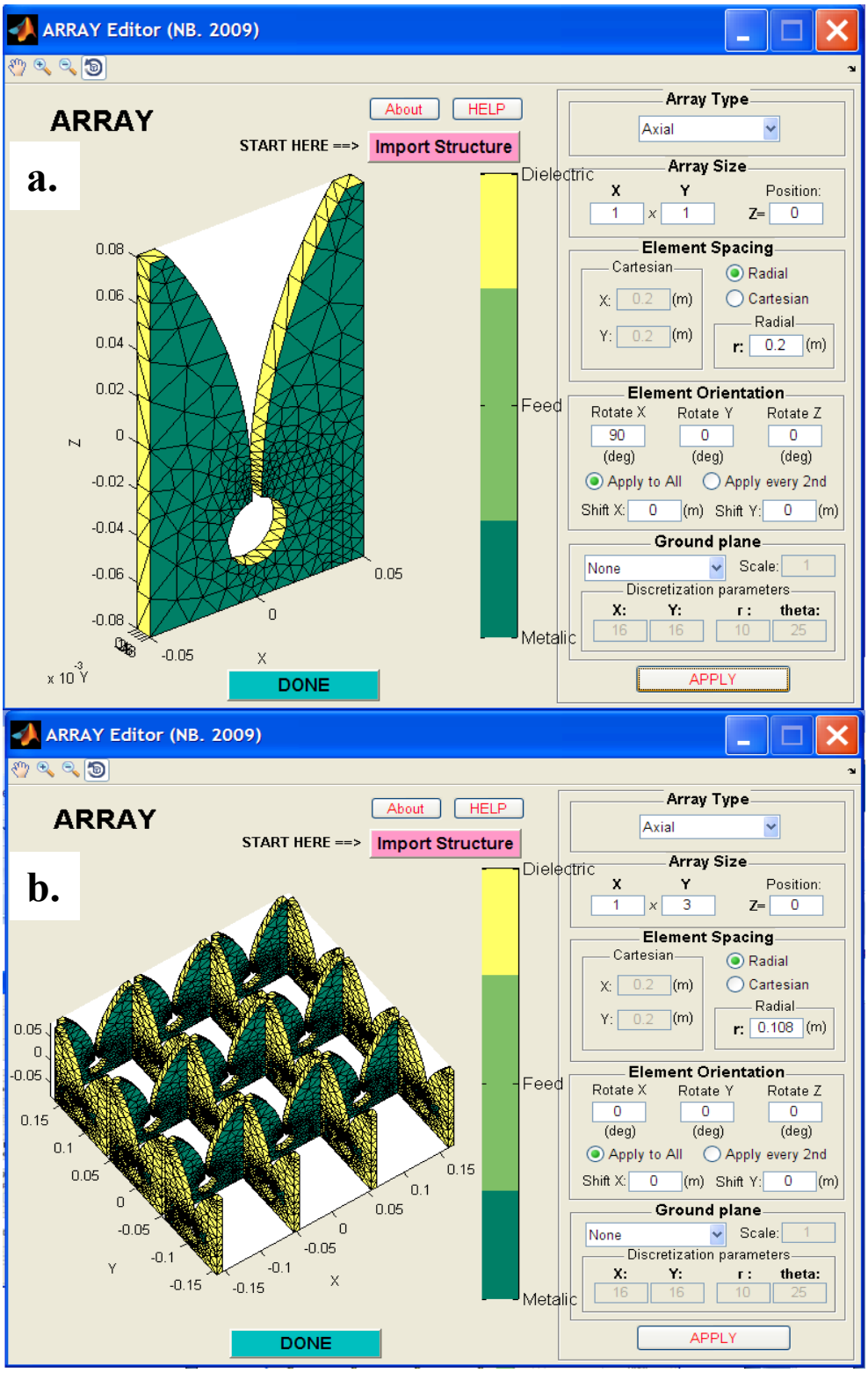

Figure A- 24 a) Alternate variation of the Vivaldi antenna with the central portion of the dielectric removed, and b) Vivaldi antenna array

A.8 MoMADT versus Ansoft HFSS

In this section, a direct comparison between the MoMADT and the Ansoft HFSS software is obtained through modelling of two distinct antenna structures, namely the patch antenna and a monopole antenna structures.

A.8.1 Patch Antenna

The first example is presented using a patch antenna shown in Figure A.25. By design, this antenna is a Linearly-polarized patch antenna, resonant at 2.37 GHz with 1.0% bandwidth and a relative permittivity of $\varepsilon = 2.33$.

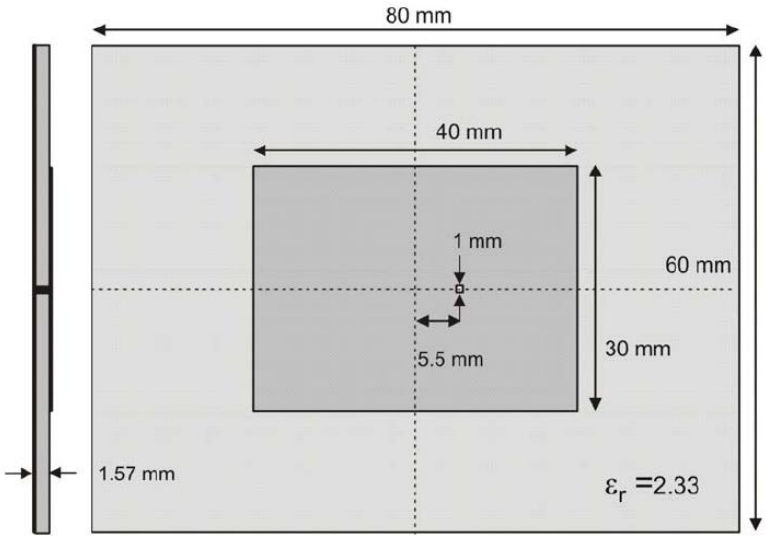

Figure A- 25 Linearly polarized Patch antenna

Through a process described in the previous sections, the patch antenna of interested (Figure A.25) was constructed through a series of steps using the 2DOG, Mesh Generator and the 3D functions from within the MoMADT interface. The complete structure is illustrated in Figure A.26.

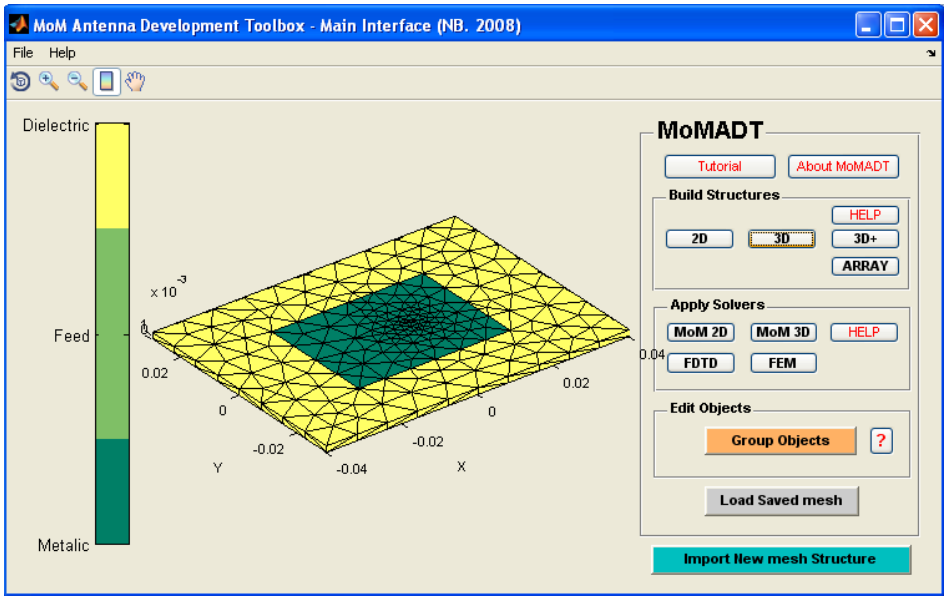

Figure A- 26 Patch antenna in Figure A.25 constructed using MoMADT

Figure A.26 shows the patch antenna of interest constructed using MoMADT. And Figure A.27 shows the impedance versus frequency solution obtained using MoMADT and Ansoft HFSS software.

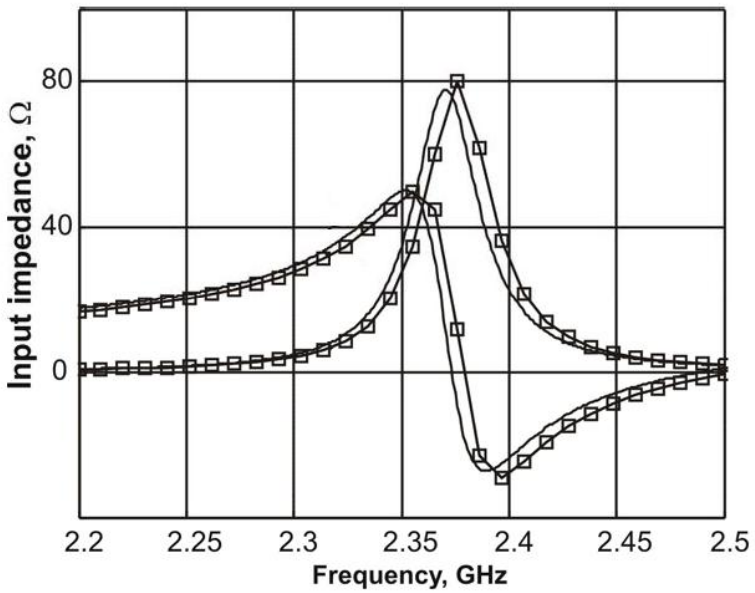

Figure A- 27 Impedance versus frequency curves for the patch antenna. Squared curves– MoM3D solution for the resistance/reactance; solid curves – Ansoft HFSS solution.

As can be seen, Figure A.27 shows that the solutions between MoMADT and Ansoft HFSS are in good agreement. The accuracy of these results can be further improved by increasing the resolution of the mesh for the patch antenna and obtaining a result with higher number of frequency steps.

A.8.2 Monopole Antenna

Another example that proves the reliability and accuracy of MoMADT solvers is demonstrated using the Monopole antenna structure shown in Figure A.28. This structure was created using MoMADT through a series of processes described above. Dimensions of the structure is illustrated in Figure A.28.

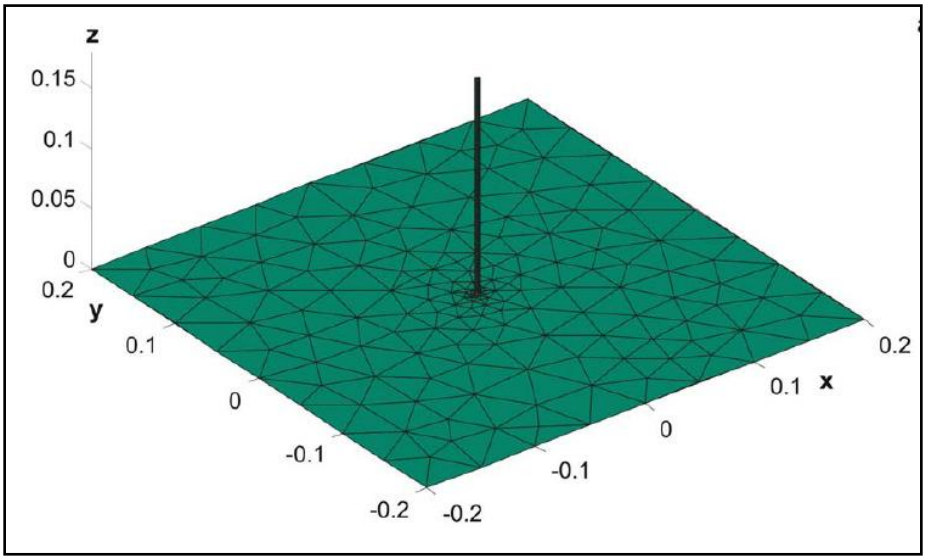

Figure A- 28 Monopole antenna structure built using MoMADT

Once again, two distinct set of solutions were generated for this antenna using the MoM3D solver found within the MoMADT interface, and the Ansoft HFSS solver. The general result compares the frequency response of the antenna between MoMADT and Ansoft HFSS FEM simulator. Results are illustrated in Figure A.29.

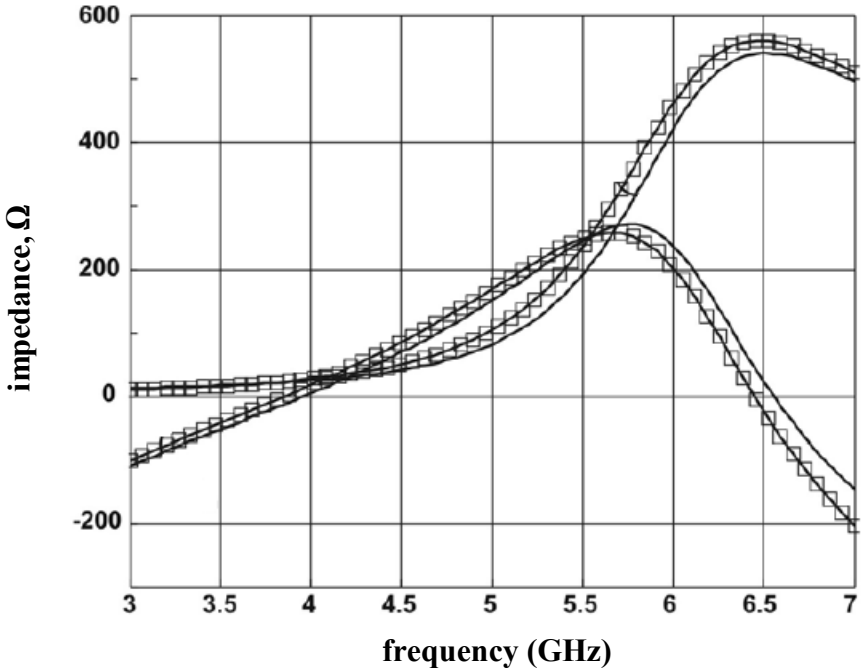

Figure A- 29 Impedance versus frequency curves for the monopole antenna. Squared curves– MoM3D solution for the resistance/reactance; solid curves – Ansoft HFSS solution.

As can be seen, Figure A.29 shows that the solutions between MoMADT and Ansoft HFSS are in good agreement.

Further proof of the method of moments and related computational electromagnetic theory, adopted in this study, is presented by Makarov [57] and Kulkarni [64].

APPENDIX B

Appendix B - The Triple-Polarized Bowtie Array

In Chapter 2 of this dissertation, a series of conclusions were presented that led to the decision of designing the FPA that provides three vectors of polarization. It was then discussed that one such system can be constructed utilizing the linearly polarized antenna elements aligned in three distinct angles about the axis normal to the antenna plane, and that such system could be designed using the linearly polarized dipole or bowtie antenna elements. In this section we present an alternate variation of the triple-polarized FPA, designed specifically in this study, utilizing the 60° linearly polarized "bowtie" planar strip antenna elements. The design of this array was derived through modelling procedures utilizing the MoMADT design tool.

The "triple-polarized" (or three-angle) bowtie array behaves much similar to the HDT array presented in chapter 3, as far as the polarization is concerned, however the feed network is much easier to realise and follows a very simple dipole network approach. The triple-polarized bowtie array is shown in Figure B.1.

The array in Figure B.1 comprises a series of 60° bowties planar strip antenna elements arranged in three distinct angles about the axis normal to the antenna plane, as illustrated in Figure B.2. In this design, each of the equilateral triangle strip antenna elements share only one feed, hence generating a circular bowtie like structure in Figure B.2. This bowtie arrangement is then assembled into a 5×5 hexagonal array with the ground plane distance set at 0.06 m beneath the radiating elements.

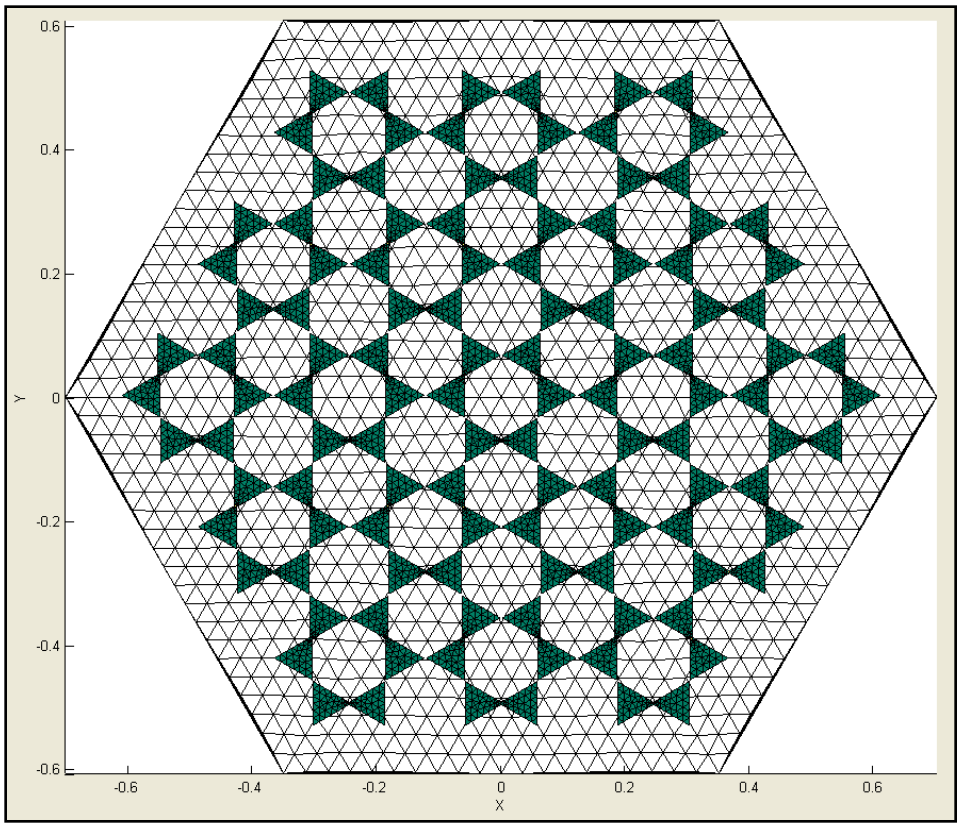

Figure B- 1 Triple-polarized Bowtie FPA

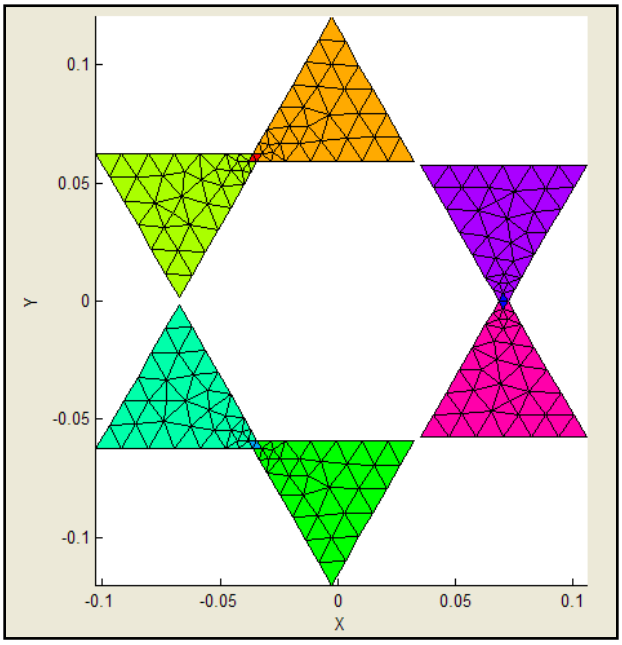

Figure B- 2 Bowtie antennas arranged in three distinct angles $(2\pi/3)°$ apart

The element pattern of the triple-polarized bowtie array provides the ability to distinguish the polarisation via three vectors at any angle normal to the antenna plane using an amplitude comparison approach, in a similar manner as obtained with the 5x5 and the 7x7 HDT arrays. The only difference is that the HDT array is a more compact array, in that the diamond planar strip antenna elements contain a larger collecting area and the element spacing of the HDT array is smaller. In addition, the bowtie strip antenna elements are much shorter than the diamond strip antenna elements, which yields limitations in the lower frequency of operation and overall decreased bandwidth compared to the HDT array presented in chapter 3. However, one advantage of the three-axis bowtie array is that the element pattern and spacing yields low distortions and reflections, as would be expected with an array containing larger element spacing. Plot of impedance versus frequency for the 5×5 triple-polarized bowtie array is shown in Figure B.3, and plot of VSWR versus frequency normalized to 300 ohm is shown in Figure B.4.

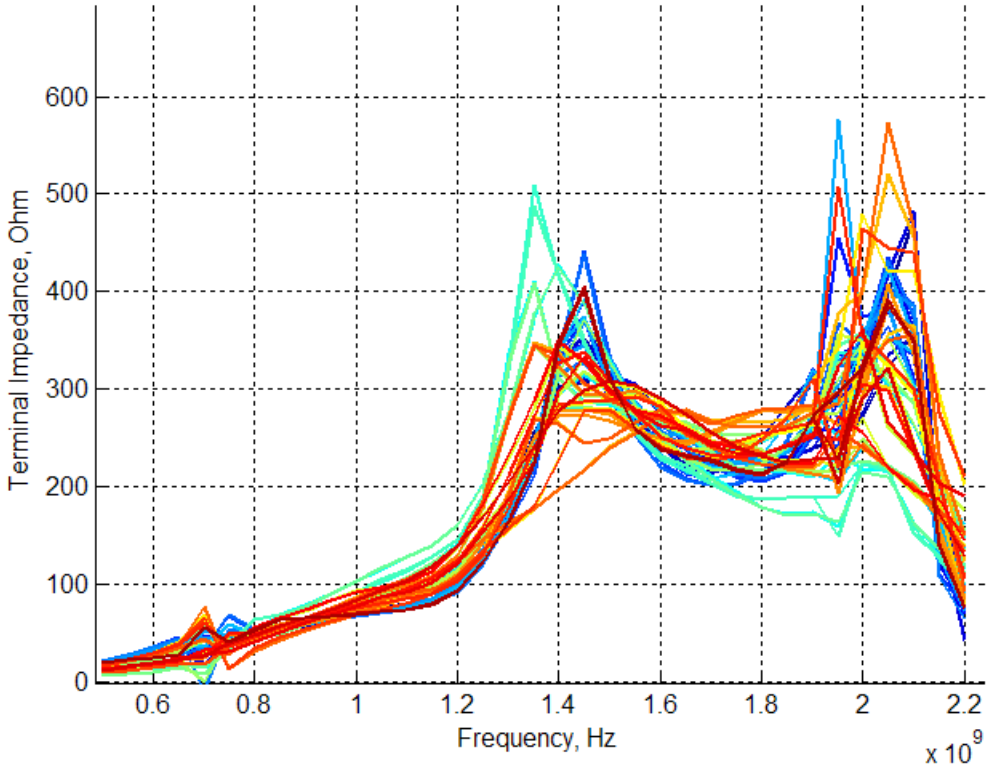

Figure B- 3 Terminal impedance versus frequency for the 5×5 three-axis bowtie array

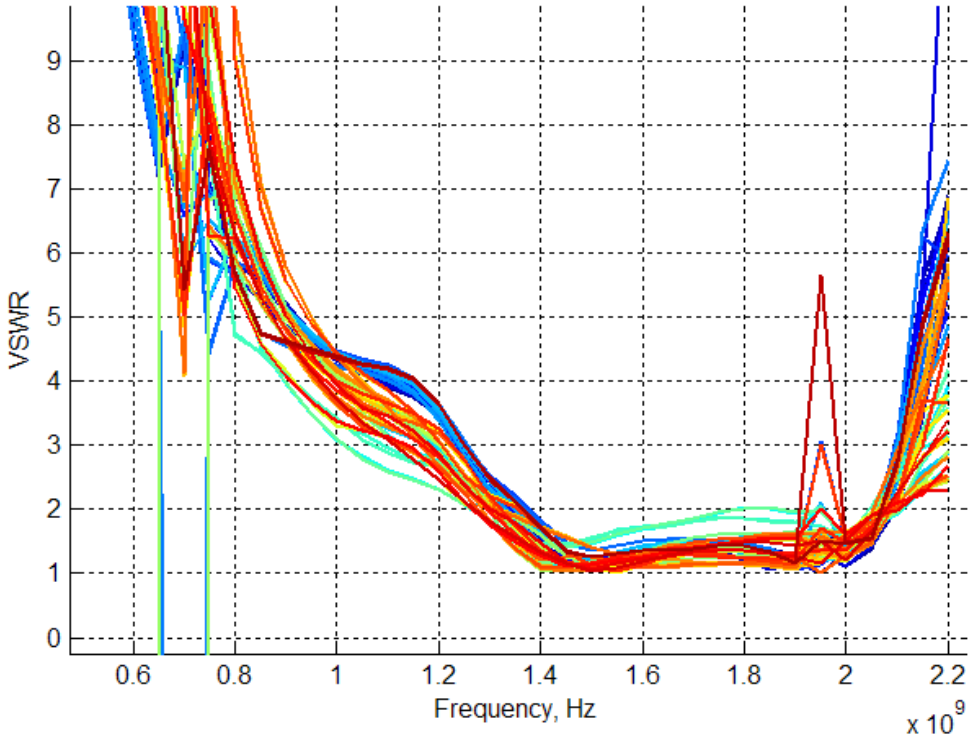

Figure B- 4 VSWR versus frequency for the 5×5 three-axis bowtie array, normalized to 300 ohm

As can be seen, the bandwidth of the 5×5 triple-polarized bowtie array is much smaller than the HDT arrays presented in chapter 3. Another disadvantage of the triple-polarized bowtie array is that it does not radiate very efficiently at lower frequencies, while the upper operating frequency is limited by the element spacing. Overall, even though the 5x5 thee-axis bowtie array provides good polarization diversity, it yields a bandwidth ratio of only ~1.6:1.

APPENDIX C

Appendix C - Instrumentation

In this section we disclose a short description of the numerous instruments used during the design, modelling and measurement procedures undertaken in this project. As discussed in Appendix A the MoMADT is a 64 bit modelling software developed under Matlab and C++ programming languages, for a 64 bit windows platform. As a result, a 2.8 GHz quad core PC based 64 bit CPU, with 8+ GB of ram was required to carry out the modelling and simulation procedures undertaken during the course of this study. This instrumentation was purchased privately together with the necessary software including Matlab R2008a, and the Microsoft Visual Studio 2008.

An ELAD SNA2550 two port network analyser (Figure C.1), with measurement frequency range of 400-2550 MHz, was then purchased and used for the measurement procedure performed on the diamond tripole antenna and the 7x7 HDT array including numerous other antennas developed in this study. For proper operation the SNA2550 is controlled by a PC trough a USB 2.0 port and dedicated software.

Figure C- 1 SNA2550 Network analyzer

SNA-2550 is an instrument capable of measuring the impedance matching and the gain of circuits with a nominal impedance of 50 ohm. The measurement is performed by generating a sinusoidal signal, not modulated, with prescribed amplitude and frequency and measuring the input signal to the receiver with a wideband detector; this method has some limitations concerning dynamic range for low level signal (minimum detachable signal), but it has the fundamental advantage that it is easy to measure the conversion gain of circuits with input frequency different from output frequency. The SNA-2550 is factory calibrated against Agilent 8753C network analyser.

As explained in chapter 4, the 7×7 HDT array was manufactured locally from range of materials described in chapter 4. The array contains a four layer formation as shown in Figure C.2.

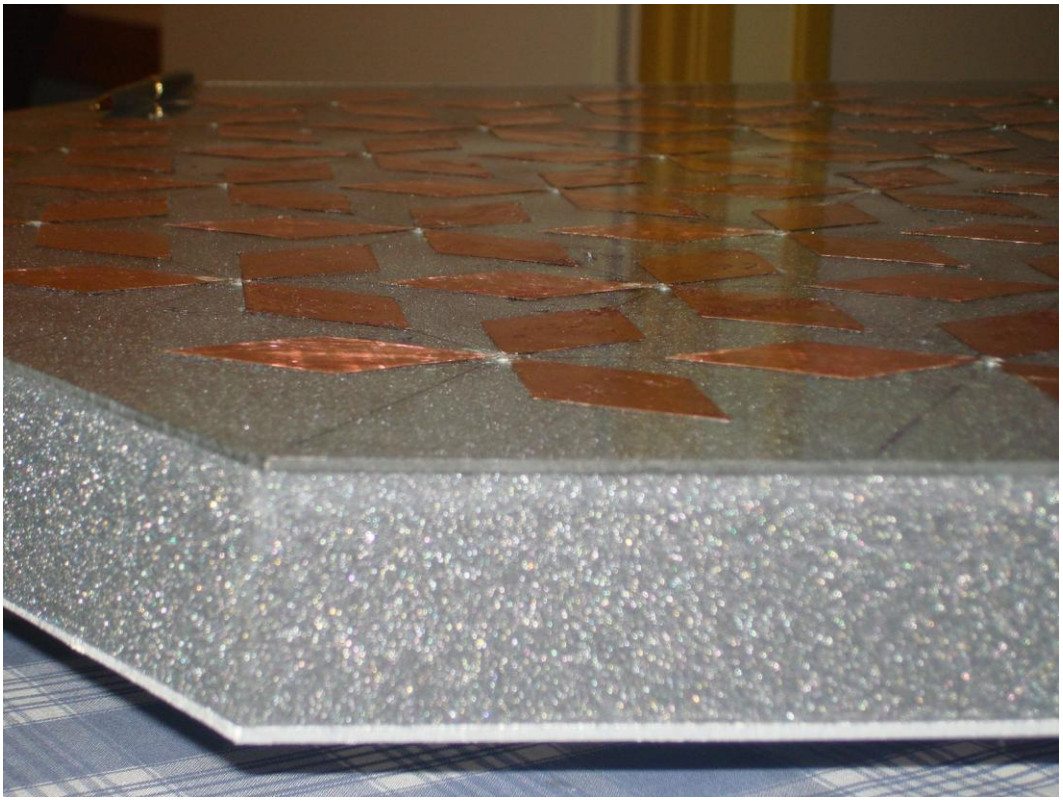

Figure C- 2 Side view of the 7×7 HDT array

The 7×7 HDT array together with related SNA2550 is shown in Figure C.3.

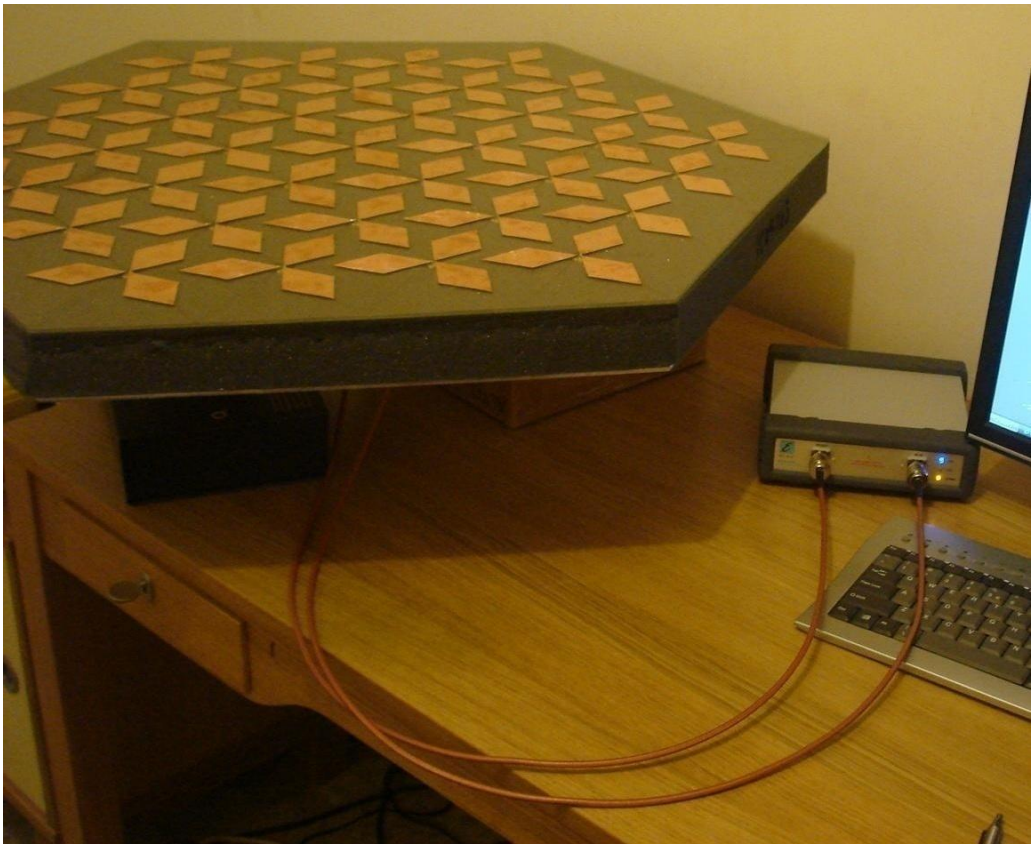

Figure C- 3 The 7×7 HDT array together with SNA2550